



Provided by the author(s) and University of Galway in accordance with publisher policies. Please cite the published version when available.

| | |
|------------------|---|
| Title | Spatio-Temporal Visual Response for Ocular Correction of Higher-Order Aberrations |
| Author(s) | De Lestrangé-angénieur, Elie |
| Publication Date | 2013-04-24 |
| Item record | http://hdl.handle.net/10379/3574 |

Downloaded 2024-04-25T05:06:00Z

Some rights reserved. For more information, please see the item record link above.



Spatio-Temporal Visual Response for Ocular Correction of Higher-Order Aberrations

by

Elie deLeStrange

Supervisor: Professor J.C. Dainty

A thesis submitted in partial fulfilment for the
degree of Doctor of Philosophy

Applied Optics Group, School of Physics,
College of Science,
National University of Ireland, Galway

May 2013

Abstract

With the development of control aberration using adaptive optics (AO), particular emphasis has been given recently to the impact of higher-order aberrations (HOAs) on visual performance, with a view to improved refractive corrections, for example using customised intra-ocular lenses (IOLs). However, to date most studies have used simple static visual tasks, whereas more complex realistic tasks are required to reveal the spatio-temporal complexity of the human visual response.

In this Thesis, we start by performing an introductory study of spherical versus aspheric IOL design, in which the need for exact ray-tracing is emphasised, demonstrating the significance of higher-order aberrations in post-operative surgery correction as well as in realistic eye models.

Turning to visual characterization of HOAs and their predictability by metrics, the development of a new adaptive optics vision simulator is addressed. We describe the design, construction and testing of this AO system. In an experiment in which we correct the natural aberrations of the eye, and introduce fixed amounts of pure Seidel aberrations, we measure how the psychophysical visual acuity changes and compare the results with metrics. By combining the aberration control of this new system with computational manipulations of the spatio-temporal stimulation based on advanced attentional paradigms, we show that the perceived degradation by HOAs is a distinctly sensitive response that varies with the nature of the stimulation and the spatio-temporal pathway visually excited. This study concludes that aberrations not only affect absolute visual performance, but also may adjust the mediative mechanism that articulates spatial and temporal visual representations. This novel result has important consequences for the expansion and assessment of customized refractive correction, and provides a new method for understanding cortical plasticity and visual function.

Acknowledgements

I would start by acknowledging the softness that enveloped my stay in Ireland and the particular kindness of its inhabitants.

There are many persons to thank. Alcon Ireland Limited and The Irish Research Council for their financial support which made this work possible and in particular Barry Walsh of Alcon for his encouragement and support. My colleagues and friends who were really something in the to and fro to the lab, interrupted by the pub light. I must also thank many persons from whom I learned (and borrowed), like Eugenie Dalimier, Andrew Lambert, Alexander Goncharov, Charlie Leroux and Huanqing Guo . . . but indeed, at the same time, forgetting in that short list many others!

Foremost, my deepest gratitude goes to my supervisor, Chris Dainty, for the invaluable chance he offered me by integrating me in his group and as his student.

I reserve the last words to send all my love to my parents and my family for their tender and unfailing support.

Preface and synopsis

Refractive correction involves a rich variety of aspects of visual perception, and the generally accepted “gold standard” is to strive for perfect optical correction. That correction, whether accommodative or static, covers only a localized enhancement of perception (for example, the visual acuity as estimated by a Snellen letter chart) and often ignores the complexity intrinsic to the image and to visual tasks: current practice therefore regards the visual system as being static and immediate in processing. However, the visual system is highly multiplexed, and forms, at the neural stage, concurrent and interlinked representations that constitute, correct and update our perception of the visual world. Point-by-point analyses are over-simplified and do not consider the integrative properties of visual response, involved in perceived image degradation and which, we believe (and demonstrate in this Thesis), carry a spatio-temporal dimension.

Building upon the perception of stationary stimuli, this study highlights the possibility of measurement and enhancement of visual function by modulating the spatial and temporal signature of the aberration profiles, and addresses the following question: how do spatio-temporal aberration conditions influence the dynamics of signal propagation in the complex neuronal circuitry?

The Thesis is divided into three streams of research, motivated by the challenge of enhanced customized visual corrections:

- (i) optical modeling of intra-ocular lenses (IOLs),
- (ii) visual simulation of optically altered images and
- (iii) the implication of post-retinal processing in the visual performance of the observer.

In Chapter 1, we present background material on various forms of optical degradation present in the eye and some of their methods of evaluation.

In Chapter 2, the objective optical performance of a range of standard intraocular lenses (IOLs), having refractive and diffractive properties with aspherization structures, is evaluated in vitro and then simulated in the framework of a post-operative correction in the eye, using ray-tracing software and eye models. The advantage of post-operative prediction by ray-tracing power calculation over empirical formulae as well as the importance of higher-order aberration (HOAs) in moderate induced variations (e.g. occurring in surgery) is highlighted in the context of cataract refraction.

In Chapter 3, the hardware and software integration of a custom-built visual simulator for testing aberrations, and possibly IOLs, is described. We present considerations related to the optical target and performance of a compact optical design. The extension to a wider field angle is investigated for allowing the visual simulation of real daily visual tasks.

In Chapters 4 and 5, we investigate the interplay and relationship between optical degradation and neural factors by attempting to modulate the operation of post-processing. Chapter 4 describes the impact of post-processing on perceived degradation of the retinal image and develops on competitive visual stimulation methods, using post- and pre-target stimuli, for guiding the visual attention of the observer. A facilitatory effect of the presence of post- and pre-targets for a near-diffraction image is observed on visual acuity, together with an inhibitory effect when the subject looks through their own aberration, in support of distinct processing mechanisms of optically degraded stimuli.

Chapter 5 elaborates a way to test the neuronal activity propagation associated with distinct higher-order aberrations by means of a time varying aberration. A significant impact of the spatio-temporal variation of the stimulus on the degradation pattern of the perceived image of a face is shown: perceived degradation is found to be dependent on the temporal evolution of blur, and acts from the very early onset of the stimulation. Our experiment suggests a spatial and temporal signature

of the visual response, that is subject dependent. The impact of the deviation is conditioned by the mean aberration and suggests a trade-off between absolute spatial optical performance and temporal sensitivity. We interpret it as a possible strategy of the visual system to balance the amount of information accessed and consciously processed, in other words the efficacy of the neuronal response of the visual system in the context of an adaptive and dynamic spatial representation.

The research presented in this Thesis aims at unveiling the relationship between neuronal filtering architecture and aberration impact. It develops new strategies, methods and thoughts to decipher the implication of aberrations in the cognitive mechanism, and their eventual application in a customized refraction.

Contents

| | | |
|----------|--|-----------|
| 1 | Optical imaging in the eye | 14 |
| 1.1 | Image formation | 14 |
| 1.1.1 | Propagation of the complex amplitude | 14 |
| 1.1.2 | Aberration: the barrier to perfect imaging | 20 |
| 1.1.3 | The aberrated surface | 20 |
| 1.1.4 | Beyond monochromatic aberrations | 26 |
| 1.2 | Image quality measurement | 30 |
| 1.2.1 | Image formation | 30 |
| 1.2.2 | Assessment of the retinal image | 34 |
| 2 | Correction by intraocular lenses and predictability | 43 |
| 2.1 | Eye modelling | 43 |
| 2.1.1 | Static and dynamic optical features | 44 |

| | |
|---|-----------|
| <i>CONTENTS</i> | 7 |
| 2.1.2 From the coarse average normal eye to individual real eye . . . | 48 |
| 2.2 Refractive correction by IOLs | 51 |
| 2.2.1 The IOL solution | 51 |
| 2.2.2 IOLs quality | 53 |
| 2.3 Post-operative refractive correction sensitivity | 65 |
| 2.3.1 Effect of manufacturing defects of IOLs on vision | 65 |
| 2.3.2 Power calculation methods | 70 |
| 2.3.3 Thin lens power calculation methods | 71 |
| 2.3.4 Thin lens and Ray-tracing model comparison for spherical and aspheric design in condition of moderate amount of errors . . . | 74 |
| 2.4 Conclusion | 79 |
| 3 Adaptive Optics Visual Simulator | 81 |
| 3.1 Context | 81 |
| 3.2 Visual Analyser design | 82 |
| 3.2.1 Illumination and pupil control | 83 |
| 3.2.2 Calibration and construction | 87 |
| 3.3 Measuring ocular aberration | 90 |
| 3.4 Correcting ocular aberration | 92 |

| | |
|--|------------|
| <i>CONTENTS</i> | 8 |
| 3.4.1 AO performance | 103 |
| 3.5 Wavefront correction and retinal images | 108 |
| 3.6 Psychophysics arm | 111 |
| 3.6.1 The non-common path error (NCP) | 111 |
| 3.6.2 Chromatic shift and best focus strategy | 111 |
| 3.6.3 Visual stimulation using a microdisplay | 112 |
| 3.6.4 Characterization of the visual branch within the isoplanatic path of central vision | 115 |
| 3.7 Conclusion | 121 |
| 4 Post-processing of higher-order of aberration | 123 |
| 4.1 Higher-order aberrations impact on retinal image quality | 124 |
| 4.1.1 Visual performance test | 124 |
| 4.1.2 Optical performance with degraded images | 125 |
| 4.1.3 Objective quality measurement | 126 |
| 4.1.4 Origins of discrepancy between objective and subjective mea- surement | 129 |
| 4.2 Role of awareness in post-processing of altered images | 131 |
| 4.2.1 Plasticity of post-processing and image constancy | 131 |
| 4.2.2 Degradation and level of representation targeted | 133 |

| | | |
|----------|--|------------|
| 4.3 | Methods based on a competitive stimulus processed by the brain . . . | 139 |
| 4.3.1 | Implementation of several methods | 140 |
| 4.3.2 | Temporal masking techniques | 142 |
| 4.3.3 | Combining visual masking and ocular aberration manipulation | 144 |
| 4.3.4 | Multiplexing of optically degraded images | 150 |
| 4.4 | Conclusion | 152 |
| 5 | A time-varying input aberration | 153 |
| 5.1 | How far is the eye from an AO system? | 154 |
| 5.1.1 | Neuronal activity and propagation | 154 |
| 5.2 | Spatio-temporal dynamism of the image | 159 |
| 5.2.1 | Previous studies | 159 |
| 5.2.2 | Method | 160 |
| 5.2.3 | Role of time and spatial amplification on perceived sharpness and image appearance | 161 |
| 5.2.4 | Evidence of a 'mobilization state' of the neuronal workspace with respect to time and space | 169 |
| 5.3 | Conclusion | 182 |
| 6 | Summary and discussion | 185 |

6.1 Future work: neural noise and aberration in customized correction . 187

List of Acronyms

AO Adaptive optics

AST0 Zernike astigmatism at 0 deg balanced with defocus

AST45 Zernike astigmatism at 45 deg balanced with defocus

AT spherical intraocular lens design

b_i coefficient of Seidel aberration

Casao control loop interface

CL AO closed-loop

CSF Contrast sensitivity function

CRT Cathode ray tube

D Diopters

DDE Dynamic data exchange

DEF Zernike defocus

DL Diffraction-limited

DM Deformable Mirror

FT Fourier transform operator

GRIN Gradient refractive index lens

HASO32e Shack-Hartmann wavefront sensor manufactured by Imagine Eyes

HOA Higher-order aberration

HofferQ Power calculation formula based on 2-lens

Holladay Power calculation formula based on 2-lens

HSF High spatial frequency

HTF High temporal frequency

HWHM half-width at half maximum

IFM Influence function matrix

IOL intraocular lens

LCD Liquid crystal display

LOA Low-order aberration

LSF Low spatial frequency

LTF Low temporal frequency

Mirao32e Deformable mirror manufactured by Imagine Optics

MEMs Micro-electromechanical mirrors

MPE maximum permissible radiant power

MTF Modulation transfer function

NA Natural aberration of the subject

NA45 Natural aberration of the subject rotated at 45 deg

OCT Optical coherence tomography

OLED Organic Light emitting diode

OPL Optical path length

OTF Optical transfer function

P Pupil conjugate

PSF Point spread function

R Retinal conjugate

ROC Receiver operating characteristic

rms Root-mean square

S_i Seidel aberration

S_{beta} Image metrics

SA spherical aberration

SH Shack-Hartmann wavefront sensor

SLM Spatial light modulator

SLO Scanning laser ophthalmoscope

SOA Stimulus-onset asynchrony

SRK Power calculation formula based on a 2-lens model

WF aspheric intraocular lens design

Z Zernike polynomials

Chapter 1

Optical imaging in the eye

1.1 Image formation

1.1.1 Propagation of the complex amplitude

The complex amplitude

Imaging involves the propagation of the electromagnetic field, determined both in time and space, by Maxwells equations. Under the assumption of a uniform media in time and space, a simplified relationship between the scalar field U and the material properties can be developed, so-called the Helmholtz wave equation:

$$(\nabla^2 + k^2)U(\vec{r}, t, \lambda) = 0 \quad (1.1)$$

where ∇^2 is the Laplacian, t is the time and λ the wavelength of the wave. The term k is the wave number given by:

$$k = \frac{2\pi}{\lambda} = \frac{2\pi\nu}{v} \quad (1.2)$$

where v is the speed of light in the media of a particular optical frequency ν and function of the refractive index of the media $n = c/v$, with c the speed of light in a vacuum.

For monochromatic light, the optical disturbance $U(\vec{r}, t)$ at a point P image has a certain phase and amplitude, expressed following:

$$U(\vec{r}, t) = a_w(\vec{r}) \cos(\omega t - g_w(\vec{r})) \quad (1.3)$$

where $\omega = \frac{k}{c}$ corresponds to the angular frequency component of the illumination. The phenomenon of interference rises with the superposition of waves of various frequencies at a point P such that:

$$U(\vec{r}, t) = \int_0^\infty a_w(\vec{r}) \cos(\omega t - g_w(\vec{r})) d\omega \quad (1.4)$$

It results at a point image P a modulation of the field amplitude $a_w(\vec{r})$, in time and space, with the variation of the optical path of light described by the phase $\phi = \omega t - g_w(\vec{r})$. The rate and strength of the variation of the illumination is defined by the bandwidth of the source $\delta\omega$ as it can be illustrated by the complex field the superimposition of two waves, of mean frequency $(\bar{\omega}, \bar{k})$, amplitude:

$$U(\vec{r}, t) = 2a \cos\left(\frac{1}{2}t\delta\omega - \delta k\vec{r}\right) \exp(-i\bar{\omega}t - \bar{k}\vec{r}) \quad (1.5)$$

It is to note that the larger the bandwidth, the higher the irregularities of phase and amplitude, given at an instant t . Thus, for a certain time of observation, given the statistical nature of the rapid variation of the source, the degree of correlation between absolute phase of the successive wave groups forms a region of interference of light with itself, so-called region of coherence. This region is maximal if $\delta\omega \rightarrow 0$: light is said coherent. For larger bandwidth, it diminishes and the coherence is quantified by the coherence length $l_c = c\Delta\omega = \frac{\lambda^2}{\Delta\lambda}$. In this study, the polychromatic field is treated as a discrete sum of monochromatic and incoherent waves where

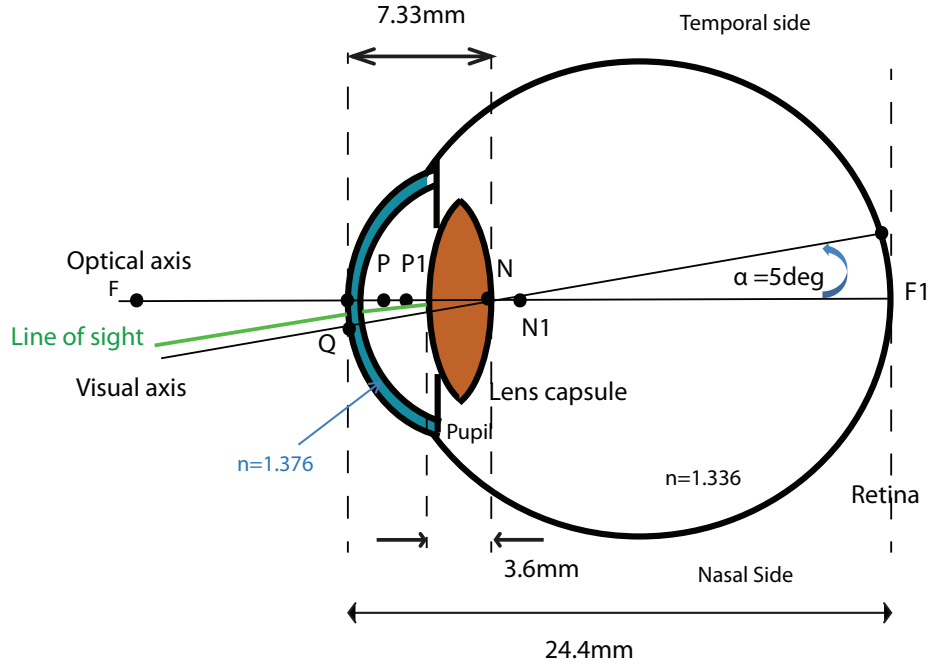


Figure 1.1: Optical schematic of the human eye.

dominate interactions with the physical environment as in refraction, diffraction and scattering.

Ray and geometrical wavefront

For a smooth field variation, the phase $g_w(\vec{r}) = k\vec{r}$ can be discretized in local surfaces of equal time from the source, that forms the geometric wavefront. These surfaces $S(\vec{r})$ obey the eikonal equation[40], derived from Maxwell's equations in the approximation of $\lambda \rightarrow 0$, and predict a displacement of a cophasal wavefield along curves collinear to the vector of flow and orthogonal to the geometric wavefront, so-called rays. Weighted by the refractive index, the curves follow an increment of $\frac{2\pi}{\lambda}$ and borrows the extremum optical path between two points along any other neighboring paths. Light rays behave as straight lines throughout homogeneous media, bending at the interface between two different refractive indices. Rays change direction by invariance of the quantity $n\sin\theta$ imposed by Snells' Law equation, where θ corresponds to the direction of the ray with respect to the normal of the surface.

Considering the regime of small angle, this relation is simplified by $\sin\theta \sim \theta$. In ideal imaging, the transformation from object to image is dictated by the ocular power, covered by the cornea curvature and the crystalline lens of the eye, such that $P_{total} = -1/f = n/f_1 \sim P_{cornea} + P_{lens} \sim 60D$.

At the exit pupil of the eye, the optical path length of the propagation at the exit pupil of the eye, is then:

$$OPL(x_1, y_1) = \frac{(x_1^2 + y_1^2)}{2f} \quad (1.6)$$

where (x_1, y_1, z) are the pupil coordinates taken at the exit pupil of the eye.

On axis, the extension of imaging is bound by Newtons formula, according to:

$$l * l_1 = f * f_1, \quad (1.7)$$

where $l = OF$ and $l_1 = O_1F_1$ are associated to the distance of a point object O and image O_1 from their focal respective and $f = PF = +22.3mm$, $f_1 = P_1F_1 = 16.7mm$ are the anterior and posterior focal length, reported in Fig-1.1.

Limit due to diffraction

The ray or geometrical description of imaging ignores diffraction, a fundamental property of waves. The Huygens Fresnel principle stipulates that any disturbance U_{II} at a point $P(x, y, z)$ on a surface, can be regarded as the superposition of fictitious elementary coherent spherical waves $\frac{\exp(ikR)}{R}$ of varying amplitude $U_I \cos(\Psi)$ and spatial frequency $f = \frac{\Psi}{\lambda}$ from an earlier surface, that is:

$$U_{II}(x, y, z) = \frac{-i}{\lambda} \int \int_{\Sigma} U_I(x_1, y_1, 0) \cos(\Psi) \frac{\exp(ikR)}{R} dx_1 dy_1, \quad (1.8)$$

where Ψ is the obliquity angle between the normal of the pupil plane Σ , and the propagation vector and R the distance of propagation between spaces. Considering

the near field of the aperture, an expansion of R in a binomial series follows the Fresnel approximation, where only terms up to the second order are retained:

$$R \sim z + \frac{x^2 + y^2 + x_1^2 + y_1^2 - 2(xx_1 + yy_1)}{z} \quad (1.9)$$

Thus, in the Fresnel approximation:

$$U_{II}(x, y, z) \propto \int \int_{\Sigma} U_I(x_1, y_1, 0) \exp(i\frac{k}{2z}(x^2 + y^2)) \exp(-i\frac{k}{z}(xx_1 + yy_1)) dx_1 dy_1, \quad (1.10)$$

When no aberrations are present, i.e. the phase delay of a perfect spherical lens:

$$U_I(x_1, y_1, z = 0) = \exp(-jkOPL(x_1, y_1)), \quad (1.11)$$

By putting $z = f$, the relationship 1.10 is reduced to an exact Fourier transform [122].

$$U_{II}(x, y, z) \propto \int \int_{\Sigma} \exp(-i\frac{k}{z}(xx_1 + yy_1)) dx_1 dy_1 \propto F(A(x_1, y_1)), \quad (1.12)$$

where A is a clear circular aperture pupil. The image coordinates $(\tilde{x}, \tilde{y}) = (kx/z, ky/z)$ have the units of inverse distance and are the spatial frequency of the pupil function.

In polar coordinates, the normalized field becomes:

$$U_{II}(\rho, \theta) = \frac{2\lambda f}{\pi D \rho} J_1\left(\frac{\pi D \rho}{\lambda f}\right) \quad (1.13)$$

where J_1 is the Bessel function of the first kind, order 1. The distribution of the field forms the well-known Airy pattern, series of concentric rings encircling a central lobe, which fixes the first limit of imaging with a resolution, function of illumination and system dimension:

$$\Psi = 1.22 \frac{\lambda}{D}, \quad (1.14)$$

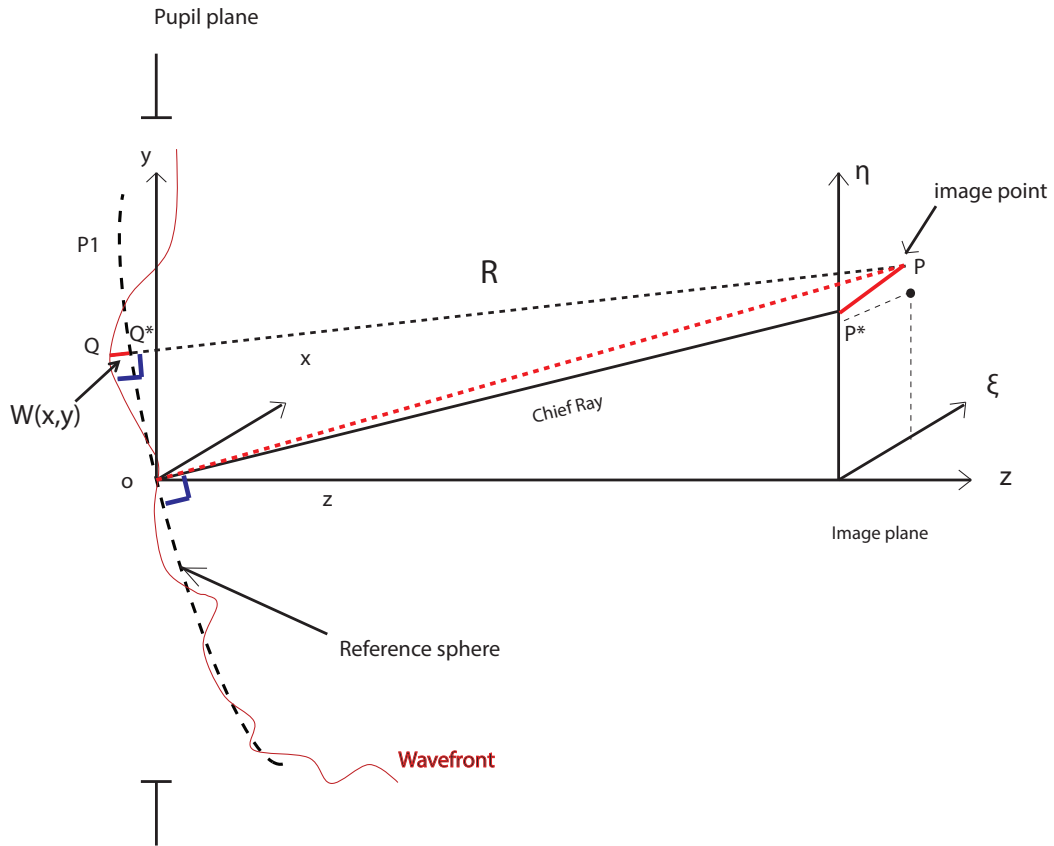


Figure 1.2: Geometrical description of wave and ray aberration.

The size of the spot is affected of a certain depth of focus given by $\lambda(\frac{f}{D})^2$. A common criterion for quantifying this resolution is provided by the minimal distance between peaks of two point-sources. For an averaged eye [6], with a standard effective focal length of $16.7mm$ and a circular pupil of a diameter of $6mm$ illuminated in green light ($550nm$), the minimum angle of resolution is $\theta \propto 23$ arcseconds radius (i.e. $1.8\mu m$ on the retina) is theoretically attainable, which corresponds roughly to the physical dimension of the cone.

1.1.2 Aberration: the barrier to perfect imaging

1.1.3 The aberrated surface

In ideal geometrical-optics imaging, the image of a point source is another perfect point, borrowing rays of equal optical path. Set at the center of the exit pupil plane, the reference center, the surface of equal optical path constitutes a system reference. By simple transformation, it is sometimes adjusted to a nominal image position or field. The most basic variations encountered by this geometrical surface are piston, tip-tilt and defocus and can be simply added when rays enter close to the optical axis, i.e. in paraxial condition. In presence of aberration in the system, rays deviate from their initial trajectory resulting in a complex disparity of rays around the focus spot, divided in both transverse and longitudinal ray aberration components $P * P = (\xi, \eta)$. Since rays are normal to geometric wavefront, it follows that transverse ray aberrations are proportional to wavefront slope. The wavefront deformation QQ^* is measured as the deviation of the wavefront surface from the reference, i.e. Gaussian sphere in the eye, as pictured in Fig- 1.2. For a given a wavefront deformation, assumed relatively small, the following variation of the ray aberration P^*P is derived:

$$\begin{cases} \delta\xi = \frac{R}{n} \frac{\partial W(x,y)}{\partial x}, \\ \delta\eta_0 = \frac{R}{n} \frac{\partial W(x,y)}{\partial y}. \end{cases} \quad (1.15)$$

Re-written, in polar coordinate so that:

$$\begin{cases} \delta\xi = \frac{R}{n} \left(\frac{\sin\theta \partial W(x,y)}{\partial \bar{\rho}} + \frac{\cos\theta \partial W(x,y)}{\partial \theta} \right), \\ \delta\eta_0 = \frac{R}{n} \left(\frac{\cos\theta \partial W(x,y)}{\partial \bar{\rho}} + \frac{\sin\theta \partial W(x,y)}{\partial \theta} \right). \end{cases} \quad (1.16)$$

where $\bar{\rho}$ correspond to the normalized radial coordinate in the pupil and θ the angular coordinate in the pupil.

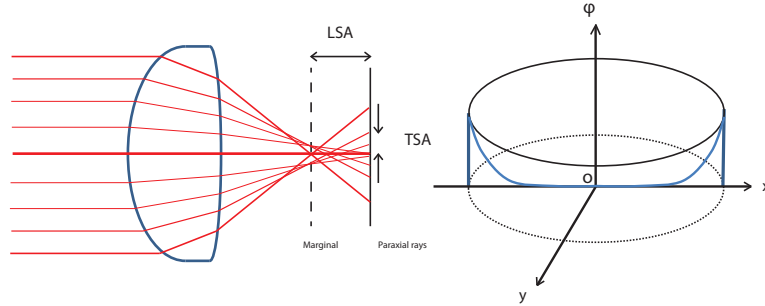


Figure 1.3: Lens and wave aberration with primary spherical aberration.

Seidel aberrations

Aberrations are classified and categorised in a variety of ways that intend to capture different natures of image blur. For a rotationally symmetric system, the wavefront aberration $W(\rho, \theta, \eta)$ can be expanded as a power series in the pupil coordinates (ρ, θ) and the field η . The Seidel aberrations [179] are the lowest order aberration, classified into five types: spherical aberration, coma, off-axis astigmatism, field curvature and distortion. Spherical aberration is an intrinsic feature of spherical lenses. Independent of field angle, its wavefront shape is given by:

$$S_I = b_1 \rho^4. \quad (1.17)$$

As a result of spherical aberration, paraxial and marginal rays come to different foci and there is no unique focal point. Seidel defocus and spherical aberration balance each other across the pupil and the best image is often referred to as the circle of least confusion. The distance between the paraxial and marginal ray foci is the longitudinal spherical aberration (LSA), and the difference in the ray height is the transverse spherical aberration. LSA is given by the transverse ray, increasing across the pupil as:

$$\delta\xi = \frac{-4b_1 R \rho^3}{n}. \quad (1.18)$$

Coma is an odd aberration. Its wavefront deviation from a perfect sphere varies

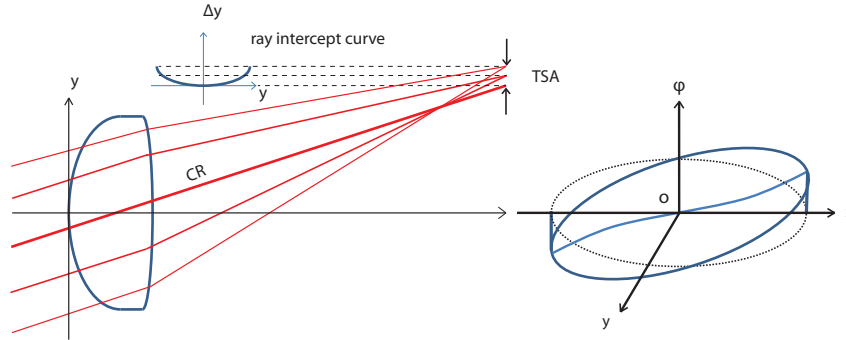


Figure 1.4: Lens and wave aberration with primary coma.

linearly with field height following:

$$S_{II} = b_2 \eta \rho^3 \cos \theta. \quad (1.19)$$

For a given field angle, there is a zonal variation of focal length from center to periphery that results in a focus having a comet-like shape. The important aspect of its presence is that the centroid is shifted from the chief ray and varies with change of focus. The light coming from the center of the lens is directed to the head, in focus, and the marginal rays form a circular rings varying in radius, associated to the tails out of focus displaced laterally (bounded by two segments inclined to the y-axis at 30 deg). A possible measure of the strength of the wavefront in primary coma is given by its lateral spread, given by:

$$\begin{cases} \delta\xi = -b_2 \eta \rho^2 \sin 2\theta, \\ \delta\eta = -b_2 \eta \rho^2 (2 + \cos 2\theta). \end{cases} \quad (1.20)$$

The wavefront shape in primary astigmatism is given by

$$S_{III} = b_3 \eta^2 \rho^2 \cos^2 \theta. \quad (1.21)$$

Also derived from S_I , primary astigmatism rises from a decentering of the lens. The obliquity of the rays results in a difference of magnification along the sagittal and

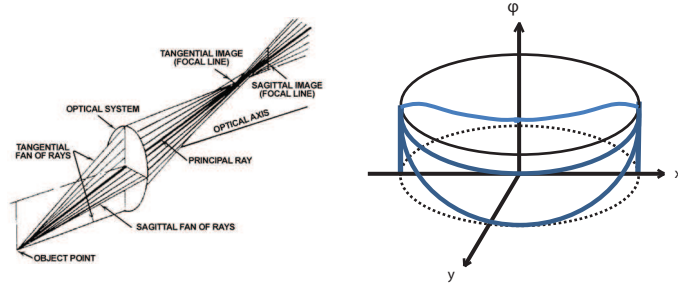


Figure 1.5: Lens and wave aberration with primary astigmatism (taken from internet at <http://llis.nasa.gov/>).

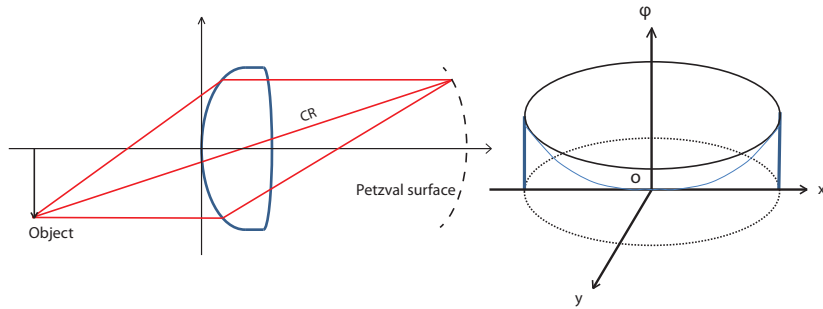


Figure 1.6: Lens and wave aberration with field curvature.

tangential meridians of the lens such that:

$$b_3 = \frac{1}{4n} \left(\frac{1}{R_t} + \frac{1}{R_s} \right). \quad (1.22)$$

where R_t is the tangential curvature and R_s the sagittal curvature.

A closely related aberration is the even aberration called, field or Petzval curvature.

Its wavefront shape is given by

$$S_{IV} = b_4 \eta^2 \rho^2. \quad (1.23)$$

It corresponds to a zonal variation of the axial magnification taking place with varying the object height and results in a curved image locus, instead of a planar image.

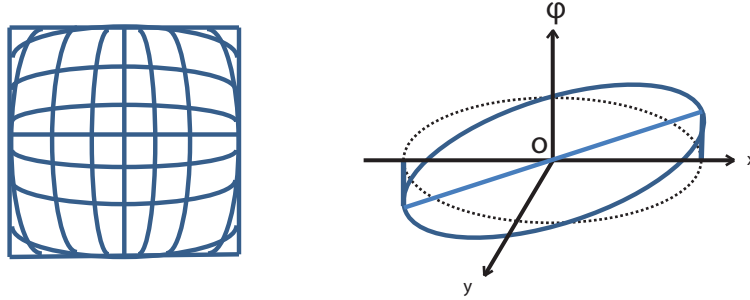


Figure 1.7: Image and wave aberration in presence of distortion.

For distortion, the wavefront shape is given by

$$S_V = b_5 \eta^3 \rho \cos \theta. \quad (1.24)$$

It results in a modification of the geometrical similarity between object and image with field height: pincushion distortion, corresponds to a radially stretched image whereas barrel distortion, to a squeezed image.

$$\begin{cases} \delta\xi = 0, \\ \delta\eta = -b_5 \eta^3. \end{cases} \quad (1.25)$$

Because of its independence to ρ and θ , it preserves stigmatism. Seidel theory is remarkable to analyze the interrelation between aberration with respect to field angle and the geometry of the system. On the other hand, it lacks the flexibility of a complete basis to explain aberration balancing and represent higher-order aberration, predominant when the third-order aberrations diminish. This description is also limited to rotationally symmetric optical system and ignores the phase errors induced by the inhomogeneity and the surface irregularities of the materials.

Zernike Polynomials: a meaningful basis

The adoption of a meaningful representation of aberrations is at the heart of the question of the effect of aberration in the eye. Because aberrations are often mixed

and interact together, a basis consistent with their anatomical organization is an imperative. Owing to their properties of (i) orthonormality over a unit circle, (ii) invariance in form with respect to rotation of the axes about the origin, and (iii) the existence of an infinite set of polynomial, the polynomial expansion of Zernike $Z_j(\rho, \theta)$ constitutes a complete and unique basis for expressing the ocular wavefront [71]:

$$W(\rho, \theta) = \sum_{s=0}^{\infty} a_s Z_s(\rho, \theta), \quad (1.26)$$

The convention adopted in this thesis is the normalization of the OSA/VSIA convention [285], see table 1.1. This is the convention that we use throughout the present thesis. The +z Cartesian axis is pointing outside the eye. Hence, $W > 0$ if the wavefront errors is phase-advanced with respect to the reference wave. Standard in ophthalmology practice for prescription and description of the eye, other coordinate frames and indexing are used in other applications.

Each Zernike term is indexed by a number $j = 0, 1, 2, \dots$ and belongs to a double indexing (m, n) associated to a radial polynomial $R(n, m)$ and an angular frequency function $\exp(im\theta)$, so that:

$$Z_j(\rho, \theta) = Z_n^m(\rho, \theta) = \begin{cases} \sqrt{2(n+1)} R_n^{|m|}(\rho) \cos(m\theta) & \text{if } m \neq 0 \text{ and } j \text{ even} \\ \sqrt{2(n+1)} R_n^{|m|}(\rho) \sin(|m|\theta) & \text{if } m \neq 0 \text{ and } j \text{ odd} \\ \sqrt{n+1} R_n^0 & \text{otherwise} \end{cases} \quad (1.27)$$

where:

$$\begin{cases} n = \text{roundup} \left[\frac{-3 + \sqrt{9 + 8j}}{2} \right] \\ m = 2j - n(n+2) \\ j = 0, 1, 2, \dots \end{cases} \quad (1.28)$$

The index n imposes an increasing degree of complexity of the wavefront with radial coordinate, whereas m describes the degree of symmetry of the wavefront in angle.

$$R_n^{|m|}(\rho) = \sum_{s=0}^{(n-|m|)/2} (-1)^s \frac{(n-s)!}{s![(n+|m|)/2-s]![(n-|m|)/2-s]!} \rho^{n-2s} \quad (1.29)$$

Thus, the wavefront is made of a sum of even and odd aberrations, as shown in the Table-1.1, and we distinguish the terms independent of θ , such as primary and secondary spherical aberration, defocus; and the terms varying as $\cos(\theta)$ and $\cos(2\theta)$ for coma and astigmatism, respectively.

A remarkable property [179] of Zernike aberration is that the elementary power terms of $R_{nm}(\rho)$ compensate so that the highest degree of a Zernike term is optimally balanced with those of equal or lower degree, as observable in table-1.1, which allows a maximum intensity at the Gaussian focus for small aberrations. Over the unit circle pupil, Zernike polynomials have zero mean and a minimum variance. The variance of each Zernike mode across the pupil is equal to its coefficient squared. Consequently, the root mean square is equal to the standard deviation given by the root mean square of the sum of each zernike coefficient square.

$$rms = \sqrt{\sum_{j=0}^N a_j^2} \quad (1.30)$$

However, when aberrations are high, the complex tail of the image gains importance in the system quality. Combined, modes can produce positive interaction and extended focus and the issue of best focus is increasingly complex [124]. Optimization of the Gaussian focus is commonly performed by balancing distinct modes such as spherical aberration/defocus or astigmatism/secondary astigmatism. Such positive interactions are found in the real eye wavefront suggesting potential tuning in the arrangement of the wavefront variance [192]. The segregation of the wavefront in adequate modes of correction is a difficult problem that visually refer to the visual and optical impact of their conjunction in the image geometry.

1.1.4 Beyond monochromatic aberrations

Other physical phenomena, in addition to monochromatic aberrations, determine image quality. We discuss the role of chromatic effects, scattering and the retinal

| index j | $Z(\rho, \theta)$ |
|-----------|--|
| 0 | 1 (piston) |
| 1 | $2\rho \sin \theta$ (tip) (tip) |
| 2 | $2\rho \cos \theta$ (tilt) (tilt) |
| 3 | $\sqrt{6}\rho^2 \sin(2\theta)$ (astigmatism 45 deg) |
| 4 | $\sqrt{3}(2\rho^2 - 1)$ (defocus) |
| 5 | $\sqrt{6}\rho^2 \cos(2\theta)$ (astigmatism 0 deg) |
| 6 | $\sqrt{8}\rho^3 \sin(3\theta)$ |
| 7 | $\sqrt{8}(3\rho^3 - 2\rho) \sin \theta$ (coma) |
| 8 | $\sqrt{8}(3\rho^3 - 2\rho) \cos \theta$ (coma) |
| 9 | $\sqrt{8}\rho^3 \cos(3\theta)$ |
| 10 | $\sqrt{10}\rho^4 \sin(4\theta)$ |
| 11 | $\sqrt{10}(4\rho^4 - 3\rho^2) \sin(2\theta)$ |
| 12 | $\sqrt{5}(6\rho^4 - 6\rho^2 + 1)$ (spherical aberration) |
| 13 | $\sqrt{10}(4\rho^4 - 3\rho^2) \cos(2\theta)$ |
| 14 | $\sqrt{10}\rho^4 \cos(4\theta)$ |
| 15 | $\sqrt{12}\rho^5 \sin(5\theta)$ |
| 16 | $\sqrt{12}(5\rho^5 - 4\rho^4) \sin(3\theta)$ |
| 17 | $\sqrt{12}(10\rho^5 - 12\rho^3 + 3\rho) \sin \theta$ |
| 18 | $\sqrt{12}(10\rho^5 - 12\rho^3 + 3\rho) \cos \theta$ |
| 19 | $\sqrt{12}(5\rho^5 - 4\rho^4) \cos(3\theta)$ |
| 20 | $\sqrt{12}\rho^5 \cos(5\theta)$ |

Table 1.1: Listing of Zernike Polynomials up to 5th order

mosaic.

Chromatic aberration

The magnetic and electric states associated with the atoms interactions differ with the wavelength and results in phenomenon of dispersion, characterized by a variation of the refractive index of material: $n_\lambda = \sqrt{\mu\epsilon}$, where μ is the magnetic permeability, unity for non-magnetic substance, and ϵ the permittivity, leading to the phenomenon of dispersion. Equivalently, the refractive index is the ratio of the speed of light in a vacuum to the speed in the material. It produces a change of light bending at an interface which affects the wavefront aberration and diffraction. It results in variations of the longitudinal and transversal magnification. The detection of this image is not trivial with respect to the object nature and is considered here as a

sum of incoherent, monochromatic images, with varying weights [234].

Longitudinal chromaticity dominates in the eye and, with good agreement between objective and subjective measurement, indicates a magnitude of about $2.5D$ [60, 143] from 400 to $700nm$. A question rises then: should one correct for chromatic aberration? In this regard, it has been suggested that monochromatic aberrations may provide a partial compensation for chromatic aberration [191]. The reduction of the longitudinal chromatic aberration varies with spatial scale, providing up to a two-fold improvement for $32cpd$ [143, 304].

In the visible spectrum, a common estimator of dispersion is the Abbe number, constant of the material that relates its refractive index at different wavelengths, as follows: $V = (n_D - 1)/(n_F - n_C)$ with $\lambda_D = 587nm$, $\lambda_C = 656nm$; $\lambda_F = 486nm$. The strength of the Abbe Number is inversely proportional to the dispersion of the glass, ranging from 25 to 70. Typically in the eye, it is about 47 (compared to 37 for the IOLs material, so-called polymethyl methacrylate (PMMA) [265]). Chromatic aberration is commonly avoided in optics by using mirror instead of lenses. It can also be nulled by combining lenses so that they oppose in phase chromaticity, usually choosing distinct indices of refraction with an adequate adjustment of the curvatures. The popular achromatic doublet comes from this blending, made up of one positive lens and one negative lens.

Forward and backwards scattering

Scattering [228] is a manifestation commonly occurring in subject having cataract or laser surgery, which dominantly rises from the cornea, the crystalline lens, and can be particularly visible at night for the subject experiencing glare disability and discomfort. Corneal and lens scattering tends to follows a Rayleigh/Rayleigh-Gans scatter and are an inverse power of wavelength. It encompasses all the local perturbation of the wavefront on the scale of the wavelength, usually associated to

inhomogeneities of the index of refraction (such as introduced by micro-structured corrective optics) and differentiates from standard aberration by a substantial spatial higher frequency component owing to larger angle of refraction, which reduces the contrast in scene at all spatial frequencies. For subjects with significant amount of scattering, such as cataract or dry eye subjects, the double pass measurement technique, based on projecting a point source onto the retina and observing its alteration, is a good indicator when quantifying the high frequency spatial frequency of the intensity image. Because of diffuse light in the less pigmented retina at higher wavelength [68, 293], a subjective measurement routine is used in the clinic based on psychophysical measurement, the so-called “compensation method” [292, 112], where stray light is tested by adjustment of a temporal modulation of an object intensity guided by peripheral stray light to a counter phase temporal modulation of the object intensity itself. When dealing with coherent light, the interference can be in fact so strong that the Airy disk is totally smeared and the shape of the psf is gone, the first pass impulse function then requiring additional processing such that averaging of the signal or modification of the light source. A model of the light scattered, proposed by Navarro [205], describes scattering using an equivalent Gaussian diffuser, placed on the pupil plane.

The retinal mosaic

Owing to a highly structured cone mosaic, the retina also plays an active role on image filtering, in the domains of spatial resolution and light apodization. The phenomenon of apodization, or Stiles-Crawford effect, in the eye refers to the variation of the light-coupling efficiency of the detection of light with the position of ray entering the eye due to an optimal acceptance angle of the cone, acting as optical fiber. Commonly modelled by a weighting parabola of the pupil function, rays efficiency decrease towards periphery reducing the contribution of aberration at the pupil edge. Let note that the cones are tuned to the directionality of the ray [1].

These directional effects on the way into and out of the eye can play an important role in determining image quality.

The last optical barrier is related to the spacing of the photoreceptors and determines the finest resolvable pattern. Distances vary from a highly concentrated centre, the foveola, to less dense region towards the periphery. Anatomical and psychophysics [313] studies estimate the spacing of the cones at the fovea of about 0.51 minutes of arc, i.e. 118 cycles per degree (cpd) the sampling rate of cone, which impose a maximum allowable frequency above which there is aliasing [312]. Aliasing is the manifestation of spurious spatial frequency from undersampled high spatial frequency that appears lower. The Nyquist Shannon sampling imposes that the observable frequency should be a maximum of half the sampling frequency, which enables the aberrated-free eye a resolution of about 60cpd. Let us note that this physiological barrier is not reached for off-axis vision [252].

1.2 Image quality measurement

At this stage, one may wonder what is the effect of these various sources of alteration on image quality and on the properties of the visual system, how they combine and interfere with respect to image quality. We discuss different strategies of classification.

1.2.1 Image formation

Any input $U_0(x, y)$ that passes through a certain system (S) can be decomposed as a collection of elementary functions, mathematically described by displaced-delta function $\delta(x_1, y_1)$ and endowed with a certain weight $U_0(x_1, y_1)$ such that:

$$U_0(x, y) = \int_{-\infty}^{\infty} \int_{-\infty}^{\infty} U_0(x_1, y_1) \delta(x - x_1) \delta(y - y_1) dx_1 dy_1 \quad (1.31)$$

Each delta point position of the object $\delta(x_1, y_1)$ is then associated to the whole system at the output $U_i(x, y)$ by the relationship:

$$U_i(x, y) = \int_{-\infty}^{\infty} \int_{-\infty}^{\infty} U_0(x_1, y_1) h(x, y; x_1, y_1) dx_1 dy_1 \quad (1.32)$$

where $h(x, y; x_1, y_1)$ is an operator characteristic of the imaging process, called the impulse response of the system. Two properties of the operator are usually assumed: linearity, meaning that a change in the input reflects with the same proportion in the output, and shift invariance, meaning that any of those inputs are seen by the system the same way, regardless of their spatial location in the input. Under these assumptions, the output-image $U_i(x, y)$ of the geometrical object $U_0(x, y)$ becomes a simple convolution:

$$U_i(x, y) = \int_{-\infty}^{\infty} \int_{-\infty}^{\infty} U_0(x_1, y_1) h(x - x_1, y - y_1) dx_1 dy_1 \quad (1.33)$$

or re-written in notation as:

$$U_i(x, y) = U_0(x, y) \otimes psf(x, y), \quad (1.34)$$

where the $psf(x, y)$ is the amplitude point-spread function of the system, equivalent to the image of a Dirac-point object.

The complex amplitude transmittance of the pupil $P(\xi, \eta)$

$$P(\xi, \eta) \propto A(\xi, \eta) \exp(ikW(\xi, \eta)) \quad (1.35)$$

where $A(\xi, \eta)$ the aperture stop of the system, $W(\xi, \eta)$ is the wavefront aberration, (ξ, η) are coordinates in the pupil.

The point-spread function $psf(x, y)$ amplitude is the Fourier transform of $P(\xi, \eta)$,

evaluated at the coordinates ($\mu_x = \frac{x}{\lambda z}$, $\mu_y = \frac{y}{\lambda z}$):

$$h(x, y) = FT(P(\xi, \eta) \exp(ik \frac{\xi^2 + \eta^2}{2z})), \quad (1.36)$$

z being the distance of propagation between plane.

The intensities $I(x, y, z) = \langle |U(x, y, t)|^2 \rangle$ are linear with respect to the incoherent process:

$$I_i(x, y) = I_0(x, y) \otimes PSF(x, y), \quad (1.37)$$

where $I_0(x, y)$ is the geometrical object intensity and $PSF(x, y) = |psf(x, y)|^2$ the point-spread function intensity.

In coherent light, the process is linear in amplitude:

$$I(x, y) = |(U_0(x, y)_{object}(x, y) \otimes psf(x, y))|^2 \quad (1.38)$$

The characteristic band-pass of the system is given by the Fourier transform of the PSF normalized to unit volume, i.e. the normalized autocorrelation of the scaled pupil transmittance, so-called the optical transfer function OTF :

$$OTF(\mu_x, \mu_y) = \frac{\int_{-\infty}^{\infty} \int_{-\infty}^{\infty} P(\xi + \frac{\lambda z \mu_x}{2}, \eta + \frac{\lambda z \mu_y}{2}) P^*(\xi - \frac{\lambda z \mu_x}{2}, \eta - \frac{\lambda z \mu_y}{2}) d\xi d\eta}{\int_{-\infty}^{\infty} \int_{-\infty}^{\infty} |P(\xi, \eta)|^2 d\xi d\eta} \quad (1.39)$$

where $OTF(\mu_x, \mu_y)$ corresponds to the degree of overlapping area associated to the spatial frequency.

A summary of the aforementioned representation of the system is presented in Fig-1.8. The wavefront aberration (on the top) of the system, described up to the 5th order by single Zernike modes, presents a typical amount of ocular blur of $\lambda/2$ of *rms* and the PSF and modulation transfer function (MTF) transformation counterparts appear in the bottom.

These blurs differentiate by their index position (n, m) and distinguish themselves

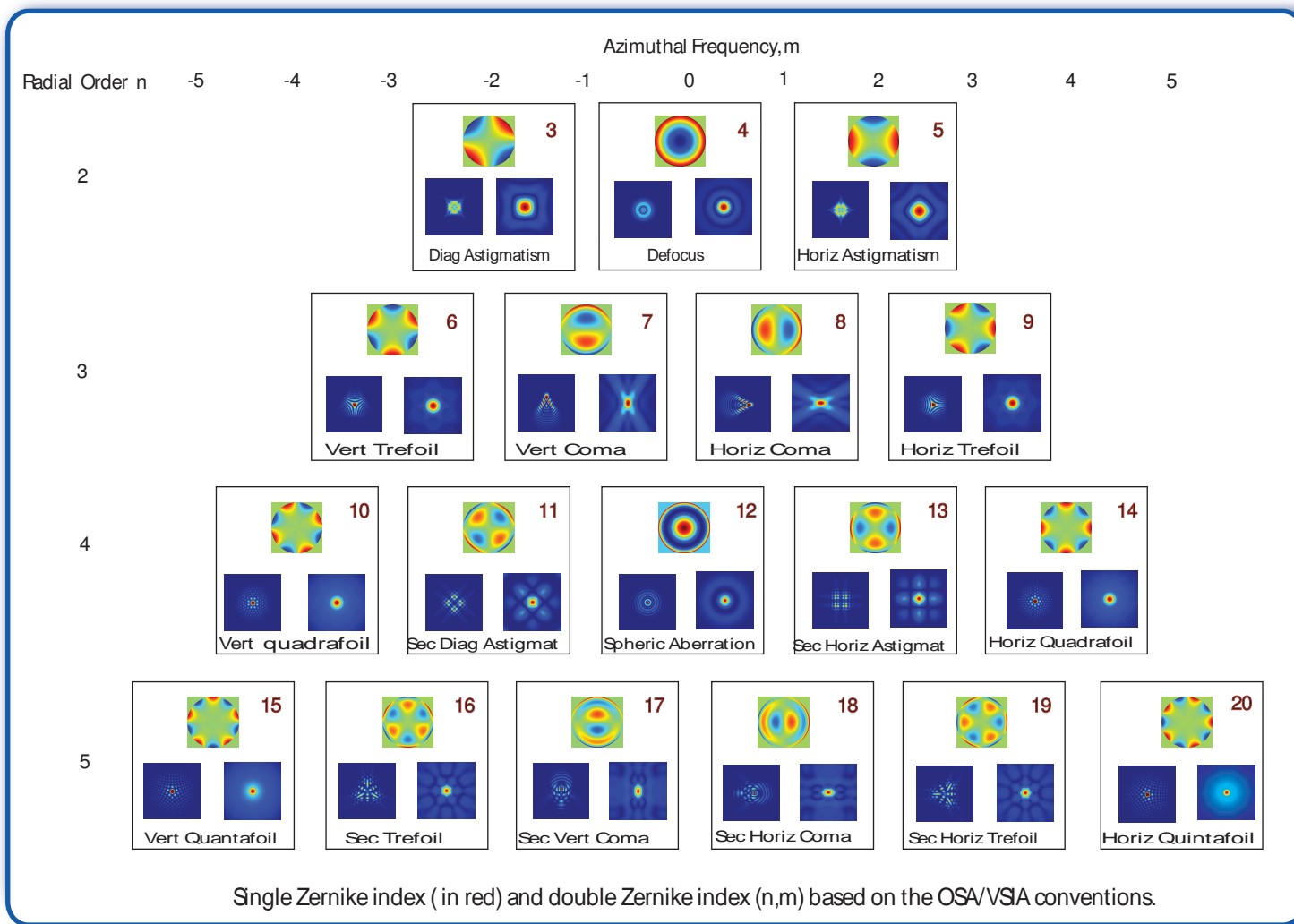


Figure 1.8: Wavefront aberration (top), PSF (left bottom) and MTF (right bottom) trans-
formations corresponding to each Zernike mode from 2nd to 5th order, for $\lambda/2$ of wavefront
errors rms over a 6mm diameter pupil.

by their symmetry invariance. For a given azimuthal frequency, the higher the radial order, the higher the finesse of the wavefront description. Independently of the radial order, spatial symmetry is a function of the azimuthal frequency.

Central terms are symmetrical and can possibly compensate each other; the other terms are asymmetric and present a variety of symmetry with the axes, reciprocal for positive and negative azimuthal frequencies, and increasing with both radial and azimuthal order.

Terms like coma ($Z7$ and $Z8$) results in a shift of the maximum intensity that appears on the PSF image. A visual classification comes out from the psf image where absolute mode effects are the most distinct: tails and center intensity are the main characteristic of the PSF. One can note that the higher the azimuthal frequency, the smaller the impact of aberration on the shape of the PSF. The changes on the MTF reflect well blur symmetry and differentiate mainly directionally and radially over spatial frequency. Note that these expressions are only an illustration of the effect of aberration and may borrow more complex formation when combined as in positive interaction (e.g. defocus-spherical aberration coupling). An important issue rises from this illustration: can we compare the impact of aberration? And if yes, to what extent, and using which criterion? How to equalize optical blur from distinct aberration modes?

1.2.2 Assessment of the retinal image

Assessment of retinal image can be done objectively or subjectively. The empirical approach of iteratively testing different dioptre of spectacle until the observer finds the best fit ($\pm 0.25D$) for reading a chart, has long predominated. Its sensitivity to internal and external variation as well as its experimental predicament, in surgery event has reinforced the need for objective refractive measurements and predictions [287, 129, 131]. What are the methods to get an objective measurement able to

envelope the different criterion of quality (visibility, detectability, mediation...) examined by the eye is what we explore in this section.

Retinal image quality

The simplest metric for assessing retinal image quality is the sharpness metric, S_f . Using gradient and second derivative of the metric, maximization of the sharpness metric S_f rests on the strategy of finding the maximum of the contrast and variance of the overall image. Metrics of this type [199, 101] are principally based on higher-order moments of the form :

$$S_\beta(f) = \int_{-\infty}^{\infty} \int_{-\infty}^{\infty} f(I(x, y))^\beta dx dy, \quad (1.40)$$

where the power $\beta = 2, 3..$ and $f(I(x, y))$, function of the intensity of the image are parameters to be adjusted to the characteristic of the scene, e.g. spatial extension of the intensity variation. A related metric, based on information theory, quantifies the average uncertainty of the signal as:

$$S_f = - \int_{-\infty}^{\infty} \int_{-\infty}^{\infty} I(x, y) \ln(I(x, y)). \quad (1.41)$$

In this formula, S_f can be regarded as the amount of uncertainty pertained to the event of a pixel having intensity $I(x_i, y_i)$, or amount of information contained in the event. Asymetry, broken symmetry, or less symmetry lead to higher entropy. A reference can also be used in pattern recognition and matched filtering application to analyse phase shifts or amplitude variation. In the cross-correlation function [41], convolution of an image with the object, the impulse function that connects two signals is quantified. Several metrics and criterion can be applied to it, the main one being either the central peak or maximum.

Optical quality of the system

Point-spread function metrics of the quality of an imaging system Resolution and contrast are quantified by several metrics listed in Table 1.2.

| | |
|------|--|
| SRX | Strehl ratio computed in spatial domain |
| LIB | light in the bucket |
| D50 | diameter of a circular area centered on PSF peak, which captures 50% of the light energy |
| EW | equivalent width of centered PSF (arcmin) |
| SM | square root of second moment of light distribution (arcmin) |
| HWHH | half width at half height (arcmin) |
| CW | correlation width of light distribution (arcmin). |
| STD | standard deviation of intensity values in the PSF normalized to diffraction-limited value. |
| ENT | entropy of the PSF inspired by an information metric |

Table 1.2: PSF metrics.

The Strehl ratio **SRX** is a measure of image contrast. It is the ratio between the peaks intensity of an aberrated system and a diffraction-limited system. Particularly relevant when aberration are small, if $SRX > 0.8$ the system is generally considered to be “almost diffraction-limited”.

$$SRX = \frac{\max(PSF(x, y))}{\max(PSF_{DL}(x, y))} \quad (1.42)$$

The encircled energy **D50** accounts for both compactness and sharpness of the image by measuring the smallest radius that is sufficient to gather a certain amount of energy (here 50% of the total energy), as in:

$$\frac{\int_0^{2\pi} \int_0^r PSF(r, \theta) r dr d\theta}{\int^{psf} PSF(r, \theta) r dr d\theta} = 0.5 \quad (1.43)$$

An analogous compactness metric is the light in the bucket **LIB** that measures the amount of energy falling within a defined region of the PSF, e.g. the central core of

the diffracted limited PSF, $DL_{core} = 1.22\lambda F$.

$$LIB = \int_{DL_{core}} PSF_n(x, y) dx dy \quad (1.44)$$

Another metric is the half width at half height **HWHH**. This metric is only interested in the area where the psf intensity values are above the threshold of the half of the PSF peak, usually of interest for assessment of the size of the Airy disk. It ignores the spreading of light.

$$HWHH = \int_{psf} (PSF_n(x, y) > \frac{\max(PSF(x, y))}{2}) dx dy \quad (1.45)$$

The equivalent width **EW** is a measure of the PSF compactness and, contrary to the encircled energy, ignores the level of contrast defined by the height of the central intensity of the point spread function, $PSF(x_0, y_0)$. It is the diameter of a cylinder gathering a certain amount of energy, e.g. the overall PSF energy, and having the height of the central intensity PSF. This metric can advantageously be used for determining diffractive component quality when compactness and contrast are evolving differently.

$$EW = \frac{\int_{psf} (PSF(x, y) dx dy)^{0.5}}{PSF(x_0, y_0)} \quad (1.46)$$

Metrics based on higher moments For more complex function, where both sharpness and contrast are modulated, other metrics can capture the effect of spatial properties on image quality, as follows:

The moment of inertia of the PSF **SM** weighs the contribution of the intensity values of the psf according to their spatial position: it is therefore a measure of the spread of light.

$$SM = \left(\frac{\int_{psf} (x^2 + y^2) PSF(x, y) dx dy}{\int_{psf} PSF(x, y) dx dy} \right)^{0.5} \quad (1.47)$$

The standard deviation **STD** measures the ratio of the amount of deviation of the point-spread function compared to a diffraction-limited system, using the fact that aberrations decrease the variance of the point-spread function.

$$STD = \left(\frac{\int_{psf} (PSF(x, y) - \overline{PSF})^2 dx dy}{\int_{psf} (PSF_{DL}(x, y) - \overline{PSF_{DL}})^2 dx dy} \right)^{0.5} \quad (1.48)$$

The metric in entropy **ENT** is a measure of the level of information of the point-spread function. Aberration have minimal entropy for a diffracted-limited aberration. It was shown that aberrations increase entropy by translating the intensity information towards the mean.

$$ENT = - \int_{psf} (PSF(x, y) \log PSF(x, y)) dx dy, \quad (1.49)$$

The metric **CW**, is based on the autocorrelation of the PSF, a particular case of the cross-correlation, which yields an optimal match for the impulse function. The autocorrelation denotes of the degree of complexity of the PSF and its energy. This metric extracts the area the most effective of the intensity matching, as determined by the half maximum of the autocorrelation peak for the diffraction-limited point-spread function.

$$HWHH == \int_{psf} (PSF_n(x, y) \cdot PSF_n(x, y) > \max(PSF(x, y) \cdot PSF_n(x, y)/2)) dx dy \quad (1.50)$$

Wavefront errors The wavefront aberration particular development affects profoundly the point-spread function.

$$PSF_P \sim \left| \int_0^{2\pi} \int_0^1 \exp(ikW_P) \rho d\rho d\theta \right|^2 \sim \left| \int_0^{2\pi} \int_0^1 (1 + ik\phi_P + (1/2)(ik\phi_P)^2 + \dots) \rho d\rho d\theta \right|^2 \quad (1.51)$$

Re-written for small aberration, as:

$$I(P) \sim 1 - (2\pi/\lambda)^2 \Delta(\phi_P)^2, \quad (1.52)$$

where $\Delta(\phi_P)$ is the variance of the wavefront, or rms wavefront errors.

Although the central intensity point-spread function can sometimes capture and summarize optical quality, it may also restrict the analysis of the complexity of the system when aberration increases. Some ray and wavefront metrics may then be substituted for optical designs purposes, as listed below:

| | |
|---------|---|
| RMS_w | root-mean-squared wavefront error computed over the whole pupil (μm). |
| PV | peak-to-valley difference (μm). |
| RMS_s | root-mean-squared wavefront slope computed over the whole pupil (arcmin). |
| Bave | average blur strength (diopters) |
| PFWc | pupil fraction when critical pupil is defined as the concentric area for which $RMS_w < \text{criterion } (\lambda/4)$. |
| PFSc | pupil fraction when critical pupil is defined as the concentric area for which $RMS_s < \text{criterion } (1\text{arcmin})$. |
| PFCc | pupil fraction when critical pupil is defined as the concentric area for which $Bave < \text{criterion } (0.25D)$. |
| PFWt | pupil fraction when a "good" sub-aperture satisfies the criterion $PV < \text{criterion } (\lambda/4)$. |
| PFSt | pupil fraction when a "good" sub-aperture satisfies the criterion horizontal slope and vertical slope are both $< \text{criterion } (1\text{arcmin})$. |
| PFCt | pupil fraction when a "good" sub aperture satisfies the criterion $Bave < \text{criterion } (0.25D)$. |

Table 1.3: Wavefront metrics.

Wavefront and related metrics The first wavefront metric, the root-mean square wavefront error RMS_w measures the variability of the wavefront at various points, i.e. degree of flatness of the wavefront. The system is considered almost diffracted-limited for $rms \leq \lambda/14$, in relation with the Marechal-Lord Rayleigh

criterion of $SRX > 0.8$.

$$RMSw = \left[\frac{1}{A} \int_{pupil} (W(x, y) - \overline{W(x, y)})^2 dx dy \right]^{0.5}, \quad (1.53)$$

Depending on the aberration, it results in a different maximum of deviation (e.g. defocus $Wmax = \lambda/4$). A concurrent metric is the peak to valley **PV**, measure the amplitude of phase errors and is often used for ranging the quality of optical manufacture. It is also specially helpful for optimizing a system far from diffraction.

$$PV = max(W(x, y) - min(W(x, y))) \quad (1.54)$$

The power equivalent or average power blur B_{av} is a measure of the global wavefront curvature, resulting from the interaction between low-order aberrations (LOA) and higher-order aberrations (HOA). The power equivalent is split into spherical power M and cylindrical powers, $J0$, $J45$, such that:

$$B_{av}(x, y) = sqrt(M(x, y)^2 + J(x, y)^2) \quad (1.55)$$

where $J(x, y) = sqrt(J0(x, y)^2 + J45(x, y)^2)$ This global curvature can be calculated from a wavefront by matching a quadratic surface, that can be described by defocus and astigmatism Seidel component $(\rho^2, \cos(\theta)\rho^2, \sin(\theta)\rho^2)$, equated to the Zernike terms. It provides a practical assessment of the wavefront. In spectacle refraction, the tolerance to curvature is of the order of $0.25D$.

The wavefront slope is a measure of the spreading of rays, and so connected to the width of the psf. A popular metric in optical design is derived from the wavefront slope so-called the spot diagram. It corresponds to the spatial distribution of rays that are located in the image plane. The wavefront slope rms RMS_s for a near diffraction-limited system is $1arcmin$.

Anatomy of the wavefront For highly aberrated aberration (e.g. $S < 0.8$), the variance properties affect substantially the behaviour of the complex amplitude in the image plane aberration. Two main methods of analysis [287] are applied for the previous wavefront description: (i) the critical pupil method or central pupil method, that is based on the critical diameter of the pupil for which there is a minimal wavefront impact and (ii) the tessellation or whole pupil method, that is based on the proportion of good sub-aperture of the pupil that can respond to a defined quality criterion, such as wavefront $rms_w < \lambda/4$, wavefront curvature $B_{av} < 0.25D$ or wavefront slope $rms_s = 1arcmin$. The quality criterion typically imposed is $SRX = 0.8$, and for critical diameter as well as good subapertures, can be applied for wavefront, wavefront slope, or average power blur, previously described.

Optical transfer function (OTF) The last transformation of the wavefield allows a decomposition of the image-output in both position and intensity of its spatial frequency, well suited for linear system. The modulus of the OTF , so-called the amplitude transfer function MTF , is a measure of intensity contrast of the image, resulting from both phase shift and intensity reorganization. It is used in several metrics, borrowed from previous description, such as the *radialMTF* (equivalent to the encircled energy), or the strehl ratio MTF (*SRMTF*) and OTF (*SROTF*), volume of the MTF or OTF falling under a defined cut-off frequency (typically $30cpd$ in the eye) similar to the light in the bucket. Odd aberrations produces phase-shifts varying between $[\pi - \pi]$ values and accounted by the argument of the OTF , so-called the phase modulation transfer, PTF . These shifts vary in a non-linear fashion, and there is alas no direct relation between odd and even aberration and the OTF counterpart [291]. Highly aberrated wavefront produces phase reversals [270], e.g. negative values in the image. A possible evaluation is provided by the ratio between the volume under the OTF and the volume under the MTF , though often ignored. We note that direct manipulation of the OTF can be strongly impaired by sampling issue.

A partial account of both position and intensity combination is permitted by the real part of the OTF [148], such that the area under the OTF forms the extended SROTF:

$$SROTF = \left(\frac{\int_{otf} CSF_n(f\mu_x, \mu_y) \cdot abs(Re(OTF(f\mu_x, \mu_y))) dx dy}{\int_{otf} CSF_n(f\mu_x, \mu_y) \cdot abs(Re(OTF_{DL}(\mu_x, \mu_y))) dx dy} \right)^{0.5} \quad (1.56)$$

This metric is enhanced by adding a neural visual filter accounting for post-retinal processes, and yield the popular visual strehl ratio, $VSOTF$:

$$VSOTF = \left(\frac{\int_{otf} CSF_n(f\mu_x, \mu_y) \cdot abs(Re(OTF(f\mu_x, \mu_y))) dx dy}{\int_{otf} CSF_n(f\mu_x, \mu_y) \cdot abs(Re(OTF_{DL}(\mu_x, \mu_y))) dx dy} \right)^{0.5} \quad (1.57)$$

Other metrics calculated in the frequency domain also incorporate post-retinal filtering, e.g. $VSMTF, VNOTF, VSOTF$.

| | |
|---------|---|
| VSX | visual strehl ratio computed in the spatial domain. |
| SFcMTF | spatial frequency cutoff of radially averaged MTF. |
| SFcOTF | cutoff spatial frequency of radially averaged OTF. |
| AreaMTF | area of visibility for rMTF, normalized to diffraction-limited case. |
| AreaOTF | area of visibility for rOTF, normalized to diffraction-limited case. |
| SRMTF | Strehl ratio computed in frequency domain, MTF method. |
| SROTF | Strehl ratio computed in frequency domain, OTF method. |
| VSMTF | visual Strehl ratio computed in frequency domain, MTF method. |
| VSOTF | visual Strehl ratio computed in frequency domain, OTF method. |
| VOTF | volume under OTF normalized by the volume under MTF. |
| VNOTF | volume under neurally weighted OTF, normalized by the volume under neurally weighted MTF. |

Table 1.4: OTF metrics.

Chapter 2

Correction by intraocular lenses and predictability

Peripheral to the problem of a relevant customized correction in the eye, this chapter explores the challenges of a refractive correction by IOLs and proposes an analysis of the impact of distinct designs based on various models and target corrections. A short introduction about the structure and modelling of the eye is given, followed by a description of the optical properties of different IOL correctors, their analysis and comparison with respect to different pre-operative corrections.

2.1 Eye modelling

Population statistics of the wavefront aberration have been reported [230, 168, 56, 147] and reveal significant trends about the component of aberrations into the eye [13]. Compensation mechanisms of the wave aberrations were modelled [192] and measured [11, 12, 281, 195]. To better understand the optics of the eye, we present the structure of ocular layers, briefly compare the main forms of modelling, and discuss the importance of each parameter.

2.1.1 Static and dynamic optical features

Tear film The first optical component of the eye is the tear film, a thin liquid barrier, made of three layers, lipid, aqueous, mucous, of about $4 - 7\mu\text{m}$ total thickness, situated between the air and the cornea, that renews itself between blinks to protect and moisten external tissues. Often neglected in optical modelling because of its flowing state, it constitutes a strong refractive interface, and owing to the variation of its thickness may play a role on the refractive state, especially for patients with dry eyes. Its dynamics is measured by diverse techniques [94, 154] and can sometimes affect the scattering, and eye measurements [169].

Cornea Next biological tissue of the eye, the cornea is composed of multi-layers of about 0.5mm of thickness. Optically described by an anterior and posterior surface of typical average radius of curvature $R1 = 7.72\text{mm} \pm 0.27$ and $R2 = 6.46\text{mm} \pm 0.27$, this meniscus convex lens ($R1, R2 > 0$) is attributed a typical refractive index of about 1.376 and an Abbe number of 55. Its optical description represents a major concern for refraction because it provides most of the ocular power (typically equal to $40D$) and interacts on the total and internal wave [245]. Its surface characterization begins as early as the eighteenth century with contributors such as Thomas Young (1793) who attempted measurement of his own cornea [9]. Several model eyes attributed first a spherical shape to the cornea, often confined to a paraxial accuracy, and were designed for geometrical refractive model interests, such as required for calculation of refractive errors, magnification, retinal illumination or Purkinje reflection analysis. In this category of paraxial models falls the Gullstrand-Emsley model and Bennet and Rabbetts simplified eye model, both made of one unique surface; as well as the Gullstrand-Helmholtz model, Le Grand full theoretical eye. The two last models aim at a higher degree of complexity, with an accurate account of the refractive step. More complex eye models, oriented towards a description, of accommodation variation, field angle, higher-order aberration or simply accurate

anatomical description do not use the spherical assumption and adopt a more exact description of the cornea as an aspheric surface. Such a conic can be mathematically derived from the sphere equation, based on the following solution of the sphere:

$$z(\rho) = \frac{c\rho^2}{1 + \sqrt{1 - (1 + Q)c^2\rho^2}}, \quad (2.1)$$

where c is the curvature of the lens, ρ the elevation from the center and $z(\rho)$ indicates the sag of the surface, i.e. the distance of the surface position from a plane tangent to the vertex of the lens. The asphericity factor, or conic, Q is zero for a perfect sphere. It represents the deviation of the asphere from a sphere and is related to a constant of the deviation, called eccentricity, e , by $Q = -e^2$, which measures the elongation ratio to two axis of the conic, the semi-major axis a and the semi-minor axis $b:e = d(a,b)/a$. For $Q < 0$, the surface is flatter near the edge and therefore results in negative spherical aberration, whereas it gets steeper away from the vertex when $Q > 0$. Such description is also described by an expansion in the Taylor series, to account for higher order of the surface, such that:

$$z(\rho) = a_2\rho^2 + a_4\rho^4 + a_6\rho^6 + \dots \quad (2.2)$$

Typically, the average corneal conic constant is -0.26 ± 0.18 , which reveals a hyperbolic surface, more curved in the center, and flattening on the edges. For a conic constant of about $Q = -1/n^2 = -0.53$, the corneal surface introduces no spherical aberration. A ratio of 1 : 0.823 between the anterior surface radius and the posterior radius is often assumed because the second surface of the cornea is relatively shadowed by the anterior surface. Recent studies have demonstrated more details in the description of this surface, including sagittal and transversal meridian and sometimes the complete wavefront [152]. The main device used for the measurement of the front surface are the keratometer and the videokeratoscope. The posterior surface can be probed by the slit lamp, Purkinje images or Scheimpug photography.

Pupil and wavefront Light exiting the cornea is refracted in the aqueous humor, a liquid media of refractive index of about 1.336 and propagates inside the anterior chamber depth typically 3.05mm that separates the cornea from the lens of the eye. Light then passes through the pupil stop of the eye, anatomically defined by the thin iris that is in front of the crystalline lens. The image of the anatomical pupil in object space and image space is respectively the entrance and exit pupil of the system. A shift of the center of the entrance pupil towards the nasal side of about 0.5mm breaks the symmetry of the ocular system. Because of the varying tilt and decentration of its components and the off-axis displacement of the fovea (generally temporal and slightly inferior), the eyeball do not have a definite optical axis. Visual object can be connected to the fovea via two main axis: the line of sight, that passes through the center of the entrance and exit pupil, or the visual axis, through the nodals point of the eye. The pupillary axis, which is the line defined by the normal to the cornea that connects with the entrance pupil center, forms the so-called kappa and lambda angles with the visual axis and the line of sight, respectively. The angle kappa causes corneal coma in the system and typically can reach a value of about 9 deg.

The line of sight served as a standard reference for the wavefront measurements measured in object space against the visual axis. This reference is however subject to the variations of the pupil centration that varies across subjects, but also light levels: a typical shift in the pupil center of up to about 0.6mm manifests in the natural pupil. These changes particularly affect monochromatic prediction at low light level where the pupil is larger. By varying the pupil, the subject influences depth of-focus, diffraction and aberration [23] as well as retinal image flux. These pupil changes are linked to several factors such as age, accommodation, light level, emotion, attention, the physiological activity (e.g. binocular) and challenge the best models.

The position of the pupil has a significant role in the optimization of visual correction

by refractive or diffractive IOL. Lateral and axial positioning conditions a large variability of the interaction between IOL and the portion of the convergent beam. In pseudophakic eye simulations, the pupil is generally assumed fixed with a diameter pupil of about $4mm$, regardless of light level. By substituting the crystalline lens, a crucial component of the ocular architecture dynamics is modified: the distance between the crystalline lens and the pupil, naturally zero. This distance has a direct influence on the minimization of the Seidel coma rising from the tilting of the aspherical lens [179]. Hence, the challenge of an appropriate lens geometry and model of prediction.

Crystalline lens Interfaced with the aqueous humor, the crystalline lens is a bi-convex lens composed of several layers, with a thickness of about $4mm$, able to change shape and the bending of light by the release of the ciliary muscles: this process is called accommodation. Its surfaces are modelled by a radius ranging from 7.50 to $15.38mm$. As for the cornea, its modelling has evolved towards a more accurate anatomical description of its structure, replacing its spherical representation by an aspheric surface with an asphericity coefficient of about 23.13 and 21.0 for the anterior and the posterior lens. The largest innovation of the modelling of the lens came from a description of its inner structure as composed of concentric shells of varying shape and number that renders the variation of indices from the periphery to the center of the lens from 1.37 to 1.41 [120, 59]. The integration of a continuous gradient refractive index lens (GRIN) formula resolves the multiple foci resulting from the refractive step between shells. The ability to scan a $3D$ wavefront along the crystalline lens may lead to advancement in the understanding and the accuracy of the crystalline lens modeling. Purkinje images reveal good estimator of the lens surfaces as well as Scheimpflug imaging; also, optical coherence tomography (OCT) images are currently used for measurement of the index gradient.

Retina After refraction by the crystalline lens, light propagates through the vitreous chamber, aqueous media of about refractive index 1.336, a length of $16.3mm$ that separates the crystalline lens from the retina that covers the back of the eye. As illustrated in Fig-2.1, light then propagates within the thick retina up to the retinal pigment epithelium. An image is formed at the outer retinal segment by transduction of the visual pigment of rods and cones, which differs in depth from specular and scattered reflection of the double pass image for varying colors and eye pigmentations. Its thickness varies from its center, with $0.2mm$ of depth to the periphery where it increasingly bulges. The central vision occurs in the fovea and its surface of detection for a wide field interest can be modelled by a curved/or paraboloid($Q = -1$) surface of about $12mm$ of radius to reduce the errors of field curvature. Another potential source of aberration for on axis-image is caused by the temporal displacement of fovea in reference to the optical axis responsible for a field angle, measured by the kappa angle (about 5 deg). This tilting of the lens has important consequences for the way crystalline lens and cornea are combined with each other, because both present a field angle phase dependency, which vary with respect to the pupil position. Such conformation is the explanation for difference between myopic and hyperopic eye, manifesting varying magnitude of the angle kappa.

2.1.2 From the coarse average normal eye to individual real eye

The primary task of a model is to capture the pattern or the trend expressed by a set of data from a certain population. Observable data only captures a limited amount of the reality that defines the architecture of the system, and can be multiple, hence the necessity of a clear identification of the population, if abstract. The elaboration of the eye model starts by imposing appropriate boundaries to the edification of the system (e.g. the number of surface, their geometry,...) predefines by prior and progressive level of constraint, starting from simple functional realizations (e.g. focal

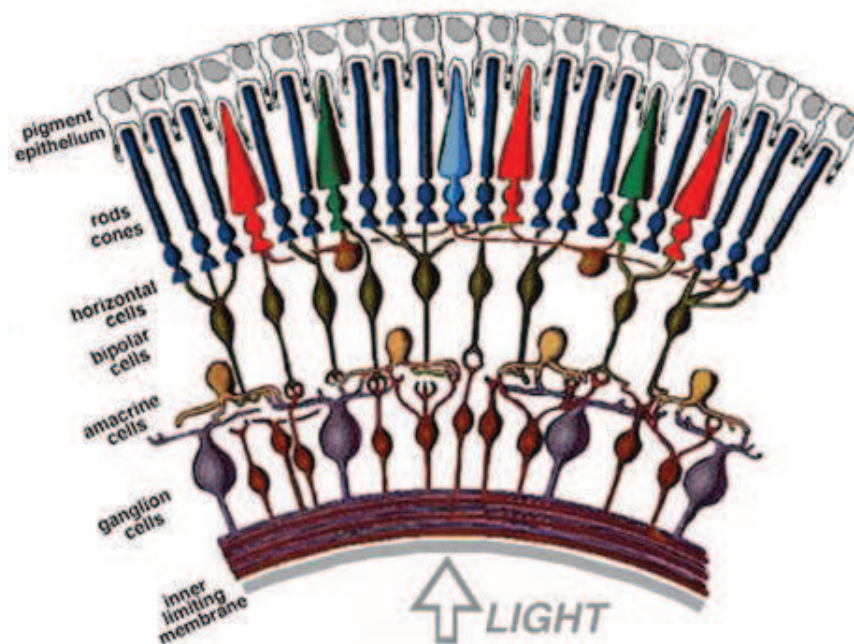


Figure 2.1: Retinal cells (taken from internet).

point of an image) to more complex ones (e.g. chromaticity, off-axis variation,...).

The first models in the eye featured low order and on axis modelling [6], and therefore did not need to expand in the marginal domain of refraction. Their development, particularly the Le Grand full theoretical eye model [165, 133], have nevertheless become the basis for more advanced eye modelling, and converge on an accurate representation of distance, refractive media and layers, which brought about the proposal for an anatomically accurate eye model by Liou and Brennan [173]. The contribution of a large body of data, and, the addition of parameters such as the angle kappa, a gradient index of the lens [120, 5], or aspherization of the surfaces[176], brought a new generation of eye models, capable of finer representation.

However, at this stage lots of operators, like the crystalline lens structure, still ill-defined in their interplay, hide the potential trends that govern a certain population (e.g. accommodation or aberration with ageing). One common tactic then consists of discarding the fuzzy or unknown pattern variations by freezing some parameters to capture the most veridical observation. Several models are based on this

simplification, such as:

- the Indiana Eye model [283, 284], meant to measure off-axis astigmatism, chromaticity and spherical aberration. It is based on a reduced eye model with a single elliptical refracting surface by contrast with the Liou and Brennan eye model.
- the Navarro eye model [99], Kooijman [155], extension of an on-axis model for wide-field aberrations. It presents an homogeneous crystalline lens by contrast with the shells or GRIN models, used by Pomerantzeff [227], Siedlecki [266].
- the Dubbelman eye model for age and level of accommodation [93]. The corneal asphericity is maintained fixed contrary to the asphericity of the homogeneous adjustable lens, regardless of mechanism of compensation of the spherical aberration of the two lens.

The great difficulty in this watershed is to design a model, which avails a prudent balance between simplicity/generality of the description of the model (to encapsulate diverse realities such as age, accommodation or field angle) and level of accuracy of the target set. The tomographic reconstruction from wavefront measured at different off-axis angles, proposed by Goncharov [121] as well as scanning of the wavefront at different planes in the eye could permit to meet more accurately the mechanism of the eye. In this respect, we note a growing interest for a personalized eye model, which introduces the account of the asymmetry of surfaces. Several proposal and attempts have been done in this direction, especially for the pseudophakic eye [245] owing to the simplification of the characterization of the lens. The success of these efforts expresses the tight interplay between the architectural constraint and the finesse of reconstruction and optimization of ocular data [31, 35]. For the personalized eye, advanced modelling might be a particular key for revealing the degree of freedom of the ocular architecture imposed by the functionality of the eye optically and visually, and so enlighten the level of organization and tuning of the visual

system.

2.2 Refractive correction by IOLs

2.2.1 The IOL solution

Foundation of modern cataract surgery

One aspect of ageing is the development of a cataract: the crystalline lens gets opacified, and the visual field, if obscured, requires surgical removal of the lens. Reported as early as the 6th century BC by the physician Sushruta in India, a palliative operation consisting of pushing the lens into the rear of the eye, simply out of the visual field, was established. Under the title of “couching” this practice travelled to the West and to Africa. Complications caused by potential migration of the lens and added to other dangers, lessened this practice for the so-called technique of cataract extraction, born in the 2nd century. Its first practice refers to a Greek physician named Antholius, and was reported in Persia, by the physician Muhammad ibn Zakariva al-Razj. That operation with large incision handled by use of hollow needles persists until now, first performed in 1748 in Europe by Jack Davie. Its development remained contained because of complications and failures, waiting for improved surgical techniques to meet with the challenges of an operation being less invasive. In 1949, in the middle of the problematic of the ocular loss of power, Sir Harold Ridley proposed a new concept: that of a lens inserted inside the eye: the **Intraocular lens (IOL)**. This solution to drastic distortion cases requiring spectacles was followed by other significant advances, for example the phako-emulsification method combined with the remarkable progress towards a lens compatible to biological tissue, anatomy, that exhibits the extraordinary feature of being foldable.

Intraocular lens design

Widely accepted since the early 1980s and extensively developed, the intraocular lens is a piece of lens (IOL), unadorned of appearance: sometimes yellow or transparent and simply made with plastic; with its quite minuscule dimension, it consists of a circular, sometimes square, diameter of $6mm$ and a thickness below the millimeter, prolonged by spiraled loop or plate extension, generally two, called haptics that anchor the lens into the posterior chamber of the eye. Fantastically prosaic, its action is to bend the rays of light behind the posterior cornea to restore to the eye its focusing power. This property is commanded by the surface shape first and the property of the materials; usually for covering a range of power from 15 to $30D$. The fabrication process (of Alcon IOLs) proposed is based on molding techniques such as: injection molding, liquid injection molding, compression molding and transfer molding. A mold cavity is formed to the requisite shape by one or multi-part assembling anterior and front surface of the IOLs as well as the haptics. Several issues indeed are encountered in the manufacturing process: finished edges in relation to tissue damages, treat of aberration (particularly of astigmatism), cleaning for safety purposes, handling. The IOLs can be made with one of several materials, according to their properties. Typically the choice is: hard and rigid materials such as polymethyl methacrylate (PMMA), or soft and resilient polymeric materials such as, hydrogel, acrylic, or silicone. The characteristic of lightness, compatibility with biological tissues, as well as deformability-foldability for insertion of the lens are a fundamental feature of the IOL success story.

Diversity of designs

As for spectacles or contact lenses, many refractive solutions currently exist, mostly governed by optical considerations. In effect, refraction demands an optimum correction for far-field and a particular interest for the extension of through field vision

in compensation of the accommodating crystalline lens. Manufacturing advances have allowed significant optimization in the concept and design of IOLs, leading from aspherization, initially controversial [177], to even more provocative models such as a wide-field IOL, accommodative, achromatic, or corneal compensator. A great diversity of designs is commercialized based on refractive, diffractive, or hybrid optics. Concretely, these targets are concentrated in improving daily tasks; and, by lack of means, often accept incomplete correction in near vision, assuming the use supplementary glasses. The challenge is to cover daily visual task requirement without the additional use of glasses.

2.2.2 IOLs quality

Standard assessments are concerned with the optical quality of the manufactured IOL and authorized a maximum of $\pm 0.25D$ of diopter errors on the lens power, which encompasses both errors of curvature and higher-order terms of aberration. What is their nature for distinct designs such as the spherical and the aspheric IOL? Several methods of aberration measurement exist for responding to this question which we will briefly mention and discuss. We then present some interferometric measurement of distinct IOLs, further analysed in a ray-tracing model eye.

Aberration measurement techniques

Most aberration measurements are indirect and based on intensity measurement. Measurements can be done on either the pupil or the image plane.

Phase retrieval technique In the case of a simple aberration and under restrictive conditions, the phase can often be derived from the characteristic pattern of intensity measured by a detector on its image plane. However, as soon as the phase gets more complex, the phase terms interact in a non-trivial fashion in the intensity

distribution, and phase recovery necessitates an iterative optimization, e.g. a search direction, a criterion... The problem that consists in finding the Fourier phase ϕ_P , buried into the modulus of the Fourier transform of a complex amplitude object $P(\xi, \eta) = TF^{-1}\sqrt{PSF(x, y)}$, is called phase retrieval, and is equivalent to reconstructing an object from its autocorrelation, e.g. the optical transfer function. An iterative non-linear optimization algorithm enables a solution for the wavefront that minimizes the difference of the estimated amplitude of the field and the modulus of the detected field. Such procedure was proposed in the eye for wavefront estimation of the double-pass psf measurement but suffers from computation speed, and local minima in presence of noise. The addition of constraints such as multiple focus planes, wavelengths, or field point methods, can also be incorporated as to narrow the range of possible solutions.

Sampling Methods Wavefront sampling techniques are also extensively used for ocular measurement corresponding to isolated portions of the outgoing or ingoing wavefront and can use information(e.g. variation of the intensity position) from the image plane (wavefront sensor and wavefront curvature) or from the pupil plane (pyramid wavefront sensor) ... Both can employ for this purpose a grid, obscuration technique, or simply a restricted beam for portioning the pupil.

Tilt wavefront sensing The first technique relies on the relation between the intensity position at the focal plane of a lens associated to a certain local wavefront tilt. As it will be in the presence of a Seidel tilt β in the x direction, of the form $W(\rho, \theta) = n\beta\rho\cos(\theta)$ that the Gaussian focus gets shifted in the Fourier plane by a measurable amount $f_x = R\beta$. The tilt is imposed by the aperture size and the pixel windows and the resulting displacement, captured by the centroid of the intensity. On that principle, several ocular measurement methods were developed such as the Tscherning aberrometer, sequential aberrometry laser ray tracing and the well-known Shack-Hartmann wavefront sensor [7].

- The **laser ray-tracing** or **sequential aberrometry** [206, 207] performs sequentially the measurement of the wavefront tilt by scanning with a narrow laser beam, a range of pupil position, for example 37 for a 6mm pupil. In this method, the centroid of reference is obtained for the image taken at the center of the pupil: its displacement gives a measure of the transverse aberration.
- The **Tscherning aberrometer** replaces the scanning procedure by probing simultaneously several thin beams physically defined by a grid in front of the eye. It has an important limitation such as the need of a schematic eye for reference, and differentiation of the beam set and aperture. Note that in these double pass procedures, the beam is re-imaged through the whole pupil.
- The technology of the **Shack Hartman** reconciles the two techniques by combining the speed of a single measurement of the Tscherning aberrometer with the accuracy of the Laser ray tracing by sampling the outgoing beam. It benefits from the geometry adjustment of the device, usually oriented towards the increase of the dynamic range and the sensitivity of the measurement. The principles will be further discussed in the next chapter. Its thorough development in recent years has made it as accurate as an interferometer.
- An older technique is **spatial resolved refractometry** (or **sequential subjective ray tracing**) based on a subjective alignment method of the subject in the image space, of a reference beam non-aberrated and an image through a localized pupil aberrated, by adjustment of the object in object space. This is only measurement method allowing a single pass assessment.

Curvature sensing Proposed first by Roddier [253] in the context of astronomy, this technique is based on the idea that a phase change is connected to a variation of intensity along the propagation on the image. Curvature sensing associates the modulation of a distribution of intensity $c = \Delta(I)/I$ from two out of focus images, equally spaced from the geometrical focus to the local curvature wavefront (or second

derivative) at the pupil position following a development of the irradiance transport equation:

$$c(\rho) = \frac{z}{k\epsilon} \left[\frac{\partial}{\partial \rho} \phi(\rho) \psi - \nabla^2 \phi(\rho) \right] \quad (2.3)$$

where $\epsilon = \frac{f-z}{f}$ is the demagnification factor, $\psi = \delta(r - D)$ delimits a radial tilt impact on the pupil edge. This technique is combined to sub-aperture sampling and wavefront sensor techniques. The distance $(z - f)$ avails a controllable dynamic range, in contrast to wavefront sensing. However, the separation between plane on each side of the geometric focus as well as the pixel size may be critical.

Pyramid wavefront sensor The pyramid wavefront sensor [50] is an application of the Foucault knife edge test that also exploits the modulation of a distribution of intensity in the pupil plane associated to the truncated portion of the beam I_{tr} at the image plane. In a pyramid wavefront sensor, four images of the pupil plane are collected, split at the image plane that is sampled by a prism. The modulation of intensity from these four parts is associated in the same fashion to the phase gradient.

Interferometry The phenomenon of interference affords a possibility of direct measurement of the phase, exploited by a rich variety of interferometric techniques [181] by combining an unknown wavefront with a known wavefront taken as reference. Its principle relies on the modulation of a spatial intensity profile caused by two or more interfering waves such that, if U_1 and U_2 :

$$I = \langle |U_1 + U_2|^2 \rangle = \langle |U_1|^2 \rangle + \langle |U_2|^2 \rangle + 2\text{Re}U_1U_2^*, \quad (2.4)$$

where $\langle U_1 \cdot U_2 \rangle$ denote the term of phase.

For a uniform phase and the same intensity of the reference beam, the formula reduced to the equation $I = 2I_0(1 + \cos(\phi))$, showing a direct relationship between

the phase variation and the fringes emerging from the intensity modulation. An invaluable technique for the manufacturer is the *Twyman interferometer* [181] based on division amplitude. A collimated beam is split by a beam splitter following two branches, one corresponding to a reference wave (reflected back from a mirror) and one for illuminating an object under test. The light from the object under test and the mirror double pass in the system by means of a beam splitter, later unified on a CCD camera that records the intensity of fringes. The Twyman-interferometer is also combined with the phase shifting technique that consists in modulating the phase of the reference by three, four, or five increment phase shift of half a wavelength. By doing so, the phase becomes a function of the contrast between images, which presents several advantages among which, high accuracy and less effect of intensity variations. Another interferometric apparatus employed in our experiments is the very useful *shear plate* that permit an easy check of the state of a beam. It uses the interference of the wavefront with a tilted version of itself; method, in fact, very close to the measurement of the derivative of the phase, if considering an infinitely small shear distance dx between the two recomposed beam with intensity: $I = \frac{(\phi(x-dx)-\phi(x))}{dx}$. Following the same principles, a last class of wavefront of interest is the one using as a reference their own filtered signal.

Standard of manufacturing quality

One of the huge challenge of IOL manufacturing is the warranty of the optical quality of the IOL, and more particularly the precision of its power. The classical methods recognized by manufacturing standards for IOL optical testing are largely based on magnification, target-image assessment and model eye evaluation imposed by standards [149, 277]. Here is a short list of their requirements.

Magnification method The dioptric measurement can be reconstructed by physical measurement of its radii and its thickness using the lensmaker 's equation in

air:

$$\frac{1}{l'} - \frac{1}{l} = \frac{1}{f}, \quad (2.5)$$

As regards of the dimension and the fragility of the IOL, a second method is the measurement of the back focal length by an alternative method proposed by the ISO 11979 – 2 : 1999 standard, which consists in the precise measurement of the magnification of a line by IOLs. Repeatability and reproducibility anticipated are of 0.5 and 1% of the dioptric power, respectively.

Target resolution The resolution limit measurement, required by ANSI standards (*EN/ISO11979 – 2*) is based on a direct imaging through a circumference of $3mm$ of the IOLs of the well-known US Air Force 1951 resolution target (made up of horizontal and vertical bar groups of distinct spatial frequency). The measurement is obtained for the finest patterns, which should combine both resolvable horizontal and vertical bar, and denotes the resolution efficiency (referred to the cut off frequency of the lens). The criterion of the focusing state is the best overall balance between coarse and fine patterns. Noting the subjectivity of the method, the accuracy of the measurement is stated about 20% and its reproducibility 30% of the cut-off frequency.

Eye model quality EN/ISO-11799-2 (1999) for the imaging quality of IOLs prescribed the use of a model eye with an aberrated-free cornea illuminated by a collimated light and optimized by adjusting a camera. The model eye quality is measured for the illumination of $3mm \pm 0.1mm$ of the lens by recording the modulation transfer function MTF. ISO standard requires an MTF above 0.43 at a defined frequency of $100cycles/mm$ or alternatively for specific design above 70% of the theoretical expectation.

Aspheric and spherical IOL profile quality

A statistical sample In this study, a full description of the lens (e.g. curvature, thickness and irregularities of the IOL surface) was attempted by means of interferometric measurement in order to disentangle the various geometrical contributions of the lens in the diopter errors. For comparing and checking classical optical test, three statistical samples, each composed of 30 IOLs of $20.5D$, were measured using a Fisba interferometer as shown in Fig2.2: (i) the design of aspheric WF (model SN60WF) and (ii) spherical AT (model SN60AT) IOLs passing the optical testing (preceded by the manufacturer); and (iii) spherical design (model SN60AT) failing the optical testing. The optical testing was performed by the manufacturer using a target resolution method. The interferometric measurements were performed in

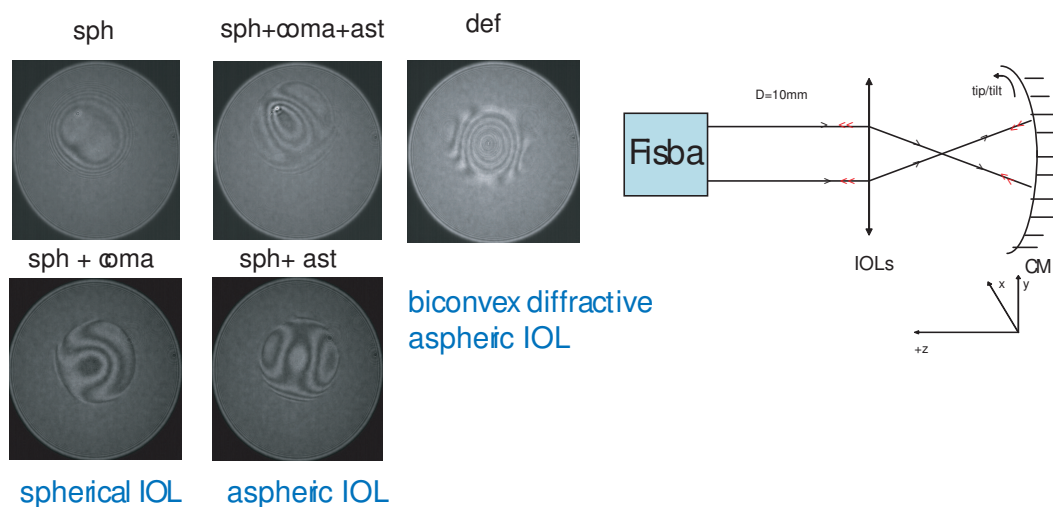


Figure 2.2: Double-pass measurement configuration and typical interferograms for three IOLs design measured in a solution.

a double pass configuration using a laser diode of $633.5nm$ illuminating the sample through a collimated beam through an objective of $10mm$ onto the lens. As shown in Fig-??, the IOL was placed in confocal position with a concave mirror of small curvature so that each ray passes twice in the IOL. The optical path length of the transmitted light was recombined with a reference beam it interferes with, before detection on the back CCD of a Twyman-interferometer (Fisba). The combination of several phase shifts applied to the reference affords a very high precision of $\lambda/100$.

After calibration of the device, the precision of the measurement is deemed of an order less than $\lambda/10$ peak to valley, but the reproducibility of IOL measurements, altered by multiples sources (e.g. gravity, positioning, rotation, change of the surface with manipulation of haptics, and temperature, sensitivity of the apparatus to vibration), is not properly quantified. Previous interferometric measurements in air could deal only with a small $3mm$ pupil, but made in water a $5mm$ diameter could be measured. The IOL sat in a cell, thick of $5mm$, made with BK7 glass of refractive index 1.5, and filled with purified water solution, inducing a negligible amount of spherical aberration, on the converging pencil entering the IOL.

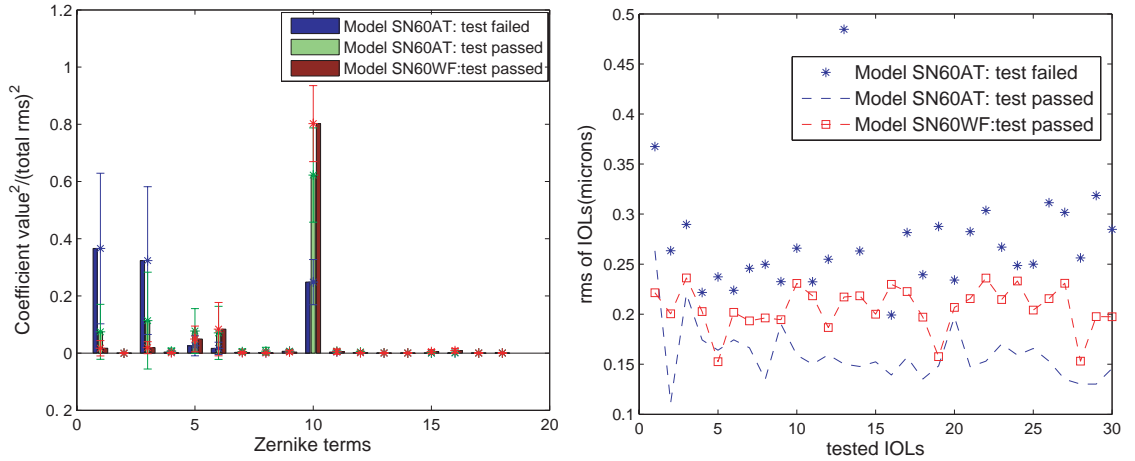


Figure 2.3: Zernike term distribution of statistical monofocal IOL samples.

The Fig-2.3 suggests clear differences in terms of wavefront rms between the three groups. The failed group has the worse optical quality with an rms of about $0.25\mu m$ compared to the two passed IOL groups respectively affected by a wavefront rms of $0.2\mu m$ and $0.15\mu m$ for the aspheric and spherical design. These discrepancies are also emphasized by the characteristic of the wavefront distribution in the three groups. In the failed group, asymmetrical Zernike modes, Z_3 and Z_5 , dominate neatly over the symmetrical Zernike term, Z_{12} . These surface irregularities suggest some manufacturing errors due to moulding process [151]. In the passed group, surfaces irregularities are significantly reduced and represents only 10% of the total contribution. Thus, the choice of design may predispose more specific sources of error as

astigmatism remains the main defect from the spherical design whereas coma tends to be stronger in aspheric IOLs. For both design, the Zernike term Z12 contributes to most of wavefront variance.

A thick or thin lens? The difference of IOL quality of the spherical design and aspheric design questions their respective impact in refractive surgery. The IOL impact is tested in the real eye by proceeding with the reconstruction of the entire lens, for both surface deformations and curvatures. The surface reconstruction is performed for the 30 IOLs of the two IOL samples having passed the optical testing of the manufacturer, using the dynamic data exchange interface (DDE) of the optical program Zemax with Matlab. The optimization of the optical configuration of the double pass measurement, illustrated in the Fig-2.2, starts by an initial estimate, borrowed from the standard IOL, specified by the manufacturer. At the entrance and the exit of the system is placed a phase plate, which is loaded with the actual interferogram measurement of each lens it simulates. In absence of aberration of the phase plate, a collimated wavefront is collected at the exit of the system by a paraxial focussing lens (placed at the return of the beam propagation only), then forming a perfect image, used as our target of optimization. When introducing the aberration measurements, the image is not a perfect point anymore and the optimization process start updating and searching the IOL surface, used as a compensator, and reshaped it until the most plausible IOL profile is constructed. We assume that of the system image quality. Our merit function or design goals, was based on the minimization of the spot diagram for a qualitative assessment, followed by the rms of the wavefront, and used the Damped Least Squares optimization algorithm. The wavefront was referenced to the Gaussian sphere centered on the centroid of the image plane. Asymmetric aberration from the double-pass measurement were assumed to originate strictly from the lens and the Zernike defocus terms in ρ^2 , as well as, tip and tilt, were removed from the interferogram. This procedure had not a single solution, and we had to make the choice of a tactic and a target. The shape factor

or ratio of the curvature $X = \frac{c_1+c_2}{c_1-c_2}$ was kept constant and only the anterior surface (fronting the anterior chamber depth) was re-modelled. Deformation of the IOL surface were added using the sag generated by a series of Zernike polynomials up to the 5th radial order, as variable. Irregularities were applied only on the spherical surface, facing the chamber anterior depth. The azimuthal frequency 4 and 5 were excluded in the reconstruction ($\cos(5\theta), \cos(4\theta)$) by reason of a frequent bias during the optimization.

The spherical term was controlled by the 4th coefficient of the sag, and the defocus and spherical Zernike terms were kept null to prevent coupling between ρ^2 and ρ^4 terms (no straight method was found to impose a proportionality factor between the terms. On the other hand, simulated small dioptr errors were admitted uncorrelated to the irregularities of the lens. Thus, we generated a set of aberrated IOLs admitting Seidel defocus errors of $\pm 0.25D$. The standard IOL were assumed with or without amount of curvature. For the same profile, the IOLs of different curvature were found having the same rms wavefront errors (excluding defocus).

Standard description and IOL reconstruction Even before the introduction of the biconvex monofocal IOLs, the aspherization of intra-ocular lenses is discussed [1, 2, 3, 177] in view of the enhancement of the plano convex IOL correction. Soon, the model SN60AT, then followed by the model SN60WF are going to mark a new generation of biconvex lens. Both IOLs presents a spherical anterior surface but they differ in the posterior surface that provides them with a different quotient of spherical aberration: positive for the AT design, described by a posterior spherical surface, and, negative, for the WF design, having an aspheric posterior type of surface. Both IOLs are characterized by a different Coddington shape factor X , which is a parameter essential in optimization [297, 280]. For a thin lens, this shape factor is related to the Seidel aberration by the quadratic expression [3]:

$$S_i = A_i + B_i X + C_i X^2, \quad (2.6)$$

where A_i , B_i , C_i depends on the Seidel terms. Following a development of this

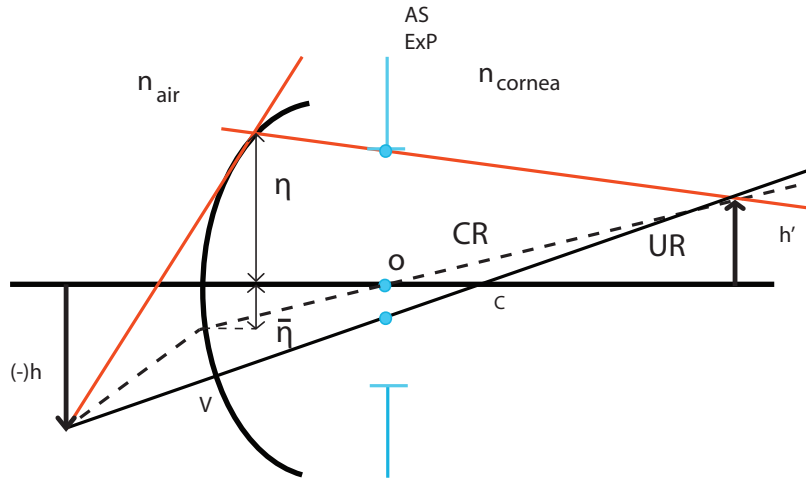


Figure 2.4: Spherical refractive surface with aperture stop not at the vertex position. CR is the chief ray and UR the undeviated ray passing through the center of curvature of the lens.

expression given by Welford [311], a common dependency of these geometric aberrations can be attributed to the parameter α , that is function of the asphericity Q and the paraxial marginal ray height η at the vertex plane of the lens:

$$\alpha = c^3 Q \eta^4 (n - 1), \quad (2.7)$$

also extended for a two lens formula by Atchison as:

$$\alpha = \frac{f \eta^4}{8 \Delta n^2} (Q_p (1 + X)^3 + Q_2 (1 - X)^3), \quad (2.8)$$

α defines the level of spherical aberration, and is linearly related to the other Seidel aberration in accordance with:

$$\left\{ \begin{array}{l} b1 = \alpha/8 \\ b2 = \alpha E/2 \\ b3 = \alpha E^2/2 \\ b4 = \alpha E^2/4 \\ b5 = \alpha E^3/2 \end{array} \right. \quad (2.9)$$

where $E = \frac{\bar{\eta}}{\eta}$ is the stop shift factor with $\bar{\eta}$ the ray height of the chief ray. The stop factor is both dependent on the stop position and the angle of the field. From this little detour, it emerged that the action of the shape factor on the geometrical aberration is intimately linked with the term of asphericity and the power of the IOLs: the stronger the power, the higher the ratio between spherical aberration and amount of aspherization. Hence, aspherization of the posterior surface introduces an extra degree of freedom with respect to the correction of aberration and the determination of the shape factor, counterbalanced by the possible emergence of undesirable odd aberrations. In the situation of the spherical design, the weak amount of positive spherical aberration generated outside the paraxial region of the SN60AT design contrasts with the negative spherical aberration targeted by the SN60WF to compensate the positive spherical aberration of the cornea. The aspheric surface is described by a hyperboloidal surface with the asphericity, $Q = -42.193$, which is converted to a nominal value of spherical aberration of -0.27λ , i.e. $0.17\mu\text{m}$ for a 5mm pupil, very close to the tested IOL. Let note that although the tested IOL provides a coefficient of 0.2λ , i.e. $0.1165\mu\text{m}$ of spherical aberration over 5mm , the absence of description of the asphericity of the SN60AT design.

2.3 Post-operative refractive correction sensitivity

2.3.1 Effect of manufacturing defects of IOLs on vision

Average eye model

The cornea typically accounts for 80% of the total ocular wavefront aberration [245]. Despite a lot of variation of the corneal profile in the population [152] and by age [12], a relatively unanimous positive spherical aberration is reported across the studies [213]. A more detailed description of corneal population may incorporate astigmatism $Z(2, -2)$, trefoil $Z(3, -3)$, shown significant in a population of cataract patients, by Holladay and co-workers. The account of asymmetric aberration involves also the complex mechanism of tuning between the two eye lens and the eye tilt. The angle κ is not comprised in the model used. Our eye model is constructed on the basis of Navarro eye model data [99] for the cornea, refractive indices at various wavelength, and the distance between iris and cornea. The cornea is described as rotationally symmetric with a spherical aberration: $c(4, 0) = 0.166\mu\text{m}$ for a 6mm diameter pupil, relatively small in comparison with other eye models [120]. The pupil size was defined by the pupil of the system, placed at the iris plane, by the beam entering the exit pupil of the IOLs. The model was tested for three different pupil diameters: 3 – 4 and 5mm. For this eye, the crystalline lens is replaced by a standard IOL, sandwiched between aqueous and vitreous media. The posterior spherical IOL surface was facing the vitreous media. Thinner than the crystalline lens, the positioning of the IOLs is of particular concern in pseudophakic eye modelling. In effect, its position substantially affects performance and behavior of the eye model because of the focusing portion and the ray angle of incidence on the lens. Here, we proposed to apply a distance matching with the derivation of empirical power calculation method (employed by surgeons) from the A-constant value prescribed by manufacturing. The distance between the cornea and the IOL,

Performance of standard refraction with different IOLs asphericity

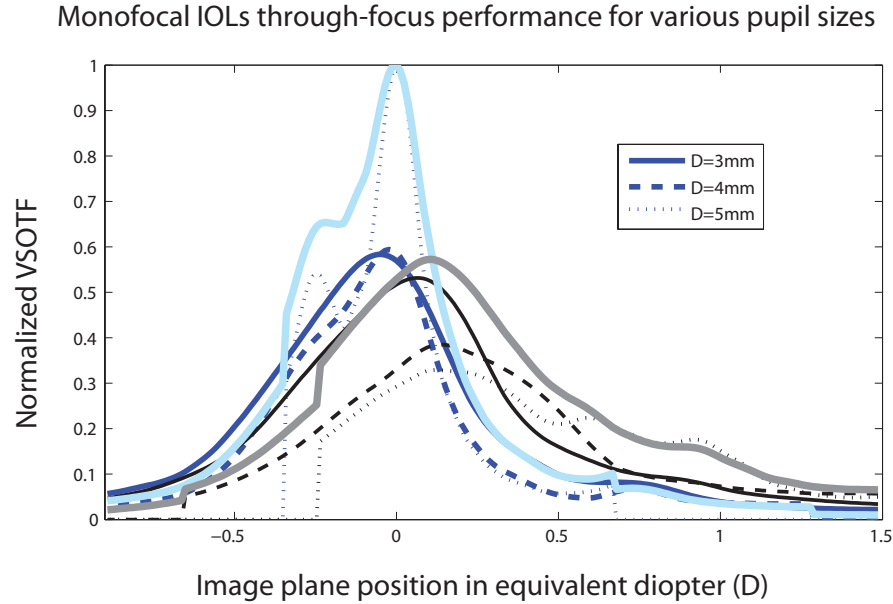


Figure 2.6: Aspheric WF (in dark blue) and spherical AT (in black) monofocal IOLs through-focus for various pupil size and the equivalent volume imaging VSOTF of the aspheric (in blue) and spherical (in grey) IOL. The metrics are all normalized to the maximum achievable value of the best design (i.e. SN60WF).

Through focus versus pupil size

Aspheric and spherical design performance for varying pupil size Based on this model eye, a calculation of the through focus of the two monofocal IOL designs is performed, for various pupil sizes, in white light. Through focus performance is referenced to the best image plane, or best refraction for the pseudophakic eye model, corresponding to the aspheric design for a 3mm diameter pupil. The two designs differ by the ideal plane of refraction by about $0.1D$. The spherical design optimal performance attains its maximum for a small pupil size (full line), and decreases for higher pupil (dot and dashed line) due to the higher amount of spherical aberration at a bigger pupil. To the contrary the performance of the aspheric design culminates at higher pupil size and decreases with smaller diameter owing to an optimal balancing of spherical aberration, for the myopic eye, at a 5mm pupil diameter. The decrease of the optimum performance is accompanied by an increase

in through-focus performance. According to Fig-2.6, the through focus performance of the aspheric design (blue dark curves) largely outperforms the spherical design (black dark curves) due to almost total cancellation of corneal spherical aberration, with a neat emphasis at bigger pupil size. The aspheric IOL performance also varies little with varying pupil sizes showing only a slight variation of the wavefront interaction between cornea and IOL. To the contrary, pupil size changes have important consequences for the spherical design, as the positive spherical aberration is lowered for smaller pupil; it results in a shift of the best-focus of the spherical design, but therefore a more extended volume of imaging compared to the aspheric design.

Towards an extended criterion metric: the Volume imaging VSOTF

Modelling should respond to the following question: on what criterion shall one define this through-focus performance and the proper combination between optimum and depth of the performance? A $4mm$ pupil is generally considered by most ray-tracing study for the pseudophakic eye, which is grounded in the narrowness of the pupil of people having cataract surgery. However, variation of pupil sizes with light level conditions and subjects focus here are shown to be essential for a proper comparison of the two design global performances and their dynamics. Which pupil domain to retain and how to distribute a correct weight over the pupil is left to the designer's arbitration. For that reason, we employ the extended metrics volume imaging VSOTF, previously mentioned, that incorporated the overall varying pupil size performance averaged. It shows that the through focus performance of the spherical design (light grey curve) is more stretched than the aspheric design (blue light curve) and its fall-off less abrupt. Setting a threshold criterion of 40% of the best-focus value for through-focus assessment, the aspheric design outperforms the spherical design; below this threshold the spherical design this ratio start changing. The design performance strongly depends on the definition of the target of the model, itself depending on both task requirement and prior knowledge. For averaged cornea and small variations of the IOL positioning, visual through-focus

performance is expected to be little affected. In the choice of design, one may account the complex interaction of the cornea and the IOL as it may strongly impact best focus over different sizes. An advanced comparison of the design is needed to enlarge the scope of comparison (e.g. look at wider field angle and through-field vision) without altering the precision found on axis.

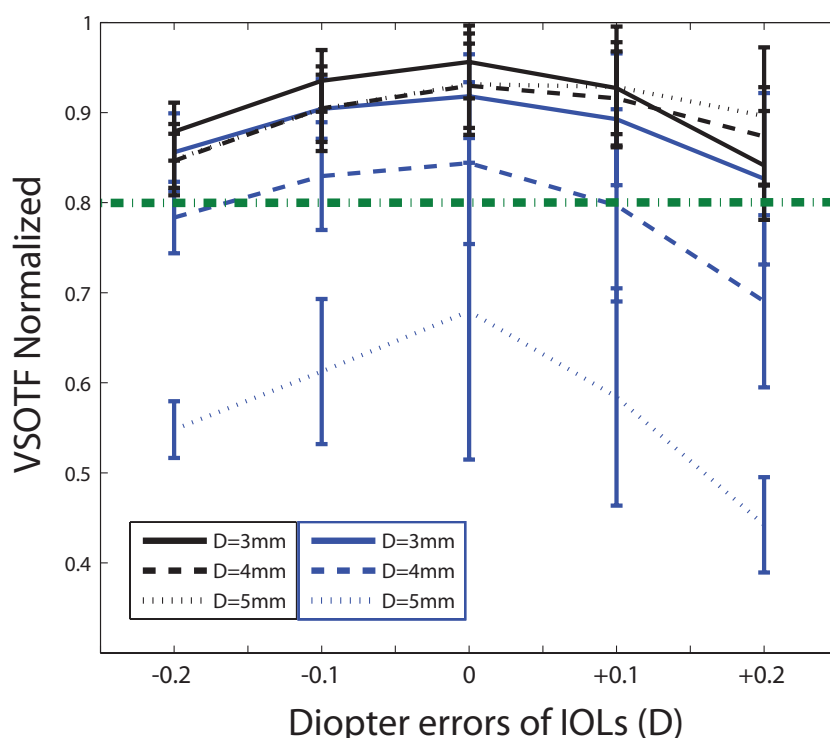


Figure 2.7: Sensitivity of the optimal refraction with monofocal IOL in presence of manufacturing defects for varying pupil sizes. Monofocal best focus correction in presence of surface irregularities, normalized by the maximum achievable value associated to the aspheric design WF (blue curve) and the spherical design AT (black curve). The green line represents the 80% visual Strehl ratio criterion above which correction is considered to be acceptable.

Impact of surface irregularities on the refraction A related analysis is performed on the robustness of an optimal corrective refraction by inducing the manufacturing errors of the intraocular lenses we measured and reconstructed in the optimized model, i.e. the standard IOL having successfully passed optical testing. For that purpose, only the IOL curvatures are modified and the surface irregularities applied. The new and actual performance of the 30 reconstructed IOLs is tested by calculating the VSOTF metrics normalized (for each IOL design by the VSOTF

value of the standard eye) at different pupil size for various level of diopters errors. As shown in Fig-2.7, for both aspheric and spherical surface, one can observe a positive interaction, respectively for lower (on the left side) and higher IOL power (on the right side) due to respectively the positive and negative aberration terms of spherical aberration and defocus residual. This compensation is more pronounced for the aspheric design by reason of the actual difference of residual spherical aberration between the two designs. The tolerance to surface irregularities is significantly different for the two designs. It comes out from this simulation that the spherical design, though less performant optically, is relatively more robust than the aspheric design to curvature errors and surface irregularities for all the pupil size, in particular at bigger pupil. For the spherical design, our simulation is in agreement with the $\pm 0.25D$ power tolerance, claimed by the manufacturer. The relative manufacturing tolerance is diminished in the case of the aspheric design, strongly affected by the deformation of its anterior surface (only this one being modified) as well as the change of its curvature. An equivalent criterion of the 80% Strehl ratio of the Marechal criterion indicating a $\pm 0.1D$ error for a $4mm$ pupil diameter, as confirmed by visual test [166]. Such response to the alteration of the surface may depend to some extent on the parametrization of the deformation. Given the little information on each surface contribution, only the anterior surface was altered. An additional point is a decrease of contribution of the $2.5mm$ pupil in the volume imaging VSOTF because of the sensitivity of the aspheric design; which should equate now the through-focus of the two design.

2.3.2 Power calculation methods

Post-operative power calculation prediction can be crucial as several sources of errors [214] can add to the subjective variability of the surgery outcome depending on the eye, the design and the target considered. Among these sources of errors are the internal: changes of the eye related to age [12], the accommodation, pupil sizes, the

cornea surface [132, 187]; but above all the errors related to the placement of the lens in the capsular bag [57] are responsible for the success of the post-operative prediction. These sources of errors come from a combination of decentration and tip/tilt, as well as the axial position of the lens with respect to the iris (related to the haptics design), extending also to the rotation of the lens in other designs [128]. These errors indeed are to carry important consequences with respect to the type of IOL design and its powers. Thus, instead of an ideal placement of the IOLs in the capsular bag related to the techniques and the surgeon skills, the problematic may figure as the optimal displacement in which the refraction can be not affected. In this study, we present the current calculation methods used in cataract surgery and proposed a comparison in the simulated real refraction conditions with more robust power calculation strategy.

2.3.3 Thin lens power calculation methods

Several formulas [261] exist for power calculation employing different terminologies for describing the most significant parameter of refraction and capturing their variance. These formulas, derived from a 2-lens formula, are empirically adjusted by using large sampling of postoperative results to fit the best fit with an optimal correction. Here is a short description of the ophthalmic strategy in vogue, advocated by some popular formula: the SRK, Holladay and Hoffer formula.

Empirical methods The Sanders Retzlaff Kraff (*SRK formula*) is one of the most employed power calculation method of IOL. As most empirical formula, it is based on a 2-lens formula using the mean corneal power, the axial length and the anterior chamber depth distance (ACD). It considers a fixed ACD in all eyes, enclosed in a standard parameter, so-called the $A_{constant}$. The A-constant indexes the optimal

corrective value of each type of IOL design based on the SRK formula, so that:

$$P_{IOL} = A_{constant} - 2.5AL - 0.9K - Rx\sigma \quad (2.10)$$

where K is the mean corneal power calculated by keratometry, AL is the axial length measured by A-scan ultrasonography, Rx is refraction desired and σ is a corrective factor rising for eyes with long axial length. The $A_{constant}$ is first fixed by the manufacturer. Typical values are: $A_{constant} = 118.4D$ for SA60AT ; $A_{constant} = 118.7D$ for SN60WF. Let note that this parameter is independent of the IOL power and ignores the transformation pertaining to the change of lens profile and the geometry of the anatomical structure of the eye.

Owing to a relation of proportionality between ACD and axial length distances, other generations of formula accounts for the interplay between cornea, axial length and IOL parameters. In its modified version, so-called SRK II formula, the ACD is adjusted to palliate the errors for long and short eyes and cover a broad range of IOL powers: this correction goes up to $+3D$ for eyes of less than $22mm$, and correspond to $-0.5D$ for eyes greater than $24.5mm$. Eyes within $22 - 24.5mm$ are considered acceptably refracted.

The *Hoffer Q formula* is also derived from this new generation and assumes a relationship between the ACD and both axial length and corneal power, that results in the updated form:

$$ACD = pACD + 0.3(AL - 23.5) + (\tan K)^2 + \tan(0.1(G - AL)^2)(0.1M(23.5 - AL)^2) - 0.99166, \quad (2.11)$$

which is based on the personalized $pACD$.

The personalized $pACD$ is derived from the manufacturers ACD-constant (or equivalently the $A_{constant}$) either personalized from a chosen $A_{constant}$ according to [142]: $pACD = ACD_{constant} = A_{constant}0.5836 - 63.896$ with a standard estimated post-

operative: for SA60AT $pACD = 5.2$ and for SN60WF $pACD = 5.3773$.

The personalization of the pACD is done by back-calculation of the ACD that minimizes the refractive errors of the surgeon population group and uses the following 2-lens formula:

$$P = \frac{1336}{AL - ACD - 0.05} - \frac{1.336}{\frac{1.336}{(K+R)} - \frac{ACD+0.05}{1000}} \quad (2.12)$$

Probably the most serious source of variance introduced is related to the lens haptic plane notion, or predictability of the lens position relative to the iris plane. The novelty of the *Holladay formula* is that it introduces an adjustable parameter named the S factor, which estimates the distance between the IOLs and the iris plane. It is given by $S = A_{constant} * 0.5663 - 65.6$ i.e. for SA60AT $S = 1.45$; for SN60WF $S = 1.4499$ and is merely sensitive to the IOL design. The Holladay formula also involves an intricate relationship between ACD and both corneal curvature and axial length. It turns into a very complicated form of power calculation: $P = f(S, Rx, K, AL, ACD)$ owing to the corrective factors. Long axial lengths are ill-estimated.

These built-parameters are attributed to the lens style, manufacturer, surgeon, and the apparatus of measure. Thus, the regression purpose enables to lessen constant bias related to devices and IOLs designs [204]. Power calculation seems to be oriented towards an effective focal length, but expresses little account for higher-order aberrations in the correction. Note that the SRK/T formula dominates for longer eyes ($> 26mm$), the HofferQ for short eye ($< 24.5mm$) while the Holladay formula best outcome dominates between 22 and 26mm.

Gaussian methods A higher degree of description was proposed by Barbero and al [33], using analytical solution based on Gaussian and primary aberration theory, which provides a detailed account of the anatomical layer of the eye, from the passage

air-tear film to the propagation in the retina, e.g. radii of curvature, thickness and refractive indices. By comparison with ray tracing, the authors found a difference of power prediction ranging from $1D$ in complex eye model to $0.12D$ for simple eye model, due to the neglect of diffraction effect, cone directionality, and misalignment errors.

2.3.4 Thin lens and Ray-tracing model comparison for spherical and aspheric design in condition of moderate amount of errors

The aspheric design aims at correcting higher-order aberrations and therefore is expected to gain in performance when using a ray-tracing calculation method [231] contrary to the spherical design, amplifying the amount of aberration of the averaged eye. Yet, part of the success of refraction belongs to a sensible prediction of the appropriate IOL power [219]. An optimal precision of $\pm 0.25D$ is affordable on the market given the constraint of manufacturing and the accuracy of the positioning of the lens depending, on which to a certain extent is the function of the prediction. In the situation of a null spherical equivalent target, illustrated by the light-adjustable IOLs, an exact prediction becomes more and more desirable. **The question addressed by this study is: should one account for a sophisticated calculation of power given the variability of the measure?**, questioning therefore the role of lower and higher-order aberrations. This study is restricted to an on-axis comparison and only compares best focus, in the initial design of monofocal IOLs.

Protocol 200 hundred eyes (generated from our averaged model) represent the perturbation of a refractive surgery correction. The cornea profile is fixed as well as the axial length of the eye; only the IOLs position fluctuates with modification of tilt and tilt, centration and axial position. The IOLs surface profile is taken ran-

domly from our data set, adapted to the variation of their curvature. No refractive index change is implemented and we did not introduce a change of kappa angle. The positioning of the IOLs was accounted by an eACD change, up to $\pm 0.227mm$ (corresponding to $1D$ in the eye). Its alignments was also randomized within a reasonable fluctuation change of $\pm 0.25mm$ for decentering and ± 2.5 deg for tip and tilt. In the Fig- 2.8, we show prior calculation performed for the two designs (on another model eye) to highlight their distinct sensitivity. Using a normal distribution,

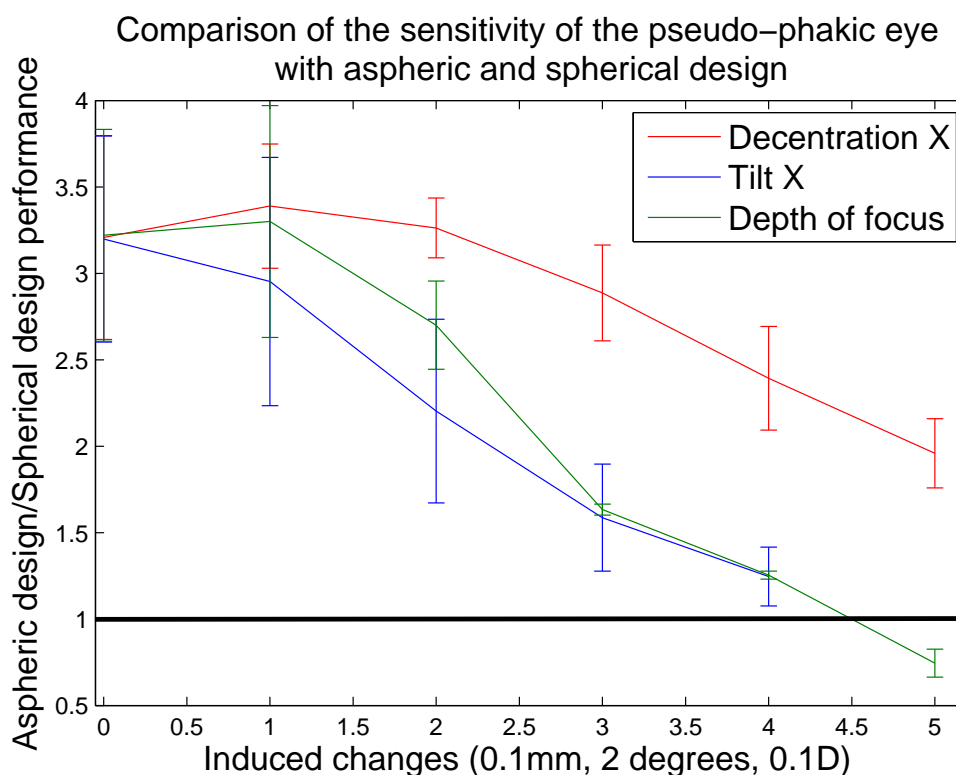


Figure 2.8: Relative optical performance of the two monofocal IOL designs in the presence of various simulated errors of an analogous pseudo-phakic ray-tracing model eye. The units of induced changes on the vertical axis are $0.1mm$ for decentration, 2 deg for tilt and $0.1D$ for depth of focus, respectively.)

the surface radius of the IOLs were modified by $\pm 0.25mm$ for the spherical anterior surface against $\pm 0.2mm$ for the aspheric; and $\pm 0.2mm$ for the posterior surface (either aspheric or spherical): a similar amount of curvature errors, within $\pm 0.2D$, was posited for the two design curvature. The thickness of the IOLs was varied by 10% of its value and we imply a constant refractive index. On this geometry, the irregularities were implemented on the surface of the IOLs. The parameters of the

Monte-Carlo simulation are gathered in the table.

| Biometric measurements | standard deviation |
|-------------------------------|---|
| anterior chamber depth (aCAD) | $\pm 0.227mm$ |
| Surgeon factor S | $\pm 0.1mm$ |
| Posterior radius | $R_p = \pm 0.25mm$ |
| Anterior radius | $R_a = \pm 0.2mm$ (for aspheric); $R_a = \pm 0.25mm$ (for spherical) |
| Thickness | $\pm 0.06mm$ |
| Surface irregularities | From interferometric measurements |
| decentrationX | $\pm 0.25mm$ |
| tiltX | ± 2.5 degrees |

Table 2.1: Biometric measurement errors induced in the Monte-Carlo simulation of the two customized eyes.

The axial length is estimated by employing four different approaches:

1. Ray-tracing of the refraction that maximizes the VSOTF volume imaging metrics (without accounting for error events).
2. Gaussian focus of the polychromatic illumination, using the same biometry of the eye.
3. Empirical power calculation based on the manufacturer ACD-constant (matched with our average eye ACD)
4. Regression formula based on a personalized ACD, back-calculated on the basis of the run of a statistically similar distribution of errors using the same average eye. This back-calculation is meant to null the spherical equivalent, here replaced by the paraxial focus.

The Fig-2.9 offers a comparison of the post-operative outcome of the two IOLs designs as well as an assessment of power calculation methods. The distribution of the optical performance of post-operative simulated correction uses the visual volume imaging metrics. For each design, the VSOTF outcome is normalized by the maximum achievable refraction, fixed by its standard (design). It should therefore

be taken into consideration that the maximum value of the aspheric design is about two-fold the spherical design (as shown in Fig-2.6).

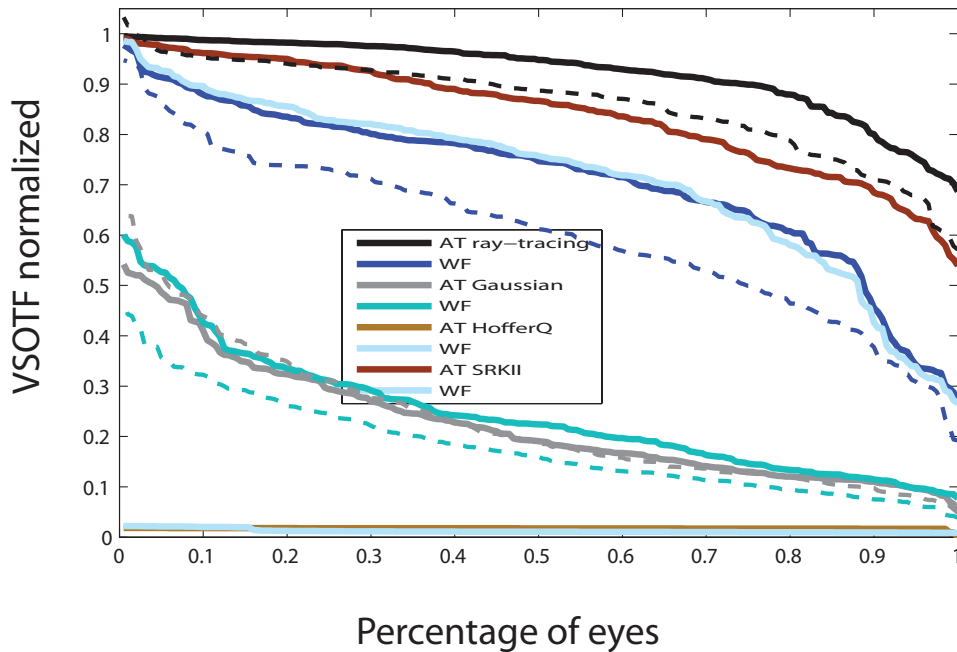


Figure 2.9: Comparison of the post-operative outcome of the spherical AT (black hue curves) and aspheric WF (blue hue curves) monofocal IOLs design obtained for paraxial power calculation and ray-tracing in the regime of small errors. Each design is normalized by its own maximum achievable refraction. The full line corresponds to the standard refraction and the dash line to the presence of the irregularities added to the lens. 1) SRK II formula corresponds to the back calculated IOL. 2) HofferQ power calculation method appears below the other curves.

Observations & results

1. Although the aspheric design best focus outperforms the spherical design, aspheric design optimal performance falls off more severely than the spherical design in response of misalignment errors IOLs and manufacturing defects. 80% of the eye being corrected by the spherical design conserved above 75% of their optimum performance against 25% for the aspheric design. Besides, the two-fold majoration of the aspheric design is nulled for the worse eyes statistic, although still in the range of moderate variation.
2. The impact of the irregularities of the surface is significant for the two designs,

but more marked for the aspheric design. This observation is reinforced in the Gaussian refraction method.

3. As expected the ray-tracing method outperforms all the other power calculation prediction, even the back-calculated SRKII method, which is in fact a pure average taken over an identical distribution.
4. An impressive fall-off affects the Gaussian method. This is an indication of a manifest robustness of higher-order aberrations in a varying-operative refraction of moderate magnitude. Higher-order aberrations are therefore determinant in terms of optimum refraction robustness to the refractive variations: only 5% of the eye benefiting from above 80% of the maximum achievable refraction.
5. The empirical power calculations calculated from the manufacturer A-constant appears in the bottom of the graph, with an error of refraction, in reference to the IOL power, of respectively 0.28 and 0.49D for the aspheric and the spherical design using the Hoffer formula; and 0.8D for aspheric and spherical design using the SRKII formula. The back-calculation of the optimal A-constant or ACD was only performing well for the corrected SRKII formula. It did not improve the HofferQ formula.

Conclusions The power-calculation method or model prediction has a role determinant in the outcome of refraction because higher-order aberrations contributes to augment the positive outcomes of a post-operative prediction for both IOL designs. The expected benefit of insuring the surface quality of the IOLs is higher for both aspheric design and spherical design, for ray-tracing model. Two lens based eye models are unvalidated by an inferior outcome of empirical power calculation method. In the context of a random variation, Back-calculation of the best ACD evidently greatly improved the HofferQ formula method when applied to an equivalent statistical variation of the sample. Although the post-operative correction based on

aspheric design outperforms the spherical design performance for the average eye in low environment variations, it is also increasingly less robust to variabilities of the predicted correction. In particular, the irregularities of the aspheric IOL exhibits higher sensitivity than the spherical design on the post-operative outcomes, exceeding the “just-noticeable change” threshold imposed by the visual system [166] for larger pupil.

These results are confined to the context of mild variations of the global model. More severe variations may results in different trends as the aspheric design is known to be less effective for larger misalignment as emphasized in other studies [128]. These results have dint of generality for the interplay of the lens with the average eye-cornea, but ignore the complementary mechanism of compensation involved by the individual eye structures [124, 189, 32]. For the customized eye, the total wave aberration is expected to combine differently with spherical equivalent and also to vary with corneal asphericity.

2.4 Conclusion

In conclusion, this study provides a robust method of comparison of IOL design performance. It highlights the predictability and the sensitivity of a customized correction with respect to cataract surgery and initiates to the challenges of a realistic eye model. In the particular situation of mild variation of prediction, a superior achievable performance of the aspheric design at one point field is shown in support of the beneficial cancellation of corneal spherical aberration, but balanced by more robust performance of the spherical design to the sources of errors of the correction. The profound limit of our model is that it considers perfect optical imaging, rarely attained in central vision and evanescent for different field positions, as the best reference. Hence, a burning question is how to finely coordinate different field positions with the requirement of high resolution central vision. To explore this

question, we propose to incorporate the presence of aberration in the visual system and analyse their particular effects. We turn in the next chapter to the participation of the subjective component of the visual stimulation.

Chapter 3

Adaptive Optics Visual Simulator

This chapter is interested in the simulation of spatial vision in real eyes and steps forward in the assessment of customized vision. The general requirement of an AO visual simulator as well as the system conception, aligned with the initial purpose of testing patients having IOL, are given. An analysis of the performance of the system and its components is also provided, followed by an extension of the optical target outside central vision.

3.1 Context

Though the eye reflects admirably the dynamism and the challenges of an adaptive optics system by its ability to track, adjust and process its visual world, the interest of a real-time correction of distorted images appears in the first instance in Astronomy in relation to celestial observations, affected by atmospheric variation and turbulence. A fastidious and complex recovery of the phase information enshrouded in altered images brings forth the concept of Adaptive Optics, envisioned

by Horace Welcome Babcock in 1953, as way of using prior phase information. The principles of its operation, phase conjugation, is equivalent to a multiplication of the field by its complex conjugate $|U|exp(-i\phi)$ reversing the distortion. It relies on a measurement of the phase distortion of the signal followed by the appliance of a compensatory action on the next coming signal by means of an active element able to mirror the path difference, where the keystone of the procedure is the operation of an intelligent feed-back communication between sensor and corrector operated by the computer control. Awaiting further technological advance in sensing and light element correction, a first implementation is realized statically for generating pure aberration mode, followed by intense development that soon includes other fields, such as laser shaping, free space communication, or the eye. In 1997, the team of Rochester brings out the first operating visual AO system able to correct this neglected contribution of retinal image degradation, already investigated by [269], so-called higher-order of aberrations. And adaptive optics is observe having a huge potential for enhancing human vision and for probing the retinal structure. Many contributions accumulate in the space of 10 years for satisfying the need of an efficient and real-time correction with more mature devices as well as lower cost [244]. In this run, the AO visual simulator seems converging towards an examination nearer to the real condition of seeing which recently include binocular AOs [100, 135], and some wider-field AO system [36].

3.2 Visual Analyser design

Overcoming the challenges of a low numerical aperture, imperfect optics of the eye, high required light levels, and eye motion are the challenge of a visual analyzer. In this context, the primer design of this custom-built adaptive system was to provide high efficiency of phase errors correction, compactness/flexibility, and comfort for potential older subjects. Driven by these targets, we attempt to reduce each ramification found in a typical adaptive optics system. The evident advantage is a gain

of light, flexibility and usability, balanced though by the cost of more onerous technologies and materials, and to some extent selectivity in the target of the imaging. Three main branches compose a visual simulator:

1. an illumination path and alignment pupil
2. a wavefront sensing arm
3. an imaging and visual arm

3.2.1 Illumination and pupil control

Source of illumination The choice of the source plays a great deal in the imaging process. If probing the quality of the eye equates to see the same way it sees, it averred that the higher-order aberration magnitude and dynamic remain fairly constant across the spectrum. The choice of the wavelength is then mainly a compromise between subject commodity, safety and the efficiency of the double-pass measurement. In this study, we selected an infrared source because it presents the advantage of higher retinal reflectance with about 10% of light scattered [76], less damage and discomfort over long exposure period. A higher amount of scattering and a least efficiency of detector devices in this spectrum balances these points. Higher wavelength have also an advantage in visual testing as it prevents conflicts between target and illumination brightness. To minimize the eventual overlap, stimuli and illumination beam are shifted from each other during the experiment, but at the cost of residual wavefront errors. Our second attention was turned towards a reduction of the spatially localized distribution of intensity in the pupil and speckled spots associated with the roughness of the retina. The common method of averaging the position of the ingoing beam with a scanning mirror was replaced by the use of a pseudo-coherent source with the principal advantage of suppressing the need for an extra conjugate plane. The superluminescent diode imposed itself as an ideal candidate, for its combination of the broadband LED-like optical spectrum and its

laser diode output power. The superluminescent diode was set in infrared at $836nm$ and possesses a bandwidth of $56nm$, which corresponds to a coherence length of 10μ . Such bandwidth was to overcome a standard deviation of the cone length in the scale of 0.34 to $1.88\mu m$ (corresponding to an *OPD* of 0.05 to $0.27\mu m$). Further constraint here is added with respect to a fragile stability, limited power capacity, and the conic profile of the source. For an overfilled pupil of $7mm$ to be in agreement with the ANSI Standard [77], the illumination imposed a maximum permissible radiant power (MPE): $MPE = 6.93 \times 10^{-5} C_T C_E P_{-1}$, function of the two coefficients wavelength dependent: $C_T = 10^{0.002(700)}$, P_{-1} and $C_E = 1$, as well as $C_T = 1$, a coefficient dependent on the spatial coherence of the source. For an overfilling pupil of $7mm$ the superluminescent power at the cornea must not exceed $130\mu W$. This exposure is five times smaller than the thermal threshold damage edited by the National Standards Authority of Ireland and the European Union (I.S. EN60825-1:1994/A2:2001) In our experiment, the power of the beam sent into the cornea did not exceed $40\mu W$.

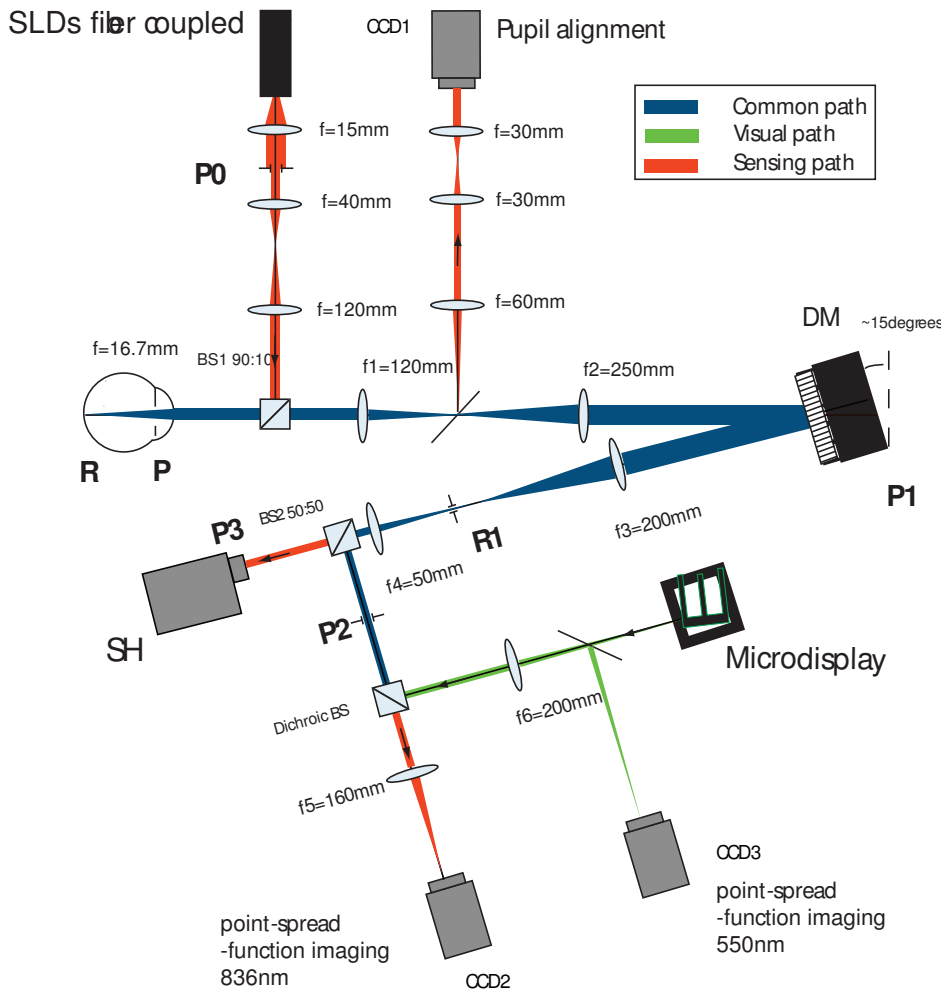
Mechanical control The illumination path, in its minimal version, consists essentially of a collimated Gaussian beam coming from a probe beam adjusted on the back focal plane of a lens. The control of the divergence of light, the power of the source, as well as the directionality of the illumination beam calls generally for the addition of relay lens and does not afford an easy and practicable solution for single lens illumination. Hence, the choice of an aspheric condenser lens with small focal length (characterized by few aberration and high efficiency illumination), followed by two relay lens.

Double-pass measurement and characteristic of the imaging Sent into the eye, light is bent and focused onto the retina. Assuming perfect optics, a tiny spot is created onto the surface of the retinal and subretinal layers, resulting then in both specular reflection and scattering. The light reflected back from that station

serves as a secondary source and affords extensive analysis concerning the optical properties of the eye and on how the eye alters light on its way back. Such a method implies indeed equivalence of the ingoing and outgoing optical path with respect to the pupil. The principal difficulty resides then in the fact that the phase of the extracted light is a combination of the information from the interaction of the light coupled with the photoreceptor antenna and the second pass. Therefore, the size of the spot that is sampled by the photoreceptors matters significantly. If the beam is sufficiently small, the aberrations are minimized on the first way and the spot on the retina averaged among photoreceptors [14, 86, 175]: the contribution of the first pass is then ignored. However, this approximation becomes increasingly inaccurate for bigger pupil diameter with the increase of aberration and the conservation of the averaged phase information which leads in the situation of a single scatterer to a reversible process characterized by a rotationally symmetric wavefront. In contrast to a retinal imaging optical system using full pupil for illumination and imaging, in this set-up, light is restricted to a small ingoing beam which enters the eye with a diameter of 1.84mm , leading to a spot size of $18.5\mu\text{m}$ (e.g. 3.81arcmin). The focusing of the spot onto the retina was separately deemed by asking the subject to minimize the spot size; by contrast with some system on which the illuminated beam is simultaneously adjusted with visual refraction. The beam is displaced in the center core of the pupil, 1mm off axis from the center of the pupil typically, to avoid the corneal reflection onto the detector and maintain the efficiency of the ingoing beam, in view of the Stile-Crawford effect.

Pupil monitoring and alignment The pupil monitoring branch conjugates the pupil of the eye P, axially and laterally movable thanks to micrometer stages and fixed on a chin rest, to a camera of alignment coupled with a monitor. It is composed of two pairs of relay lens initially designed to match some constraint of conformation of the pupil and of the arm length. The pupil imaging enables to see the edge of the pupil sharply, which is important for accurate axial position in the case of the

generation of aberration in a particular plane (e.g. IOL implantation simulation). The corneal aberrations and the off-axis sensitivity of the achromat lens were the main disrupter of image quality. This branch is introduced by a tip/tilt mirror in the wavefront path, immediately after the lens facing the eye, L1 (which determines the depth of focus of the pupil image). This is an advantageous trick to avoid additive illumination in the system or a loss of light, though it necessitates a reliable position of the eye during the test and a possibility of tracking of the image through the Shack-Hartman spots. Its cost: during wavefront sensing, the portion of the subject pupil is now undefined without the edge information. Given the application of our test, this was not a major limitation. Practically, the pupil adjustment of P is done along the line of sight of the subject by displaying a crossbar target on the display, and aligned with the physical pupil P3 of the visual path. The software mask pupil is matched with the circular area of P3, the generation of a defined aberration relies on. For complete removal of aberration in a closed-loop correction, the pupil mask may be automatized.



3.2.2 Calibration and construction

Commanded by the obligation of common path seen through the three elements, the imperatives of the wavefront sensing branch is essentially the matching of the device dimension and a conjugation control for the pupil and retinal plane. A refractive system faces the non-negligible back-reflection associated with a lens of about 1% and therefore addresses the need of off-axis mirrors, as employed in many ophthalmic systems [125, 316, 243, 172]. An excellent advantage of mirrors, alleviation of chromatic issue is counterbalanced by undesirable rise of astigmatism with alignment errors and the field angle subtended at the retinal plane [118]. To satisfy the criterion of compactness and light efficiency, no mirror was employed and the system

was restricted in its number of pupil and retinal planes. The scaffolding was then mobilized by the insertion of the mirror, in this arrangement relayed by achromat lens and positioned with a slight angle of 15 deg. That option releases the addition of optical element such that a beam splitter or mirror placed in front of the DM, with yet a drawback that now the pupil conjugation on the mirror would produce a slight bias when simulating an aberration. The arrangement was tested in Zemax, and validated experimentally by calibrating the system.

Geometry Based on these keystones, the geometry of our system comprises a central afocal unit coupled with the eye lens and the visual branch. Characterized by an f-number near 15, the afocal unit is made of two relay lenses that conjugates the eye pupil with the deformable mirror and the Shack-Hartman wavefront sensor, following a magnification factor of 2.08, and 0.4 (e.g. total magnification of 0.52), which allows a maximum pupil measurement of $6.9mm$ of the eye. Such configuration provides both pupil and retinal control. The compactness of the branch is principally defined by the back focal plane of the first lens fronting the eye in coordination to the size on the various pupil plane. This same lens plays the role of a Badal Optometer by getting translated as an ensemble with the eye relative to the rest of the system: it can be said that the eye is matched to the system alignment. Light from the retina is physically filtered by a diaphragm that enables to reduce diffusion from the reflection of unfocussed retinal plane. By setting a region of interest during measurement based on the image lenslet spots of the wavefront sensor, the corrected light can be selected.

Alignment The alignment was achieved by using a laser, insuring that the optical axis was centered on each lens and on each device. Because of the elevation of the system in two blocks, some limitations were imposed in this task. The retinal and pupil conjugate were assessed by using the wavefront sensor, a shear plate, or simply the size spot. More elegant solutions such as interferometry, or the knife-edge

technique were not required. A second precaution concerned the collinearity between single pass and double pass illumination. The construction consists of aligning the center of all our lenses with the axes of the set-up defined by the optical axis of the artificial eye, confounded in reality with the line of sight of the subject. Every time the subject is aligned the first step is to align him with respect to the optical axis of the artificial eye (ideally confounded with the direction of fiber beam) for which the Haso is calibrated.

Calibration The calibration of the system is achieved using an artificial eye consisting of a probe beam of about $10\mu\text{m}$ collimated by a unique lens, with a focal length of 30mm limited by a diaphragm acting as the entrance pupil seen by the DM and the SH. Comparison of our calibration with a finer calibration obtained with a longer focal length show only slight differences. Assuming that the aberration from the artificial eye is negligible, the aberration of the system is of the order of $\lambda/4$ of rms over the full 6.9mm pupil when the mirror is off. These are principally due to the tricky centering of the system associated in great majority to an offset of the two juxtaposed platform. When the mirror is on, this rms converts into an rms of $\lambda/2$, largely dominated by astigmatism and owing to the irregular surface of the DM (near 0.1μ of rms) . An indication of the success of the calibration could be accounted for by the number of iteration necessary for the AO correction to reach its minimum rms value: for full application of the corrective command (e.g., gain set to 1), the complete correction requires two frames in order to get twice smaller, and three frames, to attain the order of $0.02\mu\text{m}$. The residual wavefront rms reaches $0.13\mu\text{m}$ of rms wavefront error over a 6.9mm pupil. This reduction is validated by visualization of the ring of our Airy disk on the single pass point spread function (for both camera and display). The double pass point spread function is also examined by rotating the artificial retina to remove speckle. The beam diameter sent into the eye was approximated both by using the reflection from the pupil on the shack-Hartmann, and by measuring the double pass PSF using our artificial eye.

The PSF behavior is also used to examine the generation of aberration.

3.3 Measuring ocular aberration

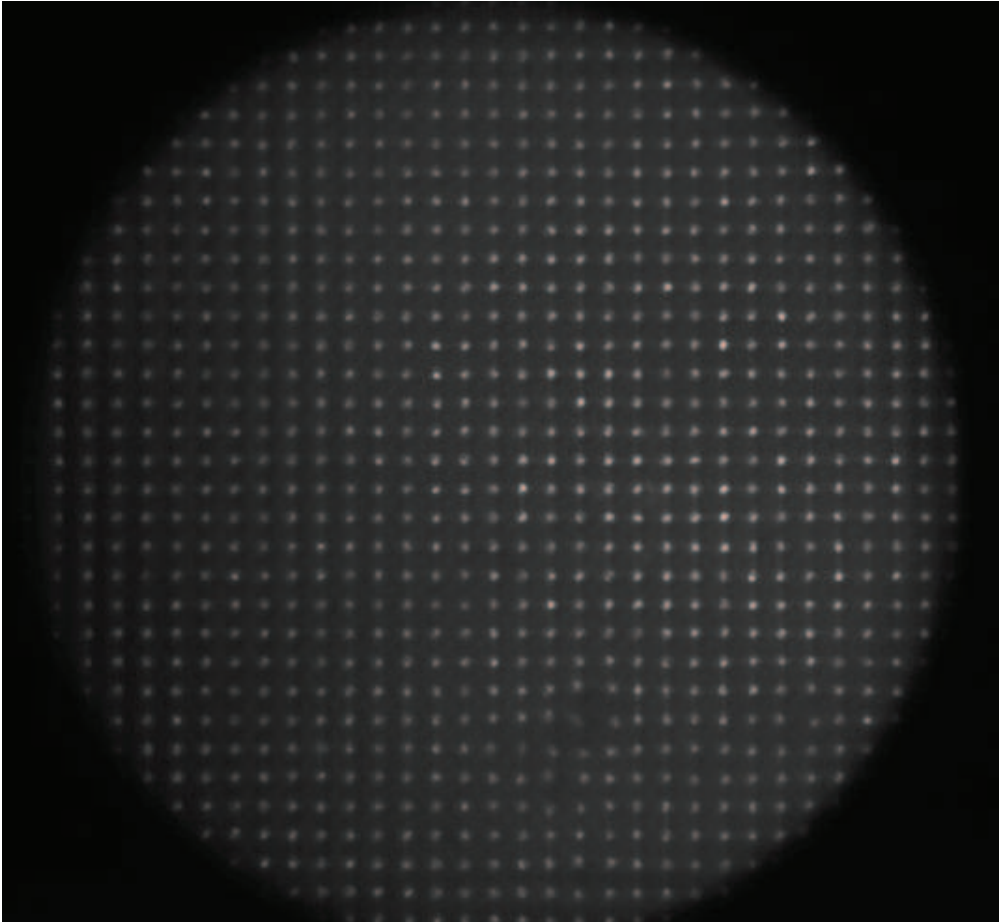


Figure 3.1: Shack-Hartman spots array of a typical eye

The Shack-Hartmann wavefront sensor is a powerful technique that samples the wavefront by means of an array of lenslets, which produces several copies of the retinal object. Their displacement from the ideal position of the plane wavefront is a measure of the wavefront gradient and is supported by various centroiding algorithms and geometry of detection accounting for the noise embedded in the retinal image copies. For an undersampled system, the wavefront reconstruction is confronted to a multiplicity of solutions determined by the geometry of the problem

[279]. The position of N lenslets relative to M actuators of the modified wavefront, classically borrowing Hudgins, Fried or Southwell configuration, imposes a certain relationship between the slope measurement vector s and the reconstructed Zernike mode of the wavefront Z , that is encapsulated in the optimal geometry matrix A so that:

$$Z = [A]^{-1}[s] \quad (3.1)$$

The Haso32e wavefront sensor (from Imagine Eyes), implemented in this study, circumvents this issue by oversampling the number of lenslets, 32 by 40, therefore increasing the spatial frequency of the detection, with a resolution of the ocular wavefront of about $150\mu\text{m}/$ per lenslets. The retinal image, distributed between 1280 spots, requires longer exposure time $40 - 50\text{ms}$ for a $30 - 40\mu\text{W}$ beam infrared shines on the cornea. If optimally the HASO32e runs at 60Hz , in real eye measurement, good readings fall at 15Hz . With smaller lenslets of about 0.114mm of pitch, the demands is turned on the pixelation of the CCD camera with 16.4 pixels per lenslets, for a diffracted image $39.4\mu\text{m}$, as well as the requirement in terms of sensitivity (i.e. the smallest slope measurable) and dynamic range (i.e. the highest slope measurable) of the measured wavefront, which becomes a function of the pixel size and the focal length (set at 2.2mm). The focus is more or less fixed and the optimization is concentrated on the pixellation and centroid algorithm that often may augment in noise. The quality of the spots, less sensitive to manufacturing defects or curvature of the sampled wavefront, varies with diffusion and the size of the beam on the retina. In this regard, our experiments are giving satisfactory results, as can be noted from the image of the Shack-Hartman in Fig-3.1. A diaphragm is added in one of the retinal plane to cut the undesirable diffusion from the back retinal layers. And a dark frame is subtracted to reduce noise. A calibration of the wavefront sensor is made for a wavelength of 850nm . It takes into account errors and defects (such as misregistration, imperfections of the microlens) due to the device architecture. An absolute measurement is claimed by the manufacturer owing

to the use of monomode fibers delivering perfect spherical wavefront. The precision of the wavefront measurement prevents the addition of an arm of calibration of the system.

3.4 Correcting ocular aberration

The eye: an active element

Eye movements The eye movement encapsulates lots of information about the dynamics of the visual world as well as perceptual processes that governed the treatment of the information at a neural-motor level. Immobilizing them, i.e. the image, means the vanishing of the image; but often failed since the eye may always move, that despite paralyzing drop, or physical fixation such as chin-rest, bite bar. These fluctuations present an important amount of diversity: displacing the optics not only backward and forwards, but also laterally and by rotation. These movements are the sum of both voluntary and involuntarily movements where pulsation cardiac, head and body, as well as oculomotor movements conducted by six extraocular muscles participate both to the capture the signal and interfere with its image formation. The best known of them is the accommodation, mostly involuntary process, inducing a change of a quarter of diopter at about $2Hz$ [?]. Lower and higher-order aberration undergoes fluctuation up to $30Hz$ [139, 87]. Other eye movements are pertained to the processing of the scene:

- pursuit eye movements concern with moving target. The pursuit tries to null the velocity of the object and is preceded by a period of latency of $100ms$ and engaged area such as the superior colliculus.
- vestibular eye movements, manifested by rotation of the eye that compensates head and body movement when gazing at a stationary object

- saccadic eye movements involved in attentional task such as search, reading fixation. This periodic phenomenon governed by a preprogrammed latency of longer duration (about $150ms$) at interval of 300 to 200 ms , is a major concern for visual stimulation as it affects processing of the image, through the accuracy of its allocation and by a fall of sensitivity during its occurrence (which hits its summit in the saccadic suppression). The movement is rapid and depends on the distance of the target, somewhat lesser in the fovea; and follows a certain strategy such that at midpoint from its goal, its velocity is maximal and then drops. It should be also pointed now that this saccade is found coupled with attention as well as task-related.

The last category of eye movement, related to foveal correction encompasses:

- the tremor, aperiodic motion, extremely rapid ($> 90Hz$), in fact, constant through observation (connected to the firing of the nerves cells in the retina and some perceptual activity) and therefore of weak magnitude (about $0.2arcmin$).
- the slow drifts, progressive motion (of few milliseconds) that produces a shift of the image of a few photoreceptors ($1 arcmin$). Its origins would be mainly oculomotor, directed by the nervous system.
- the microsaccade, jerk movement of very short duration rate of 1 to $2Hz$, appear generally in compensation of a drift, but reach higher magnitude ($5arcmin$).

The tremendous appeal of both controlling retinal fluctuation and wavefront is provided by the scanning laser ophthalmoscope (SLO).

Lower-order aberration correction

Low-order aberrations are predominant in the ocular wavefront, masking higher-order errors. A long history of tuning and refinement by applying lenses characterizes its application in lens design. The Badal optometer is one of its expression based on the additivity of the vergence: it can be realized through mirrors, prism or in more advanced form with rotating cylindrical lenses affording low cost adaptive correction by automatized adjustment of these order. In this system, a rudimentary expression of the Badal is implemented, based on one movable lens, situated at a fixed distance in front of the eye at the back focal distance, advantageous in terms of light efficiency. An important mechanical constraint results from this choice as regards the displacement of the couple lens-eye as one single unit in front of the system. A robust mechanical piece was used for translation and the set-up was elevated as a result. A recurrent problem was the introduction of a tilt due to, first, the limited precision of the mechanical stage (in X and Y), and due to, a tilt in Y induced by the offset between the two blocks of the set-up. These two errors were accounted for by calibration of the measurement. However, it imposes a strong limitation of the system outside the image and pupil planes. A focal length of 120mm is the compromise between target vergence change and spacing views (nose, beam splitter, mobility of the subject on the bench). For 1cm of translation, a defocus compensation of $0.7D$ is obtained. The maximum change allowed was $-8.3D$. Let's note that the focal length of the system is determined by the Badal lens.

Active corrector elements for complex phase

Active corrector elements are supported by several technologies, structures and spatial geometries. Their selection is mainly turned towards the dynamic and type of aberration targeted. Two main elements are distinguished: the **spatial light mod-**

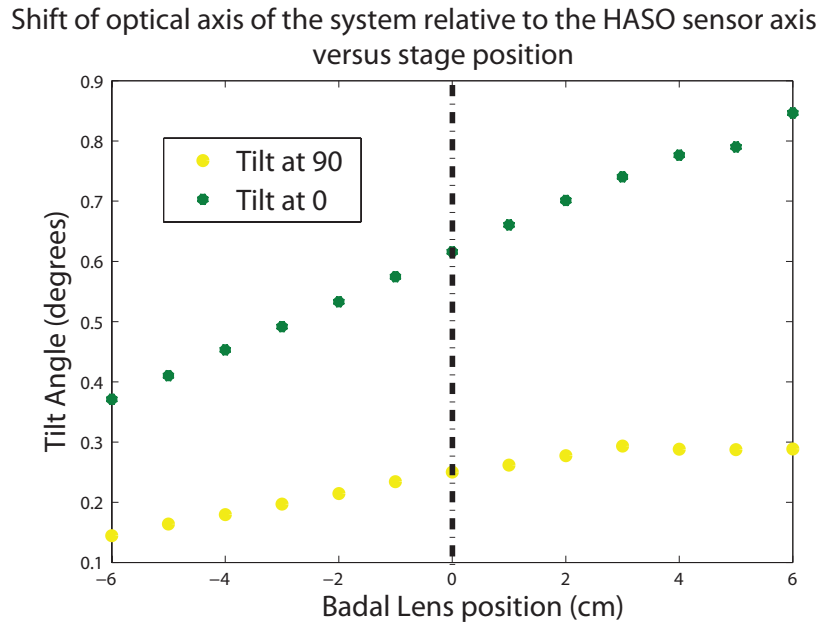


Figure 3.2: Tilt variation for various position of the Badal Optometer.

ulator (SLM) and the **deformable mirror (DM)**, often discriminated by the cost. Both work on radically different basis, as the first interacts by modifying the pathway distance undergone in reflection while the other, transmissive structure, changes the optical path length through variation of its refractive indices.

SLM The SLM is favoured for its rather low cost and a formidable spatial resolution, that can reach a few microns. It also benefits from a wider range of function associated to its electro and magneto optics properties, and is able to modulate intensity, phase and polarization of light. For a standard ocular refraction, this device presents tremendous advantages; but limited with respect to light efficiency, the polarization dependence of the phase changes, and more importantly a lower dynamic range as well as a slow frequency response. It is an important rival of the deformable mirror for visual application such that multifocal testing or binocular adaptive optics arrangement [103].

Deformable mirror In limited parameter freedom or for highly requiring correction, the more conventional DM is still predominant in vision and astronomy. Its reflective application offers reduction of the loss of light and chromaticity as well as dealing with potential off-axis aberration induction [related to their working angle and the variations pertained to the imaged surface (zone, cone angle...)]. Its working modality is typically based on actuation of the surface and modulated in efficiency by the number of actuator, their pitch as well as its relative and absolute stroke. Structural aspects conditions strongly the interplay of the actuators and their freedom, and follows two classes: the segmented and continuous mirrors.

Segmented mirrors are very appealing corrective solution [90, 184], common in astronomy: they provide a zonal response, actuated by separated piezoelectric following a piston/tip/tilt type of motion, which affords non negligible gain in the degree of freedom as well as in the dynamic range. Their geometry is indeed a crucial parameter of the efficacy of the correction as well as the fill factor of each units, which is known to cause diffraction effects and losses of light.

In contrast, the less binary approach of a continuous surface induces a response to the local perturbation of the type modal that involves the whole surface: this deformation is captured by the influence function of a given actuator. A fierce number of techniques orbits in the industry of these mirrors where stands out:

1. the **bimorph mirror** is composed of a piezo material (e.g., ceramic, fluoride) coated by a metallic mirror, the dimension of which are modified by applying voltage commands to its back and front electrodes pattern. A very high response characterizes this technology however limited in its application in the eye by a stroke of about $8\mu\text{m}$ and hysteresis issues.
2. the **membrane mirror** is composed of a thin conductive and reflective membrane electrode interfaced below by a unique group of individual electrode actuators in the back that controls its shape electrostatically, without the need of piezo element. The surface membrane is moved back and forth with

respect to a bias position. It is characterized by little hysteresis, but high currents that require cooling and damping. Because it is possible to operate the mirror with only one group of electrodes, it deliver little stroke.

3. the **micromachine-electromechanical mirrors MEMs** is another form of membrane mirror, composed of tiny and highly packed actuators made in silicon or meta substrate mechanically displaced by electric forces. Its technology, based on bulk and surface micromachining, offers a cheap solution. It combines high response rates, precision and reduction of hysteresis issue. Commonly used in the eye, it is though limited by the stroke.
4. the **ferrofluid deformable mirror** are made with a suspension of colloidal ferromagnetic nanoparticles dispersed in a liquid carrier. Their deformation is driven by a magnetic field that modifies their shape in combination with gravitational and surface tension forces. These DM have high potential for low cost application.

Assessment of the Mirao32e performance

The Mirao32e, provided by Imagine Eyes, stands out from most of electrostatic DM by a huge capability of stroke, owing to its electromagnetic based technology. As illustrated in Fig-3.3, it is composed of a flexible membrane, nearly flat (when off, below $0.1\mu\text{m}$ RMS over the entire pupil) coated with silver that is highly reflective both in infrared and visible tasks. Its surface is deformed by a set of 52 magnetic actuators, spaced by 2.5mm , which are stretched over 17mm and works over an effective area of 15 mm. Because edges of the aperture are often poorly represented, it is currently using only 80% of its surface. Each voltage is applied to a coil that creates a magnetic field pushing or pulling the magnet of the actuator, which deflects the surface in accordance with sign of the voltage. The time response is extremely quick ($< 5\text{ms}$) but counters by an important sensitivity of the spatio-temporal response of the mirror that convert into high frequency fluctuation of the mirror

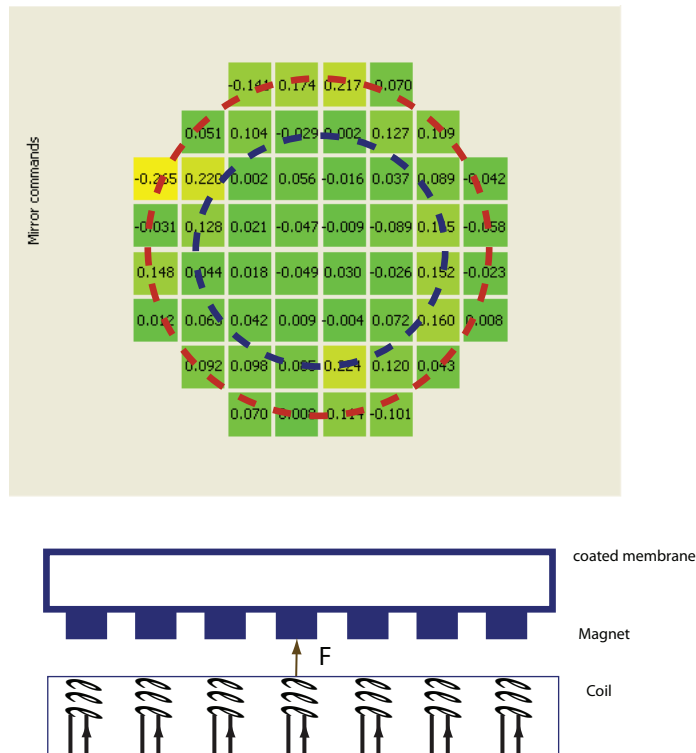


Figure 3.3: Schematic of the Mirao mirror.

surface after an applied change. This increased sensitivity is quantified by the time of stabilization of the mirror response and its spatial deviation from the target; and is controlled by the means of the response, either smooth or abrupt, as well as the rising time of about $5ms$. Low-pass filtering indicates a possible solution of this important issue [216].

Influence matrix of the actuators To figure out the performance of the DM, we proceeded to the recording of its actuator's responses using a standard method [72, 104]. A fixed voltage of ± 0.5 is applied to each of the 52 actuators (little hysteresis was assumed) and we measure the resulting DM surface shape with a Twyman-Green interferometer, as shown in Fig-3.4. The maximum command sent

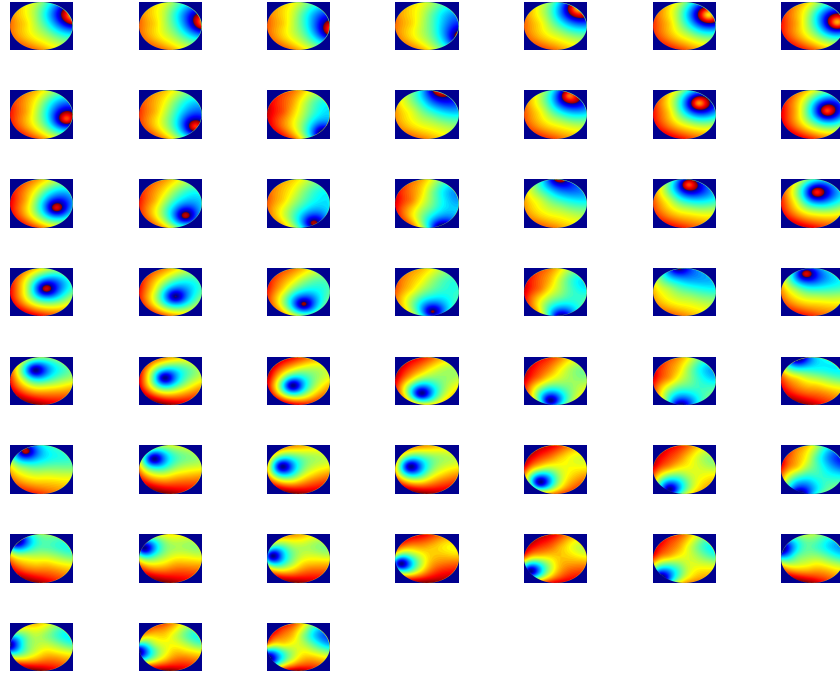


Figure 3.4: Influence function of the 52 actuators of the Mirao measured for a voltage command at half the maximum.

to an actuator is ± 1 , but owing to the stress on the surface it must not in practice exceed 0.8. The deformation of the surface, the so-called influence function (IF) of the actuators, is approximated by a set of 20 Zernike polynomials, Z , up to the fifth radial order using a least-squares fit. The piston term is removed. The set of influence function obtained for each actuator forms a matrix $N * M$, the so-called interaction matrix ($[IM]$). Assuming the linearity of the actuator responses with the applied current, often revealed by coupling or prior signal, this matrix relates the deformation of the surface to a set of voltage:

$$Z = [IM]c \quad (3.2)$$

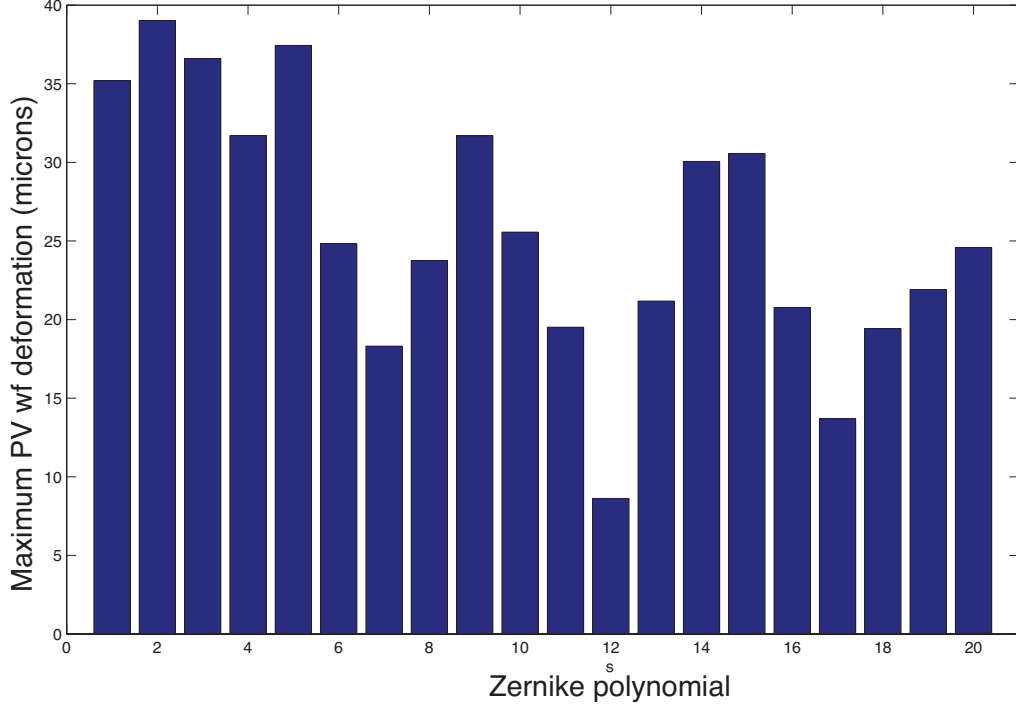


Figure 3.5: Zernike generation in terms of Peak-to-Valley wavefront produced by the Mirao. The piston is removed.

Zernike generation To produce a desired surface deformation, the matrix $[IM]$ must be inverted but because the system is overdetermined (more known value of c than Z unknown), there is no exact solution, and instead one must seek an approximation. One solution to this problem is to make a least square search or more common, in AO system, apply a singular value decomposition (SVD). This method, fast to compute, decompose the matrix $[IM]$ onto an orthonormal basis corresponding to the spatial modes of the mirror $[U]$ and its commands modes $[V]$:

$$[IM] = [U][S][V]^T, \quad (3.3)$$

where $[S]$ is a diagonal matrix containing the singular value of $[IM]$. In this new basis, the inversion of $[IM]$ yield the control matrix $[CM]$:

$$[CM] = [IM]^{-1} = [V][S]^{-1}[U]^T, \quad (3.4)$$

During closed loop, the command mirror for a desired target can be directly calculated from the discrete slope vector following:

$$c = [IM]^{-1}[A]^{-1}s \quad (3.5)$$

This method bypasses the representation of the wavefront and aliasing induced by misrepresented zernike modes: this is the zonal method. For simulating a given wavefront map or pure Zernike modes, the indirect calculation by the wavefront reconstruction is necessary: this is the modal reconstruction, used throughout this study. In practice, the advantage of both solution can be combined. The amplitude of the singular values of $[S]$ gives an indication of how well the Zernike mode is being generated. The smaller the singular value, higher the command voltage to be sent, and the noise. Hence, the DM will be able to produce aberration only with a certain efficiency depending on the mode. For the modes that are poorly represented, the singular value is set to zero. In the Casao, only 45 modes typically were used for large pupil, and 35 for small pupil. Moving towards the periphery, the actuators are less well represented. Besides, the maximum deformation delivered by the DM (for a voltage of 1) for each single Zernike mode decreases with the higher radial order as shown in the Fig- 3.5. The peak to valley (PV) peaks at $40\mu\text{m}$ for tip and tilt (e.g. term 1 and 2), and for the second order at $30\mu\text{m}$. Note that the spherical aberration term, term number 12, is weakly represented with a maximum of $10\mu\text{m}$ compared to defocus (term 4). Practically, the interaction matrix of the system is calculated directly along the wavefront sensing arm and therefore accounts for the non-linearities of correction due to the propagation in the system, as well as the mismatch between mirror deformation and actual pupil measurement (due to the tilt of the mirror). The amplitude of the command applied for the interaction matrix calculation is typically set at 0.2. The software provides a calculation of the control matrix based on the SVD method. The evaluation of the number of mode required is done by means of an artificial eye typically reaching 45 modes for an efficient correction over a pupil of 6.9mm . The global tip and tilt of the 52 actuators is

filtered before measurement by subtracting the measurement slope of each actuator as those modes can be highly dominant. Terms such as piston or others modes on the edge, poorly detected by the HASO32e, are removed for an optimal correction.

Fidelity of the generated mode The theoretical residual wavefront rms errors found in the replication of single Zernike modes was below $\lambda/100$. Fernandez et al [105] claims that the actual reproduction of the Zernike terms as measured by a sensor is ranging from 1 to $8nm$ for rms value of $1\mu m$ in a pupil of $11.89mm$ diameter.. In fact, a substantial coupling for terms such as spherical aberration, astigmatism or coma affects this ideal situation beyond this amount of *rms* as it was specifically observed in a series of simulations aiming at generating pure spherical aberration for open-loop and closed-loop. An illustration of this coupling between Z_4 , Z_{12} and Z_{24} is shown in Fig- 3.6 for various spherical aberration amount generated over a $6.7mm$ pupil in the eye. No clear way around it was really found, except a possibility for these terms of compensation of defocus with the Badal stage.

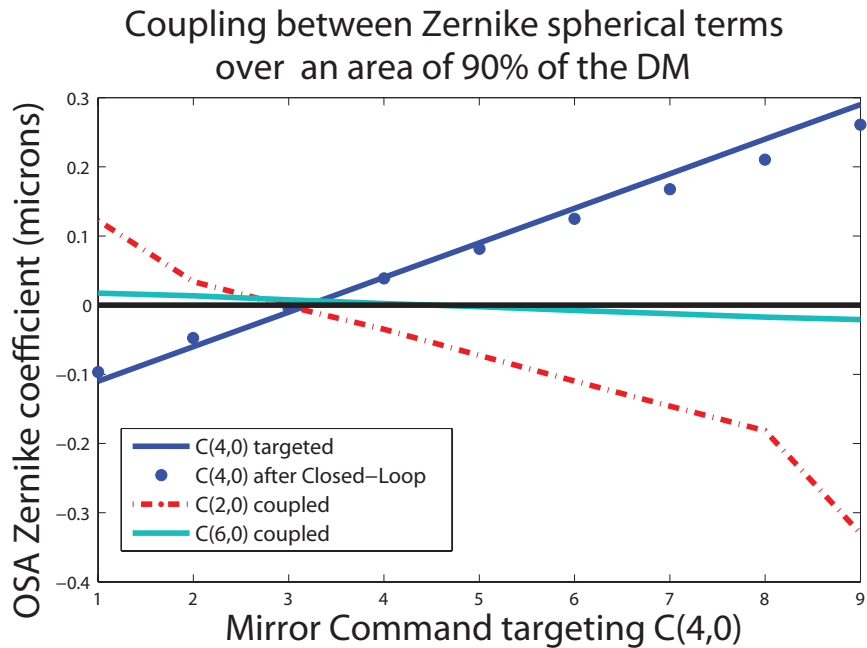


Figure 3.6: Coupling associated with generation of spherical aberration over a $6.7mm$ ocular pupil, i.e. 90% of the DM.

3.4.1 AO performance

Parametrization of the AO loop The performance of an AO loop depends on the ability of the system to compensate a given static aberration and the difference in the input. This static correction is limited by the accuracy of the detection, imposed by the centroiding (corrupted by speckle, readout, photons noise), the reconstruction of the spots (e.g. zonal or modal, number of Zernike terms) and the mirror precision (sampling of the modified wavefront, precision of the command matrix). The residual correction involves a trade-off between sensitivity of the compensation and optimization of the amount of the corrected target, which depends on the statistic of the ocular aberration dynamic [87] and the frame rate of the correction. The frame rate of the correction varies between 10 to $20Hz$ and is split in three steps: the expose and the readout of the wavefront sensor, pipelined, the computational processing of the control computer, and the application of the voltage command to the DM. These defined the **bandwidth errors** and the **measurement errors** of the correction, trade-off between a maximum step correctable without overshoot and the precision of the correction on account to the dynamic. Typically, we can observe in this system a bandwidth error varying from 2 to $5Hz$, which can be considered sensitive given the dynamics of the aberration of the eye and the frame rate of the closed-loop. The residual rms at best for a pupil size of $6.9mm$ is about $50nm$. This value goes up when including tip and tilt. But typically, the non cycloplegic eye fluctuates around $0.1\mu m$ of rms during a stable closed loop.

In Fig- 3.8, a periodogram of the Zernike mode of the subject, before and after AO correction confirms this benefit along low spatial frequency for various Zernike mode with slight variation between symmetric and asymmetric modes.

Theoretically, convergence and stability of the AO loop are derived from the closed-loop transfer function of the system $H(\tilde{f})$ developed through Laplace transform

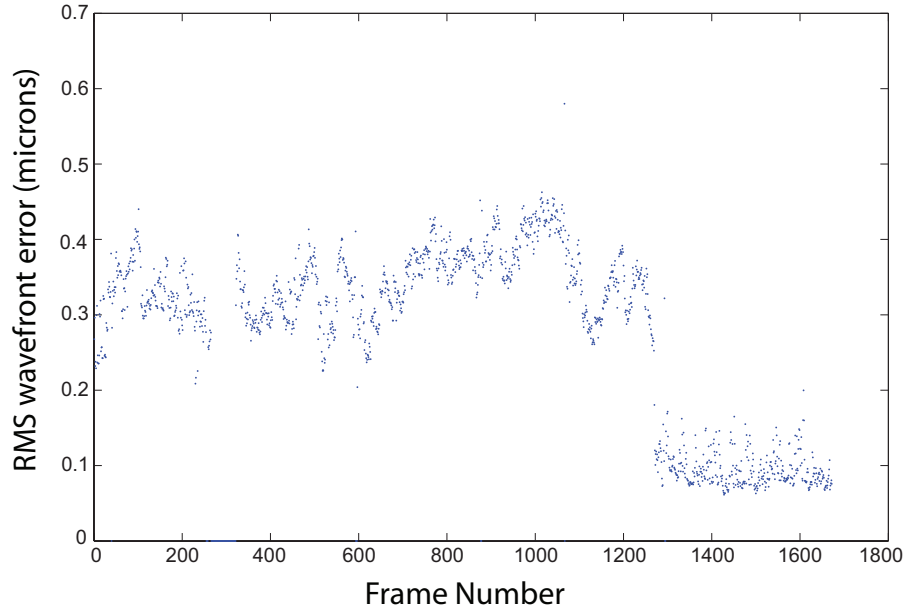


Figure 3.7: Temporal evolution of the wavefront rms of an aberrated eye non paralysed before and after closed loop correction. The closed loop correction runs at a frame rate of $15 - 20Hz$, and a gain of 0.5. The wavefront error is measured over a $6mm$ diameter pupil. Tip and tilt are excluded. The correction is reached in approximately 7 frames and reach about 0.1μ for a $6mm$ pupil diameter.

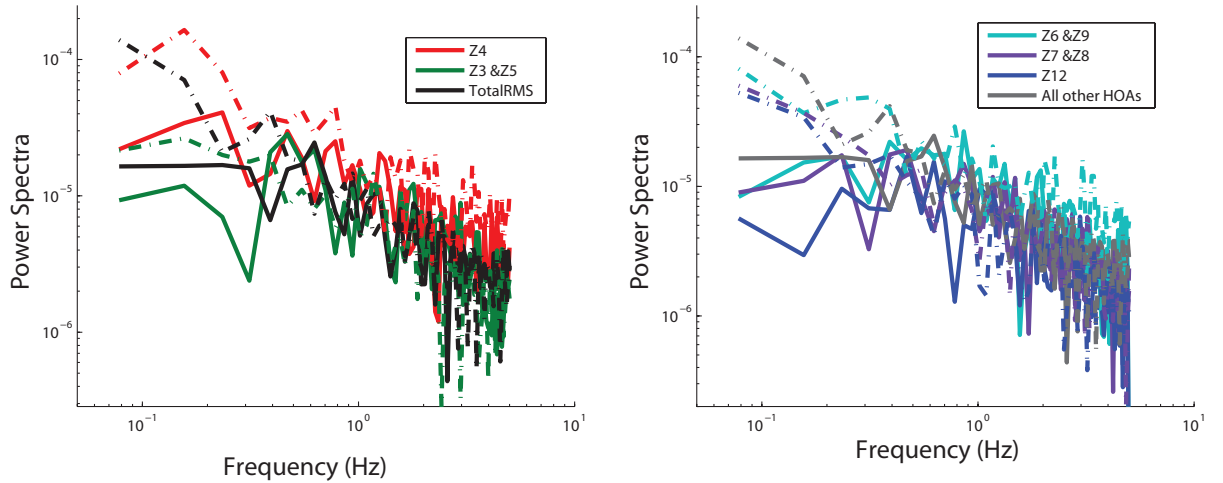


Figure 3.8: Power spectra of the fluctuation before (dash line) and after (full line) of the wavefront rms measured over a $5mm$ pupil undialted for various Zernike mode, for a closed loop frequency of $10Hz$. The minimum frequency spectra is $0.05Hz$. The AO loop demonstrates a substantial benefit over $0 - 1Hz$.

formalism [290]. $\tilde{f} = \sigma + i2\pi f$ is the complex frequency in *radian/s*. It accounts for the propagation of the input wavefront $X(\tilde{f})$ through each individual unit of the

loop, as pictured in Fig 3.9 (this figure actually shows an open-loop system).

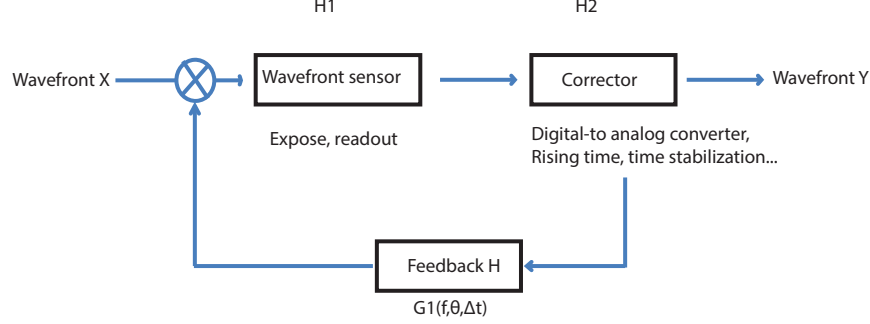


Figure 3.9: Block diagram representation of an open-loop AO system

That is [140]:

- the CCD integration time of the wavefront sensor WS: $H_{WS}(\tilde{f}) = \frac{1 - \exp(-T\tilde{f})}{T\tilde{f}}$
(integration over the exposure time $T = 50 - 40ms$)
- the sources of delay D: $H_D(\tilde{f}) = \exp(-\tau\tilde{f})$
($\tau \sim 16.7ms$, this includes the CCD frame transfer, the slope calculation)
- the deformable mirror DM: $H_{DM}(\tilde{f}) = 1$
(the deformable mirror is assumed to change instantaneously, i.e. $> 5ms$)
- the control computer CC: $H_{CC}(\tilde{f}) = \frac{K}{1 - \exp(-(T+\tau)\tilde{f})}$,
where K is the gain of a simple integrator control that defined the residual:
 $res = c_i - c_{i-1} = K * [IM]^{-1}[A]^{-1}s_i$

The open-loop, closed loop and error transfer function of the system $H(\tilde{f})$ are defined as:

$$\begin{cases} H_{OL}(\tilde{f}) = H_{WS}(\tilde{f})H_D(\tilde{f})H_{DM}(\tilde{f})H_{CC}(\tilde{f}) \\ H_{CL}(\tilde{f}) = \frac{Y(\tilde{f})}{X(\tilde{f})} = \frac{H_{OL}(\tilde{f})}{1+H_{OL}(\tilde{f})} \\ H_e(\tilde{f}) = \frac{H_{OL}(\tilde{f})}{1+H_{OL}(\tilde{f})} \end{cases} \quad (3.6)$$

In absence of a statistical model of ocular aberration dynamic, experiments on real eye prevail for tuning the AO loop. The relation input-output is experimentally

modulated by measuring the performance of the AO closed loop on subjects cycloplegic (e.g. having their accommodation paralyzed), non cycloplegic, as well as subject wearing spectacles. An optimal parametrization of the computer controller is tested for the number of Zernike modes of the reconstruction, the number of modes employed in the interaction matrix, and the amount of voltage correction calculated effectively sent, K . As pictured in Fig- 3.10, a comparison of different gains and Zernike terms indicate a relatively stable AO correction for the gain of 0.2 and 0.5. In agreement with previous investigation [171], it turns out that in both conditions a higher number of Zernike terms used in the decomposition translates into better measurement errors. The gain factor of 0.5 yields in both conditions (blue and green curve) a sensitively better measurement errors with relatively small fluctuation compared to a smaller gain of 0.2, which indicates rather small non-linearities of the AO response. In conclusion, it seems that an optimum bandwidth error, residual rms are associated with finer decomposition of the response and that the correction is little bound by the dynamics of the subject wavefront as well as non-linearities of the system.

In advanced correction Zernike can also be generated by a modal correction. As shown in Fig- 3.11, the generation of an aberrated wavefront is successfully achieved using the AO closed-loop for the non paralyzed eye with moderate fluctuation of the targeted spherical aberration mode. The correction is strongly dependent on the alignment of the eye pupil and the wavefront reconstruction; the amount of asymmetric aberration is weak. However, a strong coupling of defocus aberration accompanies the generation of spherical aberration.

Note that those experiments were in great deal influenced by the sort of subject and the motion of his eye

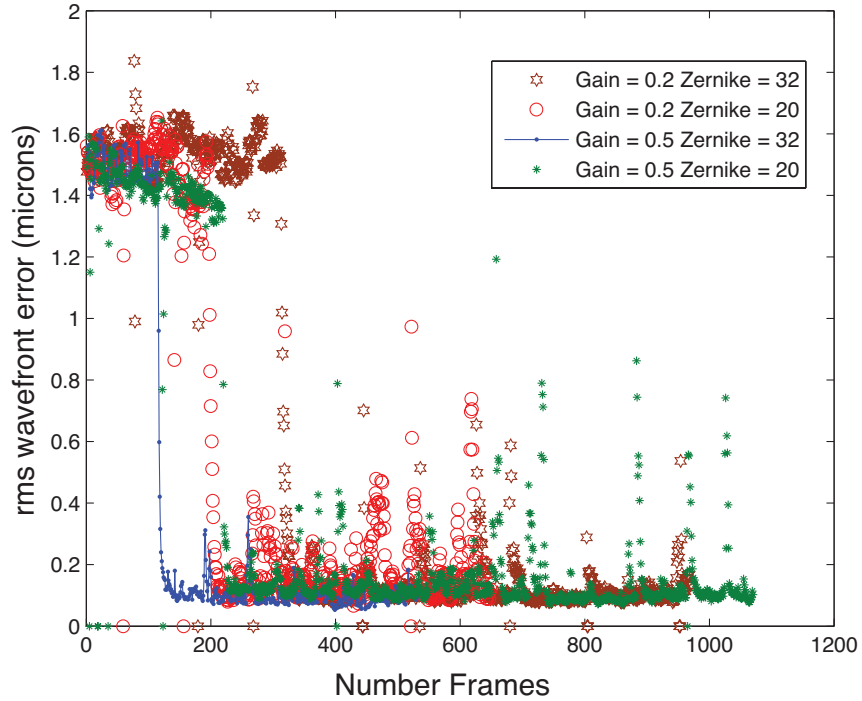


Figure 3.10: Comparison of the efficiency of the AO closed-loop at about $15Hz$ for various combination of the gain and the number of Zernike modes based on a dilated eye with $6mm$ pupil. Only slight variation are found with smaller amplitude of fluctuation for gain of 0.5. Low gain and small level of reconstruction translate in reduced performance of the AO on the red curve.

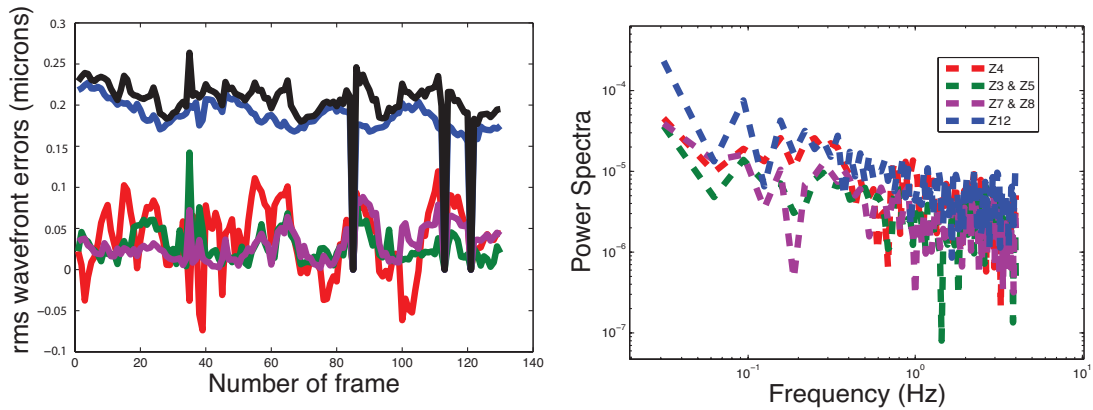


Figure 3.11: Temporal evolution of the wavefront rms of a simulated single Zernike mode spherical aberration in AO closed loop correction at a frame rate of $10Hz$. On the left side, the rms fluctuation is displayed over time and, on the right side, its power spectra for various Zernike terms of the generated wavefront. The targeted rms wavefront errors is $0.2\mu m$ over a $5mm$ pupil and is generated in a non paralysed eye. The generation of spherical aberration appears remarkably stable through time. The fluctuation in power spectra of Z4 and Z12, and in some extent of the other terms, reveals some coupling between the modes of the mirror.

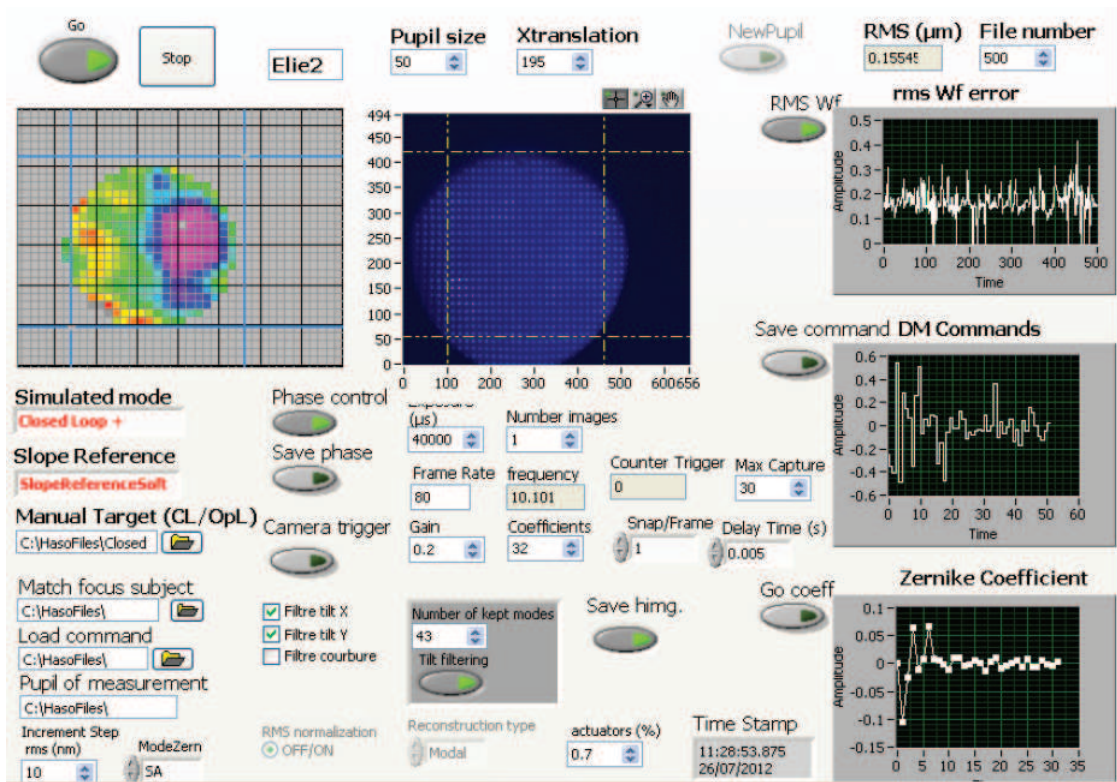


Figure 3.12: Labview interface built for the testing of the AO closed-loop performance showing the Shack-Hartman spots array

3.5 Wavefront correction and retinal images

For assessing the performance of the AO, we also looked at the double pass retinal images from the infrared illumination, that for varying size of the retinal object. A Q-imaging CCD camera was synchronized with the wavefront sensor and control through the Labview interface Fig- 3.12, built for accessing and extracting data. The camera was attributed different level of binning to boost its speed and compensate for the 50% beam-splitter and a partially reflective dichroic.

For a naive observer from observation of a point spread function, we would expect a compact shape for the imaging of the spot formed on the retina resembling the perfect diffraction limited psf. It can be seen that the psf of the eye looks more like some stardusts (see Fig-3.13). The intensity measured on the camera is a combination of the interaction of the coherent psf from the first pass with the bleached

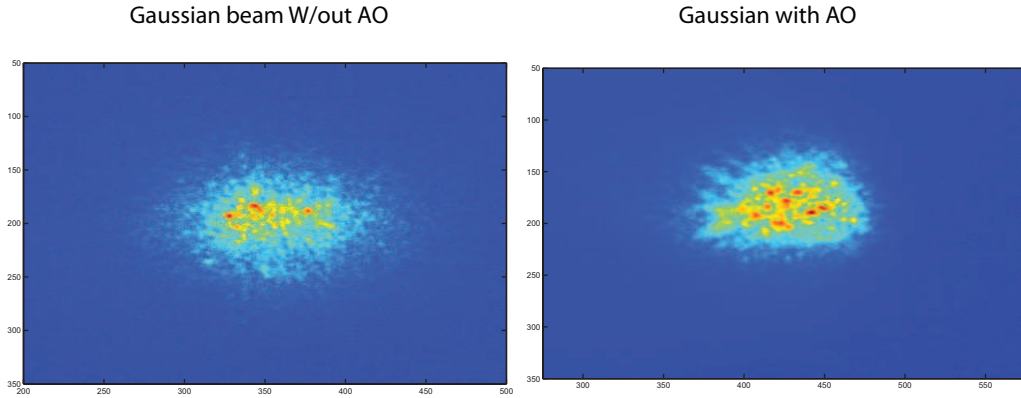


Figure 3.13: Short exposure of a double-pass point-spread function image of an accommodating eye a/before and b/after single pass AO correction using a gaussian beacon beam over a $6mm$ pupil in infrared.

cones mosaic, upon which the diffusion from the layers behind receptors is added. A series of operation are conducted on this signal such that physical filtering of the diffusion by a diaphragm, subtraction of dark frame and removal of blink. How diffusion and specular reflection combine is not clear with respect to the analysis of the data. The signal exhibits some structures: several bright spots scattered more or less randomly. Those bright spots cover on average $5 * 5$ pixels (e.g. $64\mu m$) corresponding to $3.48\mu m$ in the retina. The speckle size expected for a $5mm$ pupil is about $3.40\mu m$. Note that those structures are the size of the cones. The fluctuation and the arrangement of the spots do not allow to conclude that those would be retinal features; and the cross correlation between frames is not conclusive. A way to identify these structures would be to change the effective pupil size during the measurement and vary the exposure time. Fitting with metrics is hindered because there is not one single maximum non a pure gaussian profile that can be strictly modelled. The confrontation of the wavefront measurement errors with double pass-psf indicated little connection in the fluctuation of the psf with the wavefront rms errors; this most probably because of the moving and variable retinal object owing to the lack of accounting for variation in the first-pass, e.g. accommodation and eye movement. A possible source of noise could have been introduced by a tilt variation pertaining to the on and off position of the DM. Besides, the accommodation of the subject was not paralyzed when the AO is on, added to a slight decentering of

the beam entering the camera lens, due to the transmission on the thick dichroic beam-splitter. We note a slight improvement of the psf images associated with the decrease of the wavefront errors rms in closed loop correction. This is reflected on both the theoretical and experimental peak of the psf PSF_{th} and PSF_e , measured from this position, as shown in Fig-5.7. The improvement gain is probably partially absorbed by the uncontrolled variation taking place on the first pass. Additional testing of the double pass psf was undertaken in relation to modifications of the wavefront in the presence of a Bessel type illumination for an artificial eye and a real eye [159].

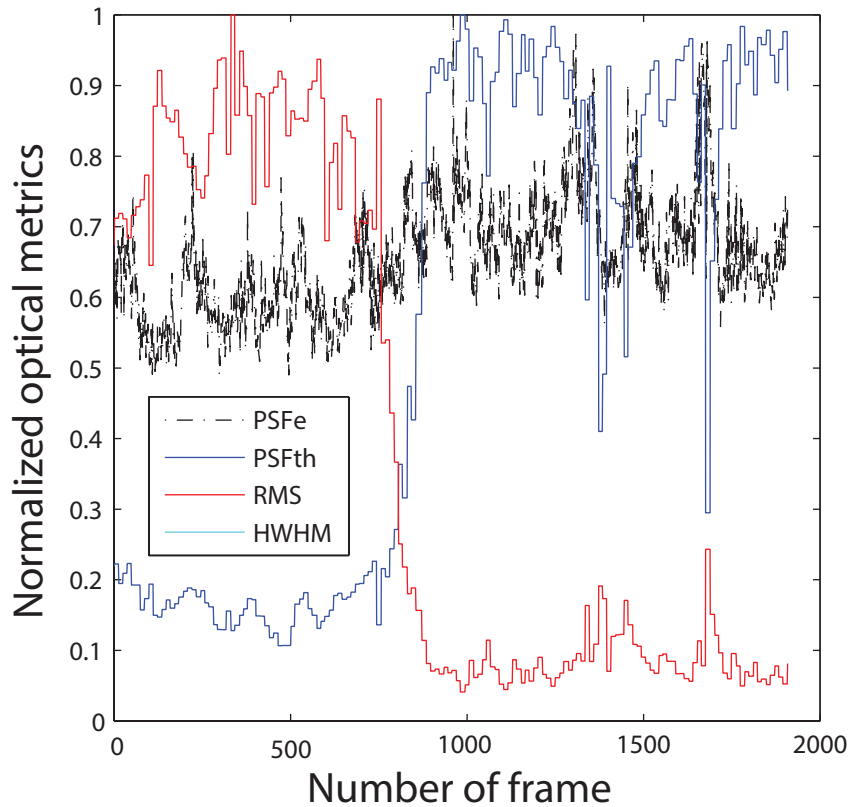


Figure 3.14: Theoretical and experimental double-pass point-spread-function variation, measured by the Strehl ratio versus single-pass wavefront (RMS) of an accommodating eye, before and after AO correction, for a $5mm$ pupil diameter and an infrared beacon of about $600\mu m$ on the retina

3.6 Psychophysics arm

3.6.1 The non-common path error (NCP)

The non-common path errors consists in all the optical elements through which light travels and that are not seen by the SH when a stimulus is displayed to the eye, i.e. one lens and two beam splitters in reflection (one is a dichroic). Several ways of accounting for it can be proceeded such as interferometry measurement of the individual component. However, the combination and placement of the optics will also contribute to the optical path difference. Here, we evaluated the NCP by measuring the aberration left in the position of the pupil of our artificial eye while the aberrations of the system were corrected by the DM. The light was shining from the retinal plane R3 and measured by the SH, adjusted for this purpose. As expected, a significant reduction of the aberrations occurred with the rms wavefront error below $\lambda/10$. The restriction of the measure over the bound dimension of the wavefront sensor as well as the spectral shift did not perfectly fulfil this assessment, later enhanced. A tricky arrangement rises at this ramification because of the necessity to couple three beam splitters within a distance not exceeding the focal lens facing the wavefront sensor. We therefore moved slightly away from an ideal 4-f system by the positioning of the collecting lens of the visual branch at some distance from the confocal distance.

3.6.2 Chromatic shift and best focus strategy

Studies showed that higher-order of aberration are mostly stable along the spectrum [183, 106], yet a marked defocus shift remains when the subject is perfectly focus in infrared, and the eye is hypermetropic in green light. To eliminate that chromatic shift between the sensing and psychophysics arms two methods are available; either an adjustment of the Badal optometer (visible on by the sensor), a direct compensa-

tion with the DM or adjustment of the display (invisible for the sensing path). This pre-correction is commonly performed either objectively or subjectively. The option of the mirror is indeed not handy. A Badal motion though appealing introduce large defocus for sensing. Besides, in both configuration, light on the common path differ in terms of angular incidence. In the objective situation, defocus correction can be estimated for each particular eye by using eye model. The order of the defocus shift of the eye is typically of about $1D$ between $550nm$ and infrared. The subjective method is rather an assessment of the best focus of the subject. It shows a great variability among subjects, aberration state (e.g. natural aberration or corrected condition for instance) and target. It is know that the best focus is not systematically associated to the minimum aberration. For eliminating the chromatic shift, a predefined image target, a Tumble E of $10arcmin$, was computed on the display and presented to the subject, free of aberration. The target was translated by employing the same movable display towards the lens until it was identified at its summit of sharpness. A difficulty resided in the change of the spatial frequency used by the observer during the optimization, as the angular magnification get modified. The mean defocus shift found between 836 and $550nm$ is about 0.9 to $1D$ for most of the subjects that corresponds to a placement of the display set at $l = 100mm$ near the lens vertex. This measurement was performed on the dilated pupil and applied to non-cycloplegic measurements.

3.6.3 Visual stimulation using a microdisplay

Microdisplay and visual interface

For the psychophysics arm, an incoherent light source is used: a monochrome Green Microdisplay (and a color one) based on organic light-emitting diode (OLED) technology. Built on silicon chips, the array of light-emitting diode produces light in response to an applied power which displays the stimuli. Visual tasks are usually

mediated through a monitor for accurate control of parameters such as contrast, size, luminance and spatial and temporal parameters of the stimuli in which this thesis were interested. The stimuli here is coded with a 8 bits graphics cards (e.g. $2^8 = 256$ gray levels) and appears on a circular window at a chosen speed. Using the “psychtoolbox” of Matlab, several textures are created in advance and then flip on the screen according to the response or the request of the subject. The maximum speed of refresh of the OLED meets the temporal resolution of the human eye (near $30Hz$) with a frame rate of $30Hz$. Yet, higher refresh rate reduces flickering and eye strain and can be availed by CRT monitors (with $100Hz$) and to some extent, LCDs. An asset of the OLED is fast time response ($< 1ms$) that enables smoother visual motion along the frame.

The stimuli available are the following: grating and gabor (e.g. grating with a temporal and gaussian envelope), Landolt C and tumble E (letter typically used for their spectrum similarity with daily life stimuli), letter of acuity in Sloan font. Some additions are currently updated to have an automatic control on the temporal aspect. We coded various procedures for a dynamic visual experiment in order to control the input value for the stimuli along trials, e.g. either contrast, size, exposure time, orientation...Those procedure are the following: the “Bayesian procedure”, which is an adaptive psychophysics procedure that estimates the most probable threshold of the eye for a specific stimulus based on its previous trials history and a first guess, made by the experimenter. The “reversal procedure” that define the threshold of acuity as the value for which a given alternation of right and wrong responses have been counted. The method of adjustment for which the subject adjust himself the stimulus appearance to match a sensation. The method of constant stimuli, for which a set of pre-selected stimuli are randomly presented as to access the probability of seeing of the subject. The parameters of the visual task are gathered in the GUI interface of Matlab as shown in Fig-3.15, and that enables the control of the stimuli by the experimenter. Most of these tests are confined to acuity task because of the limited step-size and range of the luminance levels, which prevent visual contrast test. The response of the subject is obtained through a computer mouse

or a keyboard; the crucial part of the response is that the manual task should not interfere with the visual task processing: ideally, the response should be automatic. Thanks to this mouse, the subject can also control the parameter of the stimuli or the aberration of the target.

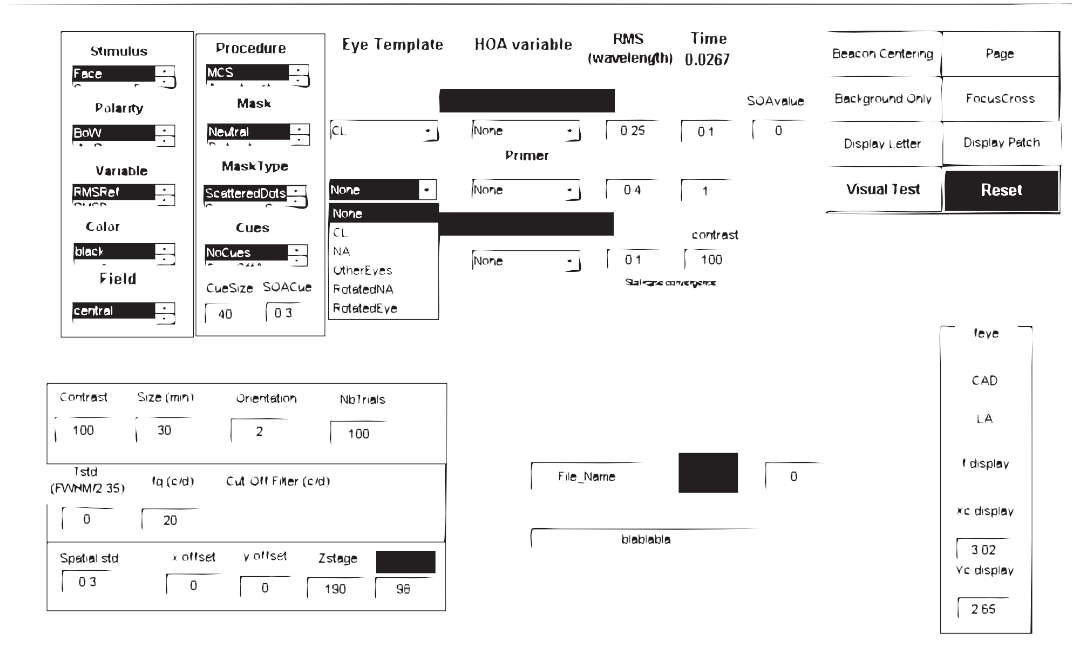


Figure 3.15: Matlab Guide Interface for control of the visual input by the experimenter

Range of visual stimulation

Trade-off between field of view and resolution The main advantage of such a display is its compact dimension ($9 * 12.78mm$ for $852 * 600$ pixels) allied to small pixel size, which suppresses the need of a magnification branch necessary in the case of a projector. The display situated at infinity in green, subtends a field angle within the isoplanatic patch of a nominal value of 2 deg on the retina, which roughly corresponds to a feature of $600\mu m$ onto the retina. The minimum angle of resolution (MAR) is the angle, expressed in minutes of arc, which the strokes of the letter (e.g.

gap of the Landolt C or tumble E) subtend at the person's eye. From normal vision 20/20 to 20/10, the angle of resolution varies from $1arcmin$ to $0.5arcmin$, which is the value typically reached for a free aberrated eye. The maximum resolvable feature of the display is theoretically of about 1 pixel, e.g. $0.2arcmin$, assuming sufficient energy and stability of the response. For a visual task of acuity, it allowed testing of letters down to about $3.5arcmin$, e.g. $16 * 16$ pixels. Optionally, the display can illuminate wider field of view (up to 160 deg) thanks to its angular emitting properties in contrast to LCDs.

Luminance and contrast A prior concern remains the quantity of light outputted by the microdisplay as substantial losses at each interaction of the light with the optical components of the system occurs. In our context, the main optical element reducer is the BS3, which cut 50% of the light of the wavefront sensing and of the visual arm. The monochrome green display outputs about $5500cd/m^2$ at its maximum (corresponding to only $1000cd/m^2$ for a color display). Note that it has its peak wavelength emission at $520nm$ and a full width at half maximum of $80nm$ (no filter is applied). We use a photometer in our study to measure the brightness of the green stimuli at the pupil position of the eye, with a maximum luminance of $2.9mLux$, i.e. a human spectral response from psychophysics test is integrated in the measure of the detector. In reason of the absence of backlight, the OLED technology can afford true black level with a high contrast ratio (10 000:1) and therefore better sharpness in the displayed image. Yet, its range of luminance is limited for contrast sensitivity measurement.

3.6.4 Characterization of the visual branch within the isoplanatic path of central vision

Wavefront reconstruction Using a Lumenera camera, distinguished by its high resolution ($5.2\mu m$) and a high quantum efficiency in the green, the image of a set of

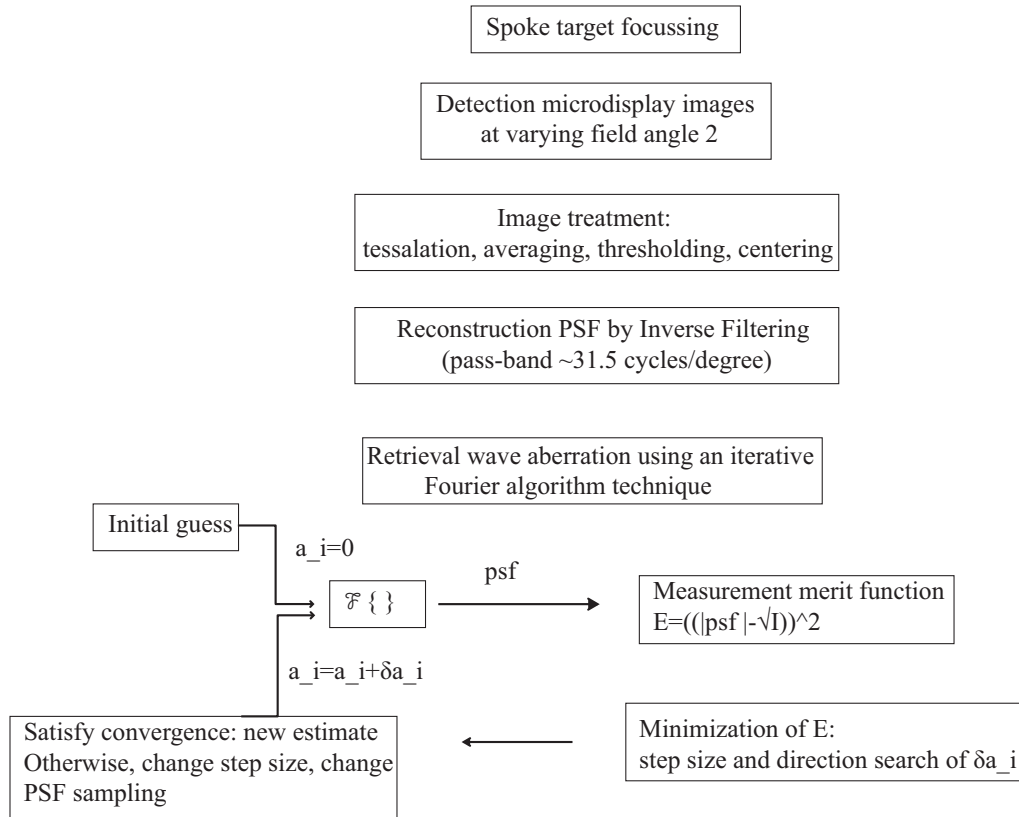


Figure 3.16: Procedure of field aberration retrieval

object projected from our micro-display (i.e. a point like-source, tumble E, spoke target) was evaluated on the back of our artificial eye. a higher focal length was chosen to boost our sampling. The purpose of that operation was to (i) study the quality of the PSF of our system along both the NCP and CP errors (ii) characterize the spatial uniformity and homogeneity of the microdisplay and (iii) control off-axis stimuli to simulate phase effect within a larger portion of the isoplanatic patch. The procedure consisted in applying a set of mirror command for cancellation of the system aberration. The location of the best focus in green light was first determined position by imaging a spoke target for which one could get a rapid visual estimate. Several exposures of $510ms$ were averaged for the image, yielding an estimation of the noise of the recovered image (after dark noise subtraction). After a series of operations on the image, we calculate the psf of the system by deconvolving the detected image \hat{I} using an inverse filter of the form $H = 1/\hat{O}$, where \hat{O} is the Fourier transform of the initial object projected onto the display. In order to remove, the

| | |
|--------------------------|---|
| Parameter reconstruction | |
| Artificial eye | $D = 5mm; f = 200mm$; pixel camera: $5.2\mu m$ |
| Source | $\lambda = 550nm$, pixel size= $15\mu m$; homogeneity 80% |
| Field object | 1.2 deg covered by 3 rings spaced by 0.2 deg $\pi/4$ rotation |
| Object | 25 dots-like of $72.8\mu m$ (e.g. $5 * 5$ pixels) |

Table 3.1: Parametrization.

effect of the ill-defined high frequency on the inverse filter, a cut off of the frequency superior to $31.7cpd$ (corresponding to $MTF > 0.56$) was set, which was acceptable in consideration to the range of the observable spectrum of human eye. We compared it to a Wiener filter of the form $H_w = H \frac{1}{1+K}$, where K is the power spectra of the noise-to-signal ratio corresponding to the ideal signal. Our noise-to-signal ratio uses white noise and we assume the same power spectrum for the ideal and detected image. Both filtering methods yield equivalent outcome owing to the slight noise in the post-filtered image and we obtain the psf of the combined common and non common path in green light.

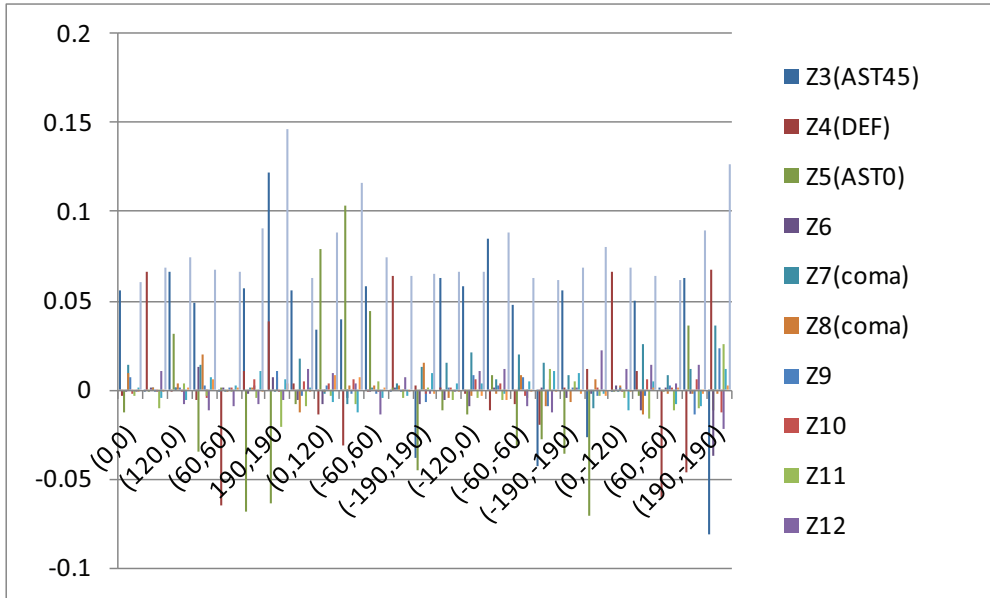


Figure 3.17: Zernike coefficient distribution of various field point of the visual channel in green illumination for a $5mm$ pupil aperture in open-loop

A qualitative description of the field aberration was drawn through the defocused plane measurements. For a quantitative description, a reconstruction of the wavefront mode was performed based on optimization of the PSF.

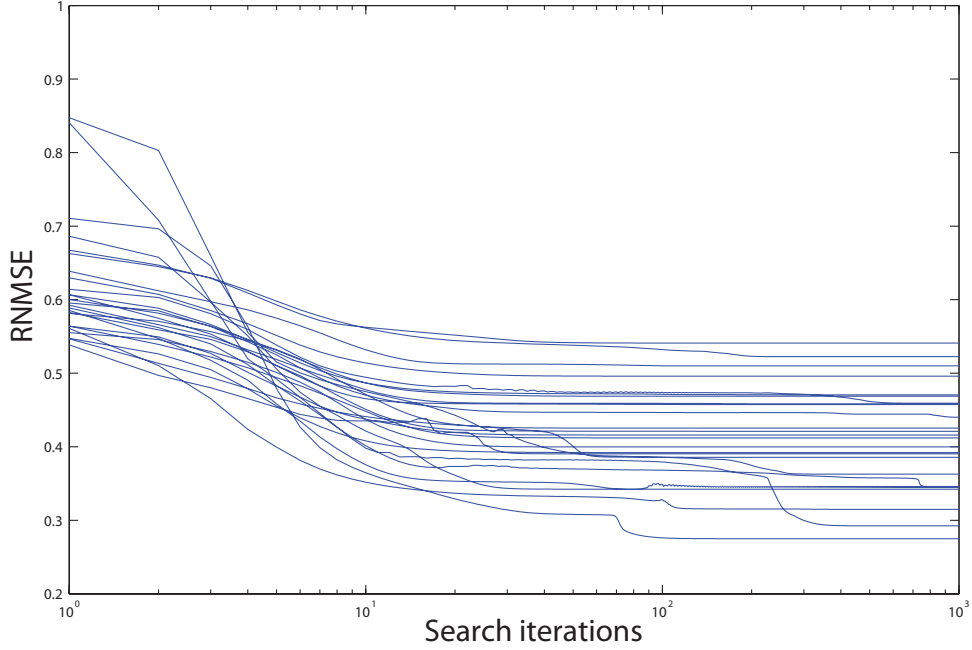


Figure 3.18: Procedure of field aberration retrieval

Starting with an initial guess of the wavefront aberration $\mathbf{a}_0 = a_1, a_2, \dots, a_n$, set at zero for instance, evaluation of the residual is performed that is iteratively updated by new estimate a_1 .

The strategy consists of minimizing the difference between detected intensity PSF and an estimate of the PSF. The evaluation of this residual is measured by using the normalized root-mean square metric, $RNMSE$:

$$E(\mathbf{a}) = \frac{\sum (\sqrt{PSF_{cam}} - |psf(\mathbf{a})|)^2}{\sum |psf(\mathbf{a})|^2}. \quad (3.7)$$

Because of the nonlinear relationship between the Zernike coefficient and the PSF, such minimization is not trivial and several algorithms can be applied. We used an iterative gradient search method proposed by Iglesias et al. [146], the so-called Levenberg Marquardt technique. The technique of Levenberg Marquardt is based on a local linearization of the variation of E to the second order term:

$$E(\mathbf{a}_1) - E(\mathbf{a}_0) \propto - \sum_k H_l \delta a_k + \sum_{kl} G_{kl} \delta a_k \delta a_l \quad (3.8)$$

where δa_k is the variation of the Zernike coefficient that relates $E(\mathbf{a}_1)$ and $E(\mathbf{a}_0)$, $H_l = \frac{\partial E}{\partial a_k}$, and $G_{kl} = \frac{\partial^2 E}{\partial a_k \partial a_l}$.

An analytic form of the gradient is derived by Fienup [108]:

$$H_k = -2Re(\sum_{pupil} iPZ_k P_w^*) \quad (3.9)$$

where P_w^* is derived from:

$$psf_w = psf_{cam} \frac{psf}{|psf| - psf} \quad (3.10)$$

More complex, the Hessian or curvature matrix is given by:

$$\begin{cases} G_{kl} = \sum_{pupil} u_k(a)u_l(a), \\ u_k(a) = 2Re(\frac{-i2pi}{\lambda} P * (a)Z_k(\rho, \theta)FT[\frac{psf}{|psf|}]). \end{cases} \quad (3.11)$$

The minimization of the residual $\Delta E(\mathbf{a}_1, \mathbf{a}_0)$ leads to the relationship:

$$G_{kl} \delta a_l = H_k \quad (3.12)$$

The ratio of the Hessian matrix and the gradient yields an indication for the scale and the direction of the coefficient variations.

In the technique of Levenberg Marquardt, this minimization is further controlled by introducing a tuneable parameter ϵ , called the damping factor, which modulates iteratively the balance between first and second derivative inside the Hessian matrix

H_k , following:

$$\begin{cases} H'_k = H_k, if k \neq l \\ H'_k = H_k(1 + \epsilon), if k=l \end{cases} \quad (3.13)$$

Following the success of the minimization, the damping factor is adjusted at each iteration. The higher the damping factor, the closer the algorithm to a simple gradient descent search; the smaller the closer to the GaussNewton algorithm.

Optical performance

The parameter of the reconstruction were tested and selected to restrain the number of solutions and local minimum, but preserved the precision of the reconstruction. As shown on the Fig-3.17, a limited number of 10 Zernike coefficients was used discarding the weaker mode such as trefoil. Piston and tip-tilt were removed as we found they may bias the reconstruction. Problems of stagnation in local minima were further circumvented by adapting the level of sampling of the psf, applied at the pupil. No weighting filter was affected on the *RNMSE* metrics. A good match was found between estimated and detected psf in all cases with a residual errors of 0.1 for the merit function E.

This reconstruction yields an insight of the evolution of the system off-axis, in green light. The slight radial asymmetry of the field angle can be inferred from a slight angle between optical and visual axis of the system. Aberration increases from about $0.5\mu\text{m}$ to $0.1\mu\text{m}$ from center to periphery: this variation remains acceptable within 0.5 deg. This amount seems reasonable on account of the infrared wavefront correction and the nonlinearities resulting from the relay lenses, as well as the residual errors by reflection from the beam-splitter. This study was designed for wider field angles characterization, but constrained by the dimension of the camera. Field curvature must also be accounted for in the periphery owing to the imaging from plane to plane. A full completion of this procedure necessitates applying the conjugate of the reconstructed phase on the deformable mirror, since the phase orientation (from

the even contribution) is lost in the intensity point-spread function.

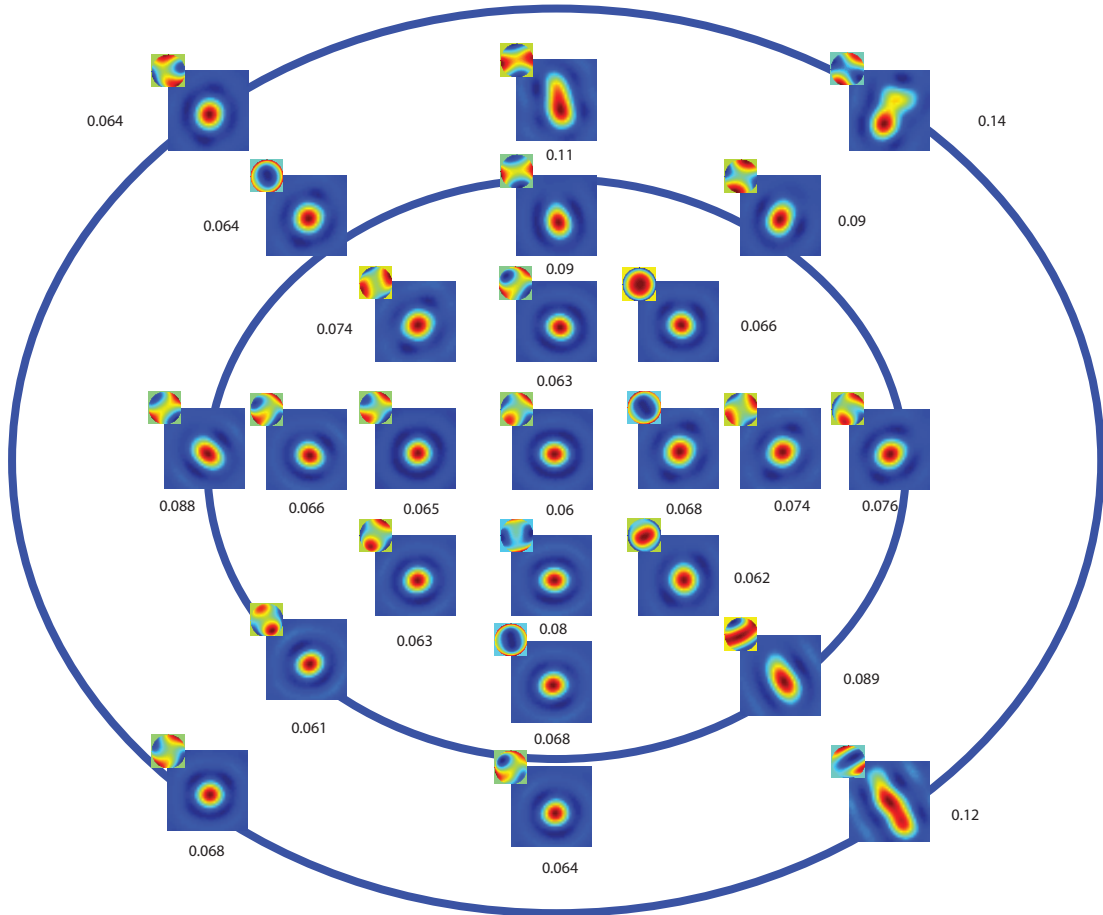


Figure 3.19: Field angle description of the visual simulator from post-processed PSF and wavefront aberration over 1.2 deg with the corresponding rms wavefront errors.

3.7 Conclusion

Simplicity and generalisability are two major assets of a system. In this chapter, we describe the conception of a compact and easily tuneable AO visual simulator constrained to two relay lenses for the operation of the ensemble wavefront sensing and corrector-Badal double pass retinal image. The primary criteria of comfort and easy access that governs the system scaffolding are successfully met, by vertical elevation of a slidable system. Calibration of the system is shown and validated for both common and non common path using different light. The optical performance is tested

and optimized for artificial and real eyes with non dilated pupil, and demonstrates high efficiency for visual simulation. Some examples of measurements, corrections and generations of aberration in real time are presented for real eyes, as well as some investigation of the correlation between wavefront corrections and double pass retinal PSF images. The visual path stimulation control is supported by a detailed interface that allows simple and complex visual simulations. A future project-ideas of development of the system off-axis is proposed for wide-field visual simulation to fit with real life vision testing.

Chapter 4

Post-processing of higher-order of aberration

Higher-order aberrations participate in our visual experience and potentially interfere among bigger actors, such as lower-order of aberration. Their peculiar influence is reported through subjective and objective measurement. However, the rational of their idiosyncrasy is veiled by neural factors. The challenge is to understand what in the neural architecture supports the differentiation of aberration having equivalent amount of blur. We will try to demonstrate through these chapters that, beyond the problem of an absolute performance (or the maximum ability to see), a covert issue resides on the impact of blur pattern, which concerns the exertion of the visual system during visual stimulation.

4.1 Higher-order aberrations impact on retinal image quality

4.1.1 Visual performance test

This study was performed on the visual simulator built by Eugenie Dalimier and Karen Hampson at Imperial College London and Eugenie Dalimier at the Applied Optics Group NUIG. To assess the visual performance of the subject, a test of visual acuity consisting of identifying the orientation of the gap of a landolt C was performed. The stimulus was generated in green light by a projector and presented with a $100ms$ standard deviation gaussian temporal envelope as the visual system is more sensitive to stimuli in motion. In a forced-choice discrimination task, the subject had to choose between 6 positions indicated by guide bars. Command mirrors were sent in a pseudo-dynamic closed-loop to correct the subject's natural aberration, shown in Fig-6.1, and to add single Zernike mode aberration over a controlled pupil of $6mm$ of diameter. The aberrations introduced had an RMS of $0.2\mu m$ and the reproducibility of the mode generated was found acceptable with the exception of coma, coupled with some additional terms. We used here an adaptive psychophysical method, called the Quest procedure [306], provided by the psychophysics toolbox [42] software tracking the threshold in a probabilistic way, based on prior trials history and maximum likelihood function. At each trial, the stimulus was presented with different size corresponding to the current most probable Bayesian estimate of threshold (corresponding to the posterior pdf) calculated. The visual performance of the subject is reported for these different conditions by determination of the acuity threshold and compare to optical quality metrics. We then discuss the different potential actors of perceived and experienced degradation.

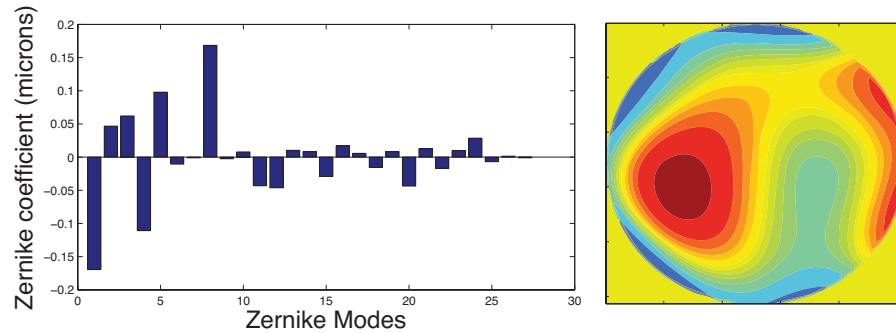


Figure 4.1: Wavefront errors of the subject Edl and Zernike decomposition coefficient up to 5th order.

4.1.2 Optical performance with degraded images

From Fig-6.2, the first observation from the subject performance is that aberrations [20, 62, 129, 64] affect very distinctly the acuity performance of the subject in a way that is mostly corroborated by the nature of the degradation. As pictured by the visual appearance of the simulated retinal image, defocus is the most harmful aberration, with a performance of 20/25. It is followed by the astigmatism at 0 deg whereas coma and trefoil and astigmatism at 90 deg have relatively minor impact, with about 20/20 of performance. In agreement with previous report[304], the gain associated with the correction of higher-order aberrations is substantial, attaining 1.4. The diffracted-limited image in closed-loop affords an acuity task performance of 20/12.5, near to the limit imposed by photoreceptor sampling. To what extent this visual task performance is generalizable is strongly dependent on the visual mechanism aroused by the visual task and its relevance to real life vision. The discrimination of the gap of the Landolt C can be regarded as the evaluation of a dot-like having a complex surround. This situation introduces a complex relation between the discrimination of the feature of interest [39] and the discrimination of the overall object. The degree of perceptual interaction of global and local features is far from being understand [110, 109], and its link to visual degradation. The Landolt C image of the subject's natural aberration exhibits complex patterns due to the finely degraded overall image, which contrasts with the saliency of the gap.

This spatial and temporal dichotomy of the perception receives special emphasis in this Thesis, later analyzed with respect to the mechanism of attention. A possible test may focus on the incidence of the degradation of the surround of a given feature on its detectability. Note that the level of blur perceived and the size of the letter are intimately related in the acuity task. This test assumes that sensitivity linearly varies with the object size, independently of the modification of its overall spectrum and the cue employed by the subject [39]. Visual degradation depends on the task criterion and the complex cues of the signal, which make an absolute measurement of aberration and their classification impossible. Despite stimuli dependence, we should emphasize later in the Thesis that the exposition to a given aberration might involve a different degree of coordination of those task across the visual spectrum of a typical scene.

4.1.3 Objective quality measurement

An objective quality measurement can be achieved based on optical metrics, here split into image metric, PSF, OTF and wavefront metrics, represented in Fig-4.2. Differences in the predictions are observed with respect to the classification of the image quality, as shown in Fig-4.3. Optical quality metrics largely outperform image quality metrics with consistently high predictions found for PSF, OTF and wave based metrics (respectively, with a correlation coefficient up to 0.75, 0.65 and 0.75) against low predictions of image metrics. As shown in Fig-4.3, image based metrics are characterized by poor predictions of visual performance (with a maximum correlation coefficient peak at about 0.4) whereas high predictions are obtained for PSF, OTF and wave based metrics with correlation coefficient peak at about 0.75 – 0.65. That questions the relationship between global optical quality of the system and quality of visual object/image with respect to one's performance. The highest predictions are obtained for the PSF metrics. In effect, contrast intensity in this task is particularly important given the major function of the gap in the discriminative

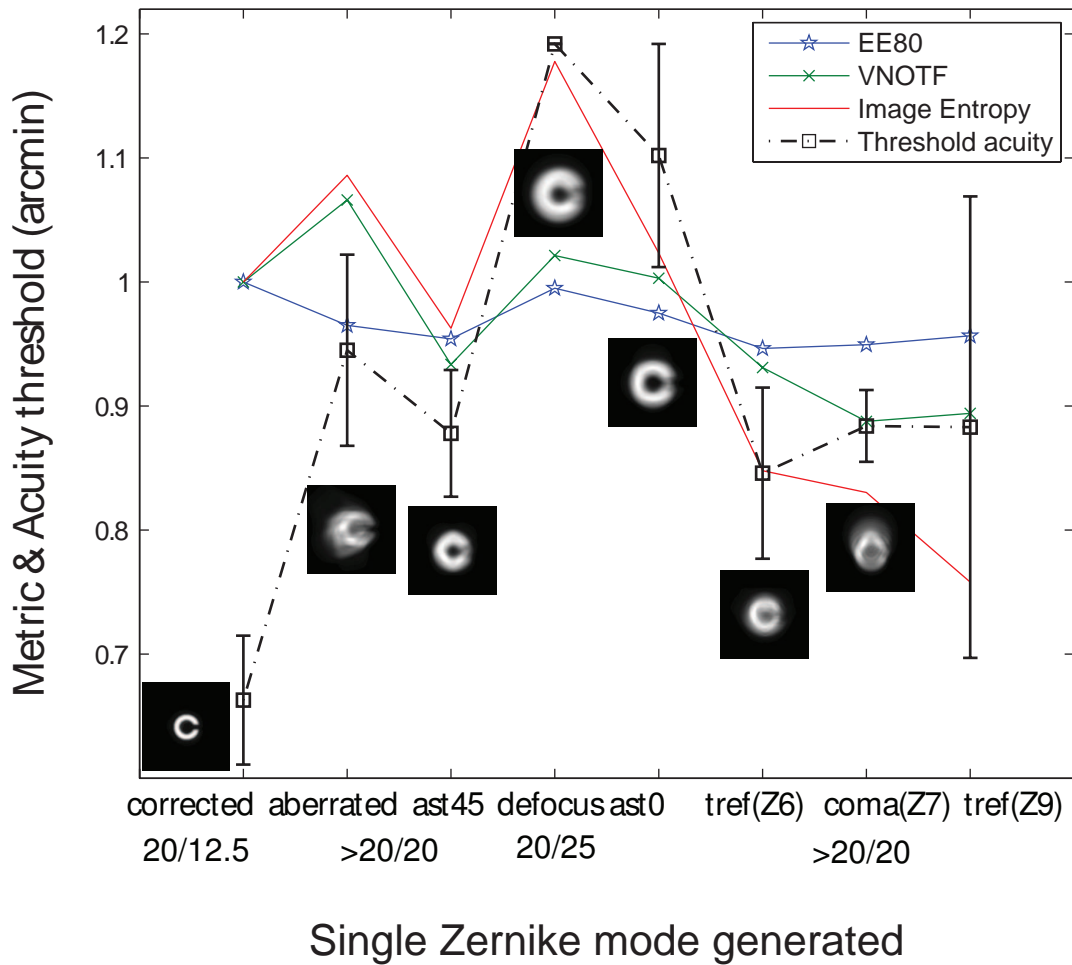


Figure 4.2: Comparison of a landolt C visual acuity with optical metric for various simulated retinal images generated through AO. Optical metrics are adjusted to the visual prediction by linear least-square fitting. Note that the corrected condition is not included in the fitting.

task. Metrics evaluating contrast intensity are highly predictive, as SRX or LIB. However, shift of intensity in the image made PSF metrics poorer as for the metrics LIBc and D50 applied at the maximum intensity peak of the PSF. More advanced metrics based on the nature of the PSF distribution led only reasonable predictive outcomes. Analogous metrics were computed in the frequency domain such as the SRMTF or SROTF showing concurrent outcomes with respect to SRX and LIB. Post-retinal filtering additions did not enhance metrics, as it may combine with the nature of task, as well as the properties of the stimulation. Note that the contribution of the phase shift of the OTF calculation systematically reduces the predictive outcome of the objective measurements, in particular in the VOTF and VNOTF metrics. Other metrics based on wavefront were strongly influenced by the calculation method. We found that pupil fraction methods, such as PFWc and PFWt, brought better predictions than the methods accounting only for standard deviation of the wavefront.

Globally optical metrics prove to be predictive for the individuals by fitting the optical trend of our acuity task. The nature of this prediction is however limited by the issue of a right scaling and the choice of a baseline optical performance as previously discussed in previous works [308, 74, 75, 211]. It also comes out from this experience that aberration may be good predictor for certain aspect of blur, and not capture some others. In other words, metrics do not behave like the eye that can adapt following the context of the stimulation. To what extent metrics are extendable and can comprehend neural idiosyncrasy is a real question for blur perception measurements and corrections.

Previous studies also demonstrated the ability of optical metrics to predict visual performance for a dilated [62, 129, 287, 303] as well as natural pupil [65], for functional acuity tasks at high contrast acuity for both monochromatic light and polychromatic light. A good correlation was observed with a matching (coefficient of correlation up to 0.7 – 0.8) for polychromatic aberration change. The metrics RMS

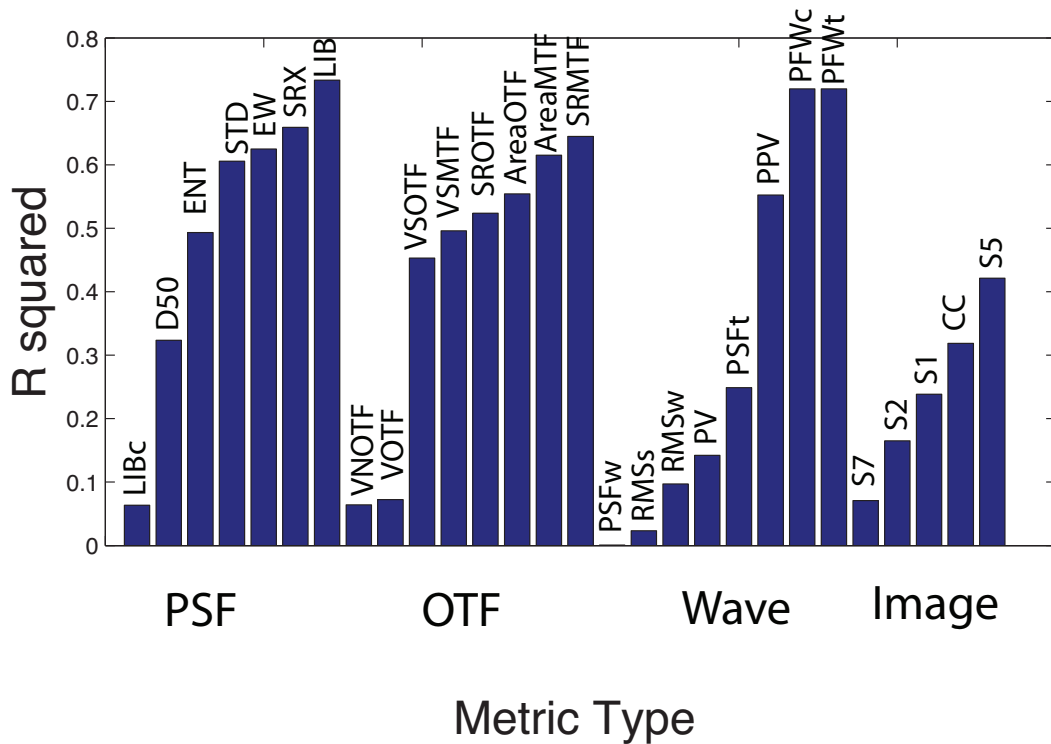


Figure 4.3: Correlation of visual performance and 28 visual metrics for the set of simulation.

wavefront errors, HWHH, VOTF, demonstrated a poorer match with human observation and performance. An advantage was observed for metrics selecting the relevant portion of the image quality such as tessalated wavefront metrics or spatial frequency based metrics [287, 64]. The former uses standard neural filter band-pass in order to account for the effective degradation. The VSOTF is one of its successful products.

4.1.4 Origins of discrepancy between objective and subjective measurement

This matching lessens when post-processing dominates. The limit of predictability of visual performance was raised by several studies with respect to depth of field [296, 294], subject aberration[15], as for example in young subjects with normal or excellent spatial vision. Post-processing is strongly determined by the character-

istics of the stimulus itself: object nature [222] and attributes [273, 117, 29, 107], spatial frequency content [39, 188], surround [66, ?], duration [289, 307], luminance and contrast level [73, 188] and pupil size [51], task and its feedback prior exposition [197]. Neural sensitivity to optical degradation was isolated in several studies that unmask a compensation of the optics by the brain and points to important discrepancies between objective and subjective measurement. An illustration is proposed for eyes with 20/17 visual acuity. Best matching between objective and subjective measurement is found when optical quality dominates over neural filters as in the mesopic regime with low contrast letter (image quality metrics may account for 40% of the variance in visual acuity). When neural filter dominates, as for photopic light condition with high contrast letter, the match is poorer. A successful account of neural sensitivity impact, in various illumination condition, on performance was provided by Eugenie Dalimier [73] with respect to the benefit of an entire correction image, showing that in daily life the experience of optical degradation is relative to the combination of the neural filter and the pupil size of the eye. Several acuity models [308, 211, 74, 75] further developed the modelling of a neural sensitivity filter in the frequency domain, supported by the linear encoding response evoked on neurons by spatial frequency [52, 53], held for most spatial frequency, and measured by the contrast sensitivity function CSF that defines the threshold of sensitivity of the eye associated to the detection of a given spatial frequency. The CSF is modeled by highly selective frequency cortical channel band theory, associated with cortical cells (simple cells) specificity and arrangement, characterized by a certain peak and bandwidth, also strongly orientation selective. The strength of this description resides in a variable channel gain. Each spatial frequency is attributed a threshold that is evaluated by interference technique using two coherent beams focused on the pupil plane [52] that interfere on the retina. The neural threshold accounts for the level of detectability of the grating, but does not account for its apparent contrast. At threshold, high frequency gratings though barely visible are endowed with high contrast in comparison to low spatial frequency, as shown by Georgeson and al [113]. The mechanism involved in detectability, or conscious access of the

stimuli, and visibility of visual features imply a dynamic processing. Or, the CSF varies with the temporal properties of the image [47, 48, 241, 315], such that the exposure duration. The perceived neural image can be described following:

$$Img(f_x, f_y) = OTF(f_x, f_y, t) * CSF(f_x, f_y, t) * OBJ(f_x, f_y, t) * G(f_x, f_y, t). \quad (4.1)$$

where $G(f_x, f_y)$ is the suprathreshold gain and refers to the modulation of the apparent contrast of the detectable image resulting from the amplification processes in the cortex.

4.2 Role of awareness in post-processing of altered images

Visual stimuli are both modulated optically and physiologically by the observer. How these both factors interplay through time and space distance is not known. Because it is obvious that aberration provides an insufficient filter to fully arbitrate the variation of competitive stimulation in the field of vision, the coordination of attention may be involved. This is the complex matter we present and discuss.

4.2.1 Plasticity of post-processing and image constancy

Exposition and image sharpening If neural filtering has important effects in the intra and inter-variability of individual performance, it is also shown that its peculiar dynamics can evolve and noticeably modify appearance of the object following the occurrence of a prior event or state of excitation. Such impacts of post-processing were first highlighted by Blakemore et al. [37, 137] showing that prolonged observation of a grating having particular frequency tends to affect the sensitivity of the spatial frequency and its surround. Based on complex stimulation, this modifica-

tion of channel frequency gain was later ascertained in several studies [197, 310, 246] showing a shift of spatial sensitivity towards higher frequency of the overall spectrum when the eye is exposed to a simple blur (for about 30min to one hour). An almost immediate shift of perception (of about few seconds) was later shown by Webster et al. [310] for the exposition to bias images (i.e. too blurry or too sharp) resulting in judgmental change on post-target appearance. The postulation of a calibration mechanism by the authors corroborates the phenomenon of lateral inhibition of low spatial frequency, advocated by a seminal study, for compensation of the optics, and termed contrast constancy [113]. The huge finding is that the perception of the whole image can be mediated by the previous spatial content of the representation. What are the spatial and temporal prerequisite of this adjustment is not clearly defined. The relationship between this calibration and the role of attending the image is not developed, nor the distribution profile of the objects. In an advanced study, they showed that neural adjustment or distribution-specific perception for directional blur of astigmatism [258].

A finer perceptual level of organization A finer perceptual level of organization was concomitantly demonstrated regarding contrast distribution related to higher order of aberration. Subjects were found to experience some preferences in relation to certain organization of blur related to their own aberration. A first demonstration of this adaptation to HOA was deduced by impairment of perceived sharpness associated with rotation of the natural wave aberration [15], later confirmed by other studies [260] that further explored the phenomenon in methods such as induction of unfamiliar real eye pattern. Several clinical reports support this deviation between optical gain and visual benefit showing a subject adapting to a special optical state, as brilliantly illustrated by astigmatic observers. It was more startling in the former study as it tended to indicate a finesse of sensitivity to blur at a higher level of description in comparison to coarser oriented cues. Practically Lasik [223] and Keratoconous [255] and older patients [150] also demonstrated neu-

ral adaptation processes, sometimes pertaining to neurophysiological modifications as in myopia[250]. That interest probably was stimulated by the observation of a fine-tuned interaction mechanism within the eye of the corneal wavefront profile and the lens [195, 281]. An attempt at quantifying adaptation to higher-order aberration was produced by Chen [63] using a subjective task where the subject was asked to assign its rotated higher-order of aberration a certain defocus level; the adaptation could be then estimated to account for about 12% of the eye sensitivity. The malleability of this perceptual bias is less pronounced than blur neural adjustment, reversible for a given target after a few minutes only, which may suggest little neural control (or long-lasting calibration) for HOA. We note only one report of this neural adaptation in an objective task such as acuity [16]. In fact, neural adaptation of normal subjects was dominantly emphasized by an unconventional target, so called binary stimuli (stimuli complex with little directional cue) involving subjective perceptual matching. In conclusion, two categories of blur are announced: a reversible perceived blur, associated with substantial variation of contrast distribution, either rotational (defocus blur) or directional (astigmatism blur); on the second hand, a blur embedded in the visual system architecture and, associated with finer perceptual representation of the image. To what extent these two aspects are interrelated? How is this malleability compatible with the neuro-optical architecture of the visual system? In effect, a paradox raised by neural adaptation to ones natural aberration is the plurality of effective ocular PSF, varying with accommodation, the object scale and orientation to be encoded by the system.

4.2.2 Degradation and level of representation targeted

Aberration and cortical plasticity Aberrations reduce variance of the signal by their action of degradation emphasizing the plurality of the object and also adding to the singularity of the image. Looking at three basic aberrated images of the same object in Fig-4.4, one can see that they differ vividly by their dimension, resolution

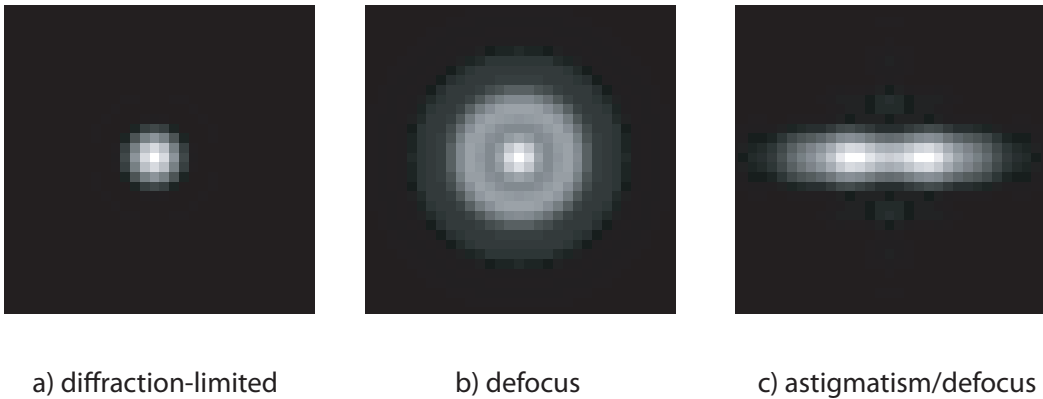


Figure 4.4: Image of an object-point formed by three distinct aberrations : (a) the Airy disk of a diffraction-limited image, on the left side(b) defocus, in the center (c) defocus + astigmatism, on the right side.

and shape. A general observation is that when aberrations are introduced the image gets worse. Worse means bigger for a basic object, meaning also that the dot enlargement should afford larger band of detection with respect to frequency. In the case of basic objects, one can see that the amount of blur consciously experimented suggests a trade-off between visual detection and finesse of the object representation (which inscribed degradation in a time process). For more complex blur, not only the attainable level of precision of the reconstruction is affected, but also the conjectural aspect that relates different spatial frequencies within a scene. The level of capture or optical deblurring refers to the degree of knowledge of the stimulus and the knowledge of the eye neural filter. To what extent the reconstruction matches its initial inputs may be the basis of a malleable cortical plasticity.

Recent studies have shown that aberrations are not equal with respect to learning aptitude [252] and cortical plasticity [318]. An almost immediate and stable benefit is shown from correcting ocular aberration, with a certain impermeability of improvement of resolution performance through training of the naive eye which contrasts with the impairment of resolution task in natural conditions [252]. Outside the fovea, post-retinal processing binds AO correction [251], and it would be interesting to test the effect on this region of training. The second study [318] is in favour of constraint of degradation on the neural filter or cortical plasticity as

revealed by a greater degree of neuronal plasticity on contrast sensitivity improvements when the HOAs are corrected compared to natural conditions. Interestingly, the same authors pinpointed a higher robustness to noisy stimulation in presence of aberrations [170].

These two studies did not explore the underlying mechanisms of these neuro-optical differences nor the basis of their construction. The importance of what is attended, defined by the solicitation of the retinal image, might be crucial in the issue of learning or adapting to a given distribution of the images [26, 257]. In this respect, a huge bundle of studies demonstrated that an important part of processing of the retinal image is performed without accessing subject consciousness [137, 136]. Hence, the following questions:

- (1) are attended and non-attended aberrated target-features governed by the same neural rule (or subject to the same interactions) and therefore leading to the same perceived appearance?
- (2) And what is the impact of aberration in the distribution of attended versus non-attended feature?

Combinatorial awareness Visual task demand and visual experience can define a neural pre-filter (as for instance, for letter identification [273]) that match prior knowledge of the target. Yet, objects convey complex information that implies a multiplicity of representational combinations that are difficult to measure. The combination of the information at the neural stage is determined and limited by the finality of the visual representation (aimed at by the brain) as well as the gradual and serial development of analysis. Competition between visual information is engaged by the limited storage capacity [83] of the visual system, which requires regulation of information and raises the notion of spatial attention.

Selective, spatial attention acts as a spotlight and creates contrast in the information in both space and frequency-space: some information processing is facilitated

with respect to some other by gain and sensitivity amplification resulting in higher cortical activity, via increased firing rate [274], in the regions of visual interest. Such activation enhances spatial frequency sensitivity [54], spatial resolution [84], even reaction times, but at the cost of impairment of performance in adjacent visual tasks at unattended locations [302]. The question is then: how well is a detected signal going to be represented and bound to the global representation of the object, so as to become seen and measurable?

Segmentation of the signal Neurons are assumed to be optimally tuned to possible structural units of the visual stimulus (e.g. dot, bars, gratings) in agreement with Fourier analysis of the visual response [144], probably veridical up to the primary visual cortex V1 where awareness is not at stake. From this perspective, linear modeling [162] is very attractive for predicting the representation of simple stimulus (e.g. Gabor gratings) and can be further exploited by a contrast gain function, that would account for neural compensation and control.

However, for a complex stimulus, the relation in space between adjacent features is not unique, and imposed that the eye segments signals from their background into distinct features following a decisional process. Doing so, segmentation has a direct consequence on the quality of processing of the news units and their binding. Several models assume that features are detected on the basis of their energy peaks regardless of their phase, as physiologically supported by the properties of complex cells. In energy models [198] two distinct stages mechanism are distinguished: a primary and early processing stage, non-linear energy-based, selects the relevant features then, followed by a Fourier based stage, associated to identification. Such visual strategy successfully predicts a vast number of psychophysical measurements [208, 210, 209]. It is though limited to the framework of “pre-attentive” exogenous activation and ignores the complex action of intra-cortical endogenous control, emphasizing the role of attention and awareness.

Global percept locking and feature attendance In fact, awareness raises and deploys at an advanced stage ($> 110ms$) in the propagation of the signal in the area mobilized. Favoring binding of the detected and segregated signals, it is stabilized and organized by the communication between lower visual areas (V1, V2, V3) and higher visual areas (V5/MT) via recurrent processing [160, 161, 79] of local and distant specialized areas, connected via long distance axonal connections. Afferent signals are then submitted to a higher state of analysis that forms and update phenomenal awareness [80]. How these different dimensions of the stimulus are bound may depend on the degree of connectivity and proximity between the cortical locations, which would support formation of synchronized assemblies. Synchronous patterns may be then a way of establishing links between different properties loaded of the same feature, coded in distant region [268, 126].

As frequencies congregate into different feature formations that can go from basic signal attributes to more complex conjunctions of attributes, hierarchically bound, and extending to diverse cues (luminance, size, direction, color), many errors can arise for allocating the right attribute coded in some brain regions to another one belonging to a same feature owing to weak (LC, HSF) and ambiguous (e.g. direction selectivity) signals. Hence this stage, may be more susceptible to disruption by masking.

Binding [288] regroups various forms, e.g. “part binding”, which originate from the fact that locations and objects are coded separately following concurrent visual streams. The way feature resolves this phenomenon is not trivial and involved the overall brain activity. Distinct dimensions of a feature of an object are processed in different regions of the cortex that can be more or less independent, in conflicts: hence many possible errors associated to the manipulation of attention (e.g. when attention to a specific object is biased by the quality of its surround as in crowding, displaced by invalid cues, or time constraint), which culminates for complex attributes processing [288].

In such temporal dynamism, signal lifespan is critical for effective processing and perception, as suggested by persistence [89]. We note that unconscious items lead to short-lived representation confined to the primary visual cortex compared to conscious target lasting up to $350ms$, as illustrated by masked and unseen items compared to the unmasked and seen items [239, 240, 127]. Although this difference, attended and unattended items can be processed to a high level of processing, as shown by the influence of perceptual or semantic masked priming and after-effects of unattended features [137, 136]. It results that unattended feature although influencing the unconscious state of brain activity, only acts temporarily and cannot produce the constraint of attended features grouped in assembly on new incoming stimulation. Hence this question: what dynamics dictates the relay of attended and non-attended features over space and time?

Visual function and attentional tuning Spatial attention introduces a level of priority in the spatial and temporal processing of the events, whose deployment properties are inscribed in the physiological cortical networks of neurons, principally divided into two cooperative networks: the “top down” and “bottom up” systems [69], coordinated in the enhancement of the visual response. Of cortical nature, the top down system is concerned by voluntary monitoring and emerges in the intraparietal sulcus (bilaterally), the frontal eye field, and extrastriate visual areas. The bottom up system acts at the level of the sensory response in response of unexpected or salient stimulation. It includes the right hemisphere, the temporo-parietal junction, anterior insula (INS), and ventral frontal cortex.

Owing to their distinct function, time courses of the responses differentiate these two activities [238, 275] bottom-up activation is inscribed in a rapid feed-forwards activity and follows a quick rise after onset of about 20-30ms, rapidly decaying after 100-120ms. Top down response is engaged in sustained activity and requires about 300ms to fully deploy. Relying on delayed reentrant feedback signal, it can be programmed for any desired duration. How are they tuned and interlaced along

adaptive visual processes is not clear from the neurophysiological point of view, as there is no common substrate known [55] and it is probable that it may vary with the mobilized activity in the brain. Yet, considering that practice and familiarity of the stimulation increases automaticity [274], what would be the degree of control and the influence of cognitive and visuomotor strategies of the observer on the effective realization of the finality of the representational task, required by the environment. A coarse to fine dynamics seems the template provided by the architecture of neurons [43, 111], with a shift from low to high spatial frequency of the visual response sensitivity. Several tentative models [307, 209] tackle the question of a separability of the spatio-temporal response. This theme of investigation has received particular emphasis in psychophysical studies, e.g. facial expression [116], despite little evidences. Notwithstanding, it is still unclear whether a coarse to fine dynamics drives suppression of in both orientation [92] and spatial frequency [43] domains is revealed in the early visual V1 that is shown correlated to higher tuning selectivity of the visual response [237, 236]. It is thought in this study that sensitivity to complex distribution, such as imposed by HOAs, may reveal intrinsic sensitivity constraint that would support individual behavioral responses.

4.3 Methods based on a competitive stimulus processed by the brain

How to manipulate and modulate attention is the first question for the experimenter although it appears a natural exercise for the observer when looking at things and was first highlighted by Posner [229] using valid and invalid peripheral cues, which can affect strongly subject performance. Effect of attention is here shown on optically degraded image by exploring several experimental protocol.

4.3.1 Implementation of several methods

Our objective was first to disrupt the chain of visual processing leading to the formation of an image, but without modifying the actual stimulus-target pertained to optically degraded image, and look at the change on the perception. Such objective is realized by introducing conflicts in the processed signal and evaluating at which level they impact visual performance. In this purpose, we used and combined various techniques, that are:

- **loading of distractors** positioned as pre- or post-target stimulus or concomitant mask, and subject to active or passive discrimination. Controllable distractor arrays were built for flexibility and testing of the relationship between target and mask.
- **segmentation of task:** the subjects focus of attention is turned on a competitive task (count of stimuli, voluntary fixation or diversion of attention) with varying level of difficulty, which can either influence the performing task or be neutral. The dividing task introduces a noise in performance and a first thought would be a complementary task so that the subject won't jump between one or the other execution. Such complementation can be found in the introduction of a condition in the test that identifies the target of the second task. Typically if the dot appears twice (condition), discriminate (attention command) the red letter otherwise the blue one.
- **manipulation of spatio-temporal property of the target.** In order to trick the mechanism of anticipation and attention, off-axis targets were employed as in previous study [229, 96]. Time properties were also modified as it is known that they refer to different attentional mechanism, and they affect processing [200].
- **visual priming.** Prior load affects the transit of the information and the neuronal activity available. Masked priming literature shows that a stimulus

presented too briefly to be represented (even if not consciously accessed) can facilitate report of an identical or semantically related stimulus. This phenomenon is also highlighted in RSVP studies [263, 262]: a blinked stimulus (i.e. stimulus for which the access is impaired by a previous stimulation) can nevertheless trigger a subsequent stimulus.

The protocol involved the following:

1. Passive disruption of visual acuity by interference with a loaded mask for on axis and off-axis target, using different exposure duration and contrast luminance.
2. Segmentation of a visual acuity task by using flickering dot in periphery, with on- and off-axis target at few milliseconds of time interval.
3. Voluntary or involuntary priming during visual acuity using a congruent or incongruent stimuli, with manipulation of time property and spatial properties. This was inspired by priming studies.
4. Spatio-temporal modulation of human face with varying exposure duration.

Numerous lapses must be reported for these tests:

1. Lack of systematic parametrization/ no systematic and individual optimization of the mask/ no calibration of the display/ strenuous run during experiment.
2. Variability of performance with increasing difficulty for the subject rising between the two competitive tasks/ scarcity of data.
3. Errors in coding of the performed test.
4. Conflict between luminance and degradation of the image in the matching criterion used by subjects/limitation in luminance increment of the display.

4.3.2 Temporal masking techniques

First observed in relation to luminance flashes [28], visual masking is a technique that modifies target visibility by disrupting the natural stages of the visual response taking place in the visual cortex [178]. This interference mechanism deploys with time and spatial property, borrowing a U shape for two conflictual targets, such that for small separation the disruptive interference is narrowed and peaks at a certain value of a few milliseconds from which it drops off. The mask is more effective when it shares a complementarity of form with the target or when the target symmetry is broken [138, 96]. The rationale of such property are not very well established [45] and the foundation of these spatial interaction poorly explained by spatial frequency analysis, but might rely on attentional and amplification mechanism, as suggested by the severe role of attention in masking.

A wide topology of visual masking exists, distinguished by their mechanism and properties where figures noise/pattern masking, metacontrast/paracontrast masking among other popular variant such as “four dot masking” or “common onset.” Pattern masking consists of randomly distributed fragment of the stimuli while noise masking uses superimposed pattern without structural relationship to the target. Wise spatial control seems absent in the literature of pattern masking and both types of masking are confounded [81]. Key feature of masking effect, the time distance between the onset of the mask and the offset of the mask, so-called the stimulus-onset asynchrony (SOA) modulates pattern masking strength in a characteristic U shape symmetry that corresponds to a first phase of amplification of masking along SOA increase, with a peak around $50ms$ followed by a decrease till extinction at $100ms$. Masking effect is attributed by Michaels and Turvey [194] to: (1) integration of the mask within a constructed iconic representation of the target; (2) inhibition of the target iconic representation by the activity of the mask; and (3) attention-dependent replacement during the comparison of the iconic representation with the representations stored in memory.

Masking techniques are better known under para- and meta-contrast masking where the mask consists of a closely adjacent stimulus without overlap appearing respectively before and after the target. Temporal masking strength follows a J-shape with a peak of masking at about $50ms$ for metacontrast (against $150ms$ for paracontrast), which decreases until the two visual objects are segregated at about $300ms$. Both types of masking vary with the observer's task and the stimulus properties [45]. Based on the difference of speed processing in transient and sustained channels, a feedforward and dual channel theory of interaction was proposed by Breitmeyer [44] to explain maximal masking, advocating inhibition of the sustained activity of the target by the transient or fast acting channel in metacontrast masking, and alteration of both sustained and transient activity by the mask, in paracontrast masking [218]. Yet, the asymmetry of the two branches of the J curve indicates a two components mechanism implying visual attention [217]: the descending branch, or first phase, is influenced dominantly by the mask energy (exposure duration, intensity), whereas the increasing branch is influenced by the degree of processing activity (modulated by the load size, SOA distance) and longitudinally vary across observer.

Neurophysiology shows little evidences of changes of the dual channel theory and rather emphasizes reentrant processing as it is shown that masking disrupts reentrant cortical signals, while largely leaving signals related to feedforward processing intact. These feedback connections have been suggested to play an integral role in a range of processes, such as figureground segmentation, attention, awareness, predictive coding, as well as perception of visual detail. Employing a particular form of visual masking, so-called four-dot mask, surrounding a non-attended target, Di Lollo et Enns [97, 88, 96] explored the dimension of visual attention in masking. In particular, they showed that a mismatch could be created between formed percept realized by the mask, and so inhibit the cortical representation of the target in a higher area, when the target is not attended, or simply survived by the mask, in the common-onset method.

Despite its several unknowns, masking appears as a powerful technique to probe and intervene in the phase of development of the visual information and is commonly used for studying the deficits variation between normal and abnormal clinical subject (e.g. amblyopia, dyslexia, schizophrenia..), as proposed in the case of myopia [145].

4.3.3 Combining visual masking and ocular aberration manipulation

Measurements Seven young subjects aberrations were measured, all in an undilated condition, which restricts the pupil of correction across the subject. For equity of the comparison between subjects, the pupil was set and measured over $5mm$. The limitation of the corrector stroke for a long time prevented such application of AO system. In our situation, this is the rate of the fluctuation that becomes more critical as we are limited to a frame rate of about 10 to $15Hz$. Another aspect is that in this range of smaller pupil, the predominance of neural filtering over the optical degradation can reduce the breadth of the AO benefit in contrast with bigger undilated eye, though it is shown that for acuity Tumble E test this is not affecting benefit [252]. By using an adaptive optic system, the ocular aberrations were both measured and corrected in infrared light, and the subject vision was modified in order to meet three types of viewing conditions that would mimic the system as free of aberration, in natural condition, or affected with a random phase profile. The first two conditions were usually easily simulated by the AO system, while certain mode generations, such as spherical aberration were more sensitive to the wavefront dynamics, the stability of the subject and the available stroke. The procedure of visual simulation begins with the measurement of the aberration of the natural eye with the system aberration removed, followed by the entire removal of its defocus in red by translation of the Badal optometer. A complete sphero-cylindrical correction is sometimes envisaged when comparing natural aberration and free aberration conditions. Here the subject had little astigmatism, except two subjects. Besides, lower-order aber-

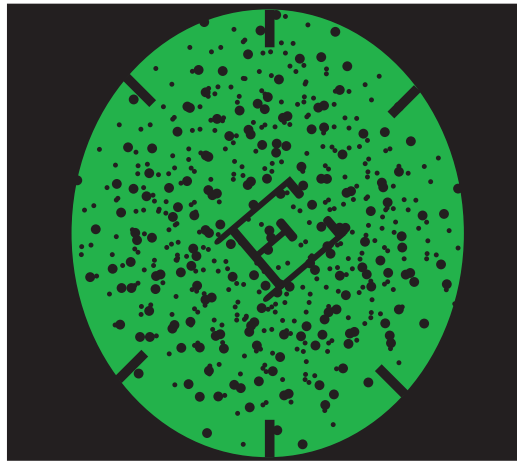


Figure 4.5: Masking pattern.

rations and higher-order aberrations were not differentiated in this study. Once the eye measurement was performed, the chromatic shift was minimized by adapting the eye best focus on a displayed target, typically a tumble E of $10arcmin$. The procedure was operated both for natural aberration and closed loop conditions to obtain consistency between the two profile tests. However, for an undilated subject this step was not possible because of the difficulty of a subjective measurement and set at a standard reference. At this stage, both arms were supposed reciprocal and the tested aberration could be selected. A software, assembled in Labview interface, was used in this purpose, where one could correct aberration and successively add a target. During the test, the eye movement was tracked at both pupil and retinal plane by the wavefront sensor and the retinal camera. This feature enables us to remove trials affected by saccadic suppression and besides control the stability of the loop.

Our test Our first protocol was based on a masking technique using dot motion and applied to a simple acuity task. A visual acuity task offers a straightforward measurement of the highest perceivable spatial frequencies that the visual system can extract from a complex stimulus. By exciting parallel visual pathway (i.e. magnocellular cells) and centers (e.g. visual area V2) than these concerned with the discrimination of highest spatial frequency (i.e. parvocellular cells), dot motion

offers a way to interact and disrupt the visual activity and the processing characteristics that underlie that performance. The subject visual acuity task consisted of discriminating a tumbling E appearing for a duration of 0.5s. The tumble akin to grating, shares similar characteristic to Landolt C acuity and measure the highest frequency detectable by the subject. Such resolution task involved the parvocellular fiber, particularly sensitive to high spatial frequency and also tuned to low temporal frequency. The letter was displayed in a Black-on-White setting, assessed with an adaptive psychophysical procedure based on an up-and-down procedure [134]. Change of the tumble E size was implemented for each consecutive right/or wrong responses. Eight trials were required for completion of the task and the three last reversal values yield our average threshold. Such method presented a particular advantage upon the Bayesian because it is less sensitive to faulty trials and more likely to converge in presence of noise. This noise here principally came from uncontrolled parameters such as the stability of the closed-loop or saccadic eye movements.

An array of scattered dots was employed that fills the overall display during 0.5s (and 0.3s) , as shown in Fig- 4.5 and had random direction displacement. Each dot was of about 0.5 to 1arcmin of diameter and lasted for 58ms. Dot motion effects have been previously investigated in number of studies [202, 201] The rapid movements of the dots between each frame were to elicit the magnocellular fiber response, sensitive to high temporal frequency, to disrupt the ongoing parvocellular visual processing of the acuity task. Note that the duration of the target stimuli (here fixed at 0.5s) potentially could modulate the interaction between the two parallel stream of the response.

Several masking methods were experimented such as forwards, backwards masks or concomitant stimulation by mask and target. We set a certain time asynchrony after offset and onset of the targets of about 58ms. Another condition was observed for the neutrality of the mask: the same colour and contrast were used for the concurrent stimulations. However, the smaller distractor underwent the same

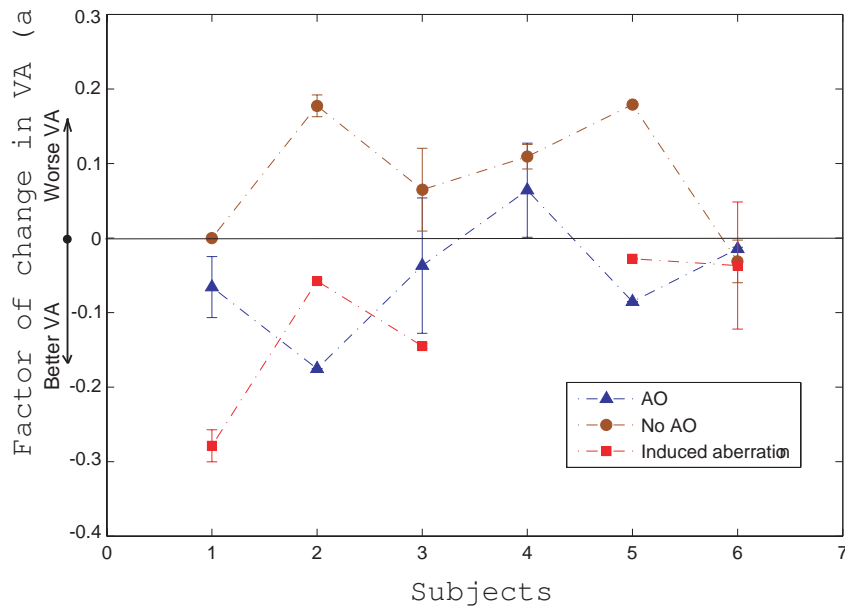


Figure 4.6: Variation of visual performance for three simulated wavefronts errors, with and without post-masking.

optical degradation as the target stimuli. The appearance of the mask was judged bothersome by most subjective reports for the first trials and provoked an objective degradation of performance both when placed before, during or after the target. However, its disturbance could be alleviated by progressive learning. The strength of the mask was tuned by developing different methods for modulating the difficulty of the task such as random field angle and lower contrast.

As shown in Fig- 4.6, the mask affects visual performance by a factor up to 0.15. In the natural aberration condition, the mask impairs the response of the subject, whereas in the other two conditions the impact of the mask is rather facilitatory. It may suggest some variations in the mechanism of post-processing pertaining to the intensity distribution. What is the nature of this interference of the mask with prior signal is unknown. Nevertheless, the effect of masking is not systematic, suggesting that attention, memory and subject strategy play a crucial role.

Unattended stimuli were shown to increase efficiency of masking [96] and, it is probable that in our study, attention was modulated in reaction to the masking agent.

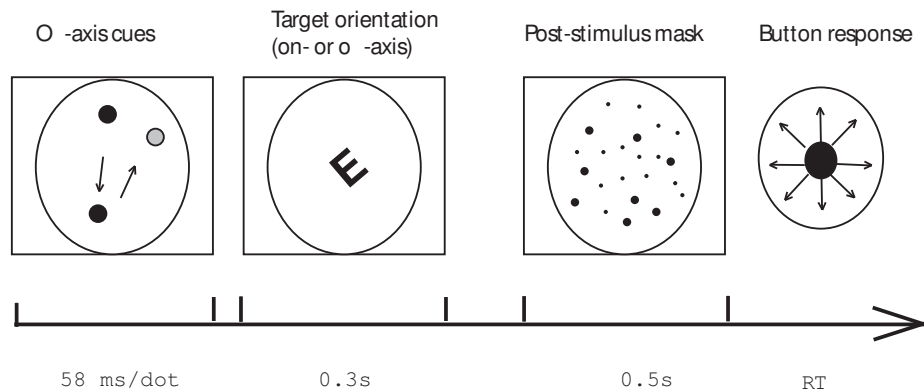


Figure 4.7: Procedure of the visual segmentation task.

An attempt to confirm this view, by using peripheral cues and a moving target, did not succeed so we designed a second test. In the second test, a segmentation task was performed using the pre-target stimulus appearing just before onset of the target, as illustrated by Fig- 4.7. The cues used consisted of one or multiple dots having a diameter of $5arcmin$ that flash in the periphery for about $58ms$. Their number of presentation fluctuates up to three times and the subject presses the arrow of the keyboard corresponding to the orientation of the Tumble E, once if the number of dot identified was inferior to two, twice if superior. This pre-target was this time the object of a manual first task that prevents the automatism of the response. The constraint of detection of the position of the dot was also meant to stimulate the magnocellular fiber response. An update of that segmenting task part also included a condition of identification to the simple localization of the target. A neat difference was again found between the natural aberration condition and the diffracted-limited system. In the natural aberration case, the distractor impairs visual performance, whereas, in the aberration free condition, the mask shows a slight facilitatory effect, as shown in Fig- 4.8. The third experiment had for objective to combine the two former protocol: starting by the competitive identification of the dots, followed by the visual acuity test, masked by the array of moving dots. Contrary to our expectation the post-target stimuli effect was not increased by the competitive task and the effect of the pre-mask was inverted by the combination of the two distractors. We think that the temporal conflict between performance of the

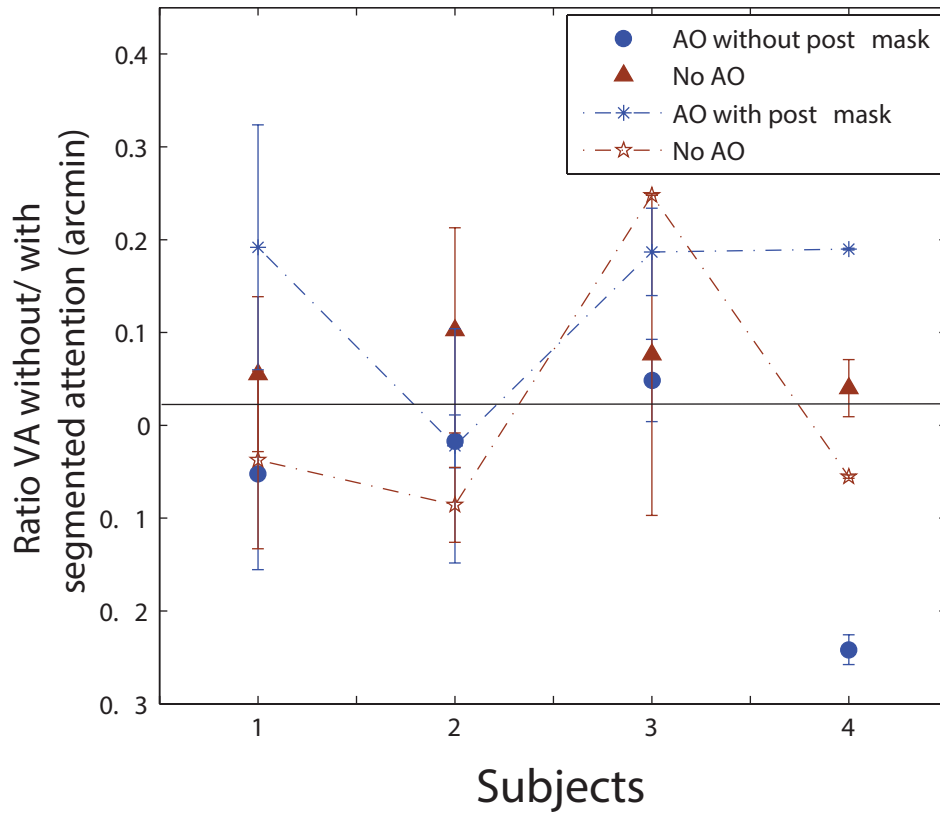


Figure 4.8: Variation of visual performance with and without spatial pre-cueing tasks.

two tasks may be in cause. Besides, the proximity of the pre-target to the Tumble E makes it subject to a forward masking effect. We conclude that careful instructions are necessary for such a protocol and further optimization of this competitive task necessary.

In conclusion, these tests may involve many variables and strong requirements in terms of control. The selection of the target shares important relation with the mechanism of recognition or discrimination involved in cortical area. We conclude that tumble E discrimination task are resistant to attention disturbance, which is supported by the nature of localization of the task, shown little sensitive to masking [218], that relies on the high frequency spectrum differences; and efforts must be turned towards better masking, and more appropriate visual task.

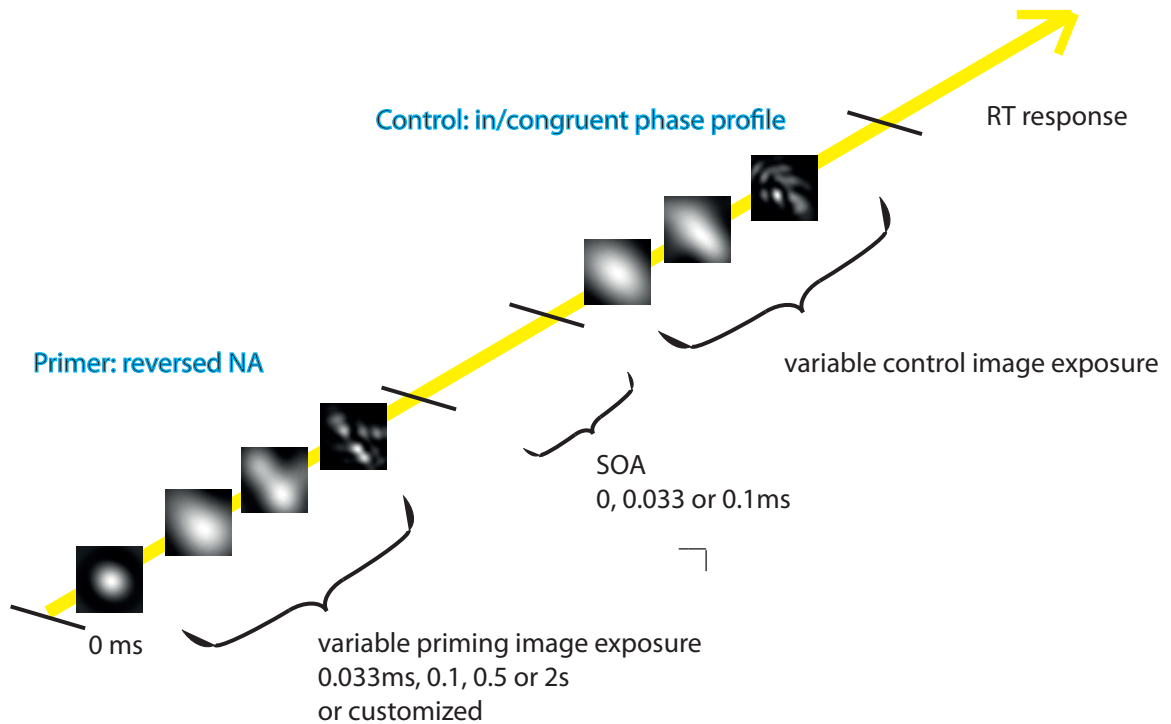


Figure 4.9: Procedure of spatio-temporal influence of aberration change.

4.3.4 Multiplexing of optically degraded images

In this study of post-processing, the main technical limitation were attributed to the field dimension of the display, the frame rate of presentation of the stimuli, and a real time control of aberration variation (because of a bandwidth limited to $5Hz$). To maximize the use of the available field, a characterization of the off-axis display was developed, previously mentioned. A control of aberration was achieved by using the display in combination with the deformable mirror. Such a choice had important consequences for the retinal image perceived, which blends into several advantages and several drawbacks. The first advantage is that one can correct for the residual aberration across the visual field plus a flexibility in the produced pattern. The second advantage is that several aberrations can be embedded and confronted in the same frame to highlight the neural stage as for example in a matching procedure. The aberrated envelope of the stimuli could be modified temporally (along its presentation sequence, i.e. 4 – 5 frames for a stimuli duration of 0.5s) to test

spatio-temporal mechanism related to aberration. Unstability of mode generation due to long trials or eye movements could be minimized. An alteration of the actual optical degradation I_o by a computer-generated filtered images I_c rises though, as comes from:

$$I_o = Obj \otimes PSF_{aperture+eye+residual} \quad (4.2)$$

$$I_c = Obj \otimes PSF_{eye} \otimes PSF_{aperture+residual} \quad (4.3)$$

A way to equalize the two acquainted images is to employ an inverse filter as to remove the diffractive effect of the Fourier transformation of the finite wavefront. It has been shown that this modification has negligible influence on the composition of the image [49]. In our situation, this discrepancy was alleviated by the comparative nature of the study. In the free aberration condition, the diffracted image served as new object. Additional considerations on the deviation of optical degradation and computer-generated aberration comes from a limited range of contrast luminance level (limiting the change of rms observable) and the sampling of the convolved target, calling for a trade off between a faithful representation of the optical degradation and the computation efficiency of the image calculation reiterated between each frame owing to the variable of the stimulus, that is associated with Fourier transform speed. The sampling of the computed image is fixed by the angular resolution of the psf, given by $Umin = \frac{\lambda f}{D} \frac{c}{n} = 0.1891 arcmin$ for a ratio of psf and wavefront sampling equal to $n/c = 2$, for an object reaching about $1 arcmin$ of minimum stroke (and sampled by 5 pixels of the display). The maximum representable frequency is defined by our wavefront sampling, set here at $c = 128$ for boosting the speed of the calculation. This technique is anterior to adaptive optics. Generally applied for small aperture pupil (about $2mm$), it reduces considerably the available spatial frequency from the MTF [172]. In here, the AO system enables us to lower diffraction effects, light loss that are associated with a small pupil aperture, at the same time that it avails a compensation for the fluctuations of the eye (accommodation, other dynamics). According to this method, the protocols 3 and 4, mentioned earlier in the section for 4.3.1, were conducted.

4.4 Conclusion

This chapter shows that visual performance is relative to the nature and the environment of the stimulation. The results indicate a possible differentiation of visual pattern processing with respect to the exertion of the system by competitive optical stimulations: diffracted images exhibit more robustness to competitive visual stimulation than the natural eye profile. We proposed that the phenomenon of visual attention could be at the origins of these variations, by hypothesizing a modification in the propagation of information for attended and unattended stimulation. Several protocols were proposed for modulating the subject's alertness. It comes from these studies that foveal resolution tasks are quite robust to the masking techniques to which subjects may build strategies to overcome visual distraction. Further development of this study on the effect of competitive stimulation would require a wide-field visual system and adequate control of eye movements, and would appreciably gain by further refinements of the spatial pattern of the two stimuli.

Chapter 5

A time-varying input aberration

The interference mechanism, highlighted through masking is an illustration of the integrative mechanism taking place during the representation within the visual system. Here another strategy is explored that consists of modulating the temporal signal, rather than the subject posture itself, to examine the spatial and temporal properties that underlies degradation and stimulus appearance. We address here the following questions: at which moment spatial degradation is propitious to be affected by these mechanism of modulation? and which degradation is the most effective? By modulating the image, one interacts with the development of the visual response and the natural flow of the information. An overview of the integrative nature of the signal is discussed where we show the key ramification of the signal between the moment of the visual excitation of the photoreceptor and the response.

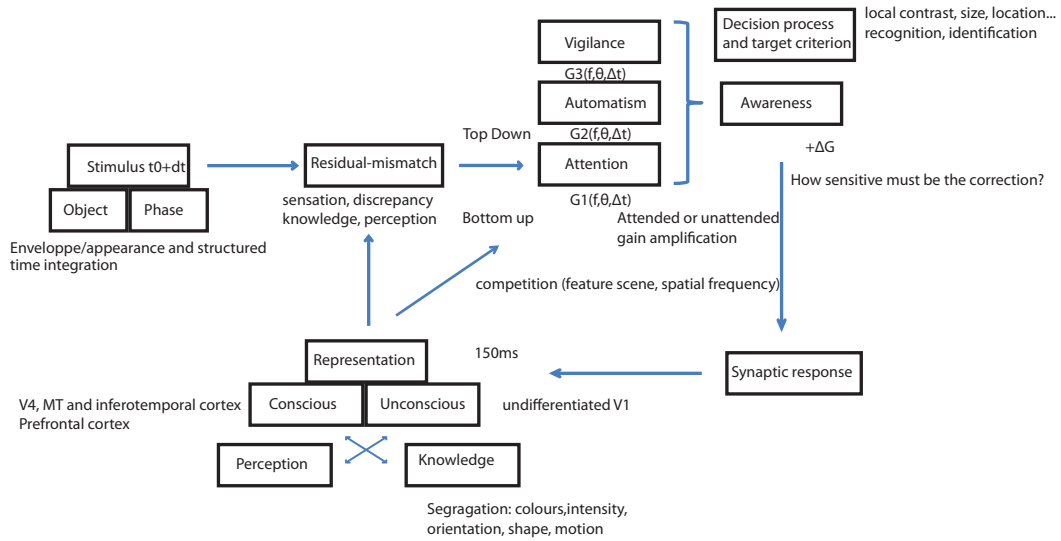


Figure 5.1: Schematic diagram of an adaptive visual response.

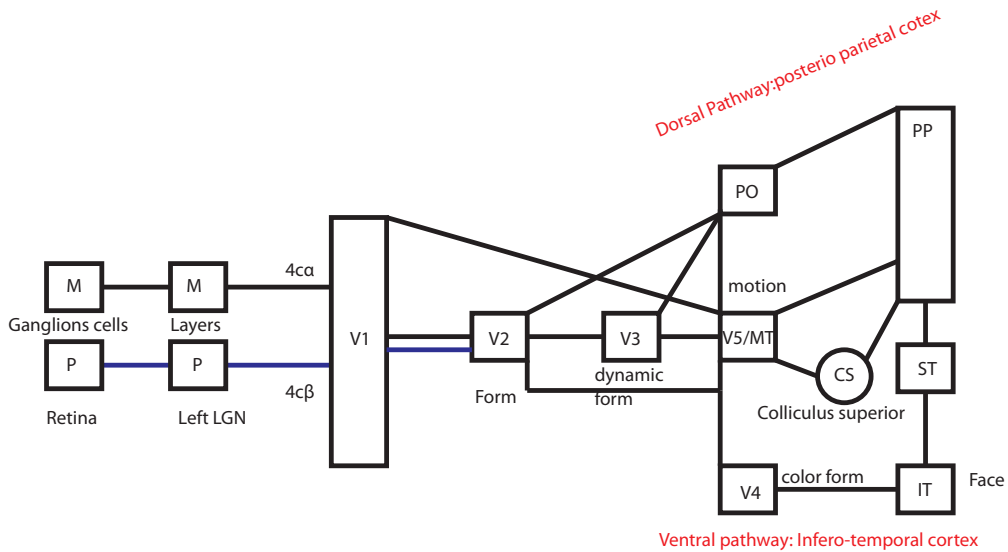


Figure 5.2: Pathway of information.

5.1 How far is the eye from an AO system?

5.1.1 Neuronal activity and propagation

The retina is a thick and transparent tissue, nourished by the choroid, comprised of several units, highly specialized and morphologically very distinct, sandwiched between the **inner limiting membrane** (josted with the vitreous media) and the

deeper **retinal pigment epithelium**.

Small and tightly packed in the center and increasingly stretched towards periphery, millions of light photo-receptors participate to the tessellation of the signal, split into two main categories of light sensitive molecules, cones and rods. Along their neural membrane, the phototransduction takes place by the absorption of photons, which propagates in a backwards fashion along the segment of the photoreceptors. Responsible for daylight vision, three types of cones are distinguished that are the short (S), middle (M) and long (L) wavelength sensitive cones, covering the visible spectrum and having respectively their peak wavelengths near 420440 *nm*, 534545 *nm*, and 564580 *nm*.

A high level of tuning appears in their organization, which indicates an important pre-processing of the image from fovea to periphery. The relationship between ocular architecture/blur, retinal and neuronal organization has important consequences with respect to blur progression and development, which has been shown to be adapted to the environment excitation for chicks [123]. In myopic eye, important morphological changes affect the retina such as bigger receptors field, stretching of the photoreceptors and thinning of the retina, which could alter signal firing time and retino-cortical conduction rate, in other words, cause spatio-temporal dynamic variation in visual information processing [85]. In this respect, numerous evidences of visual performance deficits in myopic eyes are shown principally attributed to retinal sampling [250, 8] while temporal variations are less known [145].

The photoreceptors connects to the rest of the neural network by the intermediary of horizontal cells and bipolar cells, which respectively sum their signal and administrate to the signal spatial and phase selectivity. Synapses form between photoreceptors and bipolar and horizontal cells are combined through the lateral inhibitory synapse formed by horizontal cells through bipolar cells, before being relayed by the ganglion cells: midgets, parasol and konio ganglions cells, situated in the innermost layers [70]. Sensitive to achromatic modulation, parasol cells re-

ceives additive input from the M and L cones (i.e. M-on L-on and M-off L-off), while midgest cells withdraw spectral information from the subtraction of L and M cones (i.e. L-on M-off and L-off M-on) and afford high spatial resolution and strong response to chromatic modulation. While the information propagates in the upper layers, the brain is never completely at rest, it never stops functioning and firing neuronal signals therefore integrating graded potential inputs that can vary in duration (typically 40 to 80ms), velocity and frequency (about 100Hz) [167]. It comes that the information propagation is stochastic and highly determined by the activity flow as demonstrated by masking studies. Thus, received signal could be erased, fired, or stay for a random duration in layers without being further processed and accessed at other levels, as proposed by Bugmann [46].

Retinal ganglion impulses are later transmitted to the Lateral Geniculate Nucleus (LGN), associated with about 90% of the retinal projection, and connected with the primary visual cortex V1, localized in the occipital lobe of the back of the brain. An extra pathway is also formed that projects on the Superior Colliculus and is characterized by low level featuring. Connected to several cortical and subcortical regions, it subtends an activity related to unconscious vision that demonstrated particular importance in “blindsight vision” ?? in particular on the activity of the amygdala, responsible for our emotional percept [300]. Thus, the ability of patients having lesion of visual areas and suffering from absence of consciousness to accomplish above chance visual tasks suggests that unconscious representations could support complex forms of processing that influence and participate in active vision.

From the LGN, the visual function is cleaved in two main streams so-called the ventral and dorsal pathway that projects in the brain. The discovery of these two streams had a significant impact because they are associated with particular function of brain and vision, referring to the “What” and the “Where”, or respectively the ventral and dorsal pathway. The latter one, probably older, corresponds to the motor level (e.g. saccadic eye movements, hand grasping)1, and implicates in

rapid task, or brief stimulation, automatism such as localization. Its deployment is confined to two principal layers located on the posterior parietal, but it also shares communication with the ventral stream where evidence of lateral inhibition is observed. The ventral stream is usually associated with perceptual vision, and feeds several centers corresponding to figural aspects. More extended, it deploys with four layers, located to the inferior temporal cortex.

As shown in the Table 5.1, these channels rely on two types of fiber of the LGN, with distinct physiology and anatomically segregated, so-called the magnocellular (M) and parvocellular (P) fiber (or fast and slow fibers), respectively derived from parasol and midget ganglion cells [174]. It is in particular by their spatio-temporal property and their sensitivity to color that these pathways are distinguished. The magnocellular pathway is low spatial frequency sensitive and temporally excited by high temporal frequency and also achromatic and above all. It exhibits high contrast gain, but saturates at low contrast. The parvocellular pathway is slower in speed, and much less sensitive to luminance, it is highly sensitive to high spatial frequency and exhibits chromatic opponency. It has low contrast gain, but shows a high degree of spatial and temporal linearity. This results in differences of sensitivity and coding between low and high spatial frequency as highlighted by masking studies [218]. The deployment the magnofiber, are dominantly present in the dorsal stream though contribution from the parvofiber, while the ventral pathway receives equal contribution from the two fibers [193].

These two pathways afford two parallel, but interconnected, representations owing to the independence of the M and P pathways. A dissociation of motor and perceptual level characterizes these two pathways, which is illustrated by the robustness of visually guided grasping and fast reaching to visual illusion (such as the modification of the length of a bar in presence of contextual cues) [196]. The P and M pathways, after integrating the primary visual cortex V1, in layers 4, form a new set of outputs dispatched in a complex circuitry or workspace, summed by X and Y cells, and

| Pathway | Magnocellular (2 layers) | Parvocellular (4 layers) |
|---------------------------|---------------------------------|---------------------------------|
| Spatial localization | wide field | foveola |
| Cortical projections | V1 (4C α , 6) | V1 layers (4A, 4C β , 6) |
| Response time course | Fast, Transient | Slow, Sustained |
| Task | detection, motion, stereopsis | form, resolution |
| Stimuli sensitivity [193] | HTF and LSF ($< 10cpd$) | LTF and HSF ($> 10cpd$) |
| Spectral sensitivity | broadband | color-opponent |
| CSF threshold [264] | High ($> 2\%$) | Low ($> 10\%$) |
| TCS low luminance [278] | low-pass (cut-off $\sim 16Hz$) | |
| TCS high luminance | band-pass (peak $\sim 10Hz$) | low-pass (cut-off $\sim 16Hz$) |
| Flicker | upper, limit $\sim 100Hz$ | lower |
| Contrast gain | high and saturation | low and linear |

Table 5.1: Neurophysiological properties of the magno and parvo geniculate divisions. HTF and LTF stand for high and low temporal frequency, whereas HSF and LSF, for high and low spatial frequency, respectively.

feeding other extrastriate visual areas such as V2, blob system, interblob system, MT/IT. As shown in Fig-5.2, these sites are the receptacle of intense communication between P and M pathways where ventral and dorsal streams can communicate. The correspondence between X and Y cells and P and M pathways adds complexity to the recomposition of the information and seems to favour the specialization of neuronal populations leading to complex issue of “ground-segregation” and “binding” of features (e.g. color position, form). To which extent does the fidelity of this initial decomposition interfere with the ability of re-composition of the brain? meaning what is the level of separability and interaction between a new incoming signal and the activity exerted on the neuronal workspace [78, 79]. Interestingly, a high degree of convergence dominates serial layers, denoting a hierarchical system. Owing to this convergence, propagation of the activity to upper layers necessitates the occurrence of mechanisms of amplification. The stimulation and its conscious representation becomes then crucial as demonstrated by the divergent spatial and temporal properties of subliminal and supraliminal priming. Strong priming are observed for supraliminal priming between 100 – 400ms against a peak at 67ms for subliminal priming. In this respect, a short-lived features non conscious information enclosed in span life of about 50 – 150ms, as suggested by the time asynchrony

windows necessary between target and mask for priming [127]. To the contrary, non-mask stimuli faces can keep firing up to $350ms$ against $50ms$ for the subliminal masked face of the same $16ms$ exposure duration [239, 240]. What are the managements of the neuronal amplification with respect to the function of awareness, for the conscious and non-conscious stimuli? Developed in several visual studies, a general pattern of the neuronal regulation was proposed by Watson et al [307] advocating a coarse-to-fine oriented mechanism of representation. However, how the channels of vision interfere in each individual is not well known, neither the degree of self tuning of the visual system. Hence we ask: how far is the eye from an adaptive system? and what defines the right amount of response to a given stimulus?

5.2 Spatio-temporal dynamism of the image

5.2.1 Previous studies

Perceived image appearance is influenced by prior cortical activity, which can modulate the relative distribution of contrast across objects. The causes of this mechanism are inferred to be spatial frequency interaction through inhibition and excitation among the cortical network. However, how spatial frequency interacts temporally, and combines with higher-order aberrations is not well known. Several studies suggest a possible dynamic differentiation of the spatial scales in the image over short periods conducted from coarse-detail to fine-details. In this research, we investigated the effect of varying the spatial frequency content in time on the geometry and sharpness of the images of the human face. As shown in Fig-7.3, our initial hypothesis is that identification assists discrimination of the human face.

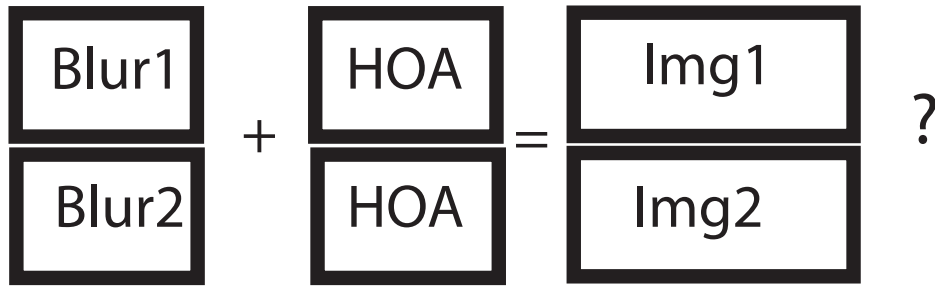


Figure 5.3: Paradigm of the test: comparison of two images with a prior information of different nature and strength.

5.2.2 Method

Our first purpose is to evaluate the impact of a zero mean time varying aberration over a short duration, i.e. 500 ms. The basic idea of the test consists of intervening during the development of the neural response by modifying the aberrated sequence of the image. Application of this idea was proposed by Neri et al. [208] using random noise, introduced in the spatial domain, to identify the spatio-temporal characteristic of human identification applied to a simple bar target. In this study, the noise input is replaced by a blur variation introduced in the wavefront in a way that the total energy of the image averaged over all frames is conserved, and several combinations are possible to satisfy this constraint. The tested variation δ is introduced over 4 frames, positioned either at the beginning, middle, or end of the sequence (position t_1 , t_2 and t_3). The average stimulus is preserved by demodulation of the variation introduced through the 11 remaining frames (with fixed luminance), balancing high (HSF) [11-30] and low spatial (LSF) frequencies [0-11] of the optical transfer function (OTF) of the temporal blur, as illustrated in Fig-7.4. In the condition (t_1 - t_3), a low spatial frequency deviation occurring at t_1 is combined with a high spatial frequency variation occurring at t_3 . In the conditions t_2 - t_3 , low spatial frequency deviation occurring at t_2 is combined with a high spatial frequency variation occurring at t_3 , and inversely for (t_3 - t_2). For computational speed, the OTF is maintained over an array of $512 * 512$ pixel, e.g. 1 pixel for 1cycle/degree . The temporal aberration corresponds to various power

spectra difference of the aberrated wavefront profile. The directional variation are extracted from a matched filter equivalent to the difference between a rotated version of 1) (astigmatism+defocus) at 0 and 45 deg (AST0deg) and 2) native aberration at 0, 45 and 90 (NA45deg and NA90deg). In addition, a rotationally symmetric temporal blur, so-called SA, is extracted from the difference of spectrum between a flat wavefront and a spherical aberration. Finally, the difference of spectrum of an unhabitual aberration for each specific native aberration is induced. The same energy power spectrum is tested for each blur variation and is associated with the wavefront errors of two astigmatism of rms of a quarter wavelength of opposite directions, sufficiently small to neglect undesirable phase reversal. It results in a series of images with distinct expressions and level of blur, as illustrated by the temporal sequence shown in Fig-5.4, an average image with AO and without AO.

5.2.3 Role of time and spatial amplification on perceived sharpness and image appearance

Over a series of 200 trials, five aberration variations randomly presented were tested by the subjects, who were asked to discriminate, in a side-by-side matching task procedure, the temporally modified aberration from a subsequent static appearing image, for each average ocular wavefront profile conditions. In a forced-choice paradigm the subject was simultaneously asked to answer the two questions: “which is the sharpest image?” and “are they the same appearance?”, sharpness referring to intensity, contrast, visibility of the image and appearance to its geometry. A small face of $40 - 30arcmin$ was chosen as a target with a spectrum well distributed in the interval of $30cpd$. Such stimulus is known to invoke a spatio-temporal response from the visual system that involves specialized processes and pathways in the brain as well as a broad range of information [300, 82]. The face represented Fritz Zernike and was taken from Wikipedia. The expression were generated by altering the geometry of selected features (the eye, eyebrow, chin, lips, nose) using

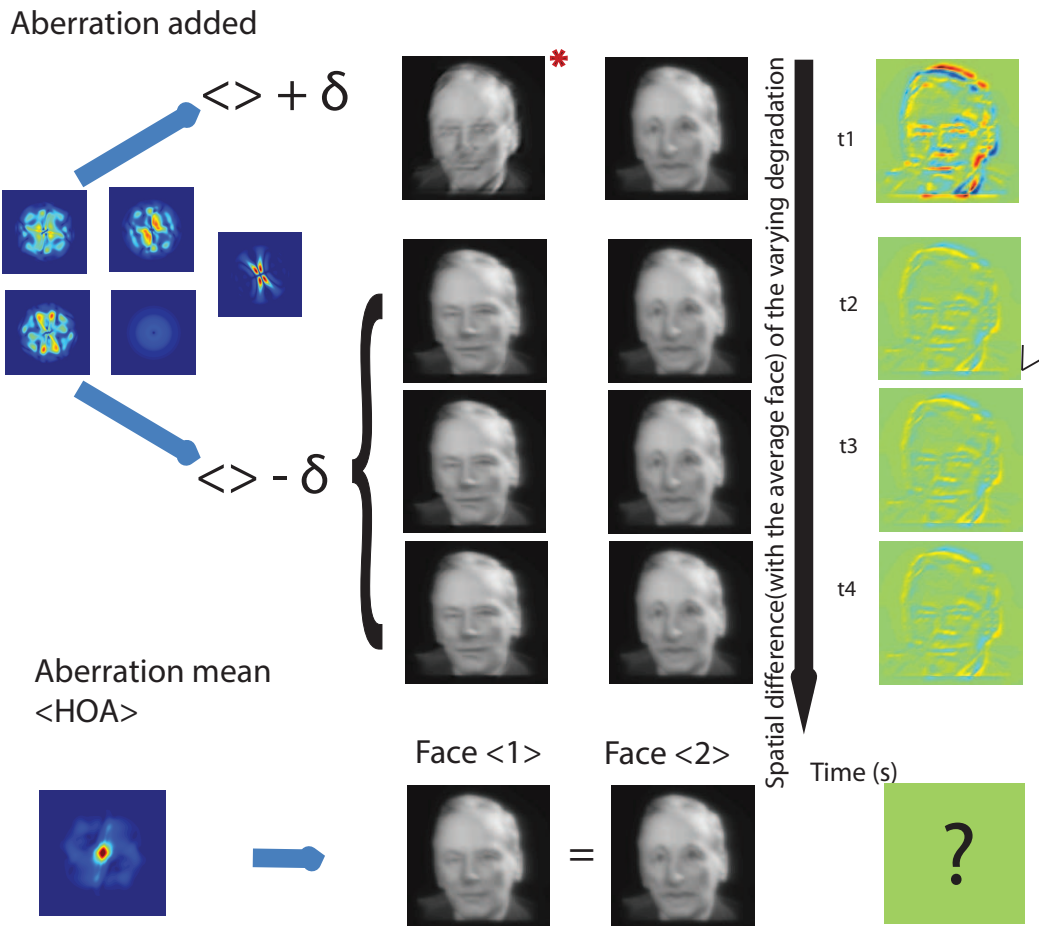


Figure 5.4: Procedure of the side-by-side matching task for testing the equivalence of two image sequences of a human face, having or not the same expression, and exposed under the same average viewing condition. These sequences are split into four phases of distinct blur, $\pm \delta$, added in phase only (experiment 1 and 3) or both in amplitude and phase (experiment 2). Each three first phase, made of four frames of 133ms in total, corresponds to the possible occurrences of the optical deviation (marked by a red asterisk) at time position t ; the last phase is made of three frames. On the left, the aberrated and first face expression is manipulated by a time-varying input blur of zero mean while on the right the second face expression suffers the same mean blur applied statically. The difference of spectra between the versions of the temporal blur and the average viewing profile, here borrowed from a subject aberration, are shown in color. The discrepancy in appearance between the two perceived faces is assessed and analysed by determining discriminability and sharpness of the integrand images.

Photoshop software; and 10 faces with various emotional content were produced smiling, dubious, inquisitor, and other. The attempt to discriminate a large sample of emotional content, rather than their basic geometry, was abandoned, since the task was challenged by the small size of our display.

Influence of the moment of the excitation

Classification of aberration impact on image quality is mainly static, selected on the criterion of performance. This study shows that perceived degradation evolves with time, even within milliseconds. We ask the question: is there a possible signature of the neural excitation attributed to each aberration profile? Such signature of aberration compensation has never been sought to date. To respond to this question, 15 different temporal aberrations are randomly tested, corresponding to five types of image variation equally distributed and three time positions of the deviation introduced, i.e. 0-133ms, 133-266ms, 266-399ms. The spatial variation introduced $\delta(f_x, f_y)$, was applied both in phase and amplitude of the Fourier image component and was the same for each average aberration. Over a series of 200 trials of an average aberration, each time position was therefore tested 66 times, and doing so, we ignore the potential coupling between temporal position of the deviation and the spatial characteristic of the variation. In a side-by side matching task procedure, the subject was asked to discriminate the modified image of the original Fritz face from its static average for each average ocular profile. In a forced-choice paradigm the subject was simultaneously asked to answer the two questions: which is the sharpest image? and are they the same appearance? (sharpness referring to visibility of the image and appearance to its geometry). We note that the notion of sharpness and contrast diverges in the complex image as the presence of multiple frequency would lead to the confusion between impression of visibility (blacker feature) and the amount of details accessible.

The global sharpness of the modulated image suggests that the sensitivity to the

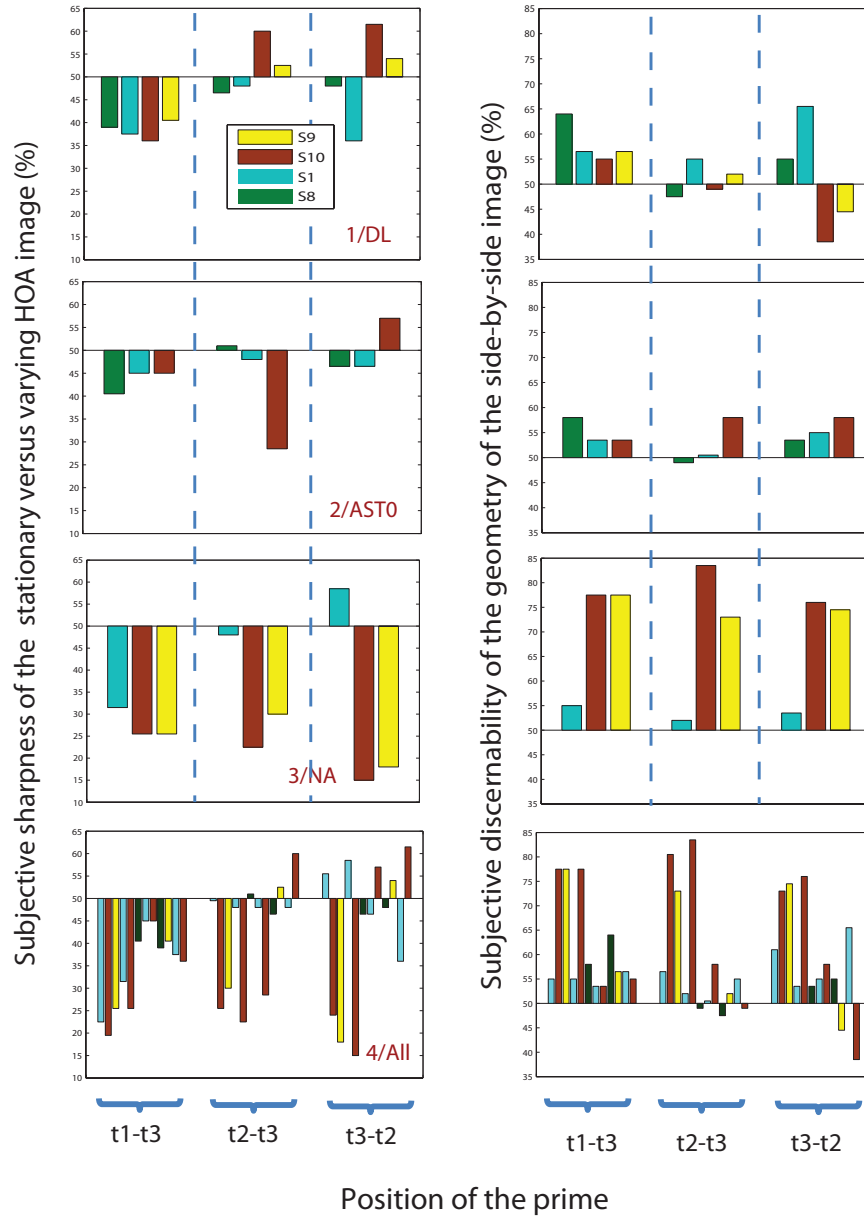


Figure 5.5: Level of sharpness and discernibility of the faces images with respect to the onset position of the temporal aberration for three different viewing conditions (DL, AST0, NA respectively) and the overall set of temporal aberration. On the left side, the baseline of 50% corresponds to identical sharpness of the stationary and varying image, whereas, on the right side, it represents an equal percentage of estimated similar and dissimilar faces perceived by subjects. Temporal noise tends to increase the sharpness of the modulated image and systematically increases the percentage of dissimilar faces. The temporal property of the blur affects perceived sharpness at the early stages of the visual response, in particular for the diffraction-limited viewing condition. Spatio-temporal noise impact varies in strength with blurring conditions. The diffraction-limited system is more robust to visual noise. We posit from these results that DL may be faster in processing and less sensitive to later visual perturbations of the image.

stationary stimulation at low spatial frequency and high spatial frequency is modified by the temporal modulation, such that the relative intensity is higher. Analogous to a masking mechanism, we believe that the technique used produces a phenomenon of interference in the amplification process of neurons between pre-loaded signal and signal entering, dependent on the signature of the observer visual response. An illustration of the relationship between sharpness and discriminability of the image is given by Fig- 5.5, showing that the variation, not only alters sharpness, but also modifies perceived image features. It indicates a transfer of the change in sharpness to the geometry of the feature of the human face. Again, the integrand signal is determinant in the effect of the deviation as one can observe a substantial difference of impact of each average distribution on perceived sharpness and geometry. For each time occurrence, the natural aberration profile led to higher variation of the perceived image, for both sharpness and geometry compared to the aberration free system and astigmatism viewing condition. A possible explanation of the higher tolerance of the free aberrated system may be that finer grating (HF), integrated in the DL condition, are destroyed by the deformation, whereas coarser grating (LF), integrated in the aberrated image, are summed constructively by the deformation, leading to higher sharpness of the aberrated image.

Development of the time response highlights the stage of the mediation between the different channels of the response and subsequent phase of the representation [271]. Early time perturbation impacts emphasize mediation between detection and identification, while a later time perturbation impact might influence higher mental processing level. The time of occurrence of the deviation exhibits an important effect on sharpness for all subjects, especially for DL where, interestingly, later transformations (e.g. $t_2 - t_3$ and $t_3 - t_2$) exhibit weaker effects, as indicator of difference in performance dynamism and probably to infer to the contrast gain vector of the neuronal amplification along Magno and Parvo pathways, and subsequently to the degree of automatism of the process (relative to bottom up and top down mechanism). It comes from these results that perceived optical degradation of human

face is not static but involves a spatial integration in the nervous system that may respond to particular laws.

The degree of mobilization and robustness of the visual system is an important aspect of the aberration impact. Other techniques may be employed for testing this hypothesis by measure of after-effects of altered images. The question rises here is: does the visual system possess the same state of activity for different distributions of contrast across the image? Such questions may find a partial answer in test and re-test experiment [249], where it is found that an increasing level of defocus-blur is associated with higher variability of the visual system performance.

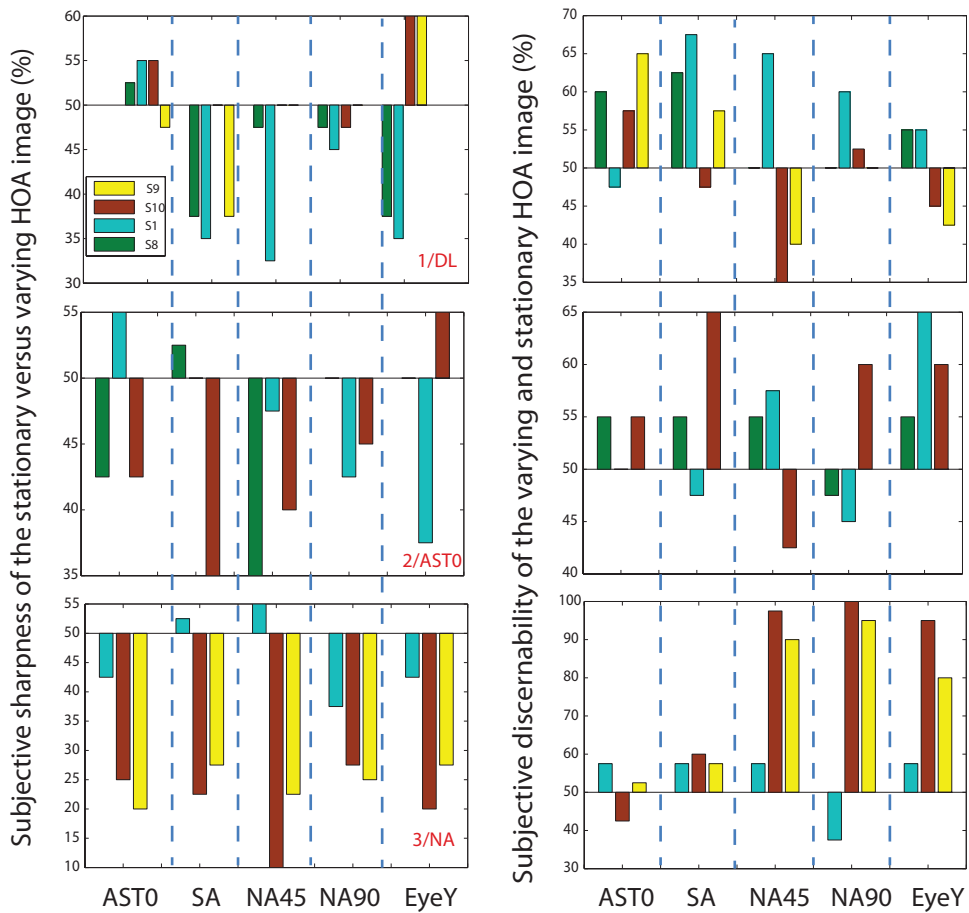
About the characteristic of the noise on the appearance of the image

- The nature of the noise has an important effect on the variation of perceived sharpness that may be intensity or phase dependent. This impact varies with the average distribution. For the near diffraction-limited image, the temporal aberration of 'astigmatism' and 'native aberration' are marked by a smaller impact than 'spherical aberration' and 'other eye'. These differences are smoothed for the aberrated average distribution and, in particular, faint for the natural aberration distribution.
- Sharpness and discernibility of the images for different types of noise is little correlated. Besides, strong divergences stand across subjects.

These observations led to a further test.

Role of the phase shift component

In order to isolate the effect of phase and magnitude variation, we limit modification of the image to the phase component in the Fourier domain. The manipulation of



Time varying aberration

Figure 5.6: Level of sharpness and discernibility of the images associated with the distinct spatial symmetry of temporal blur. The impact of spatial symmetry of the temporal blur depends on the viewing condition and varies substantially across subjects.

the phase variations map presented several restrictions with respect to aliasing and sampling [38]. To circumvent this problem, rather than a variation, a temporal aberration with four distinct phase profiles were employed (astigmatism at 45deg, coma at 0, defocus, and natural aberration at 45deg) with an rms wavefront value of λ . The appeal of such segmentation resides in the role of phase in the image, drawn in several studies [282, 235, 220, 226]. Note that the amount of perturbation perceived of the phase is weighed by the neural MTF and one may wonder if it is linearly related to the intensity variation of the retinal image. Refinement was added to this study by equating the standard deviation introduced by the variation in intensity. In opposite to the previous test, the average intensity was constant for each frame. The temporal noise was inserted on the first five frames of the image onset. Note also that the temporal aberration generated for the two distributions are fairly similar. Only the high frequency differs between the two distribution: the noise is more pronounced in the high frequency for the diffracted-limited average image. The difference between natural aberrations employed for each subject does not alter significantly the amount of degradation as supported by optical metrics. Some preliminary results are shown.

- The sharpness of the average image is strongly modified for all the subjects: the eye boosts the representation of the feature that are ill-defined or noisy by attributing them more contrast. The impacts of the phase-noise vary slightly between subjects indicating a similar visual strategy. Information is not boosted anymore by the identification stage, probably because noise cannot be overridden by the recorded signal. Therefore, the efficacy of the noise may depend on the quality of the distribution. The disruption of the image contrast is maximum for the astigmatism distortion.
- The two predominant aberrations are defocus and astigmatism. Defocus noise suppresses most of the details of the face while astigmatism introduces a strong lateral shift. The less impactful noise is associated with the natural aberration

of the subject, undergoing a rotation of 45 deg. It also preserves the features of the face. Sharpness of the modified image is maximum for the coma noise despite little change of the image, indicating that the global shift of the lowest spatial frequency is significant.

- For the diffraction-limited image, the modified image is perceived less sharp contrary to the aberrated average image. This phenomenon indicates a variation in the 'contrast mechanism' associated with the two distributions. An explanation of this difference of perceived contrast can be derived by analogy to the superposition of a static and moving grating. An aberrated grating will show higher mean stroke than a diffracted limited one. For the same variation the stroke of that last may be washed while reinforcing the former.

5.2.4 Evidence of a 'mobilization state' of the neuronal workspace with respect to time and space

Impact of image variation for distinct average contrast distribution

Protocol To better understand the influence of the temporal aberration and the transformation undergone by the perceived image, a subjective assessment of a dynamically modified image was performed on six subjects. By means of a method of adjustment, the subjects were asked to modulate the level of a temporal aberration (here, introduced at the onset of the image for a period of 130ms) until a change affects the perceived image, compared to an unmodified image (subsequently appearing). This change is ranked according to three levels, that are: (i) a just-noticeable change, corresponding to the detection of any variation, (ii) a contrast-change corresponding to the common reorganization of the perceived contrast (but in some situation, reduced to a simple alteration of perceived contrast), and (iii) a change of clarity, associated with the alteration of the image resolution. By pressing a button up and down, the subject can adjust, tune its response for each level and record

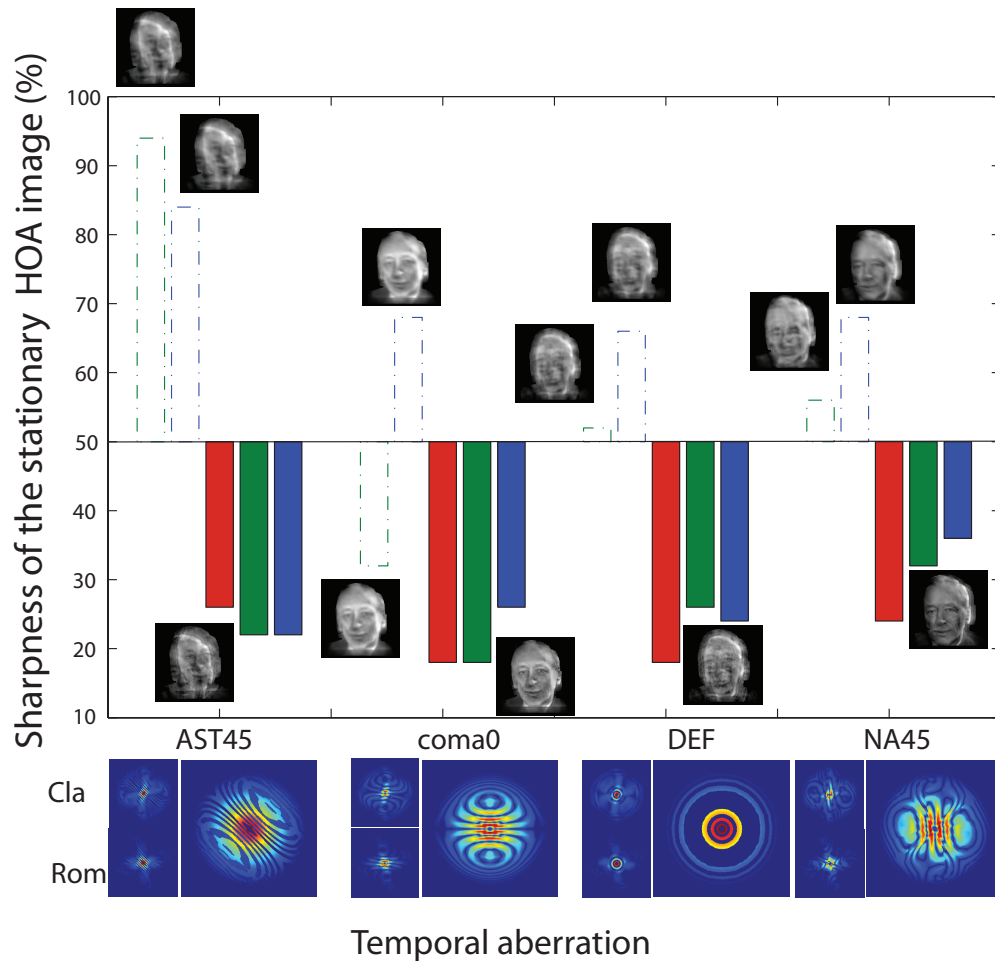


Figure 5.7: Comparison of the appearance of time-varying and stationary image faces using sharpness for distinct phase-noise symmetry, introduced at t_1 , for NA (full bar) and DL (dashed bar) viewing conditions, measured in three subjects.

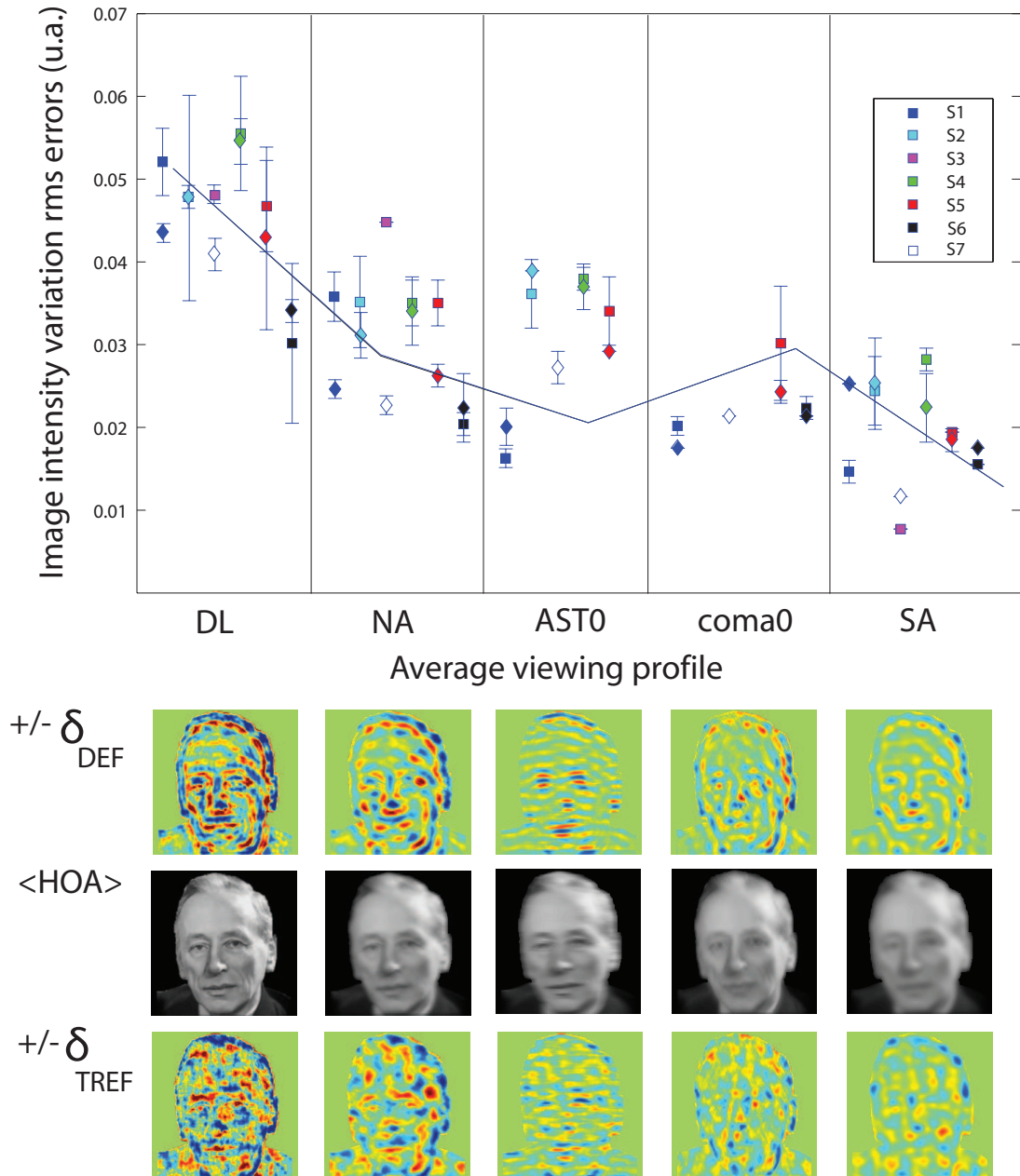


Figure 5.8: Level of just noticeable-change of the perceived average image induced by two types of temporal aberration, respectively a defocus (in square) and astigmatism/or trefoil (in diamond) phase symmetry, introduced at the onset position of the optical disturbance and measured by the standard deviation of the intensity variation (below in grayscale) of the normalized image (below in color scale) for various average contrast distribution, tested on six subjects. The drawn lines represent the optical predictions of the VSMTF metric.

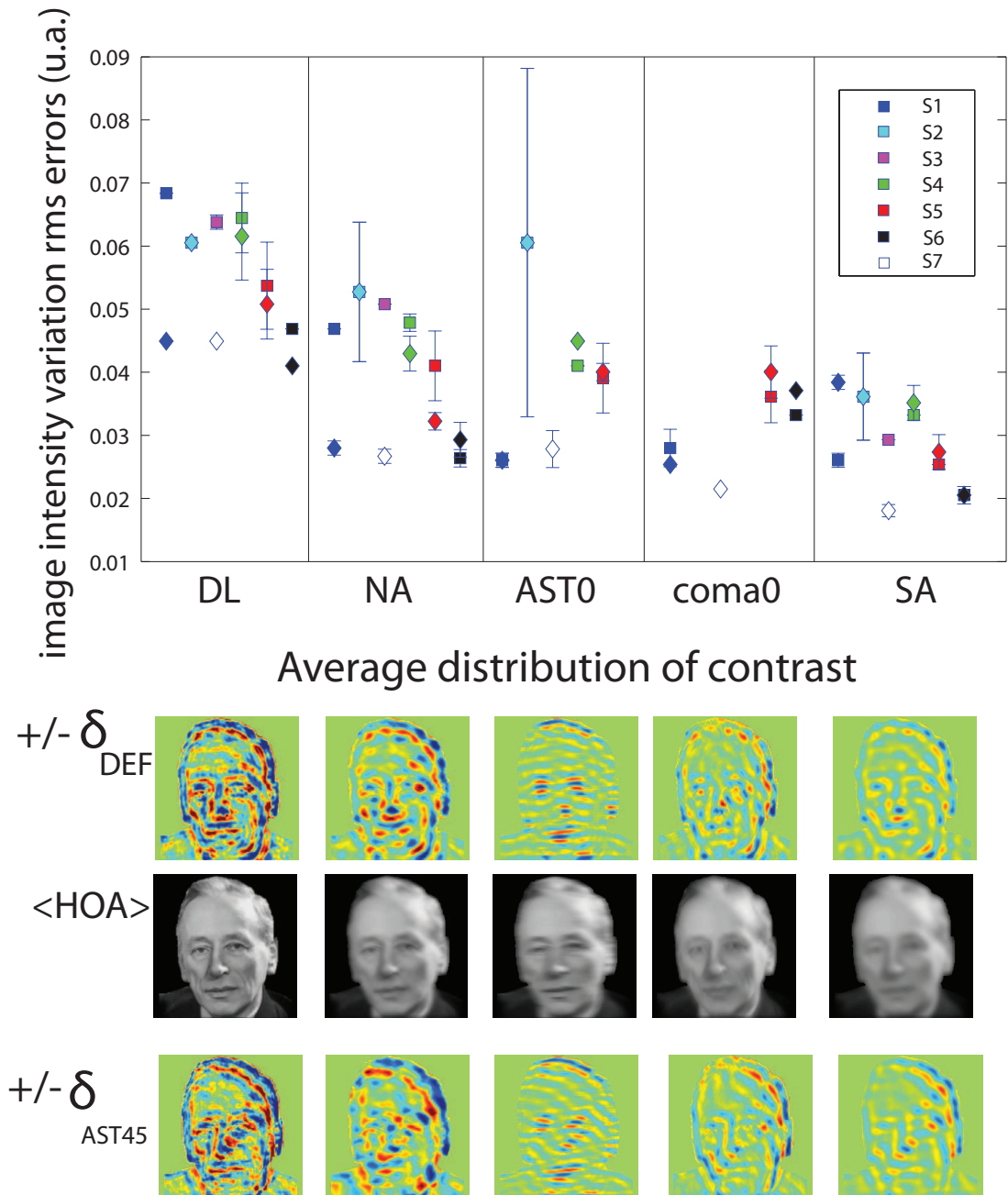


Figure 5.9: Level of change in contrast of the perceived average image induced by two types of temporal aberration, respectively a defocus (in square) and astigmatism/or trefoil (in diamond) phase symmetry, introduced at the onset position of the optical disturbance and measured by the standard deviation of the intensity variation (below in grayscale) of the normalized image (below in color scale) for various average contrast distribution, tested on six subjects. The drawn lines represent the optical predictions of the VSMTF metric.

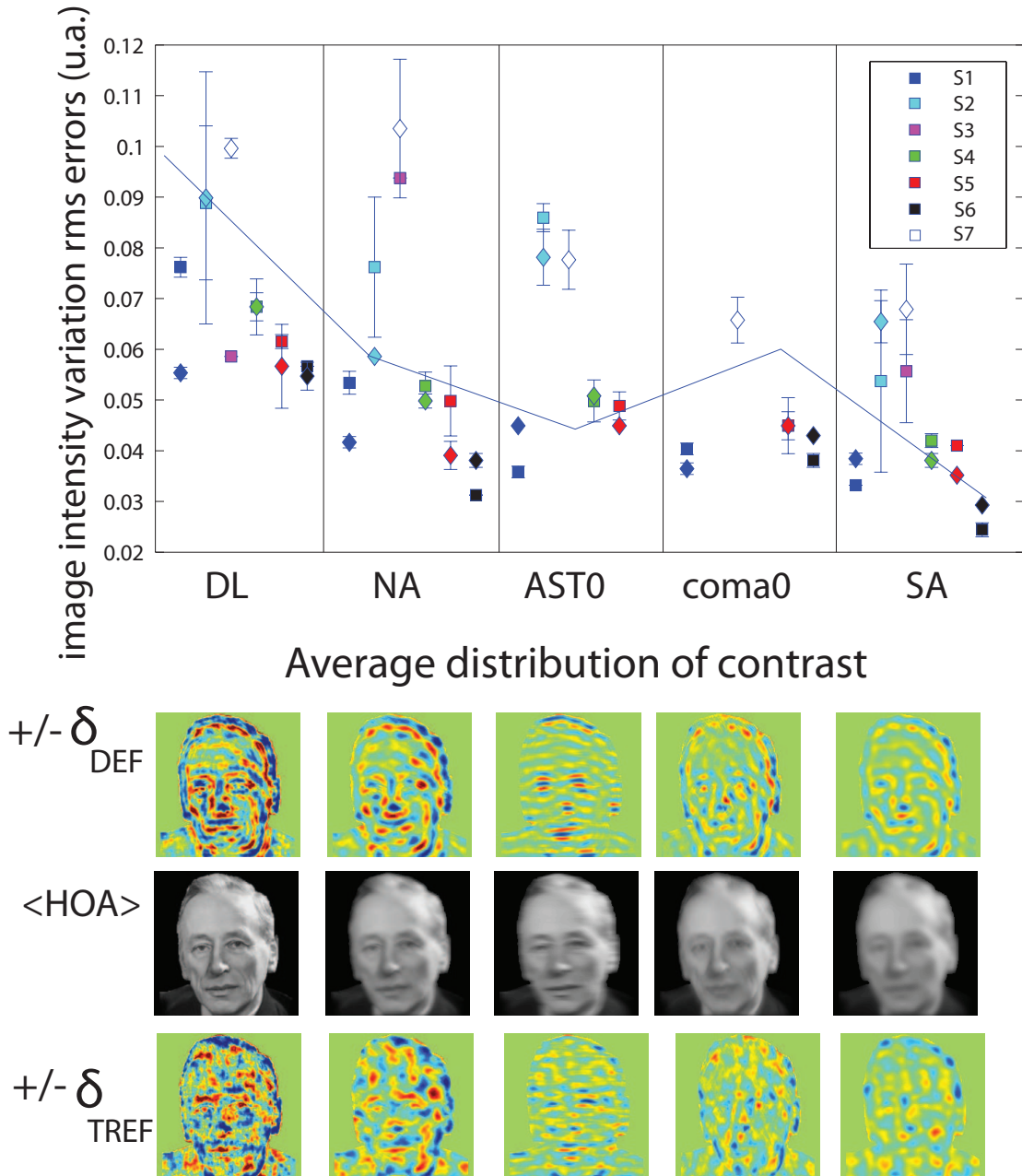


Figure 5.10: Level of change in the clarity of the perceived average image induced by two types of temporal aberration, respectively a defocus (in square) and astigmatism/ or trefoil (in diamond) phase symmetry, introduced at the onset position of the optical disturbance and measured by the standard deviation of the intensity variation (below in grayscale) of the normalized image (below in color scale) for various average contrast distribution, tested on six subjects. The drawn lines represent the optical predictions of the VSMTF metric.

them successive times. The increment of the temporal aberration was defined by the standard deviation of the intensity variation introduced in the image, fixed at 10^{-4} . This metrics affords a solid comparison and a sensitive adjustment of the temporal aberration impact; it is also found more relevant than the metric rms of a temporal aberration. This procedure was easily performed by the subject and the adjustment control allows the subjects to precisely locate the transformation occurring in the image.

Observation As shown in Fig-5.8 and 5.9, the image variation varies with both the average distribution of contrast and the temporal aberration. A first observation indicates that these variations are not equal; their impact is strongly influenced by the average distribution of contrast. In a least measure, one can observe slight difference of impact with the temporal aberration. The typical rms errors of the temporal aberration needed to produce a just-detectable variation starts at about $\lambda/4$ and reaches about $\lambda/2$ for a change of contrast and clarity, for defocus and astigmatism temporal aberration. For the trefoil temporal aberration, several wavelengths are necessary and some difficulty to create a certain intensity variation may arise. The standard deviation of the variation of the normalized image necessary to produce a change in the perceived image is comprised from 1 – 5%, 2 – 7% and 3 – 10% of the object maximum corresponding to the three perceived modifications; and strongly fluctuates in strength among subjects, which suggests a disparity in the level of temporal sensitivity across subjects. However, a general trend is observed in all the subjects that is an increase of impact of the temporal aberration from the perfect average image condition to the aberrated average image (pictured in grayscale). This observation is revealed for the each three steps of the perceived change and reflects the strength of the associated image variation (pictured at the bottom, in color scale). The subject natural aberration (here scaled to the level of rms of $0.25\mu\text{m}$) follows the near diffraction-limited image. Coma and astigmatism are less sensitive to the native aberration distribution, contrary to the VSMTF (pre-

| Just-noticeable variation | SRX | LIB | ENT | VSOTF | VOTF | SRMTF |
|---------------------------|--------|--------|--------|--------|--------|--------|
| And | 0.778 | 0.813 | 0.882 | 0.758 | 0 | 0.826 |
| Dav | 0.683 | 0.819 | 0.899 | 0.685 | 0.011 | 0.71 |
| Rom | 0.372 | 0.674 | 0.848 | 0.354 | 0.19 | 0.392 |
| Eli | 0.73 | 0.817 | 0.939 | 0.744 | 0.003 | 0.776 |
| Cla | 0.904 | 0.949 | 0.839 | 0.918 | 0.056 | 0.916 |
| Mar | 0.853 | 0.873 | 0.909 | 0.836 | 0.008 | 0.915 |
| mean subject | 0.72 | 0.8242 | 0.886 | 0.7158 | 0.0447 | 0.7558 |
| Perceived contrast change | | | | | | |
| And | 0.815 | 0.842 | 0.869 | 0.8 | 0.01 | 0.844 |
| Dav | 0.729 | 0.859 | 0.93 | 0.728 | 0.01 | 0.756 |
| Rom | 0.677 | 0.914 | 0.992 | 0.66 | 0.02 | 0.696 |
| Eli | 0.25 | 0.347 | 0.508 | 0.27 | 0 | 0.286 |
| Cla | 0.858 | 0.942 | 0.989 | 0.846 | 0.004 | 0.912 |
| Mar | 0.86 | 0.829 | 0.829 | 0.839 | 0.013 | 0.915 |
| mean subject | 0.6982 | 0.7888 | 0.8528 | 0.6905 | 0.0095 | 0.7348 |
| Perceived clarity change | | | | | | |
| And | 0.858 | 0.886 | 0.929 | 0.84 | 0.004 | 0.9 |
| Dav | 0.846 | 0.944 | 0.952 | 0.855 | 0.08 | 0.843 |
| Rom | 0.148 | 0.008 | 0.014 | 0.161 | 0.995 | 0.134 |
| Eli | 0.318 | 0.42 | 0.584 | 0.338 | 0 | 0.357 |
| Cla | 0.885 | 0.961 | 0.998 | 0.881 | 0.001 | 0.927 |
| Mar | 0.9 | 0.871 | 0.855 | 0.882 | 0.029 | 0.947 |
| mean subject | 0.6592 | 0.6817 | 0.722 | 0.6595 | 0.1848 | 0.6847 |

Figure 5.11: Level of correlation between the temporal aberration impact (measured on 6 subjects) and the quality of average image signal, predicted by standard optical metric at each perceived step.

dictions presented by a blue line). Interestingly, the average spherical aberration is strongly influenced by the temporal aberration for each step of detection. We note that each temporal aberration dominantly affects a part of the image: for the average astigmatism, the vertical features are slightly modified by a defocus noise, and affect dominantly eyes and mouth, by contrast with the average coma condition (vertically dominant), or the average spherical aberration condition (homogeneous).

Results The best optical predictions of the observation correspond to the metrics based on the point spread function of the average image, in particular with the metrics **ENT**. The metrics based on the OTF are slightly less predictive: with a pronounced advantage for the VSMTF metric and erroneous prediction of the VOTF measure, supposed to account for phase-shifts effects. The correlation of optical performance measure and observation indicates a relation between the effect of the aberration temporal and the average distribution of contrast in the image.

Only slight variations of the average contrast distribution ranking can be observed between just-noticeable, contrast and clarity change, and the optical predictions remain consistent with the observations. However, we note a general fall of metric predictability across the six subjects with the increase of the temporal aberration. The temporal aberration characteristic is clearly distinguished by the subject during the test. Some variations can be observed for certain conditions but a full comparison of different temporal aberration necessitate finer criterion of assessment than degradation and/or change detection.

Discussions and conclusions Such finding suggests that the strength in the Fourier component of the signal determines the temporal sensitivity in an opposite way in comparison with the static impact of aberration on spatial image quality obtained in previous characterizations. Our results support a higher sensitivity of aberrated profile, in comparison with the near-diffraction limited system, to external temporal variations relative to the eye and environmental transformations, with movements and focus. How is it conjugated with internal post-processing variations? Although the perfect image avails and increases representation efficiency of the discrete representation, it simultaneously intensifies the plurality of conjunct representations of the spatio-temporal channels. The gain of certainty observed in discrete representation, such as in test-retest visual acuity [249], is therefore balanced by the uncertainty conveyed by the coordination of the pathway of the neuronal stimulation in multiplex task. On the second hand, the temporal sensitivity by modifying patterns affords feedback control and relay between accessed information and non-accessed information. We claim that aberrated vision may be a compromise between absolute response and adaptive feedback performance control, in the context of attended and non- attended visual features

Time and spatial dependence of a temporal aberration influence for distinct contrast distribution of the average image

Protocol By simplifying the variable of the experiment 2, a similar side-by side matching procedure, focused this time on face expression, was performed for three average profiles tested over a series of 150 trials where the subject was asked if the two images were identical. Faces expressions involves the subjective and complex conjunction of attributes (e.g. spatial scale, directions) and higher mental mechanism. In half of the 150 trials of each test, the subjects were presented the same faces, and in the other half two distinct versions of the original Fritz face, modified through Adobe Photoshop. In each trial, the subject answers if the face expression were the same. The test is a two-class prediction problem (binary classification). The binary classification leads to four type of outcomes known as false negative responses, a true negative response, a false positive response, and a true positive response. The probability of correctly identifying the two faces relation is retained in the true positive fraction and false positive fraction commonly represented by the receiver operating characteristic (ROC) curve [134]. For each average distribution tested, nine different temporal aberrations are tested randomly corresponding to three types of image variation (i.e. defocus, astigmatism 45 deg, trefoil) and three time positions of the deviation introduced (0-133ms, 133-26-ms, 264-399ms). Each condition is tested 50 times. The standard deviation is set at the threshold of clarity of the image and fixed the same for all the temporal aberration. The deviation stresses the saliency of some image features while altering some others. True and False positive responses, corresponding to correct response to similar pairs of face and non correct prediction to dissimilar pairs of face, were analysed for each subject in relation with the time occurrence of the variation (Fig-5.12a) and the spatial characteristic of the variation (Fig-5.12b) in the ROC curve.

Each region of the ROC curve represents the proportion of these two predictions, e.g. a particular equilibrium of the variation between positive features of a pair of

identical images and the negative features of a pair of dissimilar images, therefore representative of a specific transformation of the perceived stimulus. For all the variation, the deviation impairs the discrimination of the face expression suggesting that the temporal aberration not only affects sharpness but also the global appearance of the face expression. As shown in Fig.4, regions and spreads of the encircled area of the various average images (i.e. triangle square, circle) are clustered. In fact, each viewing condition restricts the spatial frequency of the two compared faces in a certain domain leading to distinct discrepancy between the two images and interpretation. For a given viewing conditions, one may ask what are the cues used by the observer for the discrimination, and its possible variations. The visual impact of the average image differs across subjects, and is more or less localized following viewing condition: S3 distinctly processes the aberration profiles NA, DL, SA; S4 distinctly processes SA; S2 and S8, DL from SA and NA; S1 shows no clear difference. Remarkably, these differences of visual impact are concurrently influenced and driven by the time position and spatial symmetry of the temporal aberration. A particular bias is found among individuals to characteristic of temporal aberration. Not all the temporal aberration impacts are well distinct, each subjects exhibiting a particular degree of specificity. We notice a substantial bias in the impact of the temporal aberration on the discrimination for each subject which can be observed on the time and space ROC curve, with clustering of the symbol of identical color in Fig-5.12. For instance, S3 shows a neat bias for the time occurrence 133-266ms (in yellow, clustered above the line of uncertainty) for all the average distribution, with a fainter impact of the variation. S8 shows a neat bias for the time occurrence 266-399ms (in red, aligned below line of uncertainty) for all the average distribution, with a bigger impact of the variation. S1 presents a slight bias for both the time occurrence 266-399ms (in red, packed towards the right side) and the temporal aberration DEF (in red, clustered at the center of the line of uncertainty). S2 shows a bias for the temporal aberration AST45 (in blue, clustered below line of uncertainty) for all the average distribution with a bigger impact of the variation. For S3, a constant visual effect of the temporal aberration AST45 is observed (in

blue, aligned along the line of uncertainty), added to the packing of the temporal aberration DEF (in red, clustered near the center of line of uncertainty). For S4, the temporal aberration trefoil is localized (in yellow, aligned in the top corner of the curve). Bias in the time occurrence and spatial symmetry impact indicates differences of the spatio-temporal response across subjects (i.e differences in the temporal interaction of spatial frequency). Such finding is in favour of preferential attentional mechanism along transient and sustained channels as it suggests a preponderance of the response gain, demonstrated by the subject, at different time of the response, e.g. stages of the representation. This time attentional mechanism could also be oriented towards particular region of the signal. In effect, visual events formation is influenced by the property of symmetry of the propagation, as well as of scaling of spatial frequency.

We conclude from this experiment that a certain state of mobilization is provided by the viewing condition, which concomitantly admits particular fashion of the visual response of the observer. To which extent the spatio-temporal response is shaped by the viewing conditions, expected to define a certain temporal sensitivity, remained an open question, if postulating a particular state of mobilization in which the loaded signal mobilizes a certain route of neuronal activation for new entrant signals.

Existence of bias spatio-temporal responses intrinsic to the observer?

Discussion Refractive correction commonly considers a spatially static image. Dependence on time response and the relative efficiency of the stimulation in the visual field is often disregarded. It translates into a refraction that privileges a diffraction-limited optical system and sometimes envision the induction of particular aberration (e.g. spherical aberration). Or, a central problem of vision emanates from the fact that our environment confronts our visual system with more information than it can process and react in time to, therefore requiring cognitive decisions and strategies where superimposition and interconnectivity of multiplexed informa-

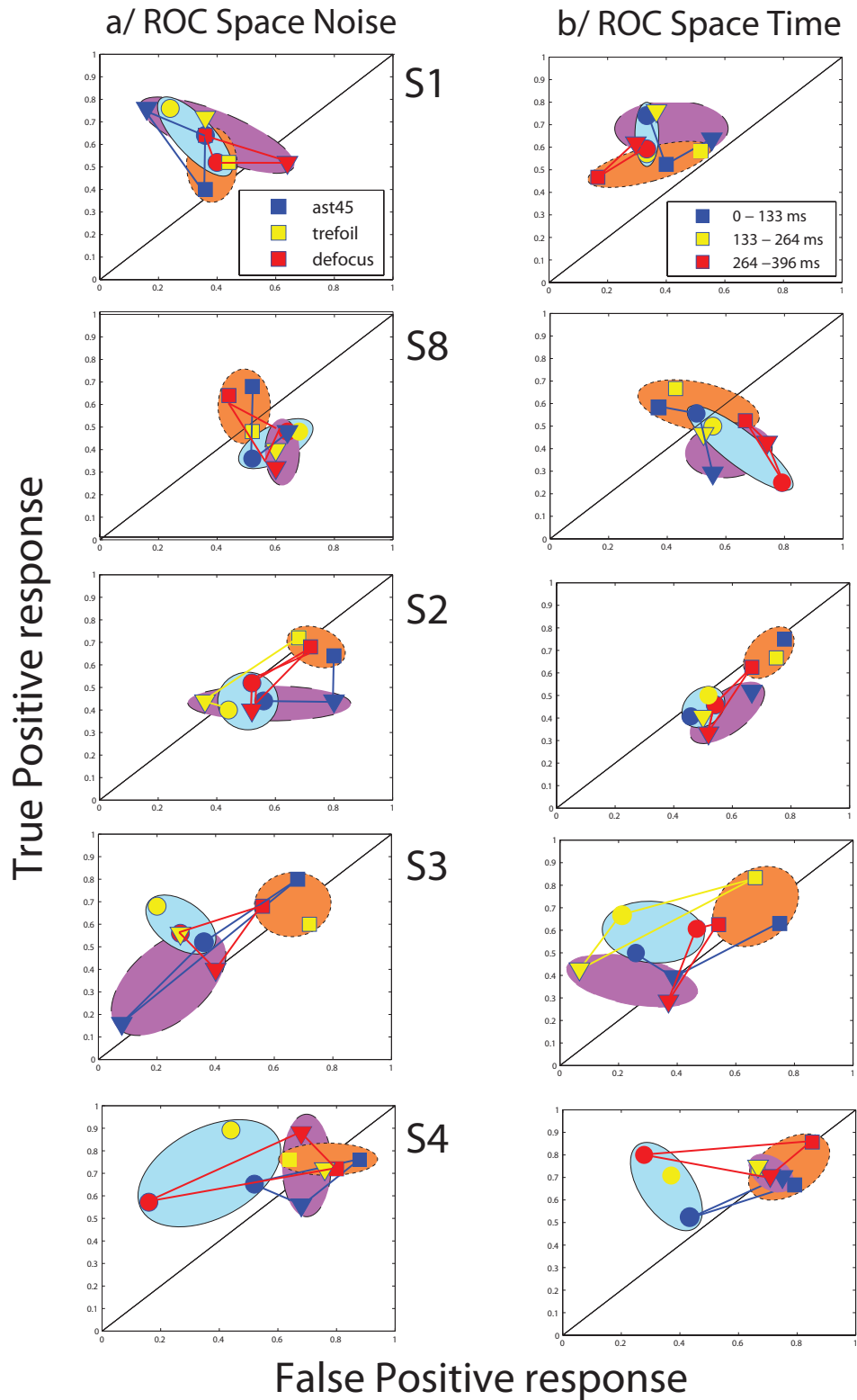


Figure 5.12: Probability of true positive response versus false positive responses associated, on the left side, to distinct spatial deviation, and on the right side, to distinct time occurrence. Three average aberrations are tested, encircled by ellipses that represent clustered visual transformations. The light blue ellipse regroup the average spherical aberration (circles), the purple ellipse, the average natural aberration (triangle); the orange ellipse, the diffraction limited condition (rectangle). Spatial and temporal noises are labelled by the blue, yellow and red colour. The clustered visual transformations are highlighted by connecting lines.

tion can question classical refractive solution. In this respect, it is demonstrated that aberration not only defines the plurality and the amount of information processed, transferred and accessed, but also a certain spatiotemporal sensitivity to external signal variation, inversely sensitive, and most probably in resonance with internal variation of processing (which oppose seeing discrete event or their unfolding). Previous studies emphasized a development of visual stimulation from a coarse-to-fine approach. Here, introducing an aberration temporal in this approach, we see that the relay of discrete representations, potentially unique and finally tuned with respect to spatial scale and direction, can modulate the propagation of the signal throughout visual channels and reveal potential temporal interaction of spatial frequency. The role of attentional mechanism is highlighted by the specificity of the observer response, both temporally and spatially articulated, for complex task. Observers are subject to particular level of sensitivity to the symmetry property of the variation, indicator of preferentiality in the directionality of the temporal direction. Concurrently, the efficiency of the time response admits differences in the relative impact of the deviation between observers. This interrogates the possible preponderance of particular channel of the visual response to spatial frequency in the stream of the mediation driven through time, along transient and sustained channel. In this case, can attention or prevalent spatial task such as identification or detection force a particular dynamism of the visual response? Recalling the spatio-temporal sensitivity determined by the viewing conditions, it is tempting to hypothesize that a diffraction-limited system, having higher contrast and robustness to variations, can emphasize an aspect of visual stimulation more immediate and spatially singular, compared to the complexity that can be engaged by an aberrated image, poorer in its transmission and robustness to variations. It appears that the relationship of propagation between attended and non-attended feature ensue then from this spatio-temporal relationship. As a consequence, we object to a point-by-point representation of perceived degradation that only accounts for transferred signal pertained to discrete task or representation, in favour of an integrative solution where rather each spatiotemporal point of the representation is

potentially interrelated and participates to the connectivity of parallel representations. It involves then a multiplicity of the circuitry of propagation. Such adaptive approach of the visual stimulation is opened to debate and rises a new problematic that concerns the global neuronal efficacy of the HOA stimulation, that we define by the amount of accessible information and the amount of information consciously accessed throughout the times of the stimulation. Considering a neural transfer function that comprehends both accessed and non-accessed information, aberration becomes then a possible strategy to limit the information non-consciously accessed during activity compared to the information accessed. A crucial question remain on how does this spatio-temporal sensitivity interact with the aspect of the visual world formed by the aberration of the observer. If the ocular aberration shapes spatio-temporal response, then the question we address is: does the spatio-temporal response can influence aberration development?

5.3 Conclusion

This study offers a new approach for understanding the neural mechanism and the architecture in which degradation is fomented. We advocate in this thesis a potential differentiation of **signal propagation**, and therefore of image appearance, through distinct visualized aberration. The possibility of manipulation of a marker-noise with particular symmetry in both intensity and phase is proposed. Its mechanism may rely on the interference between entering and loaded signal. We show that a manipulation of the image kernel could be done to modify the impression of sharpness and accessing the underlying neural mechanism of amplification related to perceived image quality and degradation. Our main conclusion is that the temporal development of the response has an effect on the perceived degradation. We confirm that identification mediates discrimination, and more generally it is shown that interference of the entrant signal can take place throughout the stimulation with varying strength. That temporal characteristic of perceived blur may be linked

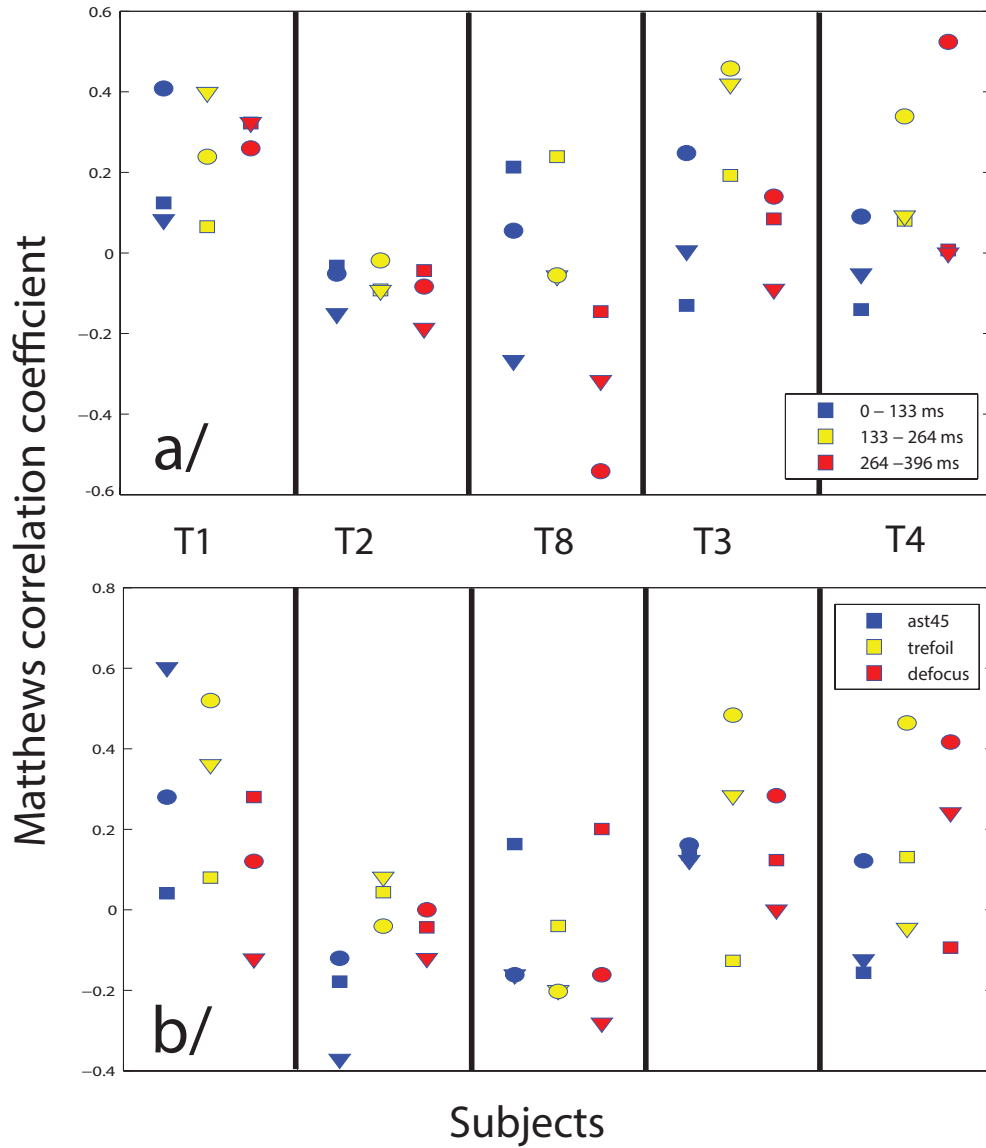


Figure 5.13: Measure of the performance of the subject to correctly discriminate two faces, assessed by Matthew correlation coefficient, and corresponding to the spatial characteristic of the temporal aberration and their time of occurrence.

to the mobility of visual processing governed by phase of varying awareness: from the automatism to the higher mental operation. It seems fundamental to re-place optical degradation in the visual environment of natural viewing and understand the interplay between the neural architecture and the mobility of the optical feature in context of representation that may aim beyond visual performance. An evaluation of post-optical image processing is yet in its infancy, and demand new techniques and methods to be unveiled: why not combined with functional brain imaging?

Chapter 6

Summary and discussion

Customized correction is discussed in this Thesis with respect to the challenge of real life vision by looking at the propagation of the visual stimulation from eye to brain. The modalities of an optimal refraction for the standard pseudophakic population is investigated by examining the prerequisite of an adequate eye model, built on distinct power calculations methods such as ray-tracing. Various sources of errors are analysed and simulated on the optimal post-operative correction including the geometry of the thick IOL, its position inside the eye, and the ocular biometry errors as well as an account of the IOL irregularities. We found that customization by IOL was highly influenced by the power calculation method that dominates over extra sources of errors. For an optimal post-operative prediction method, the aspheric design correction outperforms the spherical design optical performance, although a higher stability of spherical design in post-operative prediction is an advantage.

A further expansion of customized correction target to individual's sensitivity was conceived and conducted via the construction of an AO visual simulator affording coordinate objective and subjective measurements on the non-dilated pupil of the real eye. This visual simulator demonstrates the alliance of compactness and high corrective performance with a substantial level of freedom and tuneability accorded

with the subject's comfort and extension of the system. Using a customized visual interface in combination to the AO visual analyzer, a fine control of the method and properties of the stimulation is availed for testing aberrations in the eye.

Based on a series of visual performance tests on the real eye, an evaluation of the predictability of optical metrics is given for a set of simulated blur symmetry: several optical metrics exhibits good predictive outcomes for the objective task despite a marked discrepancy due to neural factors. An explanatory study is proposed, borrowed from cognitive visual search, to quantify the exertion of blur patterns on visual information processing. Several experimental protocols, based on parallel channel excitations, are developed to modulate and disrupt the visual response coordination. Our results show that the dynamics of the stimulation modulates blur effects, although a strong robustness of the eye to attention modulation in the context of visual resolution testing. We conclude that spatial vision involves a dynamic component that may disclaim absolute visual performance as a definitive predictor of real life vision. The noise of the optical system, i.e. the aberration, is added to another noise: the noise of the overall stimulation! A neat effect of masking techniques on visual performance was found presenting potential differences between the visual viewing conditions. An audacious explanation was further developed: does the diffraction-limited eye undergo differences of temporal responses? and, if so, may it modify the development of the visual response to the dynamic visual environment?

In relation to this burning question, we develop a novel technique that aims at probing the development of the visual response using time and consists in modifying the neuronal propagation of visual information by introduction of wise and controlled noise in the perceived stimuli. Using this perturbation technique, the existence of a singular trade-off between spatial and temporal sensitivity to altered images was revealed, which assumes a certain efficacy of the visual response in space and time. Space and time variations also shows evidences of mediative mechanisms along

the development of the visual contrast gain response suggesting subtle temporal interaction between spatial frequency acting on visual perception. In particular, we observe an idiosyncratic of the visual gain response with respect to the noise characteristic among observers, which addresses the following questions:

- 1) How does the visual system deal with time and spatial constraint?
- 2) Are ocular aberrations shaping our visual response?

6.1 Future work: neural noise and aberration in customized correction

These results share important causalities with a fundamental question asked by surgeons: what is the degree of finesse to aim at for an individual correction? By applying what residual aberration profile? It comes clear that a static and central vision analysis limits the answers often engulfed by the variability of the neural factors. Because the subject faces, during daily vision, stimulation of varying strength in the spatio-temporal domain, we suggest that an extension of customized correction therefore must go beyond old practices and incorporate the dynamics of the overall stimulation, then not only measuring aberration in account with the optimum performance of the system (often discrete) but also, with a conjoint factor: the “stress” imposed on the system by a certain type of aberration, i.e. the ensemble noise in the system. What is the relation between this stress, discrete performance and visual dynamism through varying stimulation is the new turn, we believe, new customized correction should take in the future for acquiring added freedom through spatial correction and expanding its target. This matter becomes urgent as simulation emancipates from ancient experimental boundaries with the development of constrain-free systems such as proposed in this work (e.g. natural pupil, wide-field AO, or binocular systems) that go towards real life vision measurements.

Bibliography

- [1] D. A. Atchison, Optical Design Of Intraocular Lenses .1. On-Axis Performance, *Optom. Vision Sci.* 66, 492-506 (1989).
- [2] D. A. Atchison, Optical Design Of Intraocular Lenses .3. On-Axis Performance In The Presence Of Lens Displacement, *Optom. Vision Sci.* 66, 671-681 (1989).
- [3] D. A. Atchison, 3rd-Order Aberrations Of Pseudophakic Eyes, *Oph. Phy. Opt* 9(2), 205211 (1989).
- [4] D. A. Atchison, Design Of Aspheric Intraocular Lenses, *Ophthalmic Physiol. Opt.* 11, 137-146 (1991).
- [5] D. A. Atchison and G. Smith, Continuous gradient-index and shell models of the human lens, *Vision Res.* 35,25292538 (1995)
- [6] D. A. Atchison and G. Smith. *Optics of the Human Eye.* Butterworth-Heinemann, Oxford, 2000.
- [7] D. A. Atchison, Recent advances in measurement of monochromatic aberrations of human eyes, *Clin. Exp. Optom.* 88, 5-27 (2005).
- [8] D. A. Atchison, D. A., Schmid, K. L., & Pritchard, N. (2006). Neural and optical limits to visual performance in myopia. *Vision Research*, 46, 37073722.

- [9] D. A. Atchison DA, W.N. Charman, Thomas Young's contribution to visual optics: the Bakerian Lecture "on the mechanism of the eye". *J Vis.* 2010 Oct 15;10(12):16.D. A.
- [10] P. Artal, J. Santamaria, J. Bescos. Phase-transfer function of the human eye and its influence on point-spread function and wave aberration. *Journal of the Optical Society of America A*, 5, 17911795 (1988).
- [11] P. Artal, A. Guirao, E. Berrio, and D. R. Williams. Compensation of corneal aberrations by the internal optics in the human eye. *J. Vis.*, 1:1 8, 2001.
- [12] P. Artal, E. Berrio, A. Guirao, P. Piers. Contribution of the cornea and internal surfaces to the change of ocular aberrations with age. *J Opt Soc Am A*. 2002;19:137143.
- [13] P. Artal, A. Benito, J. Tabernero. The human eye is an example of robust optical design. *J Vis.* 2006;6:17.
- [14] P. Artal, S. Marcos, R. Navarro, and D. R. Williams, Odd Aberrations and Double-Pass Measurements of Retinal Image Quality, *J. Opt. Soc. Am. A* 12, 195201 (1995).
- [15] P. Artal, L. Chen, E. J. Fernandez, B. Singer, S. Manzanera, and D. R. Williams, Neural compensation for the eye's optical aberrations, *J. Vision* 4, 281-287 (2004).
- [16] P. Artal, L. Chen, S. Manzanera, D. R. Williams. Temporal dependence of neural compensation for the eye's aberrations. *Investigative Ophthalmology & Vision Science*, 45, 1077 (2004).
- [17] P. Artal, et al. *IOVS* 2005;46:ARVO E-Abstract 3615
- [18] R.A. Applegate S.C. MacRae, R.R. Krueger. Customized Corneal Ablation. Slack incorporated, 6900 Grove Road, Thorofare, NJ 08086, 2001.

- [19] R.A. Applegate, C. Ballentine, H. Gross, E. Sarver, C. Sarver(2003). Visual acuity as a function of Zernike mode and level of root mean square error. *Optometry and Vision Science*, 80, 97105.
- [20] R.A. Applegate, E. Sarver,V. Khemsara. Are all aberrations equal? *J Refract Surg* 2002;18:S556-62.
- [21] R. A. Applegate, J. D. Marsack, R. Ramos, and E. J. Sarver, Interaction between aberrations to improve or reduce visual performance, *J. Cataract Refract. Surg.* 29(8), 14871495 (2003).
- [22] R. A. Applegate, J. D. Marsack, and L. N. Thibos, Metrics of retinal image quality predict visual performance in eyes with 20/17 or better acuity, *Optom. Vision Sci.* 83, 1611-1623 (2006).
- [23] R.A. Applegate, W.J. Donnelly, J.D. Marsack, D.E. Koenig, K. Pesudovs. Three-dimensional relationship between high-order root-mean-square wavefront error, pupil diameter, and aging. *J Opt Soc Am A Opt Image Sci Vis.* 2007 Mar;24(3):578-87.
- [24] Alcon Laboratories, Inc. AcrySof ReSTOR apodized diffractive aspheric IOL [package insert]. 1-16. 2007. Fort Worth, TX, USA.
- [25] T. Caelli, M. Hubner, I. Rentschler. The detection of phase shifts in two-dimensional images. *Perception & Psychophysics* 1985, 37, 536-542.
- [26] M. Ahissar, S. Hochstein, Task difficulty and the specificity of perceptual learning, *Nature* 387, 401 - 406 (22 May 1997)
- [27] K. R. Alexander, W. Xie, and D. J. Derlacki, Spatial-frequency characteristics of letter identification, *J. Opt. Soc. Am. A* 11, 2375-2382 (1994).
- [28] M. Alpern, "Metacontrast," *J. Opt. Soc. Am.* 43, 648657 (1953).

- [29] R. S. Anderson and L. N. Thibos, Relationship between acuity for gratings and for tumbling-E letters in peripheral vision, *J. Opt. Soc. Am. A* 16, 2321-2333 (1999).
- [30] *J Cataract Refract Surg.* 2007 Dec;33(12):2111-7. Image quality with multifocal intraocular lenses and the effect of pupil size: comparison of refractive and hybrid refractive-diffractive designs. Artigas JM, Menezo JL, Peris C, Felipe A, Daz-Llopis M.
- [31] S. Barbero, S. Marcos, J. Merayo-Llodes, and E. Moreno-Barriuso, Validation of the estimation of corneal aberrations from videokeratography in keratoconus, *J. Refractive Surg.* 18, 263-270 (2002).
- [32] S. Barbero, S. Marcos, and I. Jimenez-Alfaro, Optical aberrations of intraocular lenses measured in vivo and in-vitro, *J. Opt. Soc. Am. A* 20, 1841-1851 (2003).
- [33] S. Barbero, Refractive power of a multilayer rotationally symmetric model of the human cornea and tear film, *J. Opt. Soc. Am. A* 23, 1578-1585 (2006).
- [34] S. Barbero and S. Marcos, Analytical tools for customized design of monofocal intraocular lenses, *Opt. Express* 15(14), 85768591 (2007)
- [35] Sergio Barbero, Susana Marcos, Javier Montejo, and Carlos Dorronsoro, Design of isoplanatic aspheric monofocal intraocular lenses, *Optics Express*, Vol. 19, Issue 7, pp. 6215-6230 (2011)
- [36] P. A. Bedggood, R. Ashman, G. Smith, and A. B. Metha, Multiconjugate adaptive optics applied to an anatomically accurate human eye model, *Opt. Express* 14(18), 80198030 (2006).
- [37] C. Blakemore, J. Nachmias, and P. Sutton, The perceived spatial frequency shift: evidence for frequency-selective neurones in the human brain, *J Physiol.* 1970 October; 210(3): 727750.

- [38] V. R. Bhakta, M. Somayaji, and M.P. Christensen. Effects of sampling on the phase transfer function of incoherent imaging systems. *Optics Express*, Vol. 19, Issue 24, pp. 24609-24626 (2011)
- [39] V. M. Bondarko and M. V. Danilova, What spatial frequency do we use to detect the orientation of a Landolt C? *Vision Res.* 37, 2153-2156 (1997).
- [40] M. Born, E. Wolf, and A. Joint, *Principles of optics: electromagnetic theory of propagation, interference and diffraction of light*, (New York, Oxford, 1980).
- [41] R. Bracewell. *The Fourier Transform & Its Applications*. McGraw-Hill Science/Engineering/Math; 3 edition (June 8, 1999)
- [42] D. H. Brainard. The psychophysics toolbox. *Spatial Vision*, 10, 433436 (1997).
- [43] CE Bredfeldt, DL Ringach. 2002. Dynamics of spatial frequency tuning in macaque V1. *J Neurosci.* 22:1976–1984.
- [44] B.G. Breitmeyer, & L. Ganz. Implications of sustained and transient channels for theories of visual pattern masking, saccadic suppression, and information processing. *Psychological Review*, 87, 136 (1976).
- [45] BG. Breitmeyer, Visual masking: past accomplishments, present status, future developments. *Adv. Cogn. Psychol.* 2008 Jul 15;3(1-2):9-20.
- [46] G. Bugmann, JG. Taylor, A model of visual backward masking. *Biosystems.* 2005 Jan-Mar;79(1-3):151-8.
- [47] C.A. Burbeck and D. H. Kelly. Contrast gain measurements and the transient/sustained dichotomy. *JOSA*, Vol. 71, Issue 11, pp. 1335-1342 (1981)
- [48] Burbeck CA. Exposure-duration effects in localization judgments. *J Opt Soc Am A.* 1986 Nov;3(11):1983-8.
- [49] Burton G., Haig N.(1984). Effects of the Seidel aberrations on visual target discrimination. *Journal of the Optical Society of America A*, 1, 373385.

- [50] A. Burvall, E. Daly, S.R. Chamot, and C. Dainty. Linearity of the pyramid wavefront sensor. *Optics Express*, Vol. 14, Issue 25, pp. 11925-11934 (2006)
- [51] F. W. Campbell and A. H. Gregory. Effect of size of pupil on visual acuity. *Nature*, 187:1121-1123, 1960.
- [52] F. W. Campbell and J. G. Robson, Application of Fourier analysis to the visibility of gratings, *J. Physiol. (London)* 197, 551-566 (1968).
- [53] , F. W. Campbell and L. Maffei. Electrophysiological evidence for the existence of orientation and size detectors in the human visual system. *J Physiol.* 1970 May; 207(3): 635-652.
- [54] M. Carrasco, C. Penpeci-Talgar, M. Eckstein, Spatial covert attention increases contrast sensitivity across the CSF: support for signal enhancement, *Vision Research* 40 (2000) 1203-1215
- [55] M. Carrasco(2011). Visual Attention: The past 25 years. *Vision Research*, 51, 1484-1525.
- [56] JF Castejon-Monchon, N. Lopez-Gil, A. Benito, P. Artal. Ocular wavefront statistics in a normal young population. *Vis. Res.* 2002;42:1661-1677.
- [57] A. de Castro, P. Rosales, and S. Marcos. "Tilt and decentration of intraocular lenses in vivo from Purkinje and Scheimpflug imaging. Validation study," *J. Cataract Refract. Surg.* 33, 418-429 (2007).
- [58] A. de Castro, S. Ortiz, E. Gamba, D. Siedlecki, and S. Marcos. Three-dimensional reconstruction of the crystalline lens gradient index distribution from OCT imaging. *Optics Express*, Vol. 18, Issue 21, pp. 21905-21917 (2010)
- [59] F. Castignoles, M. Flury, and T. Lepine, Comparison of the efficiency, MTF and chromatic properties of four diffractive bifocal intraocular lens designs, *Optics Express*, Vol. 18, Issue 5, pp. 5245-5256 (2010)

- [60] W.N. Charman, J.A.M. Jennings, Objective measurements of the longitudinal chromatic aberration of the human eye, *Vision Research* Volume 16, Issue 9, 1976, 9991005
- [61] W. N. Charman and G. Heron. Fluctuations in accommodation; a review. *Ophthalm. Physiol. Opt.*, 8:153164, 1988.
- [62] X. Cheng, A. Bradley, and L. N. Thibos, Predicting subjective judgment of best focus with objective image quality metrics, *J. Vision* 4, 310-321 (2004).
- [63] L. Chen, P. Artal, D.Gutierrez, D.R. Williams (2007) Neural compensation for the best aberration correction. *J Vis* 7: 19.
- [64] X. Cheng, A. Bradley, S. Ravikumar, L.N. Thibos (2010). A comparison of the effects of Seidel and Zernike aberrations on visual acuity for monochromatic light. *Optometry and Vision Science*, 27, 300312.
- [65] A. Ravikumar, E.J. Sarver, R.A. Applegate. Change in visual acuity is highly correlated with change in six image quality metrics independent of wavefront error and/or pupil diameter. *Journal of Vision* (2012) 12(10):11, 113.
- [66] S. T. L. Chung, D. M. Levi, G. E. Legge. Spatial frequency properties and contrast properties of crowding. *Vision Research*, 41, 18331850(2001).
- [67] N. J. Coletta and V. Sharma, Effects of luminance and spatial noise on interferometric contrast sensitivity, *J. Opt. Soc. Am. A* 12, 2244-2251 (1995).
- [68] J.E. Coppens, L. Franssen, T.J. Van den Berg. Wavelength dependence of intraocular straylight. *Exp Eye Res* 82:5 (2006).
- [69] M. Corbetta, GL. Shulman. Control of goal-directed and stimulus driven attention in the brain. *Nat Rev Neurosci.* 3:201–215. (2002)
- [70] C. A. Curcio, KA. Allen. Topography of ganglion cells in human retina. *J Comp Neurol* 1990;300:52.
- [71] Guang-Ming Dai. *Wavefront Optics for Vision Correction*. SPIE Press, 2008

- [72] E. Dalimier and C. Dainty. Comparative analysis of deformable mirrors for ocular adaptive optics. (2005) / Vol. 13, No. 11 / Optics Express 427.
- [73] E. Dalimier, C. Dainty, J. Barbur, Effects of higher-order aberrations on contrast acuity as a function of light level *Journal of Modern Optics* **2008** 55, 791-803
- [74] E. Dalimier, C. Dainty, Use of a customized vision model to analyze the effects of higher-order ocular aberrations and neural filtering on contrast threshold performance *JOSA A* **2008** 25, 2078-2087
- [75] E. Dalimier, E. Pailos, R. Rivera, R. Navarro, Experimental validation of a Bayesian model of visual acuity. *J Vis.* 2009 Jul 21;9(7):12.
- [76] F. C. Delori and K. P. Pflibsen. Spectral reflectance of the human ocular fundus. *Appl. Opt.*, 28(6):1061-1077, 1989.
- [77] F.C. Delori, R.H. Webb, D.H. Sliney. Maximum permissible exposures for ocular safety (ANSI 2000), with emphasis on ophthalmic devices *J. Opt. Soc. Am. A*/Vol. 24, No. 5/May 2007
- [78] Stanislas Dehaene and Jean-Pierre Changeux, Neural Mechanisms for Access to Consciousness. *The cognitive neurosciences*, 3rd edition
- [79] Stanislas Dehaene, Lionel Naccache, Towards a cognitive neuroscience of consciousness: basic evidence and a workspace framework, *Cognition* 79 (2001) 1-37
- [80] Dehaene S, Changeux JP, Naccache L, Sackur J, Sergent C., Conscious, pre-conscious, and subliminal processing: a testable taxonomy. *Trends Cogn Sci.* 2006 May;10(5):204-11.
- [81] S. Delord. Which Mask is the Most Efficient: A Pattern or a Noise? It Depends on the Task. *Visual Cognition*, 1998, 5 (3), 313-338.

- [82] C. Deruelle, J. Fagot. Categorizing facial identities, emotions, and genders: Attention to high- and low-spatial frequencies by children and adults. *J. Experimental Child Psychology* 90 (2005) 17218.
- [83] R. Desimone, J. Duncan, Neural mechanisms of selective visual attention. *Annual Rev Neurosci.* 1995;18:193-222.
- [84] J. Moran and R. Desimone. Selective attention gates visual processing in the extrastriate cortex. 1985; *Science*, 229,782-784.
- [85] R. L. De Valois and K. K. De Valois. *Spatial Vision*. Oxford University Press, 198 Madison Avenue, New York, New York 10016-4314, 1990.
- [86] L. Diaz-Santana and C. Dainty, Effects of Retinal Scattering in the Ocular Double-Pass Process, *J. Opt. Soc. Am. A* 18, 14371444 (2001)
- [87] L. Diaz-Santana, C. Torti, I. Munro, P. Gasson, and C. Dainty, Benefit of Higher Closed-Loop Bandwidths in Ocular Adaptive Optics, *Opt. Express* 11, 25972605 (2003).
- [88] V. Di Lollo, J. T. Enns, & R. A. Rensink (2000). Competition for consciousness among visual events: The psychophysics of reentrant visual processes. *Journal of Experimental Psychology: General*, 129, 481-507.
- [89] V. Di Lollo Temporal integration in visual memory. *J Exp Psychol Gen.* 1980 Mar;109(1):75-97.
- [90] N. Doble, D. T. Miller, G. Yoon, D. R. Williams. Requirements for discrete actuator and segmented wavefront correctors for aberration compensation in two large populations of human eyes. *Applied Optics*, 46, 45014514(2007).
- [91] E. R. Dowski and W. T. Cathey, "Extended depth of field through wave-front coding," *Appl. Opt.* 34, 1859-1866 (1995).

- [92] Dragoi, V., Sharma, J., Miller, E. K., & Sur, M. (2002). Dynamics of neuronal sensitivity in visual cortex and local feature discrimination. *Nature Neuroscience*, 5, 883891.
- [93] M. Dubbelman, G. L. Van der Heijde, H. A. Weeber, and G.F. J. M. Vrensen, Changes in the internal structure of the human crystalline lens with age and accommodation, *Vision Res.* 43, 23632375 (2003).
- [94] A. Dubra, C. Paterson, and C. Dainty. Double lateral shearing interferometer for the quantitative measurement of tear film topography. Vol 44,(7) *Applied Optics* (2005).
- [95] S.L. Elliott, M.A. Georgeson, M.A. Webster. Response normalization and blur adaptation: Data and multi-scale model. *J Vis* 11:(2011)
- [96] J.T. Enns and V. Di Lollo. Object substitution: A New Form of Masking in Unattended Visual Locations. *Psychological Science* (1997) Volume: 8, Issue: 2, Pages: 135-139
- [97] J. T. Enns (2004). Object substitution and its relation to other forms of visual masking. *Vision Research*, 44, 13211331.
- [98] S.L. Elliott, M.A. Georgeson, M.A. Webster (2011) Response normalization and blur adaptation: Data and multi-scale model. *J Vis* 11:
- [99] Escudero-Sanz and R. Navarro, "Off-axis aberrations of a wide-angle schematic eye model," *J. Opt. Soc. Am. A Opt. Image Sci. Vis.* 16, 1881-1891 (1999).
- [100] E. J. Fernández, P. M. Prieto, and P. Artal, "Adaptive optics binocular visual simulator to study stereopsis in the presence of aberrations," *J. Opt. Soc. Am. A* 27, A48-A55 (2010).
- [101] J. R. Fienup and J. J. Miller. Aberration correction by maximizing generalized sharpness metrics *JOSA A*, Vol. 20, Issue 4, pp. 609-620 (2003)

- [102] E. J. Fernández, I. Iglesias, and P. Artal. Closed-loop adaptive optics in the human eye. *Opt. Lett.*, 26(10):746748, 2001.
- [103] E. J. Fernández, S. Manzanera, P. Piers, and P. Artal, Adaptive optics visual simulator, *J. Refract. Surg.* 18, S634-S638 (2002).
- [104] Enrique Fernandez and Pablo Artal. Membrane deformable mirror for adaptive optics: performance limits in visual optics, *Optics Express*, Vol. 11, Issue 9, pp. 1056-1069 (2003)
- [105] E. J. Fernández, L. Vabre. Adaptive optics with a magnetic deformable mirror: applications in the human eye. (2006) / Vol. 14, No. 20 / *Optics Express*.
- [106] E. J. Fernández and P. Artal. Ocular aberrations up to the infrared range: from 632.8 to 1070 nm. *Optics Express*, Vol. 16, Issue 26, pp. 21199-21208 (2008).
- [107] Field D. J., Brady N.(1997). Visual sensitivity, blur and the sources of variability in the amplitude spectra of natural scenes. *Vision Research*, 37, 33673383.
- [108] J. R. Fienup, Phase-retrieval algorithms for complicated optical systems, *Appl. Opt.* 32, 17371746 1993.
- [109] A. V. Flevaris, S. Bentin, and L. C. Robertson. Local or Global? Attentional selection of spatial frequencies binds shapes to hierarchical levels. *Psychol Sci.* 2010 March 1; 21(3): 424431.
- [110] A. V. Flevaris, S. Bentin, and L. C. Robertson. Attentional selection of relative SF mediates global versus local processing: Evidence from EEG. *J Vis* June 13, 2011 11(7): 11
- [111] RA Frazor, DG Albrecht, WS Geisler, AM Crane. 2004. Visual cortex neurons of monkeys and cats: temporal dynamics of the spatial frequency response function. *J Neurophysiol.* 91:2607–2627.

- [112] L. Franssen, J.E. Coppens, T.J.T.P. van den Berg. Compensation comparison method for assessment of retinal straylight. *Invest Ophthalmol Vis Sci.* 2006;47:768-76.
- [113] M.A. Georgeson, G.D. Sullivan, Contrast constancy: deblurring in human vision by spatial frequency channels, *J Physiol.* 1975 Nov;252(3):627-56.
- [114] M. Glanc, E. Gendron, F. Lacombe, D. Lafaille, J.-F. L. Gargasson, and P. Lena, Towards Wide-Field Retinal Imaging with Adaptive Optics, *Opt. Commun.* 230, 225238 (2004).
- [115] Valerie Goffaux, Jaap van Zon, Christine Schiltz, The horizontal tuning of face perception relies on the processing of intermediate and high spatial frequencies.
- [116] V Goffaux, J Peters, J Haubrechts, C Schiltz, B Jansma, R Goebel. From coarse to fine? Spatial and temporal dynamics of cortical face processing. *Cereb Cortex.* 2011 Feb;21(2):467-76. doi: 10.1093/cercor/bhq112.
- [117] Gold J. M., Bennett P. J., Sekuler A. B.(1999). Identification of band-pass filtered letters and faces by human and ideal observers. *Vision Research*, 39, 35373560.
- [118] A.Gmez-Vieyra, A. Dubra, D. Malacara-Hernandez, and D. R. Williams. First-order design of off-axis reflective ophthalmic adaptive optics systems using afoocal telescopes. 2009 / Vol. 17, No. 21 / *Optics Express*
- [119] C. Gonzalez, I. Pascual, A. Bacete, and A. Fimia, Elimination and minimization of the spherical aberration of intraocular lenses in high myopia, *Ophthalmic. Physiol. Opt.* 16, 19-30 (1996).
- [120] A.r V. Goncharov and C. Dainty. Wide-eld schematic eye models with gradient-index lens. Vol. 24, No. 8, August 2007, *J. Opt. Soc. Am.*
- [121] A. V. Goncharov, M. Nowakowski, M.T. Sheehan, and C. Dainty. Reconstruction of the Optical System of the Human Eye with Reverse Ray-Tracing. 4 February 2008 / Vol. 16, No. 3 / *Optics Express*.

- [122] J.W. Goodman Introduction to Fourier optics. McGraw-Hill.(1996)
- [123] M. D. Gottlieb and J. Wallman, Retinal activity modulates eye growth: evidence from rearing in stroboscopic illumination, Soc. Neurosci. Abstr. 13, 1297 (1987).
- [124] P. de Gracia, C. Dorronsoro, E. Gamba, G. Marin, M. Hernandez, and S. Marcos, Combining coma with astigmatism can improve retinal image over astigmatism alone, Vision Res. 50(19), 20082014 (2010).
- [125] D. C. Gray, W. Merigan, J. I. Wolfing, B. P. Gee, J. Porter, A. Dubra, T. H. Twietmeyer, K. Ahamd, R. Tumbar, F. Reinholz, and D. R. Williams, In vivo fluorescence imaging of primate retinal ganglion cells and retinal pigment epithelial cells, Opt. Express 14(16), 71447158 (2006).
- [126] C.M. Gray, P. Knig, A.K. Engel, W. Singer. Oscillatory responses in cat visual cortex exhibit inter-columnar synchronization which reflects global stimulus properties. Nature 338: 334-337 (1989).
- [127] Greenwald , A. G. Draine , S. C. Abrams , R. L. . Three cognitive markers of unconscious semantic activation. Science, (1996)273, 1699-1702.
- [128] A. Guirao, D. R. Williams, and I. G. Cox, Effect of rotation and translation on the expected benefit of an ideal method to correct the eye's higher-order aberrations, J. Opt. Soc. Am. A 18, 1003-1015 (2001).
- [129] A. Guirao, J. Porter, L. Chen, B. Singer and D. Williams. Image metrics for predicting subjective image quality. Optom. Vis. Sci., 82(5):358 369, 2005.
- [130] A. Guirao, J. Porter, D. R. Williams, and I. G. Cox. Calculated impact of higher-order monochromatic aberrations on retinal image quality in a population of human eyes. J. Opt. Soc. Am. A, 19(1):19, 2002.
- [131] A. Guirao, and D. R. Williams, A method to predict refractive errors from wave aberration data, Optom. Vision Sci. 80, 36-42 (2003).

- [132] A. Guirao, J. Tejedor, and P. Artal, Corneal aberrations before and after small-incision cataract surgery, *Invest. Ophthalmol. Visual Sci.* 45, 4312-4319 (2004).
- [133] A. Gullstrand, Appendix II, in *Handbuch der Physiologischen Optik*, 3rd ed. 1909, J. P. Southall trans., ed. (Optical Society of America, 1924), Vol. 1, pp. 351352
- [134] G. Gescheider *Psychophysics: The fundamentals*, in Psychology Press, 3rd Ed. 1997, 448 pages.
- [135] K. M. Hampson, S.S. Chin, and E. A. Mallen. Dual wavefront sensing channel monocular adaptive optics system for accommodation studies. *Optics Express*, Vol. 17, Issue 20, pp. 18229-18240 (2009)
- [136] S. He, P. Cavanagh, J. Intriligator, Attentional resolution and the locus of visual awareness, *Nature*. 1996 ;383(6598):334-7.
- [137] S. He & D.I. A. MacLeod. Orientation-selective adaptation and tilt after-effect from invisible patterns. *Nature*. 2001 ;411: 473-476.
- [138] F. Hermens, M.H. Herzog. The effects of the global structure of the mask in visual backward masking. *Vision Res.* 2007;47(13):1790-7
- [139] H. Hofer, P. Artal, B. Singer, J. L. Aragon, and D. R. Williams, Dynamics of the eye's wave aberration, *J. Opt. Soc. Am. A* 18, 497-506 (2001).
- [140] H. Hofer, L. Chen, G. Y. Yoon, B. Singer, Y. Yamauchi, and D. R. Williams. Improvement in retinal image quality with dynamic correction of the eyes aberrations. *Opt. Express*, 8(11):631643, 2001
- [141] M. J. Hogan, J. A. Alvarado, and J. E. Weddell, *Histology of the Human Eye: An Atlas and Textbook* (W. B. Saunders Compagny, Philadelphia, USA, 1971).
- [142] J.T. Holladay, T.C. Prager, T.Y. Chandler: A three-part system for refining intraocular lens power calculations. *J Cataract Refract Surg* 14:17-24, 1988.

- [143] Howarth PA, Bradley A. The longitudinal chromatic aberration of the eye and its correction. *Vis Res.* 1986;26:361366.
- [144] D. Hubel, and T. Wiesel (1962). Receptive fields, binocular interaction and functional architecture in the cats visual cortex. *J. Physiol.* 160, 106154.
- [145] Kuo HY, Schmid KL, Atchison DA. Visual backward masking performance in young adult emmetropes and myopes. *Optom Vis Sci.* 2012 Jan;89(1):E90-6.
- [146] Ignacio Iglesias. Parametric wave-aberration retrieval from point-spread function data by use of a pyramidal recursive algorithm. 1998 Vol. 37, No. 23 *Applied Optics*
- [147] Iskander D., Collins M., Davis B., Carney L.(2000). Monochromatic aberrations and characteristics of retinal image quality. *Clinical and Experimental Optometry*, 83, 315322.
- [148] R. Iskander. Computational Aspects of the Visual Strehl Ratio. *Optometry & Vision Science: Vol 83, 57-59 (2006).*
- [149] International Organization for Standardization. ISO 11979-3:2006 Ophthalmic implants – Intraocular lenses – Part 3: Mechanical properties and test methods. 2006
- [150] Jung GH, Kline DW (2010) Resolution of blur in the older eye: Neural compensation in addition to optics? *J Vis* 10(5) 7: 19.
- [151] K. S. Kamal, Intraocular lens manufacturing process, B. L. Incorporated, ed. (USA, 2002).
- [152] P. M. Kiely, G. Smith, and L. G. Carney, "The mean shape of the human cornea," *Optica Acta* 29, 1027-1040 (1982).
- [153] K.MJ, L. Zheleznyak, S. Macrae, H. Tchah, G. Yoon, Objective evaluation of through-focus optical performance of presbyopia-correcting intraocular lenses using an optical bench system. *J Cataract Refract Surg.* 2011 Jul;37(7):1305-12.

- [154] S. Koh, C. Tung, J. Aquavella, R. Yadav, J. Zavislan, and G. Yoon. Simultaneous Measurement of Tear Film Dynamics Using Wavefront Sensor and Optical Coherence Tomography IOVS 2010 51:3441-3448
- [155] Kooijman,A.C., Light distribution on the retina of a wide-angle theoretical eye, J. Opt. Soc. Am. 73, 15441550 (1983)
- [156] K. Kriechbaum, O. Findl, P. R. Preussner, C. Kppl, J. Wahl, and W. Drexler, Determining postoperative anterior chamber depth, J. Cataract Refract. Surg. 29(11), 21222126 (2003).
- [157] B. V. K. Vijaya Kumar and L. Hassebrook, Performance measures for correlation filters. Applied Optics, Vol. 29, Issue 20, pp. 2997-3006 (1990)
- [158] J. Kumler, Designing and specifying aspheres for manufacturability, in Current Developments in Lens Design and Optical Engineering VI(SPIE, San Diego, CA, USA, 2005), pp. 58740C58749.
- [159] A. J. Lambert, E. M. Daly, E. deLeStrange & J. C. Dainty, Supplementary active optics for illumination within an adaptive optics system, J. Mod. Opt. Volume 58, Issue 19-20, 2011.
- [160] V.A.F. Lamme. Why visual attention and awareness are different. Trends in Cognitive Sciences, 7, 1218(2003).
- [161] V.A.F. Lamme. Towards a true neural stance on consciousness. Trends in Cognitive Sciences, 10, 494-501(2006).
- [162] K. Langley, DJ Fleet, PB Hibbard. Linear filtering precedes nonlinear processing in early vision. Curr Biol. 1996 Jul 1;6(7):891-6.
- [163] M. Larsson, C. Beckman, A. Nyström, S. Hrd, and J. Sjöstrand. Optical properties of diffractive, bifocal, intraocular lenses.Applied Optics, Vol. 31, Issue 13, pp. 2377-2384 (1992)

- [164] Lea99 Leat S. J., Li W., Epp K.. Crowding in central and eccentric vision: The effects of contour interaction and attention. *Investigative Ophthalmology and Visual Science*, 40, 504512 (1999).
- [165] Y. Le Grand and S. G. El Hage, *Physiological Optics* (Springer-Verlag, 1980).
- [166] Legras R., Chateau N., Charman W.(2004). Assessment of just-noticeable differences for refractive errors and spherical aberration using visual simulation. *Optometry and Vision Science*, 81, 718728.
- [167] W.R. Levick, J.L. Zack. Response of cat retinal cells to brief flashes of light. *J. Physiol.* 206, 677700 (1970).
- [168] Y. Levy, O. Segal, D. Zadok. Ocular higher-order aberrations in eyes with supernormal vision. *Am J Ophthalmol.* 2005;139:225228.
- [169] K.Y. Li, G. Yoon. Changes in aberrations and retinal image quality due to tear film dynamics. *Opt Express.* 2006;14(25):12552-9.
- [170] B.Liang,, R. Liu, Y. Dai, J. Zhou, Y. Zhou, & Y. Zhang (2012). Effects of ocular aberrations on contrast detection in noise. *Journal of Vision*, 12(8):3, 115
- [171] J. Liang and D.R. Williams, Aberrations and retinal image quality of the normal human eye. *JOSA A*, Vol. 14, Issue 11, pp. 2873-2883 (1997)
- [172] J. Liang, D.R. Williams, D.T. Miller(1997). Supernormal vision and high-resolution retinal imaging through adaptive optics. *Journal of the Optical Society of America A*, 14, 28842892.
- [173] H. L. Liou and N. A. Brennan, Anatomically accurate, finite model eye for optical modelling, *J. Opt. Soc. Am. A* 14(8), 16841695 (1997).
- [174] M.S. Livingstone and D.H. Hubel. Psychophysical Evidence for Separate Channels for the Perception of Form, Color, Movement, and Depth. *The Journal of Neuroscience*, November 1987, 7(11): 3418-3488.

- [175] E. Logean, E. Dalimier, and C. Dainty, Measured double-pass intensity point-spread function after adaptive optics correction of ocular aberrations *Opt. Express* **2008** 16, 17348-17357.
- [176] W. Lotmar, Theoretical eye model with aspherics, *J. Opt.Soc. Am.* 61, 1522-1529 (1971)
- [177] C. W. Lu and G. Smith, The Aspherizing Of Intraocular Lenses, *Oph. Phys. Opt.* 10(1), 5466 (1990).
- [178] S.L. Macknik, M.S. Livingstone. Neuronal correlates of visibility and invisibility in the primate visual system. *Nat. Neurosci.* 1 (2), 144-149(1998).
- [179] V.N. Mahajan, *Optical Imaging and Aberrations: Part I. Ray Geometrical Optics* (SPIE Press Book), 1998
- [180] Virendra N. Mahajan, *Optical Imaging and Aberrations: Part II. Wave Diffraction Optics* (SPIE Press Book), 1998
- [181] D. Malacara. *Optical shop testing*. John Wiley & Sons, Inc, 2nd edition, 1992.
- [182] S. Manzanera, S. Norrby P.A. Piers, E.J. Fernandez and P. Artal. Adaptive optics simulation of intra-ocular lenses with modified spherical aberration. *J. Ref. Surg.*, 45(12):4601-4610, 2004.
- [183] S. Manzanera, C. Canovas, P.M. Prieto, P. Artal. A wavelength tunable wavefront sensor for the human eye. *Opt Express*. 2008 May 26;16(11):7748-55.
- [184] S. Manzanera, M. A. Helmbrecht, C. J. Kempf, and A. Roorda, MEMS segmented-based adaptive optics scanning laser ophthalmoscope. *Biomedical Optics Express*, Vol. 2, Issue 5, pp. 1204-1217 (2011).
- [185] Marsack JD, Thibos LN, Applegate RA. Metrics of optical quality derived from wave aberrations predict visual performance. *J Vis.* 2004;4:322-328.

- [186] S. Marcos, S. Barbero, and I. Jimnez-Alfaro, Optical quality and depth-of-field of eyes implanted with spherical and aspheric intraocular lenses, *J. Refract. Surg.* 21(3), 223235 (2005).
- [187] S. Marcos, P. Rosales, L. Llorente, and I. Jimenez-Alfaro, Change in corneal aberrations after cataract surgery with 2 types of aspherical intraocular lenses, *J. Cataract. Refract. Surg.* 33, 217-226 (2007).
- [188] S. Marcos, L. Sawides, E. Gamba, C. Dorronsoro. Influence of adaptive-optics ocular aberration correction on visual acuity at different luminances and contrast polarities. *J Vis* 8: 1112 (2008).
- [189] S. Marcos, P. Rosales, L. Llorente, S. Barbero, and I. Jimnez-Alfaro, Balance of corneal horizontal coma by internal optics in eyes with intraocular artificial lenses: evidence of a passive mechanism, *Vision Res.* 48(1), 7079 (2008).
JA. Mazer, WE. Vinje, J. McDermott, PH. Schiller, JL. Gallant. Spatial frequency and orientation tuning dynamics in area V1. *Proc Natl Acad Sci U S A.* 99:16451650 (2002).
- [190] Meripán and Maunsell. How parallel are the primate visual pathways. *Annu. Rev. Neurosci.* 16:369-402 (1993)
- [191] J. S. McLellan, S. Marcos, P. M. Prieto, and S. A. Burns, Imperfect optics may be the eyes defence against chromatic blur, *Nature* 417, 174-176 (2002).
- [192] J. S. McLellan, P. M. Prieto, S. Marcos, and S. A. Burns, Effects of interactions among wave aberrations on optical image quality, *Vision Res.* 46(18), 30093016 (2006).
- [193] Merigan & Maunsell, How parallel are the primate visual pathways. *Annual Review Neuroscience*, 16, 369-402 (1993).
- [194] C.F. Michaels, & M.T. Turvey. Central sources of visual masking: Indexing structures supporting seeing at single, brief glance. *Psychological Research*, 41, 161(1979).

- [195] Mihashi T. Howland H. C. Kelly, J. E. Compensation of corneal horizontal vertical astigmatism, lateral coma, and spherical aberration by internal optics of the eye. 4:262- 271, 2004.
- [196] Milner and Goodale, 1995, A.D. Milner, M.A. Goodale, The visual brain in action. Oxford University Press, Oxford (1995)
- [197] Mon-Williams M., Tresilian J. R., Strang N. C., Kochhar P., Wann J. P.(1998). Improving vision: Neural compensation for optical defocus. Proceedings of Biological Sciences, 265, 7177.
- [198] M. C. Morrone and D. C. Burr, Feature detection in human vision: A phase-dependent energy model, in Proc. R. Soc. Lond. B, Dec. 1988, pp. 221245.
- [199] Richard A. Muller and Andrew Buffington, Real-time correction of atmospherically degraded telescope images through image sharpening JOSA, Vol. 64, Issue 9, pp. 1200-1210 (1974)
- [200] Naccache L, Blandin E, Dehaene S., Unconscious masked priming depends on temporal attention. Psychol Sci. 2002 Sep;13(5):416-24.
- [201] Nakayama K & Silverman GH. Temporal and spatial characteristics of the upper displacement limit for motion in random dots. Vision Res. 24: 293-299, 1984.
- [202] Ken Nakayama & Gerald H. Silverman. Serial and parallel processing of visual feature conjunctions. Nature 320, 264 - 265 (1986)
- [203] Takashi Nagano. Temporal sensitivity of the human visual system to sinusoidal gratings. JOSA, Vol. 70, Issue 6, pp. 711-716 (1980)
- [204] J. Narvaez, G. Zimmerman, R. D. Stulting, and D. H. Chang, "Accuracy of intraocular lens power prediction using the Hoffer Q, Holladay 1, Holladay 2, and SRK/T formulas," J. Cataract Refract. Surg. 32, 2050-2053 (2006).

- [205] R. Navarro, J. Santamaria, and J. Bescos, "Accommodation-dependent model of the human eye with aspherics," *J. Opt. Soc. Am. A* 2, 1273-1281 (1985).
- [206] R. Navarro and E. Moreno-Barriuso. Laser ray-tracing method for optical testing. *Opt. Lett.*, 24(14):951953, 1998.
- [207] E. Moreno-Barriuso and R. Navarro. Laser ray tracing versus Hartmann-Shack sensor for measuring optical aberrations in the human eye. *J. Opt. Soc. Am. A*, 17(6):974985, 2000.
- [208] Neri P, Heeger DJ., Spatiotemporal mechanisms for detecting and identifying image features in human vision., *Nat Neurosci.* 2002 Aug;5(8):812-6.
- [209] P. Neri. Coarse to fine dynamics of monocular and binocular processing in human pattern vision. *Proc. Natl. Acad. Sci. U.S.A.* 108 (26): 10726-31(2011).
- [210] P Neri, D Levi. Temporal dynamics of directional selectivity in human vision. *J Vis.* 2008 Jan 31;8(1):22.1-11. doi: 10.1167/8.1.22.
- [211] O. Nestares, R. Navarro, and B. Antona, Bayesian model of Snellen visual acuity, *J. Opt. Soc. Am. A* 20, 1371-1381 (2003).
- [212] S. Norrby, P. Artal, P. A. Piers, and M. Van der Mooren, Methods of obtaining ophthalmic lenses providing the eye with reduced aberrations, *N. Pharmacia Groningen BV* (2000).
- [213] S. Norrby, P. Piers, C. Campbell, and M. van der Mooren. Model eyes for evaluation of intraocular lenses. *Applied Optics*, Vol. 46, Issue 26, pp. 6595-6605 (2007)
- [214] S. Norrby, "Sources of error in intraocular lens power calculation," *J. Cataract Refract. Surg.* 34, 368-376 (2008).
- [215] N. E. Norrby, L. W. Grossman, E. P. Geraghty, C. F. Kreiner, M. Mihori, A. S. Patel, V. Portney, and D. M. Silberman, "Determining the imaging quality of intraocular lenses," *J. Cataract Refract. Surg.* 24, 703-714 (1998).

- [216] Erika dlund, Henri-Francois Raynaud, Caroline Kulcsr, Fabrice Harms, Xavier Levecq, Franck Martins, Nicolas Chateau, and Adrian Gh. Podoleanu. Control of an electromagnetic deformable mirror using high speed dynamics characterization and identification. *Applied Optics*, Vol. 49, Issue 31, pp. G120-G128 (2010)
- [217] O. Neumann, I. Scharlau. Visual attention and the mechanism of metacontrast. *Psychological Research* (2006). DOI 10.1007/s00426-006-0061-7
- [218] H.Ogmens, Breitmeyer BG., R. Melvin. The what and the where in visual masking. *Visual Research*. (2003) 43;1337-1350.
- [219] T. Olsen, Sources of error in intraocular lens power calculation, *J. Cataract Refract. Surg.* 18(2), 125129 (1992).
- [220] A. Oppenheim, J. Lim(1981). The importance of phase in signals. *Proceedings of the IEEE*, 69, 529541.
- [221] *Diffractive Optics: Design, Fabrication, and Test*” by Donald C. O’Shea, Thomas J. Suleski, Alan D. Kathman, Dennis W. Prather. *Tutorial Texts in Optical Engineering*. SPIE Press Monograph. Volume 62(2004)
- [222] E. Peli (1990). Contrast in complex images. *Journal of the Optical Society of America A*, 7, 20322040.
- [223] Pesudovs K (2005) Involvement of neural adaptation in the recovery of vision after laser Refractive surgery. *J Refract Surg* 21: 144147.
- [224] P. A. Piers; Henk A. Weeber; Pablo Artal; Sverker Norrby. Theoretical comparison of aberration-correcting customized and aspheric intraocular lenses. *J. Ref. Surg.*, 23:374384, 2007.
- [225] P. A. Piers, S. Manzanera, P. M. Prieto, N. Gorceix, and P. Artal, Use of adaptive optics to determine the optimal ocular spherical aberration, *J. Cataract Refractive Surg.* 33, 1721-1726 (2007).

- [226] Piotrowski L. N., Campbell F. W.(1982). A demonstration of the visual importance and flexibility of spatial-frequency amplitude and phase. *Perception*, 11, 337346.
- [227] O. Pomerantzeff, M. M. Pankratov, and G. J. Wang, Calculation of an IOL from the wide-angle optical model of the eye, *J. Am. Intraocul. Implant Soc.* 11(1), 3743 (1985).
- [228] David P. Pinero, Dolores Ortiz, and Jorge L. Alio, *Ocular Scattering, Optometry and vision science*. Vol. 87, NO. 9, PP. E682E696 (2010)
- [229] M. Posner. Orienting of attention. *Quarterly Journal of Experimental Psychology*, 32, 3-25
- [230] Porter J., Guirao A., Cox I. G., Williams D. R. (2001). Monochromatic aberrations of the human eye in a large population. *Journal of Optical Society of America A, Optics, Image Science, and Vision*, 18, 17931803.
- [231] P. R. Preussner, J. Wahl, H. Lahdo, B. Dick, and O. Findl, Ray tracing for intraocular lens calculation, *J. Cataract. Refract. Surg.* 28, 1412-1419 (2002).
- [232] R. B. Rabbetts, Bennett & Rabbetts' clinical visual optics (Elsevier/Butterworth Heinemann, Edinburgh; New York, 2007).
- [233] M. A. Rama, M. V. Perez, C. Bao, M. T. Flores-Arias and C. Gomez-Reino, Gradientindex crystalline lens model: A new method for determining the paraxial properties by axial and field rays, *Opt. Commun.* 249, 595 (2005).
- [234] Sowmya Ravikumar, Larry N. Thibos, and Arthur Bradley. Calculation of retinal image quality for polychromatic light
- [235] Sowmya Ravikumar, Arthur Bradley, and Larry Thibos. Phase changes induced by optical aberrations degrade letter and face acuity. *J Vis*, 2010 10(14): 18; *JOSA A*, Vol. 25, Issue 10, pp. 2395-2407 (2008).

- [236] DL. Ringach, MJ. Hawken, R. Shapley. Dynamics of orientation tuning in macaque primary visual cortex. *Nature* 387:281284 (1997).
- [237] DL. Ringach, CE. Bredfeldt, RM Shapley, MJ Hawken. Suppression of neural responses to non-optimal stimuli correlates with tuning selectivity in macaque V1. *J Neurophysiol* 87:10181027(2002).
- [238] PR Roelfsema, VA Lamme, & H. Spekreijse. (1998). Object-based attention in the primary visual cortex of the macaque monkey. *Nature* 395:376-38 1.
- [239] E.T. Rolls, M.J. Tovee. Processing speed in the cerebral cortex and the neurophysiology of visual masking. *Proc Biol Sci.* 1994 Jul 22;257(1348):9-15.
- [240] E. T. Rolls, M. J. Tovee, & S. Panzeri. The neurophysiology of backward visual masking: information analysis. *Journal of Cognitive Neuroscience*, 11 (3), 300-311(1999).
- [241] J. G. Robson. Spatial and Temporal Contrast-Sensitivity Functions of the Visual System *JOSA*, Vol. 56, Issue 8, pp. 1141-1142 (1966)
- [242] M. B. Sachs, J. Nachmias, and J. G. Robson, Spatial-frequency channels in human vision, *J. Opt. Soc. Am.* 61, 1176-1186 (1971).
- [1] Austin Roorda and David R. Williams, Optical fiber properties of individual human cones. *J Vis* September 17, 2002 2(5): 4
- [243] Roorda A, Romero-Borja F, Donnelly WJ III, Queener H, Hebert TJ, et al. (2002) Adaptive optics scanning laser ophthalmoscopy. *Opt Express* 10: 405412.
- [244] A. Roorda. Adaptive optics for studying visual function: A comprehensive review. *J Vis* June 15, 2011 11(5): 6;
- [245] P. Rosales, and S. Marcos, Customized computer models of eyes with intraocular lenses, *Opt. Express* ,, 15, 2204-2218 (2007).
- [246] M. Rosenfield, S. E. Hong, S. George (2004). Blur adaptation in myopes. *Optometry and Vision Science*, 81, 657662.

- [247] S. George, M. Rosenfield (2004). Blur adaptation and myopia. *Optometry and Vision Science*, 81, 543547.
- [248] M. Rosenfield, J. K. Portello, S. E. Hong, L. Ren, K. J. Ciuffreda (2003). Decay of blur adaptation. *Investigative Ophthalmology and Vision Science*, 44, 4315.
- [249] Rosser DA, Murdoch IE, Cousens SN. The effect of optical defocus on the test-retest variability of visual acuity measurements. *Invest Ophthalmol Vis Sci*. 2004 Apr;45(4):1076-9.
- [250] E. A. Rossi, P. Weiser, J. Tarrant, A. Roorda(2007). Visual performance in emmetropia and low myopia after correction of high-order aberrations. *Journal of Vision*, 7, (8):14, 114
- [251] E.A. Rossi, A. Roorda, The relationship between visual resolution and cone spacing in the human fovea. *Nature neuroscience*. 12/2009;
- [252] E.A. Rossi, A. Roorda, Is visual resolution after adaptive optics correction susceptible to perceptual learning? *J Vis*. 2010 10(12):11
- [253] F. Roddier. Curvature sensing and compensation: a new concept in adaptive optics. *Applied Optics*, Vol. 27, Issue 7, pp. 1223-1225 (1988).
- [254] Sabesan R., Ahmad K., Yoon G. Correcting highly aberrated eyes using large-stroke adaptive optics. *Journal of Refractive Surgery*, 23, 947952 (2007).
- [255] R. Sabesan and G. Yoon. Visual performance after correcting higher order aberrations in keratoconic eyes, *J Vis* May 13, 2009 9(5): 6.
- [256] R. Sabesan, G. Yoon. Neural compensation for long-term asymmetric optical blur to improve visual performance in keratoconic eyes. *Invest Ophthalmol Vis Sci* 51: 38353839 (2010).
- [257] Y. Sasaki, J. E. Nanez and T. Watanabe. Advances in visual perceptual learning and plasticity. *Nature reviews Neuroscience*, Vol11 (2010)

- [258] L. Sawides, S. Marcos, S. Ravikumar, L. N. Thibos, A. Bradley, M. A. Webster(2010). Adaptation to astigmatic blur. *Journal of Vision*, 10, (12):22, 115.
- [259] L. Sawides, E. Gamba, D. Pascual, C. Dorronsoro, S. Marcos (2010) Visual performance with real-life tasks under adaptive-optics ocular aberration correction. *J Vis* 10: 112.
- [260] L. Sawides, P. de Gracia, C. Dorronsoro, M. Webster, S. Marcos (2011) Adapting to blur produced by ocular high-order aberrations. *J Vis* 11: 111.
- [261] H. H. J. Shammas, *Intraocular lens power calculations* (Slack Incorporated 2004).
- [262] J.E. Raymond, K.L. Shapiro, K.M. Arnell, Temporary suppression of visual processing in an RSVP task: an attentional blink? *J Exp Psychol Hum Percept Perform.* 1992 Aug;18(3):849-60.
- [263] K.L. Shapiro , J.E. Raymond. The attentional blink. *Trend in cognitive science*, Volume 1, Issue 8, November 1997, Pages 291296
- [264] R. Shapley, E. Kaplan, and R. Soodak. Spatial summation and contrast sensitivity of X and Y cells in the lateral geniculate nucleus of the macaque. *Nature* 292: 543-545 (1981)
- [265] D. Siedlecki, H.S. Gini, On the longitudinal chromatic aberration of the intraocular lenses. *Optom Vis Sci.* 2007 Oct;84(10):984-9.
- [266] D. Siedlecki, H. Kasprzak, and B. K. Pierscionek, Schematic eye with a gradient-index lens and aspheric surfaces, *Opt. Lett.* 29, 11971199 (2004).
- [267] M. J. Simpson, Optical-Quality Of Intraocular Lenses, *J. Cataract. Refract. Surg.* 18, 86-94 (1992).
- [268] W. Singer, CM. Gray, Visual feature integration and the temporal correlation hypothesis. *Annu Rev Neurosci* 1995, 555-566.

- [269] M. S. Smirnov. Measurement of the wave aberration of the human eye. *Biophysics*, 6, 776795 (1961).
- [270] G. Smith. Ocular defocus, spurious resolution and contrast reversal. *Ophthalmic and Physiological Optics*, 2, 523 (1982).
- [271] Smith, Pokorny, Lee, Dacey. Sequential processing in vision: interaction of sensitivity regulation and temporal dynamics. *Vis. Res.* 48, 2649-56.
- [272] G. O. Smith, and D. A. Atchison, *The eye and visual optical instruments* (Cambridge University Press, 1997).
- [273] J. A. Solomon, D. G. Pelli. The visual filter mediating letter identification. *Nature*, 369, 395397 (1994).
- [274] H Spitzer, R Desimone, and J Moran. Increased attention enhances both behavioral and neuronal performance. *Science*. 1988; 240(4850):338-340.
- [275] H Supr, H Spekreijse, VA Lamme (2001) Two distinct modes of sensory processing observed in monkey primary visual cortex (V1). *Nat. Neurosci.* 4, 304-310. 40.
- [276] S. Norrby. Determining the imaging quality of intraocular lens. *J.Ref. Surg.*, 34:368376, 2008.
- [277] S. Norrby. Standardized methods for assessing the imaging quality of intraocular lenses. *Applied Optics*, Vol. 34, Issue 31, pp. 7327-7333 (1995)
- [278] W.H. Swanson, T. Ueno, V.C. Smith and J. Pokorny: Temporal modulation sensitivity and pulse detection thresholds for chromatic and luminance perturbations. *Journal of the Optical Society of America A* 4:1992-2005, 1987.
- [279] W. H. Southwell. Wave-front estimation from wave-front slope measurements. *J. Opt. Soc. Am.*, 70(8):9981006, 1980.
- [280] J. Tabernero, P. Piers, and P. Artal, Intraocular lens to correct corneal coma, *Opt. Lett.* 32, 406-408 (2007).

- [281] E. A. J. Tabernero, A. Benito and P. Artal. Mechanism of compensation of aberrations in the human eye. *J. Opt. Soc. Am. A*, 24:32743283, 2007.
- [282] Y. Tadmor, D. J. Tolhurst(1993). Both the phase and the amplitude spectrum may determine the appearance of natural images. *Vision Research*, 33, 141145.
- [283] L. N. Thibos, M. Ye, X. Zhang, and A. Bradley, The chromatic eye: a new reduced-eye model of ocular chromatic aberration in humans, *Appl. Opt.* 31(19), 35943600 (1992).
- [284] L. N. Thibos, M. Ye, X. Zhang and A. Bradley, Spherical aberration of the reduced schematic eye with elliptical refracting surface, *Optom. Vision Sci.* 74, 548 (1997)
- [285] L. N. Thibos, R. A. Applegate, J. T. Schwiegerling, R. Webb. Standards for reporting the optical aberrations of eyes, in *Vision Science and Its Applications*, Vol. 35 of Trends in Optics and Photonics Series, V. Lakshminarayanan, ed. (Optical Society of America, **2000**), 233-244.
- [286] L. N. Thibos, X. Hong, A. Bradley, and X. Cheng, Statistical variation of aberration structure and image quality in a normal population of healthy eyes, *J. Opt. Soc. Am. A* 19, 2329-2348 (2002).
- [287] L. N. Thibos, X. Hong, A. Bradley, and R. A. Applegate, Accuracy and precision of objective refraction from wavefront aberrations, *J. Vision* 4, 329-351 (2004).
- [288] A. Treisman. The binding problem. *Journal of Experimental Psychology: Learning, Memory, and Cognition*, 22, 27-47. 1996.
- [289] P. Tynan and R. Sekuler , Perceived spatial frequency varies with stimulus duration, *JOSA*, Vol. 64, Issue 9, pp. 1251-1255 (1974)
- [290] R. K. Tyson, *Principles of Adaptive Optics* (Academic, 1991), pp. 213-255.

- [291] A.B. Utkin, R. Vilar and A.J. Smirnov , On the relation between the wave aberration function and the phase transfer function for an incoherent imaging system with circular pupil, *Eur. Phys. J. D* 17, 145-148 (2001)
- [292] T. J. Van den Berg. Importance of pathological intraocular light scatter for visual disability. *Documenta Ophthalmologica*, 61, 327333 (1986).
- [293] T.J. Van den Berg, J.K. Ijspeert, P.W. de Waard. Dependence of intraocular straylight on pigmentation and light transmission through the ocular wall. *Vision Res* 1991;31:13617.
- [294] B. Vasudevan, K.J. Ciuffreda, & B. Wang. Subjective and objective depth-of-focus. *Journal of Modern Optics*,54, 1307-1316 (2007).
- [295] F. Vega, F. Alba-Bueno, and M. S. Millan. Energy Distribution between Distance and Near Images in Apodized Diffractive Multifocal Intraocular Lenses. *Invest Ophthalmol Vis Sci*. 2011;52:56955701.
- [296] E.A. Villegas, C. Gonzalez, B. Bourdoncle, T. Bonin, P. Artal. Correlation between optical and psychophysical parameters as function of defocus. *Optom Vis Sci*. 2002;79:60 67.
- [297] E. R. Villegas, L. Carretero, and A. Fimia, Optimum bending factor of intraocular lenses in pseudophakic eyes with high myopia, *J. Mod. Opt.* 44, 941-952 (1997).
- [298] E.A. Villegas, E. Alcon, and P. Artal, Optical Quality of the Eye in Subjects with Normal and Excellent Visual Acuity, *Invest Ophthalmol Vis Sci*. 2008;49:4688 4696
- [299] C. Vinette, F. Gosselin, P. G. Schyns. Spatio-temporal dynamics of face recognition in a flash: its in the eyes, *Cognitive Science* 28 (2004) 289301.
- [300] P. Vuillemier, J. L. Armony, J. Driver, & R. J. Dolan(2003). Distinct spatial frequency sensitivities for processing faces and emotional expressions. *Nature Neurosciences*, 6, 624631.

- [301] L. Weiskrantz *Blindsight: A case study and implications* (Oxford UP, Oxford) 1986.
- [302] Y. Yeshurun & M. Carrasco, Attention improves or impairs visual performance by enhancing spatial resolution, *Nature* 396, 72-75 (5 November 1998)
- [303] F. Yi, D.R. Iskander and M.I J. Collins. Estimation of the depth of focus from wavefront measurements. *Journal of vision* 2010. 10(4):3, 1-9
- [304] G. Y. Yoon and D. R. Williams. Visual performance after correcting the monochromatic and chromatic aberrations of the eye. *J. Opt. Soc. Am. A*, 19(2):266-275, 2002.
- [305] MS; Geunyoung Yoon, PhD; Jason Porter, PhD; Srinivas K. Rao, FRCSEd; Roy J, MSc; Mitalee Choudhury, BS. *Wavefront Aberrations in Eyes With Acrysof Monofocal Intraocular Lenses* Prema Padmanabhan.
- [306] A. B. Watson and D. G. Pelli, Quest: A bayesian adaptive psychometric method, *Percept. Psychophys.* 33, 113-120 (1983).
- [307] R. J. Watt. Scanning from coarse to fine spatial scales in the human visual system after the onset of a stimulus. *JOSA A*, Vol. 4, Issue 10, pp. 2006-2021 (1987) .
- [308] A. B. Watson and J. A. J. Ahumada, Predicting visual acuity from wavefront aberrations, *J. Vision* 8, 1-19 (2008).
- [309] R. H. Webb, and G. W. Hughes, Scanning laser ophthalmoscope, *IEEE Trans. Biomed. Eng.* BME-28(7), 488-492 (1981).
- [310] M. A. Webster, M. A. Georgeson, S. M. Webster. Neural adjustments to image blur. *Nature Neuroscience*, 5, 839-840 (2002).
- [311] Welford, *Aberrations of Optical Systems*. Series in Optics and Optoelectronics (1989).

- [312] D. R. Williams. Aliasing in human foveal vision. *Vision Research*, 25, 195205(1985).
- [313] D. R. Williams, N. J. Coletta. Cone spacing and the visual resolution limit. *Journal of the Optical Society of America A*, 4, 15141522 (1987).
- [314] H. Zhao, Optical ensemble analysis of intraocular lens performance through a simulated clinical trial with zemax, *Optics Letters*, Vol. 34, Iss. 1, pg. 7 (2008).
- [315] M. Zeppieri, S. Demirel, K. Kent, C.A. Johnson, Perceived spatial frequency of sinusoidal gratings, *Optom Vis Sci.* 2008 May;85(5):318-29.
- [316] R. J. Zawadzki, S. M. Jones, S. S. Olivier, M. T. Zhao, B. A. Bower, J. A. Izatt, S. Choi, S. Laut, and J. S. Werner, Adaptive-optics optical coherence tomography for high-resolution and high-speed 3D retinal in vivo imaging, *Opt. Express* 13(21), 85328546 (2005),
- [317] Zemax Development Corporation. Zemax ray-tracing program. 2001.
- [318] J. Zhou et al. The eye limits the brains learning potential. *Sci. Rep.*2, 364; (2012).